



Hierarchical approach for the global chassis control of an electric vehicle

Hussein Termous

► To cite this version:

Hussein Termous. Hierarchical approach for the global chassis control of an electric vehicle. Automatic Control Engineering. Université de Bordeaux, 2020. English. NNT : 2020BORD0081 . tel-02977884

HAL Id: tel-02977884

<https://theses.hal.science/tel-02977884>

Submitted on 26 Oct 2020

HAL is a multi-disciplinary open access archive for the deposit and dissemination of scientific research documents, whether they are published or not. The documents may come from teaching and research institutions in France or abroad, or from public or private research centers.

L'archive ouverte pluridisciplinaire **HAL**, est destinée au dépôt et à la diffusion de documents scientifiques de niveau recherche, publiés ou non, émanant des établissements d'enseignement et de recherche français ou étrangers, des laboratoires publics ou privés.

THÈSE

PRÉSENTÉE À

L'UNIVERSITÉ DE BORDEAUX

ÉCOLE DOCTORALE DES SCIENCES PHYSIQUES ET DE L'INGÉNIEUR

Par

Hussein TERMOUS

POUR OBTENIR LE GRADE DE

DOCTEUR

SPÉCIALITÉ : AUTOMATIQUE

Approche Hiérarchisée pour le Contrôle Global du Châssis d'un Véhicule Électrique

Sous la co-direction de Xavier MOREAU et Clovis FRANCIS

SOUTENUE LE 16 JUILLET 2020

Devant la commission d'examen formée de :

Mme.	Lydie NOUVELIERE	Maître de Conférences, HDR	Université Evry-Val-d'Essonne	Rapporteure
Mme.	Reine TALJ	Chargée de recherche CNRS, HDR	UTC Heudiasyc	Rapporteure
M.	Hassan NOURA	Professeur	Université Islamique au Liban	Président
M.	Hassan SHRAIM	Professeur	Université Libanaise	Examineur
M.	Xavier MOREAU	Professeur	IMS, Université de Bordeaux	Co-Directeur
M.	Clovis FRANCIS	Professeur	CRSI, Université Libanaise	Co-Directeur

Title || Hierarchical Approach for Global Chassis Control of an Electric Vehicle.

Abstract

Road transportation is shifting significantly toward electrification around the globe. A market for light electric mobility solutions had emerged where all-in-wheel devices are expected to play an important role in this new trend. This technology offers new opportunities and raises new challenges in Global Chassis Control (GCC) that rises, recently, to remarkable levels. This study is based on a supervision control approach for vertical, longitudinal, and lateral control in light electric vehicles. The developed control system designs rely on the CRONE method which can ensure the robustness of the stability degree against the system parametric variations. For vertical dynamics, various control solutions are developed for automotive suspensions to improve passenger comfort and road holding. For longitudinal dynamics, a study for the ABS function is done for braking system enhancement while considering the effect of the vertical dynamics. Then, a combination of ABS control and suspension control is presented in the sense of reducing the deterioration effect of vertical dynamics. Finally, the work is concerned by the development of vehicle lateral stability control, where the effect of the vehicle vertical dynamics was analyzed. The obtained results verify the effectiveness of the designed control strategies in enhancing the vehicle comfort, handling, and safety. Moreover, the well understanding of the influence of the vertical dynamics, as well as the key role of the controlled suspension on other vehicle dynamics, will open up new prospects to the development of new strategies for global chassis control of light electric vehicle.

Keywords: ABS control, Active suspension system, Automotive, CRONE Controller, Global Chassis Control, Lateral Stability, Vehicle dynamics.

Titre || Approche Hiérarchique pour le Contrôle Global du Châssis d'un Véhicule Électrique

Résumé

Le transport routier évolue considérablement vers l'électrification dans le monde entier. Un marché pour les solutions de mobilité légère électrifiée a émergé. Les dispositifs à transmission intégrale jouent un rôle important dans cette nouvelle tendance. Cette technologie offre de nouvelles opportunités et pose de nouveaux défis dans le contrôle de châssis globale « Global Chassis Control (GCC) » qui a récemment atteint des niveaux remarquables. Cette étude présente une approche de supervision pour le contrôle vertical, longitudinal et latéral dans les véhicules électriques légers. Le système de contrôle développé repose sur la méthode CRONE qui peut assurer la robustesse du degré de stabilité contre les variations paramétriques du système. Pour la dynamique verticale, diverses solutions de contrôle sont développées pour les suspensions automobiles afin d'améliorer le confort des passagers et la tenue de route. Pour la dynamique longitudinale, une étude de la fonction ABS est réalisée pour l'amélioration du système de freinage, tenant en compte l'effet de la dynamique verticale. Ensuite, une combinaison de contrôle ABS et de contrôle de suspension est présentée dans le but de réduire l'effet de détérioration de la dynamique verticale. Enfin, les travaux portent sur le développement du contrôle latéral de la stabilité du véhicule, où l'effet de la dynamique verticale du véhicule est analysé. Les résultats obtenus permettent de vérifier l'efficacité des stratégies de contrôle conçues pour améliorer le confort, la maniabilité et la sécurité du véhicule. En outre, la bonne compréhension de l'influence de la dynamique verticale, ainsi que le rôle clé de la suspension contrôlée sur les autres dynamiques du véhicule, ouvrira de nouveaux horizons pour le développement de nouvelles stratégies pour le contrôle global du châssis des véhicules électriques légers.

Mots-clés : Contrôle ABS, Système de suspension actif, Automobile, Contrôleur CRONE, Contrôle global du châssis, Stabilité latérale, Dynamique du véhicule.

Acknowledgement

First and foremost, I would like to thank God Almighty for giving me the strength, knowledge, ability and opportunity to undertake this research study. Without His blessings, this achievement would not have been possible. In the belief that: “The most thankful among you to God is he who is most thankful towards people”-Ali Zayn Al-Abidin [AS], I would like to express some words to the people who have guided me, shared time with me, and supported me during the past three years.

First, I would like to gratefully and sincerely thank my advisors, Professors Xavier Moreau and Clovis Francis, for their scientific understanding and for their precious support during my PhD studies. I have been so lucky to work with them, who were always available and gave me the best research conditions and professional opportunities. I look forward to further collaboration in the future.

I would like to thank Professor Hassan Noura for being the president of my doctoral committee; Professors Lydie Nouveliere, Reine Talj, and Hassan Shraim for their time to review my PhD thesis. Their detailed and valuable comments have contributed to the quality of this manuscript.

I have great pleasure in acknowledging my gratitude to my colleague in IMS Lab, Emna Hamrouni, for having interesting scientific and non-scientific discussions and sharing beautiful moments with me. I would like also to thank André Benine-Neto for his time, advices, and sharing knowledge which were really helpful to me.

My PhD life and my stay in France would not have been the same without my friends in Bordeaux. I address a particular acknowledgement to Mahdi, Kasem & Kasem, Mohammad Ali, Hassan, Ali, Hussein, Maarouf, Mohammad Mahdi, Ahmad, and Farah. I am eternally grateful to them for their care and never-ending support. We have spent very good moments together during my stay in Bordeaux and without them, my work might have not run smoothly.

My sincere thanks go to Hussein in France, Mahmoud in Germany, and Wissam & Tarek from Lebanon, for always being beside me, sharing with me the joy and difficulties, and always supporting me.

Last but by no means least, I would like to express my tremendous gratitude and my love to my family, who have always encouraged me to accomplish my objectives and most importantly to wisely advise me during all my life. Finally, I would like to dedicate this work to my mother. The patience, the understanding and her love, gave me the inspiration to face this adventure. Without her support and encouragement this work would not have been possible.

Hussein Termous
Beirut, Lebanon
July 2020

General Introduction

Curiosity leads researchers from different academic disciplines to look backward in the past for the origins of their subjects. They constantly ask questions like how it was started and where was the beginning? Who invent or discover and when? Indeed, reviewing the history is essential, it helps us to understand the linkages between past and present, and analyze the legacies of the past in the present to contribute to our future. In technology, history reveals a story of great inventors with brilliant ideas and inspired events. In those days, inventions were still attributed to “inventors” and met the societal needs, however today, they can no longer compete where inventions are now developed by giant and powerful corporations.

Back to History of Automobile

To ‘automobile’, we’re at least talking about 540 years of car history. That definition is confined to vehicles that are capable to propel itself (Eckermann, 2001), otherwise, humans have possessed knowledge of the wheel for several thousand years, and we’ve been using animals as a source of transportation for nearly that long. The automobile as we know it nowadays was not invented in a single day by a single inventor. The history of the automobile reflects an evolution that took place worldwide involving many different innovators.

Sometime around the year 1478, Leonardo da Vinci drew out his plans for the world's first self-propelled vehicle powered by coiled springs (Fig. 1) (McShane, 2019). The vehicle was actually designed as a special attraction for Renaissance festivals, and like many of Leonardo's sketches, the car remained on paper throughout his lifetime. Amusingly, the first built world’s car might be meant to be a toy for the Chinese Kangxi Emperor and invented by Ferdinand Verbiest (Iannaccone, 2004). At that time, steam

technology was still in its infancy, but Verbiest was able to build a rudimentary, ball-shaped boiler, which then forced steam towards a turbine that could turn the back wheels (Fig.2). The 1700s were dominated by various inventors working to perfect the steam engine - Thomas Newcomen and James Watt are probably the most famous of these, but there were many more. The first person to take a steam engine and place it on a full-sized vehicle was probably a Frenchman named Nicolas-Joseph Cugnot, who between 1769 and 1771 built a steam-powered automobile called “*fardier à vapeur*” (Lucendo, 2019). The machine could reputedly move at a little over 2 miles per hour, but it needed to be refueled with wood every 15 minutes, for which the fardier had to come to a complete stop. One story says that the second of Cugnot's two vehicles crashed into a wall in 1771 (Fig. 3) due to poor weight distribution and so was unable to handle even moderately rough terrain, which might make it the first ever automobile accident.

Figure 1. The original design of the self-propelled car (Codex Atlanticus, f.812 r) and its replica at museum Clos Lucé, Amboise, France.

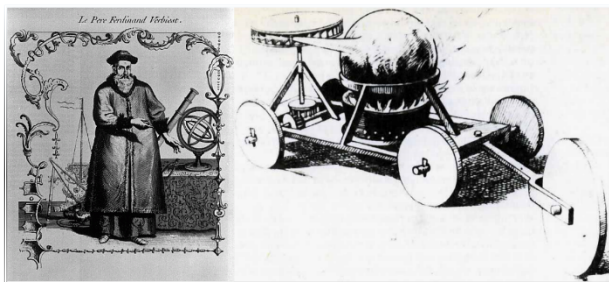
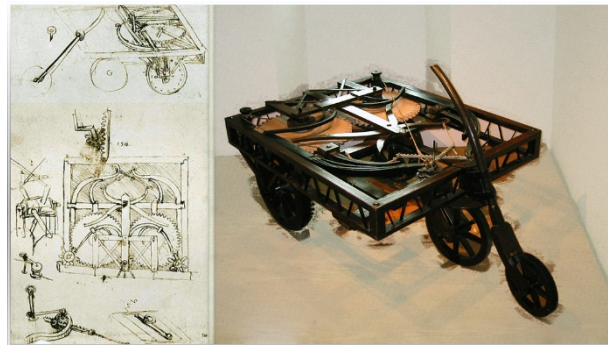


Figure 2. The steam 'car' designed by Verbiest in 1672.

Figure 3. Nicholas-Joseph Cugnot's vehicle, depicted at the famous first road accident at the Arsenal in 1770.



The development of automobile continues where American Oliver Evans receives the first US patent for a steam-powered land vehicle in 1789. In 1807 the Switzerland inventor Francois Isaac de Rivaz invented the first automobile powered by internal combustion, however, his engine turns to be unsuccessful. It takes until 1867, where significant improvement is done on the internal combustion engine by the German Nikolaus August Otto. His engine was the first to efficiently burn fuel directly in a piston chamber, then, in 1877 the four-cycle internal combustion engine considered as the first prototype of modern car engines (E.C.S, 1932). Thereafter, the internal combustion engine provided the pathway to the first modern automobiles, with Karl Benz generally getting the credit for his successful invention in 1886, the “Motorwagen”, and thus dominates the automobile market until the 1920s (Fig. 4). Later on, Henry Ford introduced the Model T and innovated mass-production techniques manufacturing over 15 million Model Ts (Fig. 5) by 1927 (Parker, 2002), and thus, Ford, in addition to General Motors and Chrysler emerged as the “Big Three” auto companies by the 1920s.



Figure 4. Mercedes Benz Patent Motorwagen 1886.



Figure 5. 1923 Ford Model T Touring.

Advancements in Vehicular Technology

The evolution of the automobile was not limited to just improving the engines. Indeed, research and innovations had increased considerably in order to improve the performance, safety, and comfort of vehicles. Among these inventions are, for example:

- the tire: invention by Robert William Thomson (1845) then first patent filings by John Boyd Dunlop (1888) and the Michelin brothers (1891).
- braking systems: drum brakes (Louis Renault, 1902), internal shoe brakes, Hydraulic brakes (Malcolm Loughead, 1918), disc brakes (William Lanchester, 1902).
- transmission systems: manual or automatic gearboxes;
- optical systems: electric headlights, mirrors;
- suspensions: mechanical suspensions, pneumatic suspensions...
- safety systems: deformable materials, seat belt by Nils Bohlin, Volvo's first safety engineer, in 1959.

In line with the increasing demands on high comfort and safety vehicles, a variety of advancements continued to appear in a wide spectrum of scientific and engineering fields. This was associated with the evolution of enabling technologies, (electrical, electronics and software technologies) such as microprocessors and wireless networks. The rapid development of electronics and software tools during the last four decades coupled with the increase in computational speeds and a reduction in the cost of these tools has touched every aspect of life, industry and, of course, the automobile. Some of the developed systems that provided a significant improvement regarding safety are:

- Global Positioning System (GPS) Navigation by the U.S. Department of Defense (DoD) in the early 1970s (Rahiman and Zainal, 2013),
- Proximity sensors,
- Anti-Lock Braking System (ABS) (Bosch, 2007),

- Electronic Stability Control (ESC) or Program (ESP)(Linder et al., 2007)
- Adaptive Cruise Control (ACC)
- Adaptive headlamps using Optoelectronic Technologies,

in addition to other systems that developed and are implemented in most nearly manufactured vehicles. Notably, the number of electronic control units (ECUs) has grown from just one or two per vehicle in the 1970s to over 70 in today’s high-end automobiles, which offer about 500 features (Gharavi et al., 2007).

Road to “Autonomous” automobile

Today, the evolution of automobile directed to the development of so-called autonomous vehicles (AV), and also known as, automated car, self-driving car or driverless car. The basic concept of road vehicle automation refers to the replacement of some or all of the human labor of driving by electronic and/or mechanical devices (Shladover, 2018). Origins of the automated driving technology can be traced back to the early 20th century. At that time, the technology was concentrated on autonomous speed, brake, lane control, and other basic cruise control aspects (Pendleton et al., 2017).

In fact, global automobile production is increasing rapidly, and almost certain to rise far higher, where annual production has nearly doubled since 1997—the year the world’s governments signed the Kyoto climate change agreement (Fig. 6). In a parallel manner, automotive companies have developed many technologies that can facilitate and improve vehicular systems to assist drivers for safe and better driving conditions (Anderson et al., 2016), paving the way for autonomy, and are referred to as Advanced Driver Assistance Systems (ADAS).

The ADAS systems range on the spectrum of passive and active systems. A passive system relies on the driver to take corrective action by providing alerts of a potentially dangerous situation. For example:

- Lane Departure Warning (LDW) alerts the driver of unintended/unindicated lane departure;

- Forward Collision Warning (FCW) indicates that under the current dynamics relative to the vehicle ahead, a collision is imminent. The driver then needs to brake in order to avoid the collision.
- Blindspot warning (BSW) systems that typically use cameras, radar, or LiDAR to detect vehicles traveling in the equipped vehicle's blind spot and provide some form of warning to the driver.
- Fatigue warning systems alert the driver if signs of drowsiness are detected based on steering input, eye blinks, and other driver behaviors.

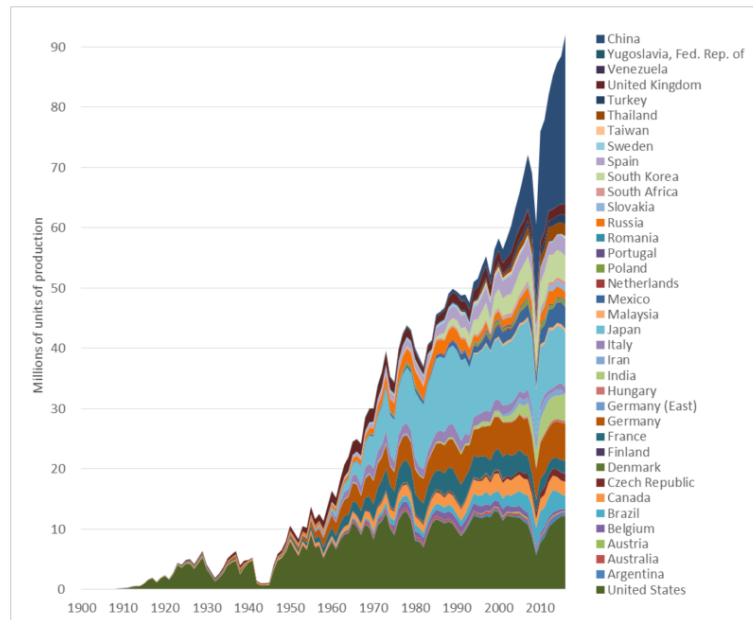


Figure 6. Global automobile production (cars, trucks, and buses), 1900-2016 (US DOT, 2016).

In contrast, active safety systems take action to help avoid a crash, like:

- The Automatic Emergency Braking (AEB) that identifies the imminent collision using typically radars, LiDAR, or cameras and then apply the vehicle's brakes without any driver intervention to avoid the crash or at least reduce its severity.

- Adaptive Cruise Control (ACC) maintains a set speed and following distance from the vehicle ahead using information from a camera or radar sensor. Frequently, it is present on vehicles equipped with FCW or front AEB.
- Lane Keeping Assist (LKA) that use cameras to determine the position of the vehicle in relation to lane markings. When the system detects that the vehicle begins to leave its travel lane it automatically steers the vehicle to prevent it from leaving the lane.
- Lane Centering.
- Traffic Jam Assist (TJA) that supports the driver in slow-moving traffic, combining the LKA and ACC.

Several police-reported vehicle crash data and insurance claim data have attempted to quantify the actual effects of these systems by comparing selected vehicles of the same model with and without the systems of interest. For example, the Highway Loss Data Institute (HLDI) found that Subaru’s EyeSight system (which includes FCW, AEB, LDW, and ACC) reduced the frequency of bodily injury liability and property damage liability claims by 35% and 15%, respectively. Moreover, early statistics found that Subaru’s EyeSight system reduced the frequency of bodily injury claims for crashes involving pedestrians by 35% (Wakeman et al., 2018). Additionally, a European study concluded that Volvo’s LDW and LKA systems reduced the systems’ target crashes by 53%, which equated to 30% of all single-vehicle and head-on crashes that resulted in injuries (Sternlund et al., 2017). Furthermore, a study by Insurance Institute for Highway Safety of police-reported crashes of similar vehicles with and without BSW systems estimated that the systems reduced all lane-change crashes of equipped vehicles by 14% (Cicchino, 2018).

Table 1 lists the potential help of some ADAS technologies in reducing crashes, injuries, and Deaths. It can be concluded that the current and future vehicle safety systems have the potential to dramatically reduce the number of crashes, injuries, and fatalities on our roadways. It is anticipated that the increasing market penetration of these systems and improvements in their functionality and performance will contribute to overall improvements in traffic safety (Benson et al., 2018).

Table 1. Numbers of Crashes, Injuries, and Deaths that LDW/LKA and FCW/AEB ADAS systems Could Potentially Help Prevent (Benson et al., 2018)

	Crashes	Injuries	Deaths
Total Unintentional Lane Departure Crashes	1,395,000	589,000	15,445
Unlikely Preventable by LDW / LKA	876,000	402,000	10,791
Potentially Preventable by LDW / LKA	519,000 ↓ 37%	187,000 ↓ 31%	4,654 ↓ 30%
<i>Road Departure</i>	240,000	109,000	2,536
<i>Sideswipe/Angle</i>	103,000	25,000	406
<i>Head-On</i>	14,000	20,000	1,320
<i>Others</i>	162,000	33,000	392
Total Rear-End and Pedestrian/Cyclist Crashes	2,484,000	1,111,000	6,933
Unlikely Preventable by FCW / AEB	490,000	227,000	2,195
Potentially Preventable by FCW / AEB	1,994,000 ↓ 80%	884,000 ↓ 79.5%	4,738 ↓ 68%
<i>Rear-End</i>	1,687,000	739,000	987
<i>Single Vehicle vs. Ped/bike</i>	83,000	81,000	3,501
<i>Turn Into/Across Path</i>	109,000	32,000	45
<i>Others</i>	115,000	33,000	205

Another example, a glance at the accident statistics in Germany over recent decades tells us that the number of fatalities has declined almost continuously (Winner et al., 2015), although of the huge increase in the distance traveled as well as the number of motor vehicles. Across all the vehicle types analyzed, the emergency braking system emerges as the most promising

ADAS. Up to 43.4 % of all car accidents in the database then become preventable (Hummel et al., 2011). The emergency braking system becomes even more effective if it is also able to address accidents with pedestrians and cyclists (Kühn and Bende, 2014). For this reason, automobile manufacturers are introducing AEB technology in their new vehicle fleets (Fig. 7). Fig. 8 shows the predicted percent of vehicles equipped with some ADAS technologies. In (Highway Loss Data Institute, 2018), significant statistics were presented that evaluates the collision avoidance technologies since 2009, e.g. for 2019 as shown in Fig. 9.

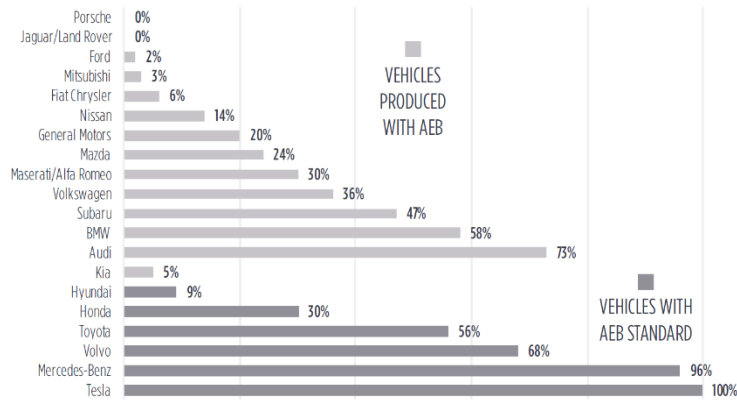


Figure 7. NHTSA - IIHS Percent of MY2017 Fleet Conforming to AEB Voluntary Commitment. (Gotsch, 2018).

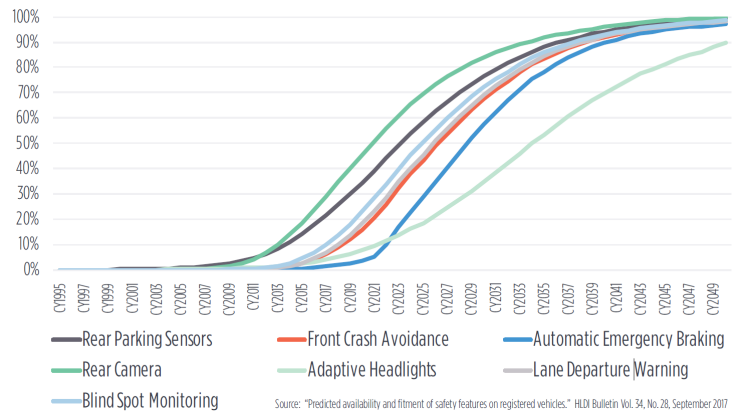


Figure 8. IIHS/HLDI Predicted Percent of Vehicles Equipped (standard or optionally equipped) with ADAS Technologies.

On the other hand, annual forums (AAA Foundation for Traffic Safety, 2019) and various studies were done to investigate the impact of vehicle

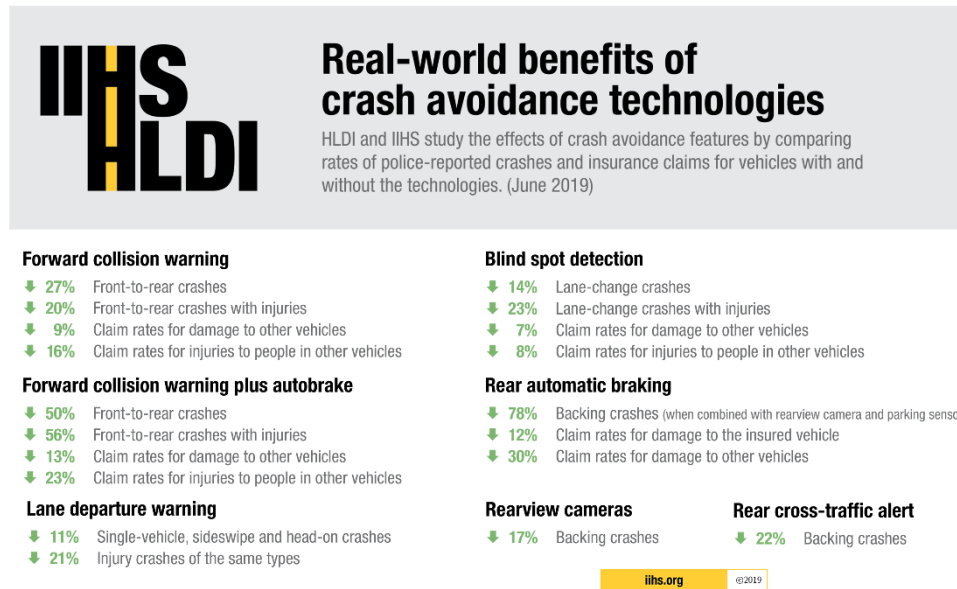


Figure 9. Real World benefits of some ADAS technologies in 2019.

technologies and automation on vulnerable road users and driver behavior and performance (Blanco et al., 2016; Schoettle and Sivak, 2015). A recent study by the AAA Foundation for Traffic Safety found a substantial lack of awareness of certain safety critical limitations of ADAS technologies among owners of vehicles equipped with the technologies (McDonald, A. et al., 2018). One main objective of their study was to investigate driver behavior and the associated risks of ADAS use. The results indicated that the use of lateral and longitudinal ADAS culminated in an increased occurrence of distracted driving behaviors (Dunn et al., 2019). Drivers with activated level 2 ADAS took more frequent and longer duration non-driving-related task glances, subsequently spending less time with their eyes on driving-related tasks. The authors, therefore, propose a three-phase model of ADAS operation, comprising a novelty phase (learning and testing in real time), a post-novelty operational phase (attain driver awareness of the limitations), and an experienced user phase. Moreover, comprehensive training for drivers purchasing ADAS-equipped vehicles may have a positive outcome. Today, every ADAS-equipped vehicle currently operates differently across functionality, ADAS activation, capabilities, and operating speeds, resulting in a learning curve each time a driver uses a different system. As such, standardization to a greater degree may also be beneficial in that it will limit the impact of novelty symptoms. The researchers claim that these propositions could help to mitigate the drawbacks of the use of ADAS (Dunn et al., 2019).

In the Horizon of Self-driving cars

At first, a 4-level taxonomy of vehicle automation was developed by the National Highway Traffic Safety Administration (NHTSA) in 2013 (Wadud et al., 2016), and then 5-level automation was introduced by the Society of Automotive Engineers International (SAE) in 2014—later on updated in 2016. In 2016, NHTSA adopted SAE’s taxonomy and automation levels (NHTSA, 2016), and thus, they have become an industry standard, and also frequently referred in the academic literature (SAE International, 2018). Fig. 10 defines the different levels of automation possible for a vehicle.

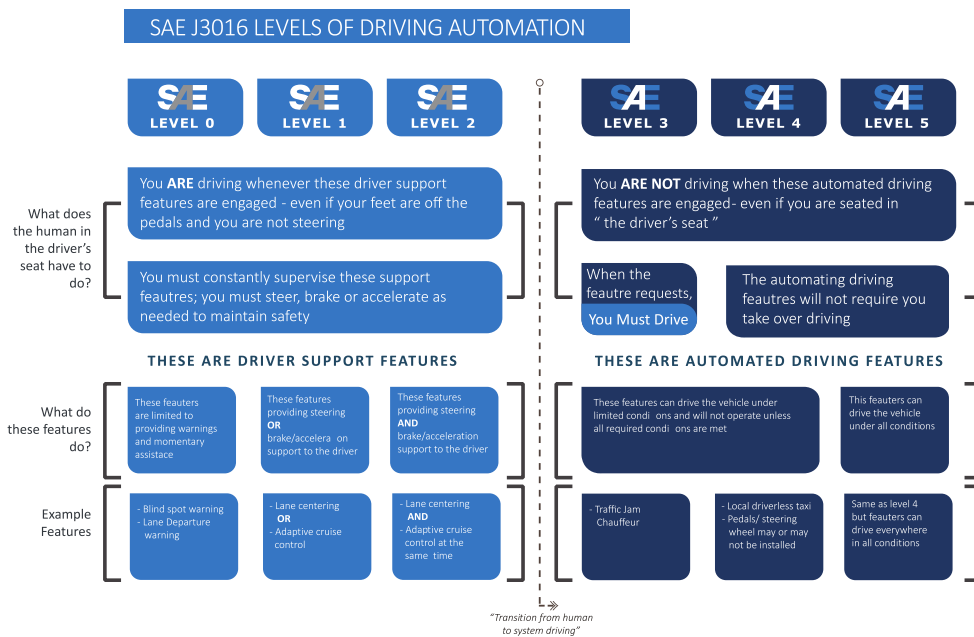


Figure 10. SAE j3016 levels of driving automation (SMMT, 2019).

Just during the last decade or so, incubating conditions of the Digital and 4th Industrial Revolutions gave birth to rapid technological advancements in the field. A recent development consists of networking vehicles and allowing data sharing. For example, wireless communication techniques such as 5G or WIFI are adapted to form so-called VANets (Vehicle Ad-hoc Networks) networks specifically developed for road traffic. These networks can thus allow vehicles and infrastructures to communicate with each other in order to transmit information without the need for central base stations or any controller (Malik and Sahu, 2019). Vehicular communication in VANETs can be achieved by exchanging information using vehicle-to-vehicle(V2V) and vehicle to infrastructure (V2I) message flows. Figure 11 illustrates the different communications possible in a VANets type network.

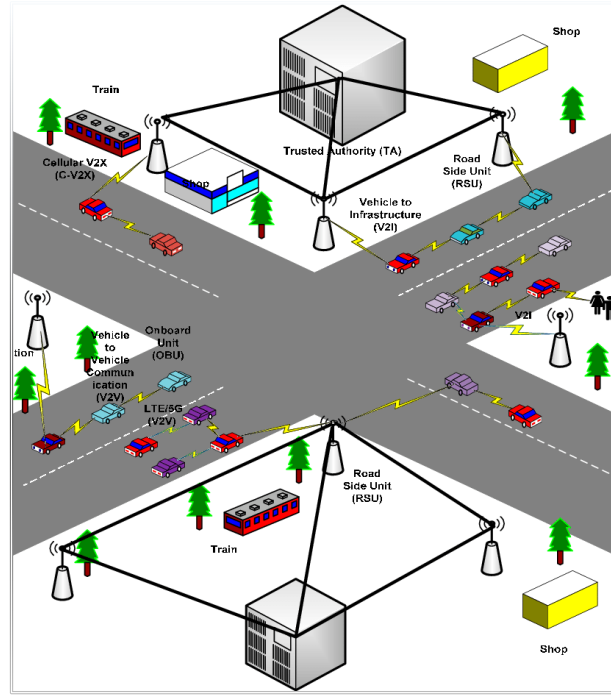


Figure 11. VANets mode diagram (Sheikh and Liang, 2019).

Autonomous vehicles are largely motivated by passenger safety. Every year numerous people die or are seriously injured in road accidents that are largely caused by human errors in perception and decision-making, or by lack of attention and sometimes by late reactions. The autonomous vehicles can use the active percept of a number of redundant sensors to timely make correct driving decisions and hence eliminate accidents. Autonomous vehicles further result in more efficient travel. This means one has to spend much less on insurance, while the insurances will naturally become less expensive. The vehicles benefit from efficient onboard algorithms, communication with the vehicles around, transportation management centers and information from different sources. This facilitates making better informed and optimal decisions. Further, these vehicles can park themselves close to each other and operate in high-speed platoons, which significantly increase the operational efficiency. The implications of a single vehicle may seem limited, but a network of such intelligent vehicles has the potential to make the overall transportation system operate efficiently. As an example, the vehicles can collectively operate to avoid congestions (Kala, 2016).

Here are some of the benefits we can reap from incorporation autonomous vehicles into our everyday lives:

- Fewer Accidents
- Increase Highway Capacity
- Enhanced Human Productivity
- Improved Mobility for Children, the Elderly, And the Disabled
- Lighter, More Versatile Cars
- Decrease or Totally Eliminate Traffic Congestion
- Lower Fuel Consumption
- Hunting for Car Parking Space Will be Eliminated
- Elimination of Traffic Enforcement Personnel.

Consequently, nowadays, numerous prototype AVs are being trailed on the roads. It can be identified over 40 companies developing road-going self-driving vehicles from the automotive industry stalwarts to leading technology brands and telecommunications companies. Beyond trendy names like Tesla, Uber, Amazon and Google chasing self-driving cars (Fig. 12), a host of auto brands are also investing in autonomous R&D. For instance, the German auto supplier Continental AG and the France-based PSA Group (including Peugeot, Citroën, and DS.



Figure 12. Waymo’s Google self-driving taxis (Google, 2019).

The PSA Group announced that the “eyes off” mode is slated to arrive by 2021, while semi-autonomous “hands-off” modes will be available by 2020. These features, along with electric vehicles and new models, form the core of PSA’s broader “*Push to Pass*” growth strategy for the period 2016 – 2021 (Holtz, 2016; PSA Group, 2016), in addition to the Autonomous Vehicle for All (AVA) program that brings together a range of driving assistance functions that will lead to the autonomous car (PSA Group, 2017). Fig. 13 shows three examples for PSA contribution in the field: AVA program collaborated with VINCI Autoroutes; a Level 4 AI-based autonomy based on Almotive sensor, computing hardware, and autonomous software, installed on a Citroen C4 Picasso test car; a collaboration between PSA and the Spain’s

Automotive Technology Centre of Galicia (CTAG) to test IoT and vehicle to vehicle/Infrastructure technologies on autonomous driving that aims to reinforce the creation of smart and sustainable cities.



Figure 13. Some of PSA Group contributions in Autonomous Vehicles.

However, high levels of vehicle automation pose regulatory challenges for the AV manufacturing countries (Nowakowski et al., 2016). The uptake of new technology like AV should be regulated through federal and state governments' pre-deployment policy. Major regulating policies are revolving around testing and deployment, cybersecurity and privacy, liabilities and insurance, ethics, and repair/maintenance and calibration. As an example, AV legislation and policies in the US, the Netherlands, the UK, and Sweden are paving the way for other countries (Vellinga, 2017). However, the first fatal crash by a self-driving UBER involving pedestrian in the US proves that more research, development, legislation and planning are needed for a safer and wider AV uptake. The Victoria Transport Policy Institute (VTPI) mentioned in its report, published in October 2019, different overlooks for additional risks that these technologies can introduce, in contrary to the claims of optimists that AVs will reduce crash rates and insurance costs by 90% (Litman, 2019). Some of these risks are: Hardware and software failures (false sensor, distorted signal, or software error); Malicious hacking; Increased risk-taking ("over-trusting" technology); Additional risks to non-auto travelers. These new risks will probably cause crashes, so net safety impacts are likely to be smaller than the 90% crash reductions that

advocates claim. Thus, VTPI concluded that autonomous vehicles may be no safer per mile than an average driver, and may increase total crashes when self- and human-driven vehicles mix (Penmetsa et al., 2019).

Zero crashes, Zero congestion, and Zero emissions!

It becomes obvious that AVs are moving from science fiction to a very near-term reality, thus, the time to consider the potential climate impacts of autonomous vehicles is now.

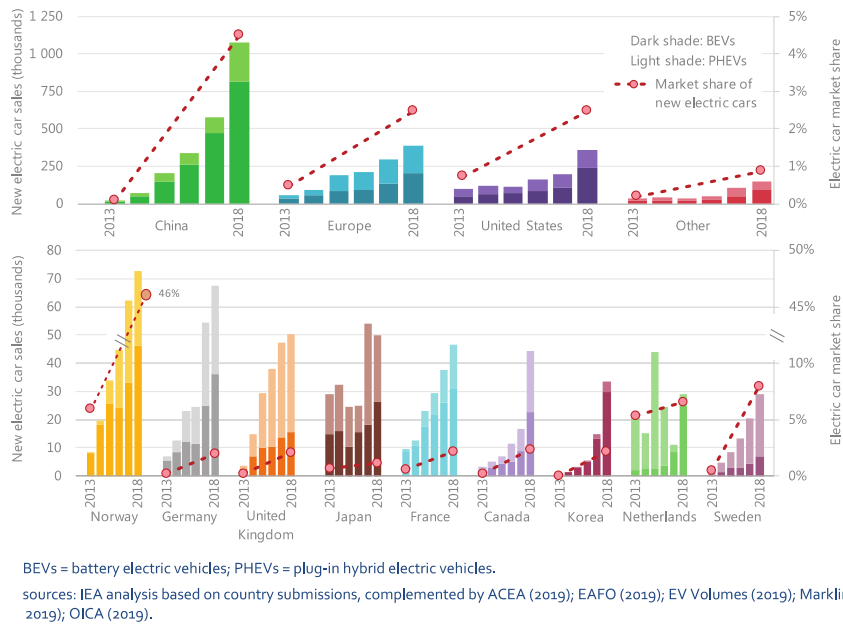


Figure 14. Projected global electric car stock compared with OEM targets (2020-25) (Till Bunsen et al., 2019).

Road transportation is shifting significantly toward electrification around the globe (Fig. 14). The potential to reduce energy consumption and greenhouse emissions are the most important driver for electric mobility. Besides the growing awareness of environmental and population pressures, the innovations market acceptance (Li et al., 2019) and government support (ER-TRAC et al., 2017; European Commission, 2017) results in the advancement of Electric Vehicle (EV) technology. This technology starts to challenge its internal combustion counterparts with large-scale investments and highly coordinated research and development (Ahmad et al., 2018). It becomes essential for meeting the goals of decarbonization and energy security (Paris agreement at COP21 2015 – C40 Committee (COP21, 2015) / Madrid COP 25 (Sustainable Innovation Forum, 2019)).

Between 1990 and 2007, the biggest increase in CO₂ emissions could be attributed to road transport with an increase of 200.7% in that period. Moreover, 40% of nitrogen oxide emissions could be attributed to road transport (EEA, 2015, 2012). According to the Lancet Commission on Pollution and Health, around 6.5 million fatalities in 2015 caused by conventional cars using internal combustion engines (ICE's) (Fernández, 2019) linked to that kind of pollution. This, therefore, has forced the implementation of new urgent measures intended to protect citizens, applying new regulations, driving restrictions and even banning most pollutant internal combustion engine (ICE) vehicles when air quality reaches unacceptable levels of toxicity (Held and Gerrits, 2019). The results show that CO₂ emission of the vehicle decreases up to 50.6% according to an urban driving cycle due to applying the electrification strategy for hybrid electric vehicles (Mourad and Mahmoud, 2019).

Many countries have already made a bold announcement regarding electrification of mobility that opt to ban diesel vehicles from their cities' center by the next decades (Pereirinha et al., 2018). Germany aims to reduce its Green House Gasses (GHG) emissions by 80-95%, where today, around 85% of these emissions are energy-related, in which 22% of them caused by road transportation (Ruhnau et al., 2019). Given the reported high energy efficiency and zero tailpipe emission, the EV has been given focus as a potential solution for enhancing the sustainability in our road transportation sector (Chen et al., 2015). Other countries that have introduced a ban include Norway (by 2025), France, and The United Kingdom (both by 2040) (Dugdale, 2018). More recently, Sweden and Denmark have announced a ban on sales for the year 2030. The EV market is taking up on this and an adequate selection of vehicles will be available (Bischoff et al., 2019).

For this purpose, in the long term, building all-electric vehicles with autonomous capabilities integrated from the beginning is the most efficient way to unlock the tremendous potential societal benefits of self-driving cars, rather than through retrofits. Electric vehicles allow for simpler integration of the advanced technologies required for the cleanest and safest operation of autonomous vehicles. Researchers assign the main advantages of All-electric autonomous vehicles over their gasoline - or hybrid powered vehicles - counterparts to:

- Cleaner Environment: It is estimated that there will be 40 cities with populations exceeding 10 million by 2040, then All-electric shared autonomous vehicles will be ideal for dense cities that need solutions for congestion and noise pollution. Thanks to zero tailpipe emissions, EVs are well suited to address air pollution issues, especially in urban areas and along road networks, where a large number of people are exposed to harmful pollutants from road transport vehicles. Moreover, increasing electric mobility in association with a progressive increase in low-carbon electricity generation can deliver significant reductions in GHG emissions from road transport relative to ICE vehicles.
- Stable Power: The advanced sensing and computing hardware on an autonomous vehicle needs a lot of electric power. Compared to an internal combustion engine, an all-electric battery pack acts as a more stable power source that can enable higher-powered AV components.



Figure 15. The 2020 Porsche Taycan is Porsche's first-ever electric vehicle.

Manufacturers see that EV/AV is a very complementary, technology-wise, equation. The existence of various EVs manufacturers evidence that the world's established and new automakers are increasingly focusing on electrified vehicles with increasing levels of connectivity and autonomy. For example, one eagerly awaited new car on the horizon is Porsche's Taycan (Fig. 15). The production Taycan is presented in September (at the 2019 IAA) and hit the market by the end of 2019. There are already more than 20,000 prospective buyers already making a down payment. A primary differentiator of the car is fast charging. Fast charging is enabled by the car's high-

voltage (around double what is EV-typical) 800-V architecture, guaranteeing its around 90-kW · h lithium-ion battery pack can be recharged in just 4 min for 100 km of range, where the total vehicle range is over 500 km (Jost and Challen, 2019).

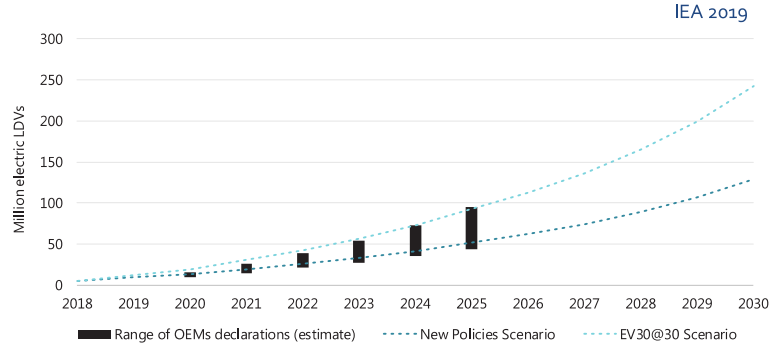


Figure 16. Projected global electric car stock compared with OEM targets (2020-25) (Till Bunsen et al., 2019).

In 2018, the global electric car fleet exceeded 5.1 million, up 2 million from the previous year and almost doubling the number of new electric car registrations. The People’s Republic of China (hereafter “China”) remained the world’s largest electric car market, followed by Europe and the United States. Norway was the global leader in terms of electric car market share (46%) (Till Bunsen et al., 2019). In the European Union, several significant policy instruments were approved. In 2030, global EV sales estimated to reach 23 million and the stock will exceed 130 million vehicles in the New Policies Scenario (Fig. 16). In the EV30@30 Scenario, EV sales and stock nearly double by 2030: sales reach 43 million and the stock is larger than 250 million. Many countries, including France, have committed to the EV30@30 Campaign, where they have set a common vision to strive to make all passenger vehicle sales electric by 2050 (Slowik, 2019).

New Dimension in the sense of Autonomous vehicles Suspensions’ Control

Nowadays, comfort driving and road safety are highly enhanced thanks to a variety of advanced technologies where inventive active suspension systems show promise in electric/autonomous fleets.

In line with the process of launching All-electric autonomous vehicles, all-in-wheel devices are expected to play an important role in this new trend. Such vehicles are able to adapt to urban lifestyles, mainly, to contribute to the air quality, noise reduction in urban cities as well as fulfilling ride quality requirements. Since a lighter vehicle means also a sharp reduction in energy consumption, a modern solution can contain integrated powertrain suspension located directly inside the wheel.

Besides the ProteanDrive project (Tran, 2017), the eCorner wheel by Siemens (Gombert, 2008), and a variety of similar approaches, the Active Wheel (AW) developed by Michelin serves as one propitious technology in this field. This advanced technology initiates a new era in road transportation where all essential components have been integrated within the wheel itself: the pneumatic part, a compact traction electric motor with regenerative braking, an electric active suspension system, and the braking system.

In fact, the ride comfort in vehicles with driving automation at level 4 or higher will need to provide a superior experience. As mentioned earlier, autonomous vehicles will offer increased productivity and convenience by freeing occupants from the responsibility of driving. However, studies indicate that the occurrence of motion sickness in autonomous vehicles will be substantially higher than in conventionally driven vehicles. Occupants of autonomous vehicles are more likely to be involved in performing tasks and activities, such as reading, writing and using a computer or tablet, that typically increase the occurrence of motion sickness (Ekchian et al., 2016). Therefore, new and different approaches needed rather than conventional solutions.

Here, the structure of the Active Wheel offers new opportunities in Global Chassis Control (GCC) that rises, recently, to remarkable levels. In AW, the conventional mechanical suspension has been replaced by a passive spring and a DC electrical motor. In comparison with other force generating actuators (hydraulic, Hydractive, hydro-pneumatic...), the DC linear characteristics of the AW's suspension system provides an extremely fast response time, low contact friction, high precision and efficiency, good controllability, and less energy consumption (Nguyen et al., 2011).

Along with active suspension systems, the innovative technologies in the frame of sensors, electronics, and advanced software, in addition to the networking and data sharing between vehicles and infrastructures, all these coordinated could inevitably provide better performance in the horizon of ride comfort and road safety. In this sense, the mechanical aspects of the systems could be linked to forward-facing sensors – cameras and LiDAR, for example – to bring a predictive aspect to the technology. Thus, in the future, what is certain is that these technologies will be needed if autonomous vehicles are to reach their full potential. This, adequately, must be accompanied by new or updated control strategies and theories. The existence of diverse dynamic control systems and a wide range of actuators integrated into the All-electric autonomous vehicle, will place greater emphasis and give more prominence to the coupling effect between the embedded active systems, and in particular, the effect of the active suspension system on other vehicle dynamics and functionality.

Thesis framework and content

This dissertation synthesizes the results of the three years PhD work (from January 2017 to April 2020), performed in collaboration between the **IMS laboratory under the supervision of Xavier Moreau**, professor at the University of Bordeaux, and the **CRSI laboratory under the supervision of Clovis Francis**, professor at the Lebanese University.

This thesis is concerned on the **Hierarchical approach for global chassis control of an electric vehicle** in the sense of improving the vehicle comfort, stability, and safety through the control of active suspension system, braking systems, and active steering.

For this purpose, the thesis is subdivided into five chapters:

- Chapter 1 provides a general introduction about vehicle dynamics, and mainly on the automotive suspension systems. It is devoted also to recall modeling concepts and the CRONE control tools in addition to some recent developments in vehicle control. Moreover, it introduces the role of the suspension in vertical dynamics and the defined the different areas of study and operating, which the suspension must meet different objectives, and sometimes even conflicting. The problem formulation and the assigned objectives to be achieved are then presented.
- In Chapter 2, entitled “**Vertical Dynamic Control**”, deals with different solutions for the inherent problems in traditional suspensions. Two main controllers were designed for two different objectives. While the first one is assigned to regulate the height of the center of gravity of the vehicle, in addition to its roll and pitch angle, the second controller offers two fractional order damping controllers. Using the

CRONE methodology, a comfort-oriented and road holding oriented controller were developed and have achieved remarkable performances.

- In Chapter 3, entitled “**Hierarchical Approach for Driver Disturbance Rejection**”, presents a hierarchical control approach where two-level controllers are proposed for the AW suspension system. The systems are controlled using the first-generation CRONE controllers while taking into account the vehicles’ parametric uncertainties. The main objective of the proposed approach is to reject the driver disturbances in light electric vehicles to enhance ride comfort. The proposed strategy permits to maximize the benefit of the embedded active suspension actuator in the Active Wheel to regulate the main chassis dynamics, namely, the heave, roll and pitch. It is worth noting that the road disturbances have been considered in this work and the strategy was announced applicable for specific road classes and profiles.
- In Chapter 4, entitled “**Study of the ABS function of an electro-mechanical braking system**”, studies have been done on improving the braking performance of the electric vehicle by an ABS control on even and rough roads. Using CRONE methodology, the controller is designed to maximize the efficiency of the braking system of Active Wheel. The study takes into consideration the road adhesion variations, vehicle mass variation, and vehicle velocity variations. The final objective of this system is to reduce the braking distances while taking into consideration system limitations and noise measurement criterion. Then, the half-vehicle model is used to study the effect of the load transfer disturbance on the performance of the ABS controller. In the end, the road disturbances were taken into account, and some testing scenarios made to find out its effect on the ABS performance. In order to minimize the performance deterioration, the fractional-order damping controllers introduced in Chapter 2, are also implemented to test for its influence on the overall system, in its different orientation, i.e. comfort-oriented and road holding oriented controllers.

- In Chapter 5, entitled “**Vehicle Stability Control**”, the study was concerned on the lateral dynamics control. The objectives were assigned to enhance the performance of the lateral dynamics of the vehicle against disturbances and parametric variations. For this reason, three 3rd generation CRONE controllers were designed: two for yaw rate regulation using braking torques and active steering, and the third one designed for the lateral position control of the vehicle. Finally, the effect of the vertical dynamics of the chassis was analyzed on the performance of the designed lateral controllers.

Table of Contents

General Introduction	i
Thesis framework and content.....	xxii
Table of Contents	xxvi
Table of Figures.....	xxx
List of Tables	xxxvi
Nomenclature.....	xxxviii
Chapter 1 Context, state of the art, and problem formulation.....	1
1.1 Introduction.....	2
1.2 Vehicle Dynamics.....	3
1.2.1 Introduction to the Global Vehicle Dynamics.....	3
1.2.2 Vertical dynamics of the vehicle	7
1.2.3 Range of Vehicle models	8
1.2.3.1 Quarter Vehicle model: a compromise between complexity and dynamics ..	11
1.3 Domains of operation and domains of study	13
1.3.1 Domain of operations	14
1.3.2 Adequation of the different domains	17
1.3.3 Conclusion.....	17
1.4 Suspension system.....	18
1.4.1 Introduction	18
1.4.2 Classification of Suspension systems.....	22
1.4.3 Some Suspension system realization	24
1.4.4 Active Wheel	27
1.4.5 Conclusion.....	29
1.5 Strategy, Approach, and Objectives.....	29
1.5.1 Introduction	29
1.5.2 Two-level Approach.....	30
1.5.3 Vertical Control Objectives.....	31
1.5.4 Longitudinal Control Objective	31
1.5.5 Lateral Control Objective	32
1.5.6 Conclusion.....	32
1.6 The CRONE Control Approach	33
1.6.1 Introduction to the CRONE Control System Design Methodology	33
1.6.2 Control diagram and data for synthesis	34
1.6.3 First-generation CRONE Control.....	35

1.6.4	Second-generation CRONE controller	37
1.6.5	The third-generation CRONE Controller.....	41
1.6.6	CRONE Control System Design Toolbox.....	43
1.6.7	Conclusion.....	44
1.7	Conclusion	44
Chapter 2 Vertical Dynamic Control		47
2.1	Introduction.....	48
2.2	Frequency domain study for quarter vehicle model.....	48
2.2.1	Exploitation of the dynamic decoupling for synthesis models	55
2.3	Vehicle's height control.....	60
2.3.1	Introduction.....	60
2.3.2	Synthesis model	60
2.3.3	Control design methodology.....	62
2.3.3.1	Defining parametric uncertainty	62
2.3.3.2	Specifications	64
2.3.3.3	Second Generation CRONE design controller	65
2.3.4	Time-domain simulations and analysis.....	77
2.3.5	Conclusion.....	79
2.4	Fractional-order damping control.....	80
2.4.1	Introduction.....	80
2.4.2	Suspension model.....	81
2.4.3	Control structure.....	83
2.4.4	Rationalized approach of FO damping control	88
2.4.5	Time-domain simulations.....	91
2.4.6	Conclusion.....	95
2.5	Conclusion	95
Chapter 3 Hierarchical Approach for Driver Disturbance Rejection		98
3.1	Introduction.....	99
3.2	Hierarchical Approach.....	102
3.3	Vehicle model	105
3.3.1	Validation Model.....	105
3.3.2	Synthesis model	105
3.3.2.1	Chassis Model.....	105
3.3.2.2	Quarter vehicle model.....	110
3.4	Control system design.....	111
3.4.1	CRONE control approach.....	111
3.4.2	Optimization approach of control parameters' selection.....	111
3.4.3	Performance specifications	113
3.4.4	Global controller design	113
3.4.5	Local control design.....	119
3.4.6	Control Allocation	123
3.5	Study requirements	126

3.5.1	Disturbance model.....	126
3.5.1.1	Random road profiles.....	126
3.5.1.2	Singular disturbance: Bump	127
3.5.2	Benchmark systems.....	128
3.5.3	Evaluation Indexes.....	132
3.6	Frequency-domain analysis.....	134
3.7	Time-domain analysis	138
3.7.1	Rejection of road disturbances.....	138
3.7.1.1	Singular event disturbance	138
3.7.1.2	Random road disturbance	140
3.7.2	Driver Disturbance Rejection Scenario.....	145
3.8	Conclusion	149
Chapter 4 Study and control of the ABS function.....		151
4.1	Introduction.....	152
4.2	Modeling	154
4.2.1	Schematization and configuration.....	154
4.2.2	Dynamic equations	156
4.2.3	Model Linearization.....	159
4.2.3.1	Tire linearization	159
4.2.3.2	Linearization of the aerodynamic resistance	162
4.2.3.3	Linearization of rolling resistance force.....	162
4.2.3.4	Equilibrium values and initial conditions.....	163
4.2.4	Synthesis model.....	164
4.2.5	Modeling of the reference.....	166
4.3	Control system design.....	167
4.3.1	Strategy.....	167
4.3.2	Control specifications	169
4.3.3	Plant definition.....	171
4.3.4	CRONE controller.....	174
4.4	Performance analysis.....	180
4.4.1	Frequency domain	180
4.4.2	Time domain analysis.....	182
4.5	Effect of Vertical dynamics on the ABS control system.....	189
4.5.1	Introduction.....	189
4.5.2	Dynamic model.....	190
4.5.3	Control structure.....	192
4.5.4	Testing simulations	192
4.5.4.1	Driver disturbance.....	192
4.5.4.2	Road disturbances	196
4.5.5	Conclusion.....	197
4.6	Conclusion	201
Chapter 5 Vehicle Stability Control.....		203

5.1	Introduction.....	204
5.2	Vehicle model.....	205
5.2.1	Schematization and configuration.....	205
5.2.2	Dynamic equations.....	206
5.2.3	Equation of the trajectory.....	208
5.2.4	Model Linearization.....	209
5.2.5	State-space representation.....	211
5.2.6	Uncertain Plants.....	212
5.3	Yaw rate regulation by corrective yaw moment.....	213
5.3.1	Specifications.....	214
5.3.2	CRONE Controller.....	216
5.3.3	PID Controller.....	216
5.3.4	Frequency-domain analysis.....	217
5.3.5	Test simulations.....	221
5.4	Yaw rate regulation by active steering.....	223
5.4.1	Introduction.....	223
5.4.2	Synthesis model.....	224
5.4.3	Control Design.....	226
5.4.3.1	Specifications.....	226
5.4.3.2	CRONE Controller.....	227
5.4.3.3	PID Controller.....	228
5.4.3.4	Frequency analysis.....	228
5.4.4	Simulation results.....	232
5.5	Lateral position Control.....	234
5.5.1	Introduction.....	234
5.5.2	Synthesis model.....	234
5.5.3	Uncertain Plants of $\mathbf{G3}(s)$	236
5.5.4	Control design.....	236
5.5.5	Test simulations.....	240
5.6	Effect of the Vertical dynamics on the lateral stability control.....	242
5.7	Conclusion.....	248
	General Conclusion and Perspectives	251

Table of Figures

1. The original design of the self-propelled car (Codex Atlanticus, f.812 r) and its replica at museum Clos Lucé, Amboise, France.	ii
2. The steam 'car' designed by Verbiest in 1672.	ii
3. Nicholas-Joseph Cugnot's vehicle, depicted at the famous first road accident at the Arsenal in 1770.	ii
4. Mercedes Benz Patent Motorwagen 1886.	iii
5. 1923 Ford Model T Touring.	iii
6. Global automobile production (cars, trucks, and buses), 1900-2016 (US DOT, 2016). ...	vi
7. NHTSA - IIHS Percent of MY2017 Fleet Conforming to AEB Voluntary Commitment. (Gotsch, 2018).	ix
8. IIHS/HLDI Predicted Percent of Vehicles Equipped (standard or optionally equipped) with ADAS Technologies.	ix
9. Real World benefits of some ADAS technologies in 2019.	x
10. SAE j3016 levels of driving automation (SMMT, 2019).	xi
11. VANets mode diagram (Sheikh and Liang, 2019).	xii
12. Waymo's Google self-driving taxis (Google, 2019).	xiii
13. Some of PSA Group contributions in Autonomous Vehicles.	xiv
14. Projected global electric car stock compared with OEM targets (2020-25) (Till Bunsen et al., 2019).	xv
15. The 2020 Porsche Taycan is Porsche's first-ever electric vehicle.	xvii
1.1. Schematic of the main vehicle dynamics.	4
1.2. Acceleration diagrams: (a) 2D representation (ax, ay), (b) 3D representation with az	6
1.3. The various type of disturbances applied on the vehicle dynamics.	8
1.4. V - cycle approach for designing of vehicles' elements (Létuvé, 2014).	10
1.5. Validation model in MATLAB/Simulink environment.	11
1.6. Schematics of the Quarter vehicle analysis model (Bouvin, 2019).	12
1.7. Representation of the domains of study on a diagram of (ax, ay).	14
1.8. Analysis model of quarter vehicle (Létuvé, 2014).	16
1.9. Traditional suspension system.	18
1.10. Main roles of the vehicle suspension system.	19
1.11. Representation of different road roughness and obstacles (Bouvin, 2019).	20
1.12. Resonance frequencies for different body segments, represented by a simplified mechanical model of a human standing on a vibrating platform (Berlin and Adams, 2017).	21
1.13. Classification of electronically controlled suspension (Savaresi et al., 2010).	24
1.14. The Architecture of Bose Suspension.	26

1.15. Representation of the attitude correction system of the standard Hydractive suspension.....	26
1.16. Hydraulic implantation of the suspension CREUAT.	26
1.17. Active Wheel structure.....	27
1.18. Light electric vehicles equipped with Active Wheel: (a) Venturi Volage, (b) Heuliez Will.	29
1.19. Block-diagram of an output unity negative feedback control system.	33
1.20. Asymptotic Bode diagrams of the (a) fractional and (b) rational CRONE regulator for $m \in [0, 1]$	37
1.21. Vertical sliding of a frequency template (bold solid line) ensuring the robustness of phase margin $M\phi$ and of resonant peak Mr (Sabatier et al., 2015a)	39
1.22. Shape of open-loop Nichols plot.	40
2.1. Active Wheel Quarter vehicle model representation.	49
2.2. Block diagram illustrating the controlled QV.	50
2.3. Formulation of sensitivity functions between inputs and outputs variables.	51
2.4. Block diagram of different sensitive transfer functions (Velocities).	52
2.5. Block Diagram of the different sensitive transfer function (Displacements).	52
2.6. Bode responses of the numbered transfer functions as described in 2.5.	54
2.7. Bode diagram of the transfer functions (a) $T20(s)$ and (b) $T10(s)$	58
2.8. Analysis model of quarter vehicle model correspondent to transfer functions (a) $T20(s)$ and (b) $T10(s)$	59
2.9. Height regulation synthesis model.	61
2.10. Range of variations of the parameters of the canonical form $P(s)$	63
2.11. Bode response of the front axle synthesis model.	63
2.12. Bode response of rear axle synthesis model.	64
2.13. Vehicle height regulation's block diagram.	64
2.14. Illustration of the effect the non-integer order 'n' on bode diagram.	66
2.15. Vertical sliding of a frequency template (bold red solid line) ensuring the robustness of phase margin $M\phi$ and of resonant peak Mr	69
2.16. Open-loop Nichols plot for the 3 front plants.....	73
2.17. Open-loop Nichols plot for the 3 rear plants.	73
2.18. Open-loop Nichols plot for the 3 front plants.....	74
2.19. Open-loop Nichols plot for the 3 rear plants.	74
2.20. Closed-loop sensitivity functions for the 3 front plants: $Pnom$ (-), $Pmin$ (--), and $Pmax$ (---).	75
2.21 Closed-loop sensitivity functions for the 3 front plants: $Pnom$ (-), $Pmin$ (--), and $Pmax$ (---)..	75
2.22. Bode plot of rational controllers' transfer functions.....	76
2.23. Closed-loop step responses for the 3 front plants.	76
2.24. Closed-loop step responses for the 3 rear plants.....	76

2.25. Simulation results of the validation model on (a) Front axle and (b) rear axle.	78
2.26. Simulation results using the full model of (a) varying height of car-body, (b) attain reference pitch angle, and (c) attain reference roll angle.	79
2.27. Control diagram of the fractional order damping control.	83
2.28. Optimized damping order n of front axle for empty vehicle.	86
2.29. Optimized damping order n of front axle for full loaded vehicle.	86
2.30. Optimized damping order n of rear axle for empty vehicle.	87
2.31. Optimized damping order n of rear axle for full loaded vehicle.	87
2.32. FO damping transformation compared to fractional and rational 2 nd generation CRONE controller for $n = 0.65$	90
2.33. FO damping transformation compared to fractional and rational 2 nd generation CRONE controller for $n = 1.1$	90
2.34. Bode response of sensitivity functions: (a) $Ha(s)$ and (b) $H12s$, with two fractional damping order $n = 0.65$ and $n = 1.1$	91
2.35. Simulation results of fractional damping control compared to passive system with sinus road disturbances of frequency 0.1 to 40Hz of amplitude 1mm.	92
2.36. Simulation results of fractional damping control compared to passive system with sinus road disturbances of frequency 0.1 to 40Hz of amplitude 2mm.	93
2.37. Simulation results of fractional damping control compared to passive system with sinus road disturbances of frequency 0.1 to 5.5Hz of amplitude 15mm.	94
3.1. Active wheel from Michelin.	100
3.2. Block Diagram of Global Chassis Control.	103
3.3. Comfort operating domain of a vehicle.	104
3.4. Description of the vertical dynamics for obtaining a model for analysis and synthesis.	106
3.5. Simplified schematics illustrating the car body dynamics: (a) Heave, (b) pitch, and (c) roll motions.	109
3.6. Frequency template in the open loop Nichols plot.	114
3.7. Bode responses of global plants' transfer functions.	115
3.8. Bode responses of global controllers' transfer functions.	118
3.9. Bode responses of global nominal open-loops.	118
3.10. Bode responses of local plants.	120
3.11. Bode response of local controllers.	122
3.12. Bode response of open-loop transfer functions of local controllers.	122
3.13. Schematic illustration for the hierarchical approach.	125
3.14. Frequency response of benchmark systems.	129
3.15. Bode responses of local CRONE and PID controllers.	131
3.16. Nichols chart of open-loop transfer functions of local systems with PID and CRONE controllers.	131
3.17. Bode response of $Wc(s)$ transfer function.	133
3.18. Nichols chart for global open-loop transfer functions.	134

3.19. Nichols chart of the open-loop transfer function of front plants with (a) CRONE and (b) PID controllers.....	136
3.20. Nichols chart of the open-loop transfer function of front plants with (a) CRONE and (b) PID controllers.....	136
3.21. Sensitivity transfer functions of the sprung mass acceleration relative to road disturbances.	137
3.22. Sensitivity transfer functions of the suspension deflection relative to road disturbances.	137
3.23. Simulation results of road bump.	140
3.24. ISO road profiles and their PSD graphs.	141
3.25. Simulation results of CRONE controller with road class A.	144
3.26. Simulation results of CRONE controller with road class A-B.	144
3.27. Driving scenario variables: (a) Steering profile, (b) introduced brake/motor torques, (c) resulted longitudinal and lateral accelerations, and (d) vehicle trajectory.	146
3.28. Simulation results of the vertical dynamics of CG.	147
3.29. Simulation results of pitch motion of the chassis.	147
3.30. Simulation results of roll motion of the chassis.	148
3.31. Simulation results of suspension deflections for different controlled systems.	148
4.1. Schematization and configuration: longitudinal bicycle models (a) and front vehicle quarter (b).....	155
4.2. Functional diagram of the EMB actuator.	156
4.3. Black box model of the tire.	158
4.4. Longitudinal forces as function of tire slip rate according to Pacejka model.	160
4.5. Overview of the steps necessary to determine the variables at equilibrium state.	163
4.6. Control schema for ABS control loop.	168
4.7. Reference generator for wheel angular velocity (flow chart).....	169
4.8. Second approach of calculating px	172
4.9. Variation of px as function of random samples of Fz and μ	173
4.10. Bode diagrams of $G(s)$; $G_{nom}(s)$, $G_{min}(s)$, $G_{max}(s)$, and the yellow lines representing the variations of magnitude and phase for each frequency considering all parametric variations.	175
4.11. Generalized (a) and optimal (b) templates of open-loop for 3rd generation CRONE controller.	176
4.12. Bode response of the fractional and rational form of the controller $CABS(s)$ (toolbox).	180
4.13. Bode response of open-loop transfer functions with CRONE controller.	181
4.14. Nichols diagram for the open-loop transfer functions.	181
4.15. Frequency responses of sensitivity functions.	182
4.16. Bode response of the controllers' transfer function.	183
4.17. Bode response of the open-loop nominal transfer functions with controllers.	183

4.18. Longitudinal velocity and wheel angular velocity of the quarter car in braking scenario (A).....	185
4.19. Slip rate of the quarter car in Scenario (A).....	185
4.20. Control input for the quarter car in braking scenario (A).....	185
4.21. Power spectrum density of control efforts in braking scenario (A).	186
4.22. Longitudinal velocity and wheel angular velocity of quarter car in braking scenario (B).	187
4.23. Slip rates of quarter car in braking scenario (B).....	188
4.24. Control input for the quarter car in braking scenario (B).	188
4.25. Power spectrum density of control efforts in braking scenario (B).	188
4.26. Half-car model.....	191
4.27. Braking performance of the system with and without vertical dynamics: (a) wheel slip rate and (b) the vehicle longitudinal velocity, front axle (—) and rear axle (- -).	194
4.28. Braking performance of the system with and without vertical dynamics: front axle (—) and rear axle (- -).	194
4.29. Braking performance of ABS controlled systems with and without vertical dynamics: (a) wheel slip rate and (b) the vehicle longitudinal velocity, front axle (—) and rear axle (- -).	195
4.30. Braking performance of ABS controlled systems with and without vertical dynamics: front axle (—) and rear axle (- -).....	195
4.31. Wheel contact forces with ABS control and FO damping control.	200
4.32. Longitudinal forces with ABS control and FO damping control.	200
5.1. Four-wheel model schematization.	206
5.2. Black box model of the tire.....	208
5.3. Lateral forces as function of wheel sideslip angle.	210
5.4. Bode responses of uncertain plants of $G1(s)$	213
5.5. Block diagram for yaw rate regulation by braking torque.....	214
5.6. Bode plot for designed controllers of $G1(s)$ plant.....	218
5.7. Bode response of the nominal open-loop transfer function.	218
5.8. Nichols chart for open-loop transfer functions with CRONE controller $C1(s)$	219
5.9. Nichols chart for open-loop transfer functions with PID controller.....	219
5.10. Frequency responses of sensitivity functions with $C1(s)$	220
5.11. Frequency responses of sensitivity functions with $C1PID(s)$	220
5.12. Steering profile of scenario (A).....	221
5.13. Yaw rate motions of scenario (A).	222
5.14. Vehicle trajectories of scenario (A).....	222
5.15. Yaw moment control efforts of scenario (A).....	223
5.16. Bode responses of uncertain plants of $G2(s)$	225
5.17. Functional diagram of yaw rate regulation by active steering.....	226

5.18. Bode plot for designed controllers of $G2(s)$ plant.	229
5.19. Bode response of the nominal open-loop transfer function of active steering systems.	229
5.20. Nichols chart for open-loop transfer functions with CRONE controller $C2(s)$	230
5.21. Nichols chart for open-loop transfer functions with $C2PID(s)$	230
5.22. Frequency responses of sensitivity functions with $C2(s)$	231
5.23. Frequency responses of sensitivity functions with $C2PID(s)$	231
5.24. Yaw rate motions with active steering control.	232
5.25. Control active steering angle.	233
5.26. Vehicle trajectories with active systems compared to passive and reference models.	233
5.27. Bode responses of uncertain plants of $G3(s)$	236
5.28. Functional diagram of lateral position control by active steering	237
5.29. Bode response of the transfer functions of the controllers.	238
5.30. Bode plot of the open-loop transfer functions with both controllers.	238
5.31. Nichols chart for open-loop transfer functions with CRONE controller $C3(s)$	239
5.32. Nichols chart for open-loop transfer functions with $C3PID(s)$	239
5.33. Yaw motion with lateral position control.	240
5.34. Active steering control angles.	241
5.35. Lateral acceleration with lateral position control.	241
5.36. Vehicle trajectories with lateral position control.	241
5.37. Yaw rate motions with CRONE controller.	242
5.38. Yaw moment control efforts.	243
5.39. Lateral forces of four tires.	244
5.40. Lateral accelerations comparison.	244
5.41. Vehicle's trajectory.	244
5.42. Steering profile of double lane maneuver.	245
5.43. Yaw rate response in a double lane maneuver scenario.	246
5.44. Active steering control angle in a double lane maneuver scenario.	246
5.45. Lateral accelerations in a double lane maneuver scenario.	246
5.46. Lateral forces at four tires in a double lane maneuver scenario.	247
5.47. Vehicle trajectories in a double lane maneuver scenario.	247

List of Tables

1. Numbers of Crashes, Injuries, and Deaths that LDW/LKA and FCW/AEB ADAS systems Could Potentially Help Prevent (Benson et al., 2018)	viii
1.1. The effect of LAS systems on global vehicle dynamics.	5
1.2. Adequation between domains of study and domains of operation.....	17
2.1. Nominal quarter vehicle parameters.	54
2.2. The variation range of suspension parameters.	62
2.3. Optimized values of the damping fractional-order n	85
3.1. Uncertain parameters of global transfer functions.	114
3.2. Range of variation of suspension parameters.	119
3.3. Control parameters of the local crone controllers.....	121
3.4. ISO 8608 values of G_d ($\Omega 0$) related to some road class.....	127
3.5. Simulation results for the controlled systems with bump road profiles.....	139
3.6. Simulation results for the controlled systems with class A roads.....	142
3.7. Simulation results for the controlled systems with class A-B roads.....	143
3.8. Simulation results of the driving scenario.....	145
4.1. Range of variation of uncertain parameters of the ABS control plant.....	171
4.2. Range of variation of px as function the chosen of slip rate.....	173
4.3. Parametric variation of $G(s)$	174
4.4. Open-loop parameters of the 3 rd generation CRONE controller.	179
4.5. Maximum gain in dB of sensitivity functions for perturbed $G(s)$	182
Table 4.6. Braking distances of systems without ABS control (front axle model).	198
4.7. Braking distances of systems with ABS control (front axle model) with $T_{opt} = 8\%$	198
4.8. Braking distances of systems with ABS control (front axle model) with $T_{opt} = 7\%$	198
4.9. Braking distances of systems without ABS control (rear axle model).	199
4.10. Braking distances of systems with ABS control (rear axle model) with $T_{opt} = 8\%$	199
4.11. Braking distances of systems with ABS control (rear axle model) with $T_{opt} = 7\%$	199
4.12. RMS values for wheel forces with FO damping controllers.	200
5.1. Parametric variations of $G_1(s)$	213
5.2. Maximum gain in dB of sensitivity functions for perturbed $G_1(s)$	217
5.3. Parametric uncertainties of $G_2(s)$	225
5.4. Maximum gain in dB of sensitivity functions for perturbed $G_2(s)$	232

Nomenclature

ACRONYMS

ABS	Anti-lock Braking System
ACC	Adaptive Cruise Control
ADAS	Advanced Driver-Assistance System
AEB	Automatic Emergency Braking
AV	Autonomous vehicles
BW	Blindspot warning
CG	Center of Gravity
GCC	Global Chassis Control
CRONE	Commande Robuste d'Ordre Non Entier
ECU	Electronic Control Unit
GPS	Global Positioning System
ESC or ESP	Electronic Stability Control or Electronic Stability Program
FCW	Forward Collision Warning
LDW	Lane Departure Warning
LiDAR	Light Detection and Ranging
LKA	Lane Keeping Assist
QV	Quarter Vehicle
TJA	Traffic Jam Assist
VANets	Vehicular Ad-hoc Network
V2V	Vehicle-to-Vehicle
V2I	Vehicle-to-Infrastructure

PARAMETERS

M	Total mas of the vehicle	kg
m_2	Sprung mass of QV	kg
m_1	Unsprung mass of QV-	kg
k_2	Stiffness coefficient of suspension	N/m
k_1	Stiffness coefficient of the tire	N/m
b_2	Damping coefficient of suspension	Ns/m
b_1	Damping coefficient of the tire	Ns/m
a, L_f	Distance from the vehicle's front axle to CG	m
b, L_r	Distance from the vehicle's rear axle to CG	m
w, c	Half width of the Axles	m
L	Vehicle length	m
I_{xx}	Moment of inertia around the x-axis	kg m ²
I_{yy}	Moment of inertia around the y-axis	kg m ²
I_z	Moment of inertia around the z-axis	kg m ²
r_0	Wheel radius	m
H	Height of the center of gravity	m
J_r	Wheel inertia	kg m ²
g	Gravity constant	m/s ²

VARIABLES

a_x	Longitudinal acceleration	m/s ²
a_y	Lateral acceleration	m/s ²
z_G	Heave vertical displacement of CG	m
φ_G	Chassis Pitch angle	rad
θ_G	Chassis Roll angle	rad
z_2	QV sprung mass vertical displacement	m
z_1	QV unsprung mass vertical displacement	m
z_0	Road elevation	m
V_x	Vehicle longitudinal speed	m/s
V_y	Vehicle lateral speed	m/s
ψ	Yaw angle of the vehicle	rad/s
Δ_G	Sideslip angle at CG	rad
Δ_p	Tire sideslip angle	rad
T	Wheel slip rate	%
Ω	Wheel angular velocity	rad/s
F_x	Tire longitudinal forces	N
F_y	Tire lateral forces	N
F_z	Tire vertical forces	N
X_G	Longitudinal displacement of CG	m
Y_G	Lateral displacement of CG	m

Chapter 1

Context, state of the art, and problem formulation

Contents

1.1	Introduction.....	2
1.2	Vehicle Dynamics.....	3
1.3	Domains of operation and domains of study.....	13
1.4	Suspension system.....	18
1.5	Strategy, Approach, and Objectives.....	29
1.6	The CRONE Control Approach.....	33
1.7	Conclusion	44

1.1 Introduction

In the past years, increasing demand for high comfort and safety vehicles had motivated the academics and industrials to intensify the studies and massively investigate vehicle dynamic control. Recently, and in line with the newly emerged markets for autonomous or/and electric vehicles, new challenges are added to the old numerous problems facing vehicular control. For safety-oriented cases, the efforts are made on stabilizing the vehicle in critical situations using the antilock-braking system (ABS) (Brugger et al., 1989; Soliman and Kaldas, 2012) and the electronic stabilizing program (ESP) (Ferguson, 2007), for example. While for comfort-oriented problems, the use of controllable suspension systems shows very promising potential in improving ride comfort (Tseng and Hrovat, 2015). Several real implementation and testing prototypes for active and semi-active suspension systems had proved their ability to fulfill comfort specifications (Casciati et al., 2012). However, dealing with these systems needs a good knowledge of the vehicle dynamics, forces and moments acting on the vehicle, and coupling effects between the embedded subsystems in both parts: the passive and the active ones.

In fact, disturbances caused by engines, gravity, aerodynamics, and road excitations are highly influencing the accelerating and braking performance, as well as steering and ride performance. Thus, control-wise, to improve the overall performance of any vehicle, convenient coordination and strategies should be applied between active systems and appropriate control rules should be adopted (Vivas-López et al., 2013).

Besides the power train and engine systems, three actuators related to braking, steering, and suspension subsystem are emphasized to enhance the vehicle's performance in this thesis. Many concerns are related to these essential systems that are very interesting in both vehicle dynamics and automatic control. A brief overview of each subsystem's characteristics reveals an important common factor between them. Braking performance defines the vehicle safety and determined by a braking coefficient that, in turn, is derived from an adhesive and hysteresis friction (Gillespie, 1992). For better braking performance, this coefficient should have high values. The ABS technology is based on this fact, where the designed strategy should keep the braking coefficient around the highest possible values. On the other side, the

handling of the vehicle is related to steering performance. One main factor in steering performance is the sideslip angle, i.e. the angle between the direction in which a wheel is pointing and the direction in which it is actually traveling. The value of the slip angle is negligible at low speeds in which cornering objectives are easy to achieve. However, at high speeds, the slip angle is significant at each wheel. Thus, the steering tasks are no longer simple and could lead to under-steering or over-steering scenarios. In fact, this is directly related to the available grip in tires. In critical steering situations and at high speeds, the available grip is exceeded and steering is no longer efficient for vehicle rotation.

The idea is that the performances of both systems, braking, and steering, are related to the tire, more precisely, its characteristics. Actually, the tire dynamics play a key role in vehicle performance. The tire characteristics have been strongly studied in the literature (Gillespie, 1992; Kiencke and Nielsen, 2005; Pacejka, 2012; Rajamani, 2012a). Here, the suspension systems, in its all kinds, turn out to be critical for the vehicle dynamics, since they provide the link between the tires and the vehicle's body. At first glance, it seems that the suspension systems influence only the tire vertical forces, i.e. the wheel load forces, but it was shown that they indirectly affect the lateral and longitudinal dynamics. Indeed, the lateral and longitudinal wheel forces are only the results of those vertical tire forces (Pacejka, 2012). In that sense, the braking, steering, and suspension systems are related to each other, thus, a well understanding for the overall vehicle dynamics and in particular, the suspension system, along with a good control design strategy, will inevitably improve the performance not only the ride comfort but also the ride safety.

1.2 Vehicle Dynamics

1.2.1 Introduction to the Global Vehicle Dynamics

Based on the laws of physics, the vehicle model can be built analytically and represents the different system dynamics. In the past, the main difficulty was in the computation process of finding mathematical solutions. Indeed, the study of global vehicle dynamics is a study of complex systems. The complexity of the vehicle dynamics relies on the form of nonlinearities, a

large number of components and systems, variations in parameters, and in particular mass and load distributions (Rajamani, 2006).

The global dynamics of a vehicle can be defined into 14 degrees of freedom (DoF) distributed into three main sections, as illustrated in Figure 1.1: longitudinal, lateral, and vertical dynamics (Gillespie, 1992). More precisely, these 14DoF are divided as follow:

- 5DoF for longitudinal dynamics
 - 1 for vehicle translation
 - 4 for the rotary motion of the 4 wheels
- 2DoF for the lateral dynamics
 - 1 for vehicle translation
 - 1 for rotational motion around z-axis: yaw motion.
- 7DoF for vertical dynamics
 - 1 translation of the chassis center of gravity (CG) in z-direction: heave motion;
 - 2 rotational motion of the chassis around the y-axis and x-axis: pitch and roll angular rotation.
 - 4 translations in the z-direction for the 4 unsprung masses (wheel).

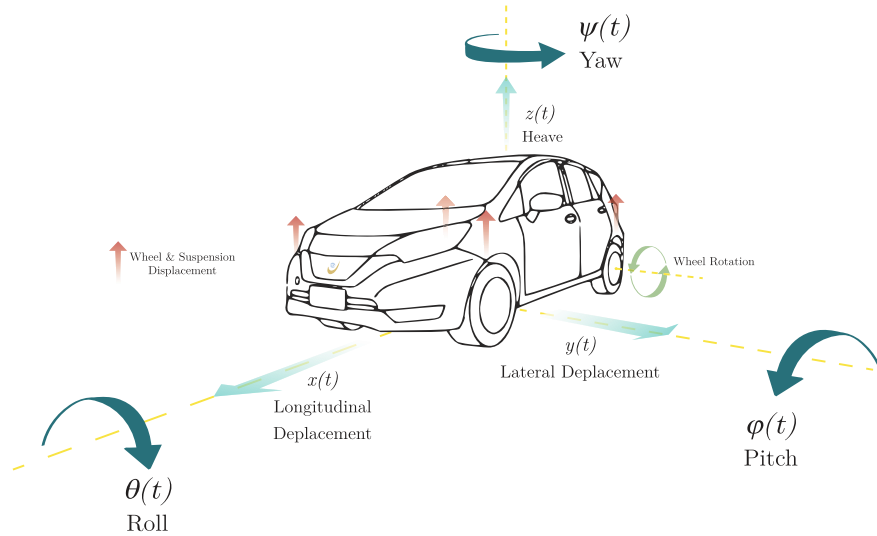


Figure 1.1. Schematic of the main vehicle dynamics.

1.2 Vehicle Dynamics

Table 1.1. The effect of LAS systems on global vehicle dynamics.

Dynamic	14DoF	Steering	Traction	Braking	Suspension
Transversal 2DoF	1 Translation	Direct	By coupling	By coupling	Indirect variation in road structure
	1 Rotational	Direct	Indirect <i>differential traction</i>	Indirect <i>differential braking</i>	
Longitudinal 5DoF	1 Translation		Direct	Direct	
	4 Rotational		Direct	Direct	
Vertical 7DoF	1 Heave	By coupling	By coupling	By coupling	Direct
	1 Pitch	By coupling	Perturbation <i>pitching couple</i>	Perturbation <i>pitching couple</i>	
	1 Roll	Perturbation <i>rolling couple</i>	By coupling	By coupling	
	4 Translation				

These dynamics are mainly excited by means of specific systems that are the linkage between the chassis of the vehicle and the road. These systems, the so-called “Liaisons Au Sol (LAS)” systems, are:

- The steering: 1 actuator (or two in case there exist rear steering);
- The traction: 2 or 4 actuators in case of 2 or 4 driven wheels;
- The braking: 4 actuators;
- The suspension: 4 actuators, one for each vehicle corner.

The action of these systems might affect the dynamics of each of the 14DoF directly, indirectly, or by the coupling effect. Table 1.1 illustrates the type of influence between the different subsystems in the vehicle. Obviously, the input action of the steering system has a direct influence on the transversal dynamics by generation lateral translational forces as well as yaw torques. But, at the same time, it indirectly generates a rolling torque on the chassis, and has a coupling effect, that affects the vertical dynamics of the vehicle. On the other hand, the traction and braking actions have a direct effect on the longitudinal and lateral dynamics, but also, they generate a pitching torque that influences the suspension (vertical dynamics). And in return, the suspension system has an indirect effect on both the longitudinal and lateral dynamics via the variation of the wheel contact forces, in addition to the direct influence on the vertical dynamics.

One main coupling effect is the one between the longitudinal and lateral dynamics on one side and the tires on the other side. The nonlinear characteristic of the tire contact forces is the critical factor that mostly influences the overall dynamics of the vehicle (Pacejka, 2012).

For best illustration, the study of these dynamics and characteristics, one can divide the vehicle operating region into different fields that are bounded by the available grip at each tire, assuming driving on dry roads. As shown in Figure 1.2a, the three domains represent the following:

- The green region, the comfort region, is defined by low longitudinal and lateral accelerations that are less than 0.4g in absolute value. In this zone, the vertical dynamics has no significant influence on the other dynamics.
- The blue region represents the limits of the linear zone of the tire model. This zone corresponds to the normal driving conditions where it represents the majority of driving time in the vehicle.
- The security region in grey represents the nonlinear zone of the tire model where safety is the main concern, e.g. obstacle avoidance, emergency braking, ...

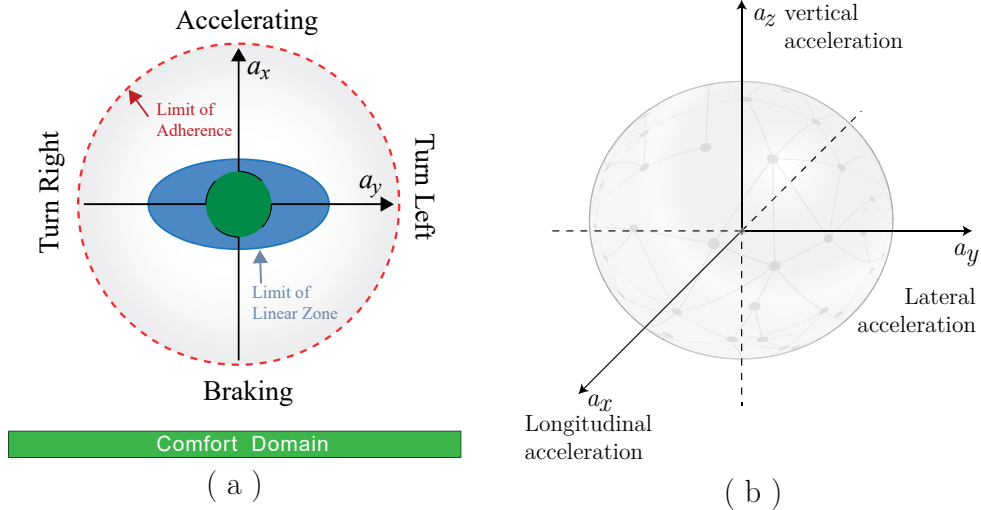


Figure 1.2. Acceleration diagrams: (a) 2D representation (a_x, a_y) ,
(b) 3D representation with a_z .

Furthermore, due to the aforementioned coupling effect between the vertical dynamics and other dynamics, the 2-dimensional diagram (g-g) related to longitudinal and lateral accelerations is extended to a 3-dimensional representation while adding a third axis related to vertical acceleration. Figure 1.2b illustrates the 3D diagram that includes the vertical acceleration, mainly the sprung mass acceleration, that is generally generated by the driver disturbance in addition to the road perturbations.

1.2.2 Vertical dynamics of the vehicle

In the context of vertical dynamics, the study is focusing on the suspension systems that are the main contributors in this framework. Those dynamics are divided into 7DoF as mentioned before.

Two main kinds of disturbances affect the vertical vehicle dynamics (Figure 1.3):

- Road disturbances, and are classified as shocks (bump, potholes, ...) or vibrations. Shocks are discrete events of relatively short duration and high intensity that causes large suspension deflections, where vibrations are typically specified as a random process that consists of high-frequency components. Thus, the road perturbations are the result of vertical variation of the road profile and are a combination of the vehicle forward speed, spectral power density, and its geometry. For this reason, dealing with these kinds of disturbances means dealing with a wide range of frequencies of interest [0-50Hz], mainly.
- Driver disturbances that are caused by the driver inputs upon braking, accelerating, and maneuvering, for example. However, the dynamics of these perturbations are related to the driver, thus, it is related to a small range of frequencies of interest and particularly at low frequencies [0-5Hz].

Road disturbances, in its all kind, directly influence the vertical dynamics and concern the ride comfort of the passengers. While the driver disturbances are affecting the same DoF but by coupling effect. Actions on

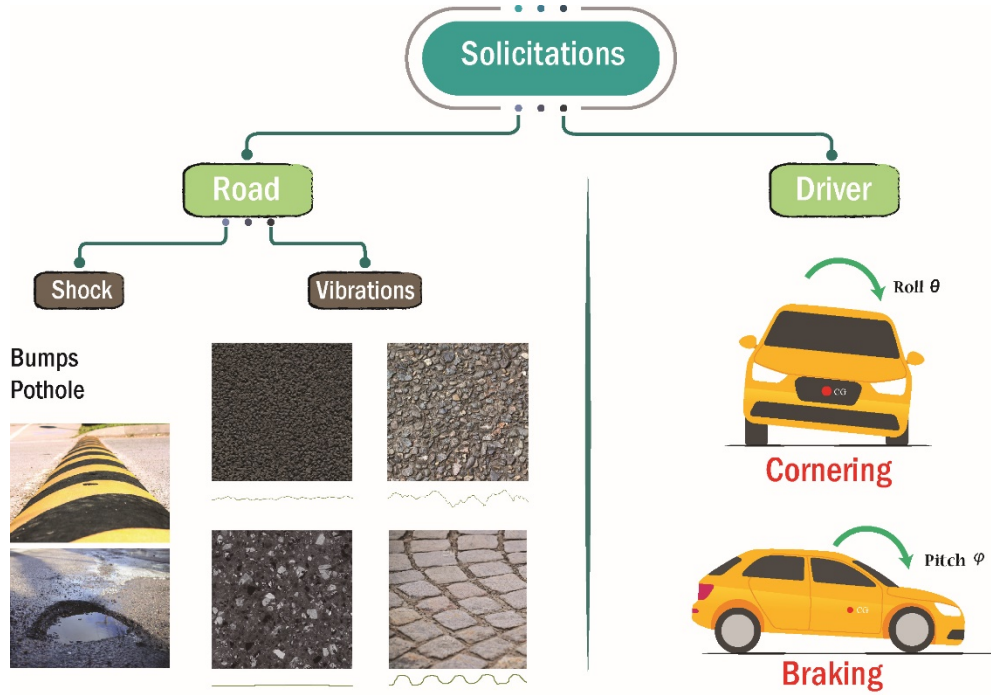


Figure 1.3. The various type of disturbances applied on the vehicle dynamics.

longitudinal dynamics (traction, braking, ...) and on lateral dynamics (maneuvering), in the form of pitch, roll, and even yaw motions, are exciting the vertical dynamics by coupling. For this reason, the effect of the vertical dynamics should be emphasized on the other dynamics (longitudinal and transversal). This study can be held by a single quarter vehicle model that is excited by road disturbances and the resulting load transfers due to driver inputs during acceleration and deceleration phases, and denoted by $f_0(t)$. The detailed modeling will be presented in the next sections.

1.2.3 Range of Vehicle models

As mentioned before, dealing with a full real vehicle model is dealing with highly complex systems that include high nonlinearities, varying parameters, etc. However, there exist three main types of vehicle modeling, each one has its own degree of complexity and role, and are introduced in the decreasing order of complexity as follow (Bouvin, 2019; L  t  v  , 2014):

- **Validation Model**: used mainly for ‘validation’, in a simulation framework, for any new high or low-level strategy or controller design. One example of these models is the vehicle simulators like SCANeR™

studio developed by Oktal (OKTALS YDAC, 2018), CarSim (Mechanical Simulation Corporation, 2020), veDYNA (TESIS, 2020), and many others. All vehicle manufacturers and their equipment manufacturers generally have such kind of models, where it combines a ‘white box’ systems of some parts, and other ‘black box’ systems for other parts, e.g. tire modeling, ...

- **Analysis Model:** deducted from the validated model by considering some simplifying assumptions. Generally used for defining new strategies, especially, the one related to the control processes. It includes the most dominant and essential behavior of vehicle dynamics.
- **Synthesis Model:** used in the designing process of the new control law of embedded mechatronics in the vehicle. It is obtained by restricting the area of interests of vehicle operations, uncertain zones, and additive dynamical assumptions, thus, get the most simplified version within the region of interests.

The resulted vehicle model leads to an imperfect representation of the real system; however, this degree of deficiency is related to the settled objectives, e.g. validate, understand/analyze, or synthesize.

One common approach adopted by researchers upon collaboration with industrials, is the V-Shaped approach, as illustrated in Figure 1.4. It is also known as the Verification and Validation model. It is based on the association of a testing phase for each corresponding development stage. The development of each step is directly associated with the testing phase. The next phase starts only after completion of the previous phase i.e. for each development activity, there is a testing activity corresponding to it. This approach is comprised of:

- The industrial side provides the “reference” vehicle model, that undergoes identifications and re-adjusting vehicular parameters to attain similar responses compared to that of real bench tests, either on track or on road. Here, the domain of validity is then determined and the degree of correlation between the reference model and the real vehicle is then identified.

- Extract from the “reference” model the needed specification related to the new prescribed implemented systems, e.g. steering, braking, traction, suspension, etc.
- Implementing and applying the newly designed strategy, part, or control that aims to improve the existing one.
- The last step is to establish a comparison of the performance of the new strategy designed with that of the “reference” model.

Full Vehicle Validation Model

The simulations for strategy validation are done using the full non-linear car model with 14 degrees of freedom taking into consideration most of the nonlinearities existing in the vehicle dynamics. This model has been widely studied in the literature (Ahmadian and Blanchard, 2007; Berger, 2014; Connair et al., 1999; Giangliulio, 2006; Gillespie, 1992; Rajamani, 2012a). This model is developed in a MATLAB/Simulink environment as illustrated in Figure 1.5, accompanied by several file scripts that define the parametric configuration of the vehicle including tire characteristics.

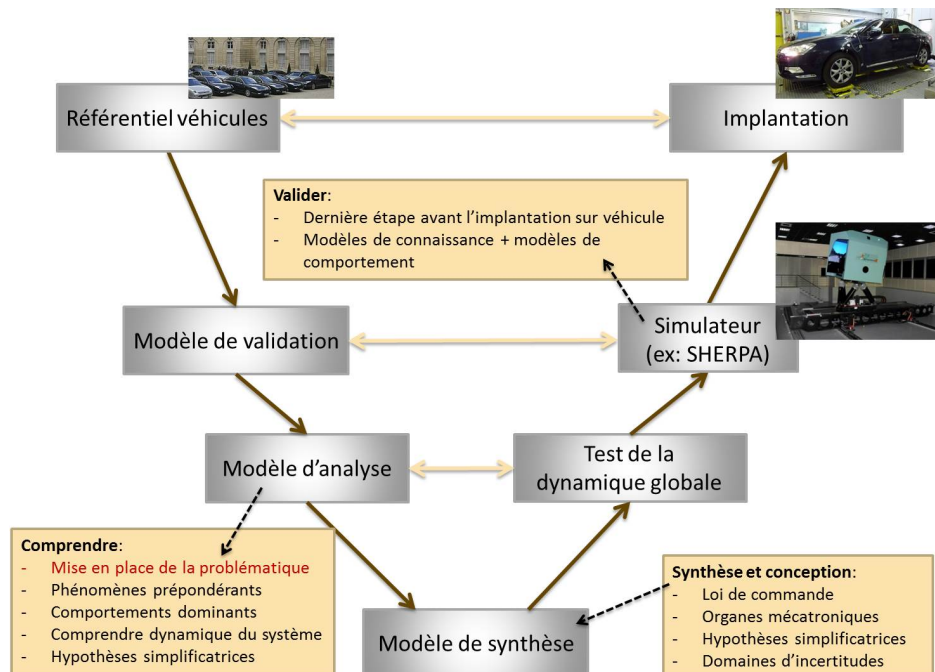


Figure 1.4. V - cycle approach for designing of vehicles' elements (Létévé, 2014).

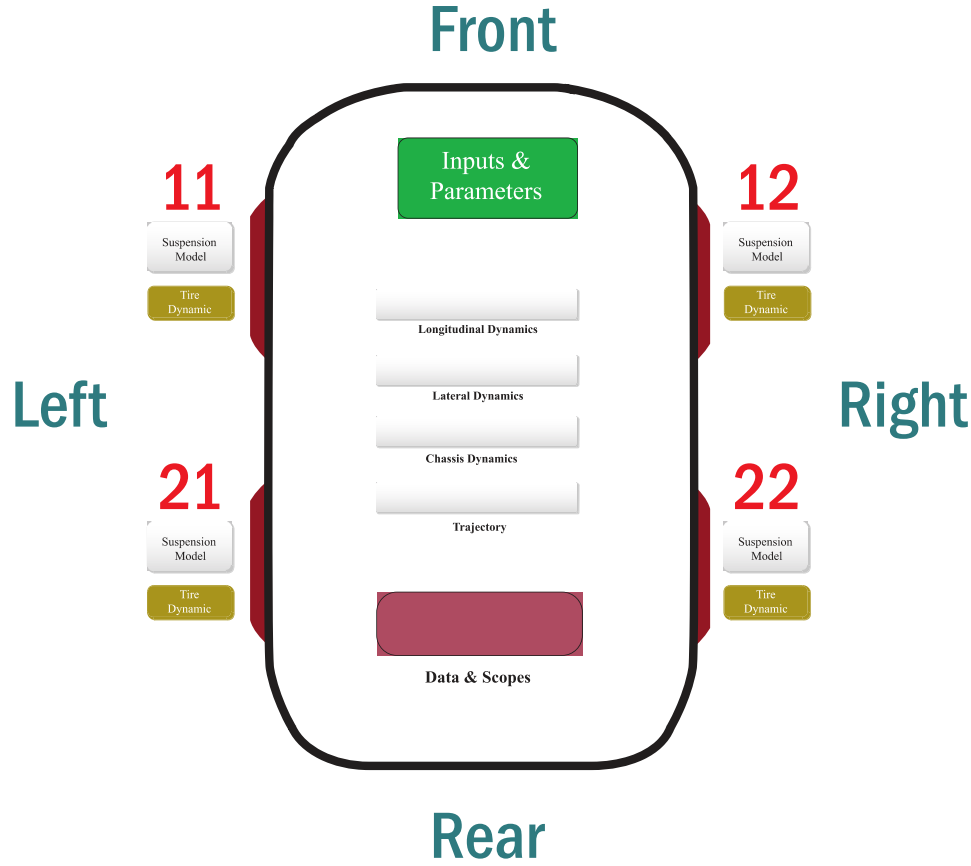


Figure 1.5. Validation model in MATLAB/Simulink environment.

1.2.3.1 Quarter Vehicle model: a compromise between complexity and dynamics

The quarter vehicle system is modeled using the well-known quarter-model that exists in the literature (Jazar, 2014; Rajamani, 2012a; Savaresi et al., 2010). This approach is facilitating the analysis where the degree of complexity is reduced from 14Dof in a full vehicle to the only 2DoF related to each corner, taking advantage of the symmetry of the vehicle properties. Here, the four wheels are assumed decoupled and the suspension dynamics are considered in the frequency range of interest for the vertical dynamics [0 - 30 Hz]. Although of the nonlinear characteristics of the suspension components, in reality, it is pointed out that such a model can be used for optimal suspension control design and analysis (Hrovat, 1997), where it represents a convenient modeling framework to evaluate the performance and robustness of a controller.

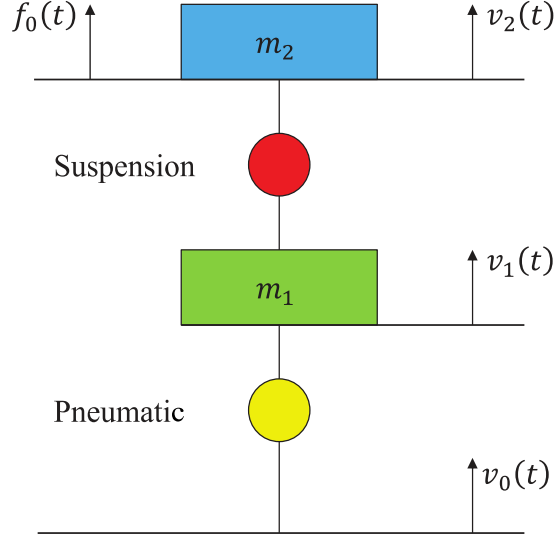


Figure 1.6. Schematics of the Quarter vehicle analysis model (Bouvin, 2019).

Figure 1.6 shows the general quarter vehicle configuration (Létévé, 2014), where m_2 represents the sprung mass (in kg), m_1 represents the unsprung mass (in kg), $f_0(t)$ is the load transfer forces mainly caused by driver disturbances (in N), and $v_2(t)$, $v_1(t)$, and $v_0(t)$ are the velocity of sprung mass, unsprung mass, and road variation at the contact point pneumatic-ground (in m/s), respectively.

By applying the fundamental laws of physics, two equations are defined representing the dynamics of the vertical velocity of the sprung mass $v_2(t)$ and the unsprung mass $v_1(t)$ in (m/s) as follow:

$$v_2(t) = \frac{1}{m_2} \int_0^t F_{\Sigma_1}(\tau) d\tau + v_2(0), \quad (1.1)$$

and

$$v_1(t) = \frac{1}{m_1} \int_0^t F_{\Sigma_2}(\tau) d\tau + v_1(0), \quad (1.2)$$

with $F_{\Sigma_1}(t)$ and $F_{\Sigma_2}(t)$ represent the algebraic sum of all forces (in N) applied on the unsprung mass and the sprung mass, respectively, such that:

$$\begin{cases} F_{\Sigma_1}(t) = F_1(t) - F_s(t) - m_1g \\ F_{\Sigma_2}(t) = f_0(t) + F_s(t) - m_2g \end{cases}, \quad (1.3)$$

where $F_1(t) = F_1^0 + f_1(t)$ and $F_s(t) = F_s^0 + f_s(t)$, are respectively, the vertical forces developed by the pneumatic of the wheel on the unsprung mass m_1 (in N) and by the suspension system on the sprung mass m_2 (in N), while $f_1(t)$ and $f_s(t)$ represent the variations of these forces around the characterized equilibrium point, where F_1^0 and F_s^0 are the static components defined at the equilibrium state.

For a given suspension configuration, the force developed by the suspension system $F_s(t)$ depends, in a non-linear manner, on the suspension stroke and its velocity. Similarly, for a given wheel pressure, size, and structure, the vertical force generated by the wheel $F_1(t)$ depends, in a nonlinear manner, on the wheel deflection and its velocity.

The study of quarter vehicle dynamics is carried out incongruent with the vehicle's domain of operation, as illustrated in Figure 1.2.

1.3 Domains of operation and domains of study

The domains of study considered in this thesis represent the different zones of operation of a light electric vehicle. As mentioned before, the study of the dynamic vehicle behavior can be divided mainly into two regions as a function of lateral and longitudinal accelerations, and independent of the road solicitations, that is:

- Linear zone that corresponds to the normal driving situations;
- The nonlinear zone that corresponds to critical and emergency situations where the grip limits of the tires could be exceeded.

In fact, by adding the effect of road solicitations, three fields of study can be defined on the (g-g) diagram as shown in Figure 1.7. These fields are as follow:

- The **vibratory comfort**;
- **Road holding**;
- **Operating limits** or active safety.

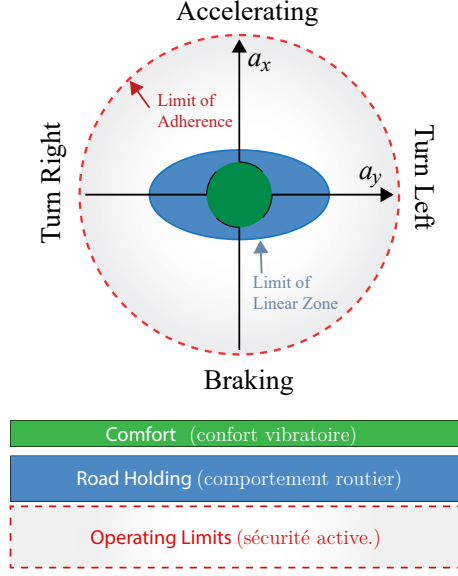


Figure 1.7. Representation of the domains of study on a diagram of (a_x, a_y) .

In the context of suspension system control and analysis, the field of studies is divided into the three defined zones, in which every zone is related to the amplitude of the variations in the suspension stroke (suspension deflection) around its static equilibrium point (Bouvin, 2019; Létévé, 2014).

1.3.1 Domain of operations

The three domains of operation shown in Figure 1.7 are then related to three types of variations:

At Small variations

This domain of operation corresponds to a small variation of the suspension deflection around the static equilibrium positions. The limits of this domain are determined generally by a predefined value of the amplitude of the variations. It is worth noted that the vehicle behavior in this zone is considered linear, thus, it permits the establishment of a linearized model around a given static equilibrium position, as well as the use of time-frequency duality. This gives the advantage for the use of the linear model for the analysis of the vehicle's behavior and to the synthesis/design of the suspension architecture/control.

The domain of “small variation” is then associated with the vertical dynamics in the field of study of “vibrational comfort”, where it won’t have a significant influence in the vehicle dynamic behavior of the “road holding” zone (Rizzo, 2012). In this framework, only a small variation of road profile variation $v_0(t)$ are taken into account, while neglecting the small variation could be generated from load transfers $f_0(t)$ applied on the vertical vehicle’s dynamics.

Using the model presented in Figure 1.6, and after linearization around the position of static equilibrium, the Laplace transform is applied with the assumption of zero initial conditions, and a linear model can then be deduced (Létévé, 2014). The diagram and the configuration of this linear model are shown in Figure 1.8a. The vertical behavior of the tire is defined by the Kelvin - Voigt model (Gillespie, 1992), where k_1 and b_1 represent, respectively, the equivalent tire stiffness (in N/m) and the damping coefficient (in Ns/m). The advantage is that this generic model is independent of the suspension architecture, where the mechanical impedance is denoted by $I_s(s)$ and defined by:

$$I_s(s) = \frac{F_s(s)}{V_{12}(s)}, \quad (1.4)$$

where $F_s(s) = \mathcal{L}\{f_s(t)\}$ and $V_{21}(s) = -V_{12}(s) = \mathcal{L}\{v_{21}(t)\}$, where \mathcal{L} denotes the Laplace Transform operator. Furthermore, $v_{21}(t) = v_2(t) - v_1(t)$ represents the velocity of the suspension deflection (in m/s).

Finally, the causal diagram, according to the Bond Graph approach (Margolis and Shim, 2001), is presented in Figure 1.8b with the representation of the admittance term $A_1(s)$ and $A_2(s)$ of the masses m_1 and m_2 , respectively, such that:

$$A_1(s) = \frac{V_1(s)}{F_{\Sigma_1}(s)} = \frac{1}{m_1 s}, \quad (1.5)$$

and

$$A_2(s) = \frac{V_2(s)}{F_{\Sigma_2}(s)} = \frac{1}{m_2 s}, \quad (1.6)$$

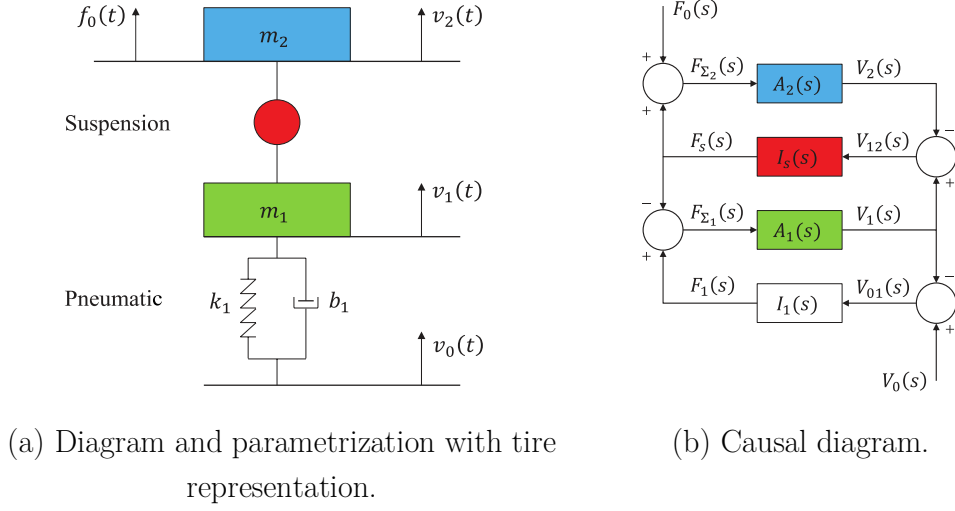


Figure 1.8. Analysis model of quarter vehicle (Létuvé, 2014).

where the $I_1(s)$ the impedance of the tire is defined by:

$$I_1(s) = \frac{F_1(s)}{V_{01}(s)} = \frac{k_1}{s} + b_1. \quad (1.7)$$

The variable $V_{01}(s) = \mathcal{L}\{v_{01}(t)\}$, where $v_{10}(t) = -v_{01}(t) = v_1(t) - v_0(t)$ is the velocity of wheel deflection in (m/s). The remaining terms that appear in the causal diagram are discussed later in detail in the next chapters.

At Medium variations

The second operating domain of the suspension is defined for a greater value of the suspension deflection corresponding to medium variation around the static equilibrium position. Here, these variations result from both: the road disturbances $v_0(t)$, and the driver disturbances $f_0(t)$ (load transfer). These variations affect the vehicle's overall dynamic behavior, except these that results from singular events that could lead to reaching the critical limits of suspension travel. This domain of operation is closely linked to the area of study of road holding, and consequently, it requires a more complex model than the quarter vehicle model to analyze all the dynamics involved (at least a four-wheel model with suspension).

At high variations

The domain of operation, in this case, is defined by the set of large variations around the static equilibrium position. These variations result mainly from road disturbances (speed bump, potholes, ...) as well as the driver disturbances (emergency braking, ...), which could lead to reaching the limits of suspension deflection.

This area of operation is closely linked to the active security region, where it is necessary to consider the limit of the suspension deflections. This is critical for comfort and safety, as well as road holding. Moreover, it requires a full vehicle model to analyze the overall vehicle's behavior.

1.3.2 Adequation of the different domains

Table 1.2 summarizes the adequacy between the areas of operating and the areas of study (Létévé, 2014). Thus, vibrational comfort can be analyzed within the framework of the three operating domains (green-fill), but the synthesis of a new suspension architecture could be done with small variations operations regions, while it couldn't be done within medium and / or large variations (red-fill). Then, road behavior can be analyzed, too, within the framework of the three operating domains, knowing that in this work no synthesis method road behavior-oriented is proposed. Finally, obviously, the analysis of the operating limits in small/medium variations are not necessary (grey-fill), only the operating domain with large variations could be studied, not only in terms of analysis but also in terms of synthesis.

Table 1.2. Adequation between domains of study and domains of operation.

		Domains of Operation					
		Small Variations		Medium variation		High variations	
		Analysis	Synthesis	Analysis	Synthesis	Analysis	Synthesis
Domains of Study	Vibratory comfort						
	Road Holding						
	Operation Limits						

1.3.3 Conclusion

The action of the LAS systems generates torques and forces that influence the overall dynamic behavior of a vehicle, i.e. longitudinal, lateral, and vertical dynamics. On one hand, the study of the global dynamics of the vehicle,

including high complex systems: nonlinearities, variable parameters, and coupling effects between various embedded systems, requires convenient and suitable modeling. In particular, concerning the suspension systems studies, the models range from the full complete vehicle model for validation to the quarter vehicle mode for synthesis. These models are based on the predefined domain of operation of the vehicle, and the objective of the study in order to facilitate the synthesis and the validation of the control/strategy designed.

1.4 Suspension system

1.4.1 Introduction

The suspension system used in the automobile is made up mainly of two components, the spring and the damping element, so-called the shock absorber (Figure 1.10). This simple system passes through one hundred years of development, from the appearance of passive dampers in Roll Royce in 1913 to the highly complex controllable Magneto-Rheological (MR) dampers used in the most recent cars, for example. Today, it plays an important role in the automotive industry due to its increased potential in improving the safety and handling of the vehicle, besides the vibration isolation and ride comfort. More detailed historical facts on suspension systems are presented in (Aubouet, 2010).

The suspension system is the system that is responsible to link the unsprung mass (e.g. wheels) to the vehicle chassis or body. As illustrated in Figure 1.9, three main roles fall on the automobile suspension system:

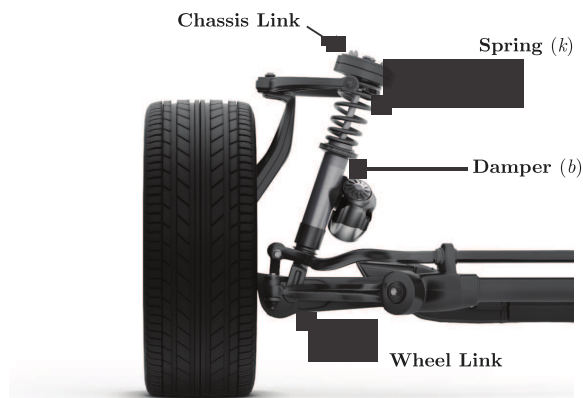


Figure 1.9. Traditional suspension system.

- Support the static load of the vehicle;
- Ensuring passenger comfort through vibration isolation;
- Ensuring road-wheel contact by road holding.

The two main components of the suspension system should work adequately to fulfill these roles. The spring should reduce the effect of traveling over rough roads, leading to improved ride quality. While shock absorbers serve the purpose of limiting excessive suspension movement and damp spring oscillations. For this reason, without shock absorbers, the vehicle is able to absorb bumps, but the undamped suspension means that the vehicle will continue to bounce which might cause the tires to lose contact with the ground. Thus, adding shock absorber in parallel to springs, means that the vehicle could dampen the motion to prevent the vehicle from bouncing, in addition to bump's absorption. In this sense, it guarantees the contact between the wheel and the ground that is necessary for maintaining road holding and therefore for passenger safety.

Indeed, the roads on which vehicles are driven are highly heterogeneous (Figure 1.11). The needed suspension characteristics depend on the degree of roughness of the road considered. Generally, road roughness has varying dimensions and shapes and consists of random distribution spatially and temporally spectrum (Bouvin, 2019). Thus, these solicitations generate continuous vertical displacements whose direction and intensity depend on the

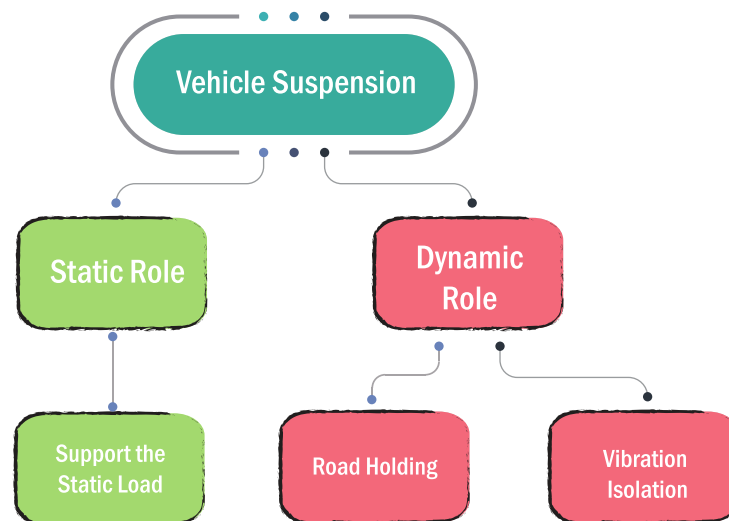


Figure 1.10. Main roles of the vehicle suspension system.



Figure 1.11. Representation of different road roughness and obstacles (Bouvin, 2019).

profile of the obstacle as well as on the speed of crossing. To further understand the suspension role, it should be worthwhile to assume a vehicle chassis that is rigidly connected to the wheel without the suspension system. Then these accelerations are directly transmitted to the body of the vehicle, thus, transferred to the passengers. Consequently, this implies a discomfort driving experience and could be harmful or even dangerous for passengers. In this sense, the suspension system fulfills its critical role by acting on the comfort of the vehicle.

Moreover, vibrations affect our ability to work in both physical and mental sense. It may impair concentration or sensing important information or signals. In the physical sense, vibrations are a risk for the body tissues and organs since they absorb the energy of such vibrations. Particularly, the muscles compensate for the small forces that vibrations expose the body to, and if the body is exposed to vibration for a long-time duration this could pose a risk to the joints and could tire the muscles (Berlin and Adams, 2017). Besides that, in vehicles where the body is sitting on a vibrating base, an additional risk factor is that different body tissues have different resonance

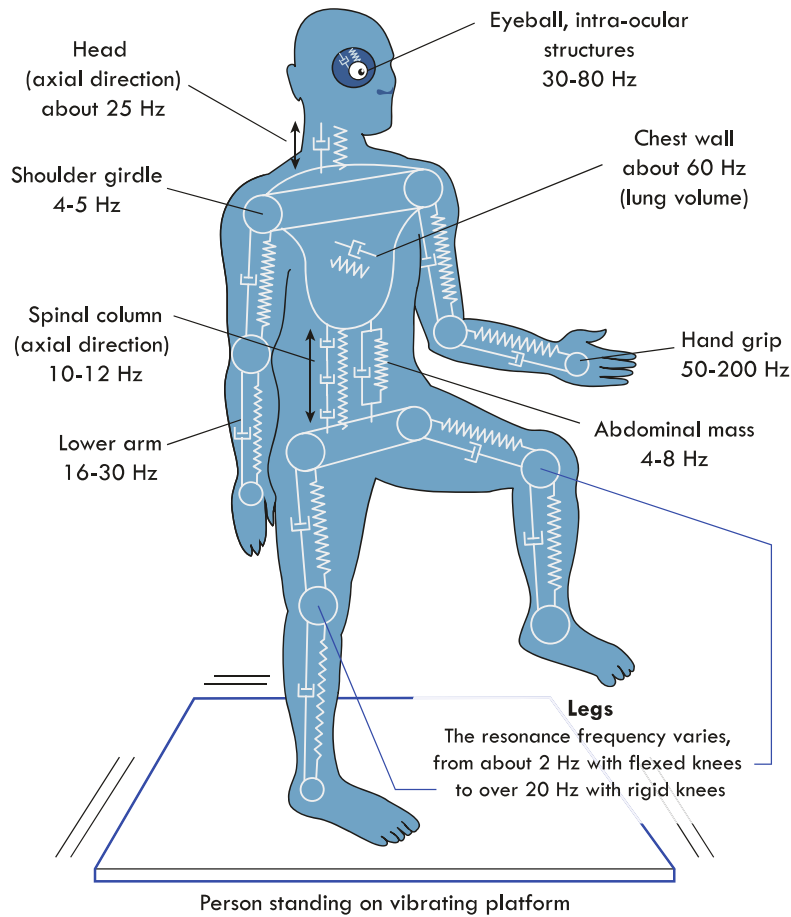


Figure 1.12. Resonance frequencies for different body segments, represented by a simplified mechanical model of a human standing on a vibrating platform (Berlin and Adams, 2017).

frequencies, meaning that there is a range of vibrations at which somebody tissue will experience local discomfort (Figure 1.12). These resonance frequencies will vary from individual to another but tend to lie within a certain range, e.g. the resonance frequency of the shoulder typically lies between 4 to 6Hz, according to (Bohgard et al., 2009; Rasmussen, 1982).

However, not only joints and muscles are at risk, even the internal organs like the brain and eyes are sensitive to vibration at different frequencies. For example, the eyes at resonance frequency cannot function properly and lead to impaired visual work, while low-frequency vertical vibration ($<1\text{Hz}$) has a particular tendency to cause nausea or drowsiness. This explains why some

people can experience motion sickness in the vehicle, while others are lulled to sleep. For this reason, it's very critical to ensure passenger comfort by filtering vibrations at a different range of frequencies. Although the tires and the seats partially absorb high-frequency irregularities, however, it is not enough to fulfill the global objectives.

In order to ensure passenger safety, the influence of the suspension on the road holding behavior of the vehicle must also be taken into account. Indeed, during emergency driving situations, the priority then goes to safety rather than comfort. Although this is mainly dependent on the tire because it's in direct contact with the road, the suspension also plays a large role in maintaining this contact. In some cases, road irregularities could lead the wheel to lift off the ground and lose contact with the road, thus, losing the ability of handling, braking, and traction functionality.

Therefore, as the suspension system could affect the overall dynamics of the vehicle, the work and studies should be oriented to optimize the performance of the suspension system in the sense of improving the overall dynamics of the vehicle.

1.4.2 **Classification of Suspension systems**

Along with the strong development of the automotive industry during past decades, the suspension system has evolved continuously to be able to meet the requirements mentioned above. The evolution was based on the mechanics, hydraulics, and electrical technological advances, as well as the control strategies applied. The suspension systems could be divided into two main sets:

- Passive suspension systems
- Controllable suspension systems.

The suspension system is passive if the characteristics of the components are fixed. These characteristics are determined by the designer of the suspension, according to the design goals and the intended application.

On the other hand, the controllable suspension may be carried out according to the energy input and the bandwidth of the actuator. Here, three features may be observed: the controllability range, in other words, the range

of forces that the actuators may deliver; the control bandwidth which is a measure of how fast the actuator action is; the power request that is mainly a result of the combination of controllability range and control bandwidth. The resulting classification is concisely shown in Figure 1.13, which highlight five families of controllable suspensions (Savaresi et al., 2010):

- **Adaptive suspension:** the control action is applied as slow damping coefficient modulation. Thus, the control range is limited by the passivity constraint. The adaptive damping control is characterized by a small bandwidth and no energy is introduced in the system; therefore, the power demand is relatively very low (few Watts).
- **Semi-active suspension:** the control action is applied as fast damping coefficient modulation, in which it features an electronic shock absorber with a relatively large bandwidth up to 40Hz. However, the generated forces follow the passivity limits of the damper, thus no energy may be introduced into the system. Therefore, the demanded power is also relatively low (tens of Watts).
- **Load-leveling suspension:** it is considered as the first attempt towards full active suspensions, where they are capable of introducing energy in the system to change the steady-state condition. This kind of suspension acts on the parameter of the springs usually, e.g. air spring suspension (Allen, 1985). The bandwidth generally is within 0.1-1 Hz, but the power request is around hundreds of Watts.
- **Slow-active suspensions:** in active suspension systems, the passivity limits are fully overcome and energy is introduced into the system. The control input is represented by a suspension force delivered by an actuator placed parallel/series to passive components or replace them. Generally, the bandwidth of such systems is relatively limited to a few Hertz, where the power consumption is in the range of kilo-Watts.

1.4 Suspension system

- **Fully-active suspensions:** the main difference here is the bandwidth relative to the slow active suspension. The fully active actuator is able to generate force at high frequencies and could reach the limit of 30Hz for some systems. This advantage comes at the expense of high-power requirements where it ranges in the region of tens of kilo-Watts.

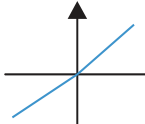
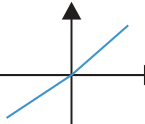
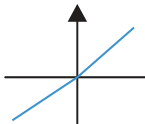
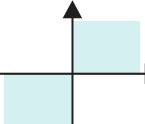
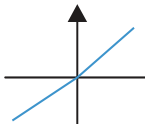
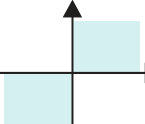
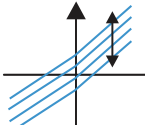
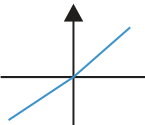
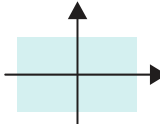
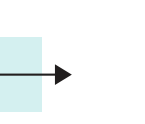
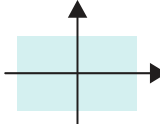
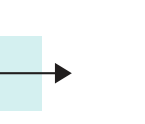
System class	Control range (spring)	Control range (damper)	Control bandwidth	Power request	Control variable
Passive			-	-	-
Adaptive			1-5 Hz	10-20 W	c (damping ratio)
Semi-active			30-40 Hz	10-20 W	c (damping ratio)
Load leveling			0.1-1 Hz	100-200 W	W (static load)
Slow active			1-5 Hz	1-5 kW	F (force)
Fully active			20-30 Hz	5-10 kW	F (force)

Figure 1.13. Classification of electronically controlled suspension (Savaresi et al., 2010).

1.4.3 Some Suspension system realization

Various attempts have been done in finding solutions for the inherent tradeoff of passive suspension systems since the 1980s. One example is the BOSE systems (Figure 1.14) (Rakshith et al., 2014). This suspension uses

an electromagnetic actuator that serves as driver and road disturbance rejection. The heart of the system is based upon a linear electromagnetic motor that is installed at each wheel. Inside the linear electromagnetic motor are magnets and coils of wire. When electrical power is applied to the coils, the motor retracts and extends, creating motion between the wheel and the car body. One of the key advantages of an electromagnetic approach is its fast response. The linear electromagnetic motor responds quickly enough to counter the effects of bumps and potholes, maintaining a comfortable ride. Additionally, the motor has been designed for maximum strength in a small package, allowing it to put out enough force to prevent the car from rolling and pitching during aggressive driving maneuvers.

Another example is the Hydractive suspension system developed by Citroën. Recent developments in electronics and computers made it possible to delegate many functions previously solved by mechanical-hydraulically components to electronic units. The latest version of this technology was the third generation, the so-called Hydractive 3+. Just like its predecessor, this system also has two modes, firm and soft. A stiffness regulator, an additional sphere and a hydraulic control block per axle, isolates or connects the corner and center spheres. The Hydractive suspension system also includes an automatic attitude correction device illustrated in Figure 1.15. This system maintains the ground clearance of the vehicle by modifying it at the request of the driver or, dynamically, depending on the speed and the road condition (Bouvin, 2019). Furthermore, the CREUAT suspension, another active form of the suspension system, is a very close solution to Hydractive one (Figure 1.16). The big difference in the CREUAT system is although it has four gas spring chambers, however, they are not allocated one to each corner of the car.

Finally, the CRONE suspension system that had been intensively studied for years and could be found in details in (Bouvin, 2019; Daou et al., 2012; Létévé, 2014; Moreau et al., 2004, 1996; Oustaloup et al., 1996; Rizzo, 2012).

1.4 Suspension system

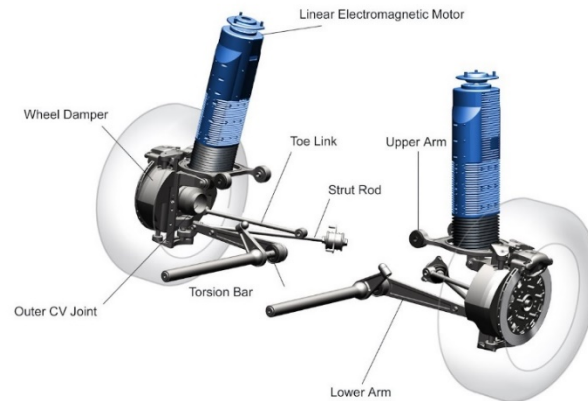


Figure 1.14. The Architecture of Bose Suspension.

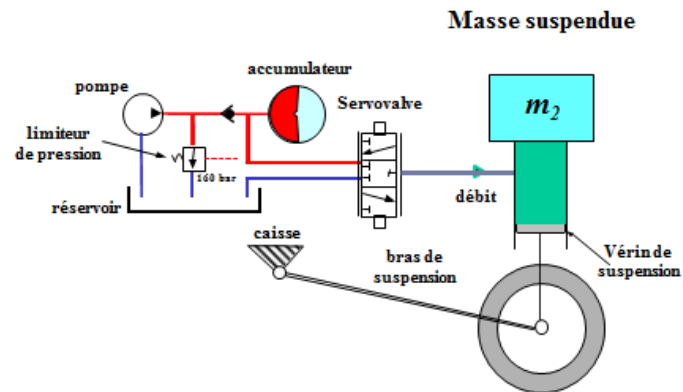


Figure 1.15. Representation of the attitude correction system of the standard Hydractive suspension.

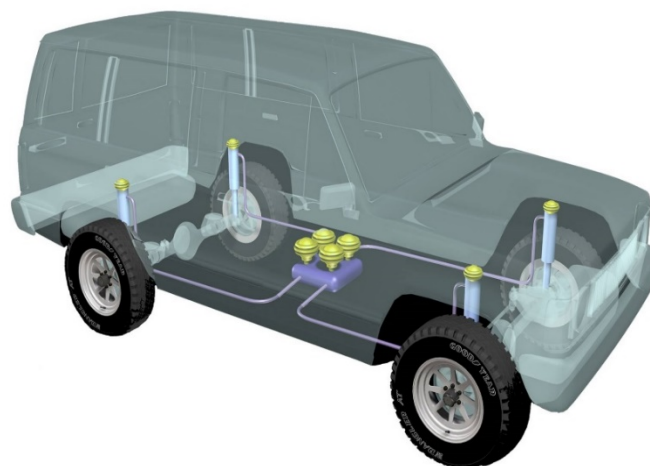


Figure 1.16. Hydraulic implantation of the suspension CREUAT.

1.4.4 Active Wheel

Automobile manufacturers are in the process of launching EVs and a market for electric mobility solutions will emerge where all-in-wheel devices are expected to play an important role in this new trend. Such vehicles are able to adapt to urban lifestyles, mainly, to contribute to the air quality and noise reduction in urban cities. Since a lighter vehicle means a sharp reduction in energy consumption, a modern solution can contain integrated power-train suspension located directly inside the wheel. One example of such technology is the Active Wheel (AW) developed by Michelin (Figure 1.17). This advanced technology initiates a new era in road transportation where all essential components have been integrated within the wheel itself: the pneumatic part, a compact traction electric motor with regenerative braking, an electric active suspension system, and the braking system.

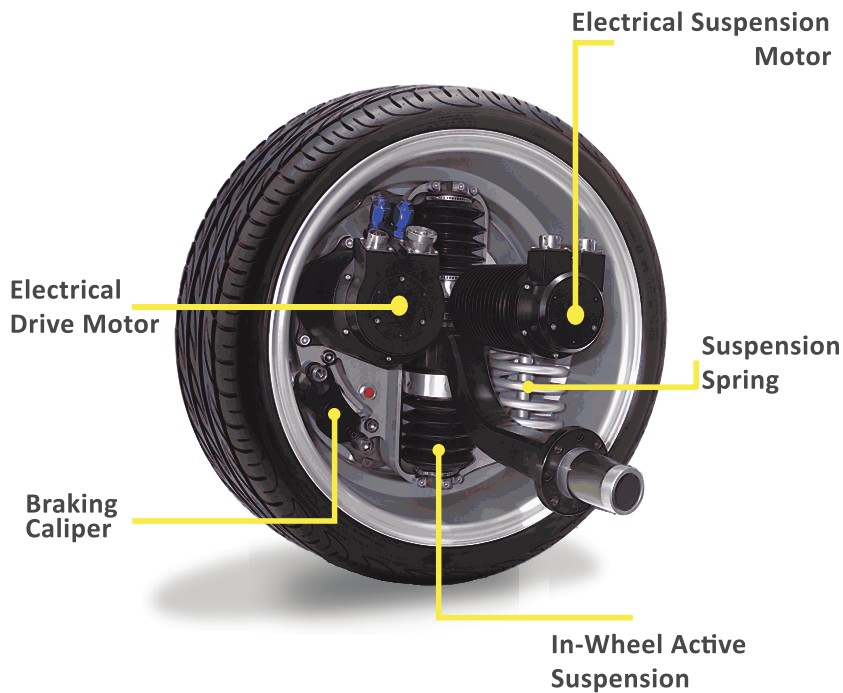


Figure 1.17. Active Wheel structure.

The structure of the Active Wheel offers new opportunities in Global Chassis Control (GCC) that rises, recently, to remarkable levels. At first, the conventional mechanical suspension has been replaced by a passive spring and a DC electrical motor. In comparison with other force-generating actuators (hydraulic, Hydractive, hydro-pneumatic...), the DC linear

characteristics of the AW's suspension system provides an extremely fast response time (just 3/1000th of a second), low contact friction, high precision and efficiency, good controllability, and less energy consumption (Nguyen et al., 2011).

Depending on the amount of power or type of usage desired, a given vehicle may integrate four motors (one in each wheel) or two motors (in the front wheels, for example). In this way, the Michelin Active Wheel allows automobile manufacturers to continue designing both two and four-wheel drive cars.

With the Michelin Active Wheel, the energy that powers the integrated motor is always electric whether it comes from a lithium-ion or other type of battery, a fuel cell, and /or supercapacitors. In all cases, these power sources offer two important benefits - zero pollution and optimal comfort - since vehicles equipped with the Michelin Active Wheel emit no greenhouse gases. What's more, electrical power trains are extremely quiet, which is an advantage not only to passengers but above all to people outside the vehicle. In short, a car powered by the Michelin Active wheel solution is like a breath of fresh air in urban environments.

The Michelin Active Wheel greatly simplifies the vehicle design process by making the mechanical components on a conventional car superfluous. Vehicles powered by the Michelin Active Wheel have no need for a gearbox, clutch, transmission shaft, differential or shock absorbers. This, in turn, makes cars lighter and thus more energy efficient. As a result, the vehicle can achieve an operating range in line with motorist expectations.

This technology is clearly a game-changer, providing an effective and elegant response to today's critical road transportation issues: energy (quantity, diversity, and cost), greenhouse gas emissions, urban congestions, and urban pollution.

Figure 1.18 shows two examples of light electric vehicles equipped with Active Wheel technology. For example, the Heuliez WILL electric vehicle, which has a maximum mass of 1000kg, and a maximum speed of 140km/h, with 2-wheel motor drive. The other example, the Venturi Volage, which



Figure 1.18. Light electric vehicles equipped with Active Wheel:
(a) Venturi Volage, (b) Heuliez Will.

has two seats only, with four Active wheels, with a maximum speed of 150km/h.

The structure of the AW is adopted in this thesis, where it considers a light vehicle equipped with Active Wheel technology. The study and the control of the suspension systems are based on the structure of the electrical active suspension systems integrated into the Active wheel.

1.4.5 Conclusion

The technology of suspension systems had been developed for around a hundred years. Much innovative passive and active versions are revealed to deal with the increasing demand for comfort and road holding requirements. They are distinct in terms of energy consumption and control bandwidth, mainly. The final objective of any designed suspension system is to full fill the specifications of the comfort, handling, and safety of the vehicle. In this work, the Active Wheel structure is adopted, taking advantage of its electrical and linear characteristics. The work is then oriented to investigate the contribution of such structure in the global chassis control of a light electric vehicle.

1.5 Strategy, Approach, and Objectives

1.5.1 Introduction

In the framework of global chassis control of a light electric vehicle, the focus is oriented to control the critical active systems embedded in the vehicle. Pointing towards the well-known and common objectives of all global chassis control strategies, i.e. comfort, handling, road holding, and safety.

Firstly, in this study, a frequential synthesis of robust controllers are taken into account, e.g. CRONE, H_∞ , QFT, ... However, the CRONE controller, in its all generations, is the most used controller along with this work in order to get the most advantage of collaborations with the CRONE group at the IMS Lab. Furthermore, the comparison between these types of controllers with temporal synthesized controllers could be as a perspective., e.g. LQ, LQG, sliding mode controller, backstepping controller,

1.5.2 Two-level Approach

The “Top - Down” Approach

In this approach the designer is looking forward for the maximum performance could be achieved, while assuming the following:

- All the state variables are considered measurable, and no limitations are existing on the number of sensors needed.
- All the sensors used are working perfectly, that is their dynamics are neglected, and no noise measurements are introduced.
- All the actuators are assumed to work perfectly, where their dynamics are neglected with no saturation limits, that is all desired control inputs are supposed to be equal to the generated one.

The “Down - Top” Approach

In this approach, a variety of constraints are taken into account and introduced to the study, as a result, a more realistic performance is achieved. Some of these realistic constraints are as follows:

- The number of sensors is limited, then the use of observers and estimators is necessary.
- The limitation of the saturation of the control input of actuators is considered as well as the dynamics of the actuator.

- The dynamics of sensors and noise measurements and the range of operating are no longer neglected.

1.5.3 Vertical Control Objectives

In the framework of Global Chassis control, the primary work done was regarding the vertical dynamics control of the light electric vehicle. The objectives are listed as follows:

1. Varying the height of the vehicle at a stop, e.g. loading and unloading phases.
2. Holding chassis against driver solicitations.
3. Holding chassis against road perturbations.
4. Attain good vibratory isolation against road perturbations.
5. Holding the wheel (unsprung mass) under road disturbances by:
 - Level 1: limiting the vibrations from the wheel to the chassis
 - Level 2: limiting the variations of the wheel deflections in the sense of control of road holding.

The global problem of vertical dynamics control of the vehicle is then decomposed into different local issues.

- At the scale of the quarter vehicle model: using the 2DoF model to deal with chassis dynamics (sprung mass) and wheel dynamics (unsprung mass).
- At the scale of the complete vehicle model, using the 7DoF model that includes: Heave, pitch, and roll motions, and the four movements related to wheel displacements.

These objectives are to be discussed in detail in the next chapters.

1.5.4 Longitudinal Control Objective

In the context of analyzing the longitudinal dynamics of the light electric vehicle, the study is focused on the effect of the vertical dynamics of the vehicle on the longitudinal dynamics. Here, the work done is related to braking behavior only.

Along with the many advances in vehicular technology development, the safety requirements for automobiles are of great importance. The techniques applied to various vehicles have already improved the system's stability and passenger's safety with the use of several significant control systems, such as anti-lock braking systems (ABS) (Dix et al., 1995; Peeie et al., 2016; Schinkel and Hunt, 2002)

Thus, an ABS CRONE controller is introduced and then a coordination strategy between the longitudinal control and the designed vertical controllers is done in the sense of optimizing the braking performance of the vehicle.

1.5.5 Lateral Control Objective

For lateral dynamics, the study is divided into different parts and can be listed as follows:

- Improve vehicle's stability by yaw rate regulation using a micro-braking system controller.
- Improve vehicle's stability by yaw rate regulation using a micro-steering system controller.
- Improve the tracking trajectory using a controlled active steering system.

Using the CRONE controller, the following objectives are to be achieved, while taking into account the effect of vertical dynamics on each system.

Then, the final objective is to establish the effect of the controlled vertical dynamics system on each of the lateral controlled dynamic systems and implement collaboration between these systems for optimizing vehicle lateral stability and tracking trajectory.

1.5.6 Conclusion

In the framework of GCC, there exists three main architecture in the literature, namely, the centralized control, decentralized control, and control by supervision (Gordon et al., 2003). This study adopts a supervision control strategy, that represents an intermediate structure between the other two ones, by a proposed hierarchical approach for vertical dynamic control of a light electric vehicle coordinated with longitudinal and lateral dynamics. The

supervisor represents the highest level of this hierarchical approach. It receives all available measurements coming from the vehicle itself (sensors, pedals, ...), environment (exteroceptive sensors, camera, LiDAR, ...), and information that could be provided by road infrastructure or by other vehicles (like in autonomous vehicles). All these data are used in the perception of the environment, observation, path planning, motion generation, and last but not least, diagnosis.

1.6 The CRONE Control Approach

1.6.1 Introduction to the CRONE Control System Design Methodology

The CRONE (the French acronym for *Commande Robuste d'Ordre Non Entier*, which means fractional-order robust control) CSD methodology is a frequency domain approach that has been developed since the 1980s (Oustaloup, 1995, 1991a, 1981). It is based on the common unity-feedback configuration presented in Figure 1.19. Three CRONE CSD methods have been developed, successively extending the field of application. In these three methods, the controller or open-loop transfer function is defined using fractional order integro-differentiation. In the frequency domain, they enable linear robust control systems to be simply and methodologically designed.

The major advantage over the H_∞ design is that the plant uncertainties (or perturbations) are taken into account with no distinction of their nature, whether they are structured (parametric) or unstructured.

The fractional-order, which is either real or complex depending on the generation of the control design, enables parameterization of the open-loop transfer function with a small number of high-level parameters. The

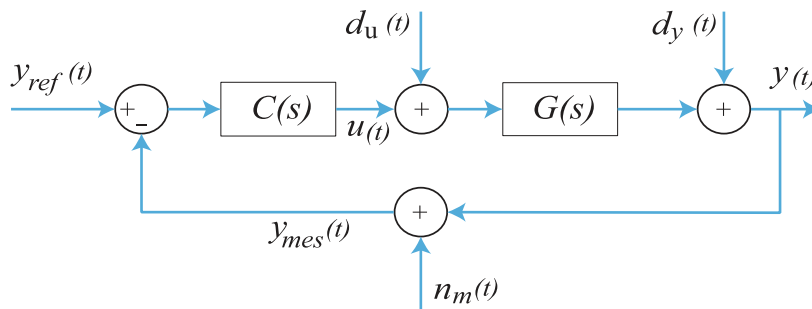


Figure 1.19. Block-diagram of an output unity negative feedback control system.

optimization of the control is thus reduced to only the search for the optimal values of these parameters.

1.6.2 Control diagram and data for synthesis

Figure 1.19 represents the control diagram used for control synthesis. The functional equations associated with this diagram are as follow:

- For the output $Y(s)$:

$$Y(s) = S(s)D_y(s) + GS(s)D_u(s) + T(s)Y_{ref}(s) - T(s)N_m(s); \quad (1.8)$$

- For the error $\varepsilon(s)$:

$$\varepsilon(s) = -S(s)D_y(s) - GS(s)D_u(s) + S(s)Y_{ref}(s) - S(s)N_m(s); \quad (1.9)$$

- For the control input $U(s)$:

$$U(s) = -CS(s)D_y(s) - T(s)D_u(s) + CS(s)Y_{ref}(s) - CS(s)N_m(s) \quad (1.10)$$

where:

$$\begin{aligned} \beta(s) &= C(s) G(s); \text{ the open-loop transfer function,} \\ S(s) &= 1/(1 + \beta(s)); \text{ the sensitivity function,} \\ T(s) &= 1 - S(s); \text{ the complementary sensitivity,} \\ GS(s) &= G(s)S(s); \text{ the input sensitivity function,} \\ CS(s) &= C(s)S(s); \text{ the control sensitivity function.} \end{aligned} \quad (1.11)$$

For Frequential Synthesis of Robust Controllers (SFCR), predefined givens are necessary, and could be divided into two parts:

- The modulization of signals (ones related to noise measurements), and the nature of uncertainty on the parametric configuration of the controlled plant $G(s)$. In the frequency domain, this uncertainty is represented by extremum transfer functions resulted from the variation on the parameters of the model.
- The specifications listed by the designer, like:
 - The stability degree;
 - Rapidity;
 - Precision at the steady-state;
 - The saturation limit of the actuator;

- The sensitivity of control input to noise measurement.

For the SFCR, it is necessary to translate the first two aforementioned points into frequency specifications, such as:

- **Degree of Stability:** this could be chosen through the value of the resonant peak factor Q_T of the complementary sensitivity function $T(s)$, or by the stability margins, i.e., the phase margin M_ϕ , the gain margin, the modulus margin, ...;
- The **Rapidity** through the bandwidth of the frequency response of the complementary sensitivity function $T(s)$ or through the frequency at the unity gain of the open-loop transfer function $\beta(s)$.

In the absence of supplementary information, mainly the one related to noise measurements, it could be difficult to determine the frequency at the unity gain of the open-loop transfer function.

1.6.3 First-generation CRONE Control

The first-generation CRONE control proposes to use a controller without phase variation around the cross over frequency ω_{cg} . This strategy has to be used when the frequency ω_{cg} is within a frequency range where the plant phase is constant (with respect to the frequency). In this range where the plant frequency response is asymptotic (this frequency band is called a plant asymptotic-behavior band), the plant variations are only gain-like.

Within a frequency range $[\omega_A, \omega_B]$ around the desired frequency ω_{cg} , the CRONE controller is defined from the fractional transfer function of an order m integro-differentiator, such as:

$$C(s) = C_0 \left(\frac{1 + \frac{s}{\omega_l}}{1 + \frac{s}{\omega_h}} \right)^m, \quad (1.12)$$

where C_0 , ω_l , ω_h , and $m \in \mathbb{R}$.

In order to satisfy the predefined specifications, the cascade form of the first generation CRONE controller is extended to include: a proportional constant C_0 , a band-limited fractional-order derivative (m) within two

corner frequencies ω_l and ω_h , an integer band-limited integrator of order m_I upper bounded by the frequency ω_I to manage steady-state error and a low-pass filter of order m_f with a cutoff frequency ω_f to manage the control sensitivity level and reduce noise amplification at high frequencies. Therefore, the general transfer function is formulated as follows:

$$C(s) = C_0 \left(1 + \frac{\omega_I}{s}\right)^{m_I} \left(\frac{1 + s/\omega_l}{1 + s/\omega_h}\right)^m \frac{1}{(1 + s/\omega_f)^{m_f}}. \quad (1.13)$$

The transitional frequencies defined are calculated so that a constant phase is achieved on a frequency range $[\omega_A, \omega_B]$ which covers the frequency range where ω_c could vary due to the plant parametric variation (Sabatier et al., 2015a). Then, the fractional-order m and the gain C_0 are calculated to ensure the required nominal phase margin M_ϕ and open-loop gain cross-over frequency ω_c .

However, for time-domain simulations, the fractional part of the cascade form should be replaced by a rational transfer function. Thanks to Oustaloup's method (Oustaloup, 1995, 1991a), using N recursive zeros and N recursive poles, this point could be achieved. Then the final cascade form of the first-generation CRONE controller is written as follows:

$$C(s) = C_0 \left(1 + \frac{\omega_I}{s}\right)^{m_I} \prod_{i=1}^N \frac{1 + s/\omega'_i}{1 + s/\omega_i} \frac{1}{(1 + s/\omega_f)^{m_f}}. \quad (1.14)$$

where $m_I, m_f, N \in \mathbb{N}$ and $\omega'_i, \omega_i \in \mathbb{R}$.

Figure 1.20 presents the asymptotic Bode diagrams for the non-integer part where:

$$\frac{\omega'_{i+1}}{\omega'_i} = \frac{\omega_i}{\omega_i} = \alpha\eta > 1, \quad (1.15)$$

$$\frac{\omega_i}{\omega_i} = \alpha \text{ and } \frac{\omega'_{i+1}}{\omega'_i} = \eta, \quad (1.16)$$

$$\alpha\eta = \left(\omega_h/\omega_l\right)^{1/N}, \quad (1.17)$$

$$\alpha = (\alpha\eta)^m \text{ and } \eta = (\alpha\eta)^{1-m}, \quad (1.18)$$

$$\omega'_1 = \omega_1 \eta^{0.5} \text{ and } \omega_N = \omega_h \eta^{-0.5}. \quad (1.19)$$

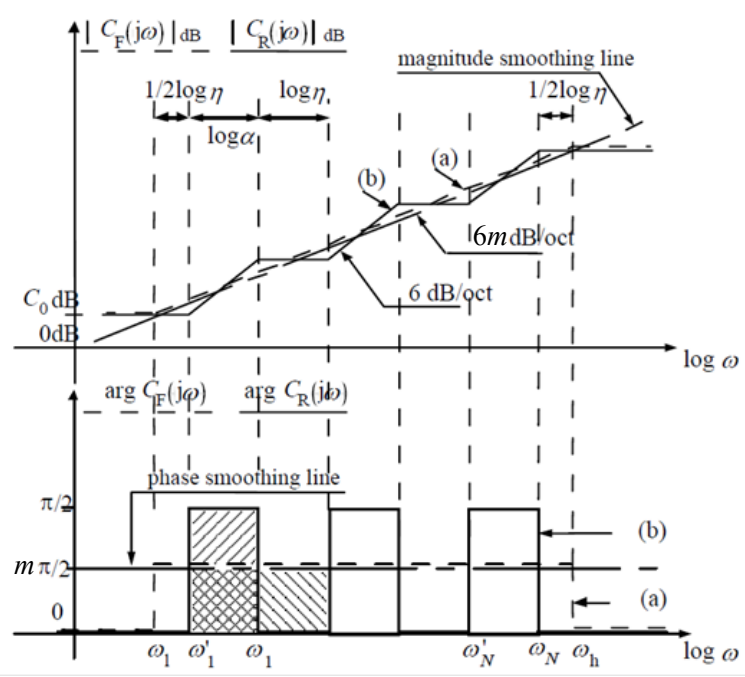


Figure 1.20. Asymptotic Bode diagrams of the (a) fractional and (b) rational CRONE regulator for $m \in [0, 1]$.

Generally, the parameters ω_i and ω'_i can be calculated by fixing a value for N which ensures $\alpha\eta \approx 5$.

The robustness of the phase margin M_ϕ is ensured only if ω_{cg} is in the frequency range where the system phase is constant. When this condition is not met, use the second-generation CRONE command.

1.6.4 Second-generation CRONE controller

For problems of control effort level, it is sometimes impossible to choose a ω_{cg} within an asymptotic behavior frequency band of the plant. Nevertheless, as Bode first state for the ‘design of single loop absolutely stable amplifiers’ whose tube gains vary, the robust controller is the one which permits the open-loop transfer function to be defined by a constant phase in a useful band. So, the CRONE approach defines the open-loop transfer function

around ω_{cg} from the open-loop transfer function of a fractional integrator (Lanusse et al., 2013):

$$\beta(s) = \left(\frac{\omega_{cg}}{s}\right)^\nu \quad (1.20)$$

with $\omega_{cg} \in \mathbb{R}$ and $\nu \in [1, 2]$.

The complementary sensitivity function $T(s)$, and sensitivity function $S(s)$, can be expressed as:

$$T(s) = \frac{\beta(s)}{1 + \beta(s)} = \frac{1}{1 + \left(\frac{s}{\omega_{cg}}\right)^\nu} \quad (1.21)$$

and

$$S(s) = \frac{1}{1 + \beta(s)} = \frac{\left(\frac{s}{\omega_{cg}}\right)^\nu}{1 + \left(\frac{s}{\omega_{cg}}\right)^\nu}. \quad (1.22)$$

Around ω_{cg} , the Nichols plot of $\beta(s)$ is a vertical straight line whose phase location is determined by order ν only (Figure 1.21). This vertical straight line being the desired shape of the open-loop frequency response Nichols plot, we define it as a frequency template or simply template (with a different meaning from that given by the QFT approach where the template is a frequency uncertainty domain). The vertical template thus defined slides on its own axis as the plant parameters vary (i.e. as ω_{cg} varies).

The gray area of Figure 1.21 represents the uncertainty (or perturbation) of the open-loop frequency response.

This vertical displacement of the template ensures:

- that the robust phase margin M_ϕ equals $(2 - \nu)\pi/2$,
- a robust resonant peak M_r expressed by:

$$M_r = \frac{\sup_\omega |T(j\omega)|}{|T(j0)|} = \frac{1}{\sin(\nu\pi/2)}. \quad (1.23)$$

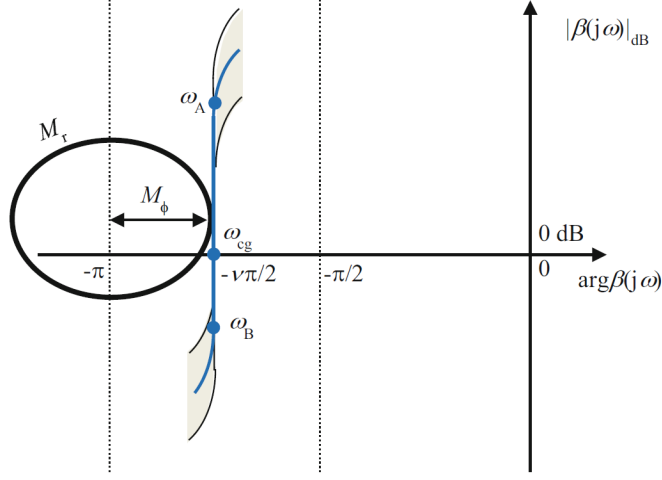


Figure 1.21. Vertical sliding of a frequency template (bold solid line) ensuring the robustness of phase margin M_ϕ and of resonant peak M_r (Sabatier et al., 2015a) .

- a robust modulus margin M_m expressed by:

$$M_m = \inf_{\omega} |\beta(j\omega) + 1| = \left(\sup_{\omega} |S(j\omega)| \right)^{-1} = \sin(\nu\pi/2). \quad (1.24)$$

- a robust damping ratio ζ directly deduced from the central half-angle θ formed by the two closed-loop conjugate complex poles of $T(s)$ and of $S(s)$.

$$\zeta = \cos \theta = \cos \left(\pi - \frac{\pi}{\nu} \right) = \cos \left(\frac{\pi}{\nu} \right), \quad (1.25)$$

thus, introducing the notion of robust oscillatory mode.

To manage the control effort level and the steady-state errors provided by the CRONE controller, the fractional open-loop transfer function (1.14) has to be bandlimited and to include integral and low-pass effects. The nominal fractional open-loop transfer function is defined by:

$$\beta_0(s) = K \left(\frac{\omega'_1}{s} + 1 \right)^{n_1} \left(\frac{1 + \frac{s}{\omega_h}}{1 + \frac{s}{\omega_1}} \right)^\nu \left(\frac{1}{1 + \frac{s}{\omega_h}} \right)^{n_h}, \quad (1.26)$$

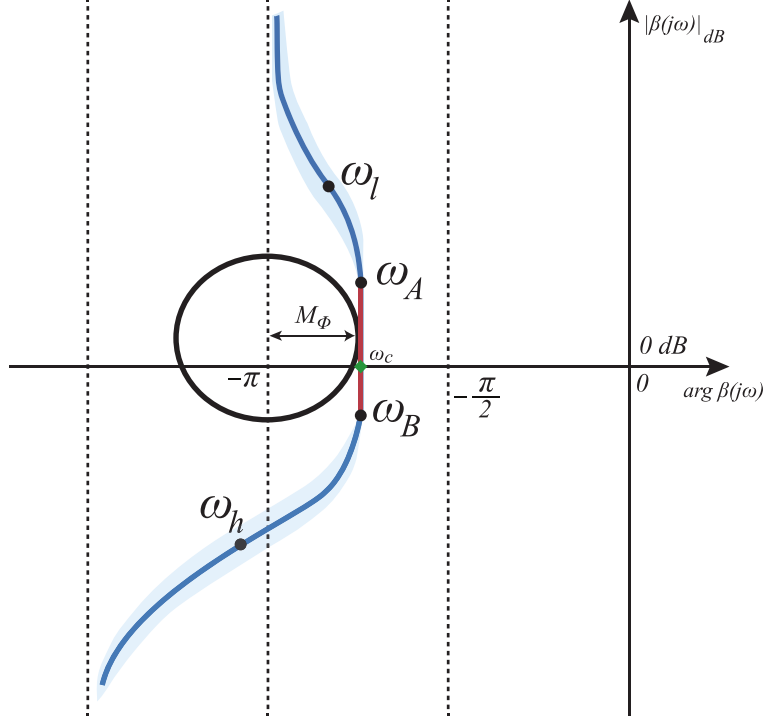


Figure 1.22. Shape of open-loop Nichols plot.

where $K, \omega'_1, \omega_h, \omega_1$, and $\omega'_h \in \mathbb{R}^+$, and n_1 and $n_h \in \mathbb{N}^+$. Figure 1.22 presents the shape of the frequency response of the perturbed open-loop $\beta(s)$ defined from its nominal value. Integer orders n_l and n_h are set by taking into account the performance specification and the plant magnitude asymptotic behavior at low and high frequencies.

The simplest way to obtain a rational controller from the fractional open-loop transfer function is to use Oustaloup's method to approximate the band-limited fractional order integrator of (1.26). Using N recursive zeros and N recursive poles, the nominal open-loop transfer function becomes rational:

$$\beta_{0R}(s) = K \left(\frac{\omega'_1}{s} + 1 \right)^{n_1} \left(\frac{1 + \frac{s}{\omega_h}}{1 + \frac{s}{\omega_1}} \right)^{[\nu]} \prod_{i=1}^N \frac{1 + \frac{s}{\omega_i}}{1 + \frac{s}{\omega'_i}} \left(\frac{1}{1 + \frac{s}{\omega'_h}} \right)^{n_h}, \quad (1.27)$$

where $[\nu]$ is the integer part of ν and with:

$$\omega_1 = \sqrt{\eta} \omega'_1, \omega'_1 = \alpha \omega_1, \omega_{i+1} = \alpha \eta \omega_i \text{ and } \omega'_{i+1} = \alpha \eta \omega'_i, \quad (1.28)$$

and

$$\alpha = \left(\frac{\omega_h}{\omega_1}\right)^{\frac{\nu-|\nu|}{N}} \text{ and } \eta = \left(\frac{\omega_h}{\omega_1}\right)^{\frac{1-\nu+|\nu|}{N}}. \quad (1.29)$$

Then, the rational controller $C_R(s)$ is defined by:

$$C_R(s) = G_0^{-1}(s)\beta_{0R}(s). \quad (1.30)$$

1.6.5 The third-generation CRONE Controller

Just as the second-generation CRONE control permits the choice of frequency ω_{cg} outside an asymptotic behavior band of the plant, and widens the application domain of the first generation of CRONE control, the third generation widens the second by permitting the handling of more general uncertainties than just gain-like perturbations.

Indeed, the vertical sliding of the previous vertical template is a requirement which is only achieved on perturbation of:

- all the parameters of the plant in the particular case when the frequency ω_{cg} is within a frequency band where the plant frequency response is close to its asymptote;
- a gain, and corner frequencies which are greatly different from ω_{cg} in the general case when the frequency ω_{cg} is not within an asymptotic behavior band.

Except for these cases, the vertical template does not slide on itself when the plant transfer function is perturbed and this template does not necessarily ensure the best robustness of the control-loop system.

The open-loop transfer function is now defined as the real part of a complex fractional order integrator, that is:

$$\beta(s) = \text{Re}_{/i} \left(\frac{\omega_{cg}}{s} \right)^n, \quad (1.31)$$

with $n = a + ib \in \mathbb{C}$.

The real order determines the phase placement of this Nichols locus, so-called generalized template, and then the imaginary order b determines its angle to the vertical. From an infinity of these templates which tangent the magnitude contour related to a required magnitude peak Q_r for the nominal parametric state of the plane, the optimal template can be defined as the template which permits minimization of the variations of Q stemming from the uncertainty domain which in turn stems from the various parametric states of the plant. The principle of the third-generation CRONE control methodology is to optimize the parameters of the nominal open-loop transfer function $\beta_0(s)$ that includes a band-limited complex fractional-order integration, that is:

$$\beta_0(s) = \beta_1(s)\beta_m(s)\beta_h(s), \quad (1.32)$$

where $\beta_m(s)$ is a set of band-limited generalized templates:

$$\beta_m(s) = \prod_{k=-N^-}^{N^+} C_k^{\text{sign}(b_k)} \left(\alpha_k \frac{1 + \frac{s}{\omega_{k+1}}}{1 + \frac{s}{\omega_k}} \right)^{a_k} \left(\text{Re}_{/i} \left\{ \left(\alpha_k \frac{1 + \frac{s}{\omega_{k+1}}}{1 + \frac{s}{\omega_k}} \right)^{ib_k} \right\} \right)^{-q_k \text{sign}(b_k)} \quad (1.33)$$

with,

$$\alpha_k = \left(\frac{\omega_{k+1}}{\omega_k} \right)^{1/2} \text{ for } k \neq 0 \text{ and } \alpha_0 = \left(\frac{1 + \left(\frac{\omega_r}{\omega_0} \right)^2}{1 + \left(\frac{\omega_r}{\omega_1} \right)^2} \right)^{\frac{1}{2}}, \quad (1.34)$$

where,

$$\beta_1(s) = C_1 \left(\frac{\omega_{-N^-}}{s} + 1 \right)^{n_1} \text{ and } \beta_h(s) = C_h \left(\frac{s}{\omega_{N^+}} + 1 \right)^{-n_h}, \quad (1.35)$$

where N^+, N^- , and $q_k \in \mathbb{N}^+$; and $\omega_r, \omega_k, \omega_{k+1}, \omega_k, \alpha_k, C_k, C_1, C_h, a_k$ and $b_k \in \mathbb{R}$.

The fractional controller $C_F(s)$ is defined then by its frequency response as:

$$C_F(j\omega) = \beta_0(j\omega)/G_0(j\omega). \quad (1.36)$$

The parameters of a rational transfer function $C_R(s)$ with a predefined low-order structure are tuned to fit the ideal frequency response $C_F(s)$ using any frequency-domain system identification technique. An advantage of this design method is that, whatever the complexity of the control problem, the reduced value of the controller order (usually around 6) can be used. More details are explained intensively in (Lanusse et al., 2013) and (Sabatier et al., 2015b).

1.6.6 CRONE Control System Design Toolbox

The CRONE toolbox, developed gradually since the nineties (Oustaloup et al., 2002) by the CRONE research group, and granted by CNRS and PSA car company, is a MatLAB and Simulink toolbox dedicated to applications of fractional (or non-integer) derivatives in engineering and science.

The toolbox is not only intended to researchers, including Ph.D. students, but also to industrials whose growing interest in fractional systems and whose readiness to invest in the development of its applications are manifest. Original theoretical mathematical concepts developed in the group were integrated in the first version of the CRONE toolbox as four main modules each of which deals with a specific application domain of fractional derivatives: the “Mathematical module” that contains several algorithms of fractional calculus, the “System identification module” that contains frequency and time-domain system identification algorithms; the “CRONE control module” that uses fractional derivatives as high-level design parameters in order to simplify the design of robust control systems; and the “Path planning module” that contains algorithms to optimize paths in dynamic environments

During the last ten years, the CRONE toolbox was only available for some privileged researchers and industrials who granted its development. On the other hand, the last two decades have witnessed a growing interest in fractional derivatives and their applications. From now on, the CRONE toolbox is freely available for the international scientific community for research and pedagogical purposes. The aim of the CRONE group is to share its

developments and its knowledge with scientists, researchers, and engineers worldwide.

1.6.7 Conclusion

The Control System Design of a controller is represented using the frequency-domain approach. It provides an overview of the three generations of the CRONE controllers. Fractional-order controllers provide more tuning parameters that are used to improve robustness by the CRONE methodology. The first-generation CRONE controllers can be used for plants with magnitude variation and constant phase. When the plant phase varies with respect to the frequency, the second generation of CRONE controllers can be used. As described before, this robust controller is designed through a fractional-order open-loop transfer function. From real, the order will become complex for both gain and phase perturbed plants. This defines the third generation CRONE methodology.

For more details concerning the design methodology of the CRONE controller, the reader could refer to the following reference (Sabatier et al., 2015b).

1.7 Conclusion

A brief overview of the overall vehicle's dynamics had confirmed the role of the suspension systems in the overall performance of the vehicle. As the suspension system influences the vertical dynamics directly, it affects the longitudinal and lateral dynamics indirectly. Three domains of operations and three domains of studies were demonstrated. Therefore, different models are defined each one is dedicated to the domain of operation and study. They range from validation to analysis, and synthesis models. Depending on the region of study considered, suspension performance must meet multiple objectives, and mostly they are in contradiction with each other. Here the use of the active suspension system gives the ability to find solutions for the main dilemma inherent in passive systems. This had motivated many studies to investigate the optimal performance of suspension systems.

Among all types of suspension, the electrical active suspension system integrated with the Active wheel is studied. The interests and the challenges in fully active suspension systems control has been presented by

summarizing the results of several already existing studies in the literature related to modeling and controlling methodology.

This thesis deals with global vertical dynamics effects on the global chassis control's perspectives. Thus, controllers fulfilling suspension objectives are implemented, and furthermore, different controllers are designed for lateral and longitudinal dynamics, aiming to improve vehicle's performance in terms of lateral stability, tracking trajectory, and braking optimality. The CRONE CSD methodology is considered in almost every controller to examine the relative benefits of fractional order controllers in the vehicle's dynamics control.

Strategies and approaches had been indicated to pave the way for achieving the assigned objectives and provide a solid scientific reference on the context of global chassis control for the new trend technology, the so-called, all-in-wheel electric/autonomous vehicles.

Chapter 2

Vertical Dynamic Control

Contents

2.1	Introduction.....	48
2.2	Frequency domain study for quarter vehicle model.....	48
2.3	Vehicle's height control.....	60
2.4	Fractional-order damping control.....	80
2.5	Conclusion	95

2.1 Introduction

Investigations on improving suspension systems for vehicles have drawn much interest in recent years for better ride quality. Briefly, the purposes of the vehicle suspension system are to (1) isolate the vehicle body from road disturbances in order to provide good ride quality; (2) keep good road holding; (3) provide good handling; and (4) support the vehicle static weight (Rajamani, 2012a). This chapter is focusing on these global vertical control objectives that were previously listed in detail in Chapter 1.

At first, an intensive study is done on the quarter vehicle model to analyze the different modes of dynamics in the frequency domain. For analysis purposes, various transfer functions are introduced representing the relations between the input and outputs of the system, as well as the effect of the active forces, generated by the active suspension system, on each degree of freedom.

This chapter focuses on two main concepts, the chassis's height control and the fractional-order damping control, in order to handle various suspension objectives. However, other solutions are introduced in the next chapters regarding reject driver solicitations, for example. For this reason, a CRONE controller is designed in order to regulate the height of the chassis of the vehicle. Then, a comfort-oriented controller is designed to regulate the vertical displacement of the sprung mass against road perturbations using a fractional damping proposed strategy. The designed fractional-order damping controllers are tested for road disturbance rejection in the sense of comfort, road holding, and vibratory isolation.

2.2 Frequency domain study for quarter vehicle model

Following the brief introductory section related to the quarter vehicle vertical dynamics in section 1.2.3, the present study will get deeper into the frequency analysis of those dynamics. Figure 2.1 shows the quarter vehicle model with the integrated active suspension system in the Active Wheel (AW). The vehicle's vertical dynamics are modeled using the well-known quarter-model that exists in the literature (Jazar, 2014; Savaresi et al., 2010).

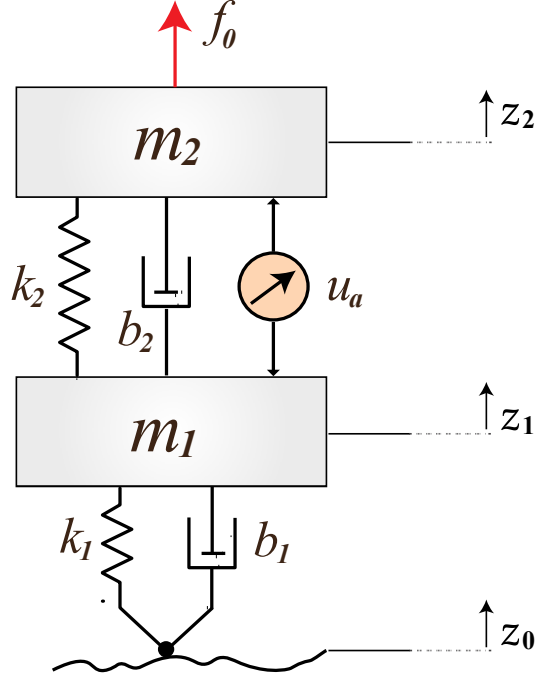


Figure 2.1. Active Wheel Quarter vehicle model representation.

Here, the four quarter vehicle systems are assumed decoupled and the suspension dynamics are considered in the frequency range of interest [0 - 30 Hz]. Despite the nonlinear characteristics of the suspension components, it is pointed out that such a model can be used for optimal suspension control design and analysis (Hrovat, 1997), where it represents a convenient modeling framework to evaluate the performance and robustness of a controller.

The suspension configuration of the AW has been considered as a high bandwidth active suspension system due to the presence of the force-generating actuator mounted in parallel to the passive spring-damper components (Sun et al., 2015). Assuming that the actuator is ideal, that is the desired force is equal to the generated force, the vertical motion of this system is described by two differential equations as follows:

$$m_2 \ddot{z}_2(t) = -f_{sp}(t) + f_0(t) + u_a(t), \quad (2.1)$$

$$m_1 \ddot{z}_1(t) = f_{sp}(t) - f_1(t) - u_a(t), \quad (2.2)$$

with,

$$f_{sp}(t) = k_2(z_2(t) - z_1(t)) + b_2(\dot{z}_2(t) - \dot{z}_1(t)), \quad (2.3)$$

$$f_1(t) = k_1(z_1(t) - z_0(t)) + b_1(\dot{z}_1(t) - \dot{z}_0(t)). \quad (2.4)$$

The force $f_0(t)$ describes the external disturbances to denote the variations of the static payload, aerodynamical loads, and inertial forces induced by driver operations, e.g. cornering, braking, and accelerating. The variables $z_2(t)$ and $z_1(t)$ represents the sprung mass and unsprung mass displacements, respectively. The term $u_a(t)$ represents the value of the desired control input that assumed to be equal to the generated force by the actuator.

Under the assumption of zero initial conditions, the Laplace transform of the aforementioned equations result in the following formulas:

$$m_2 s^2 Z_2(s) = (k_2 + b_2 s)(Z_1(s) - Z_2(s)) + U_a(s), \quad (2.5)$$

and

$$\begin{aligned} m_1 s^2 Z_1(s) = & (k_1 + b_1 s)(Z_0(s) - Z_1(s)) \\ & - (k_2 + b_2 s)(Z_1(s) - Z_2(s)) - U_a(s). \end{aligned} \quad (2.6)$$

Figure 2.2 shows the causal diagram for the different relations between the inputs into the quarter vehicle model, that is: the external forces applied to the sprung mass $F_0(s)$, the road disturbances $V_0(s)$, and the control effort applied by the actuator $U_a(s)$, and the outputs state variables. Figure 2.3 shows the various sensitivity functions ($G(s)$) that represent the relationships between the input and the outputs of the controlled quarter vehicle model.

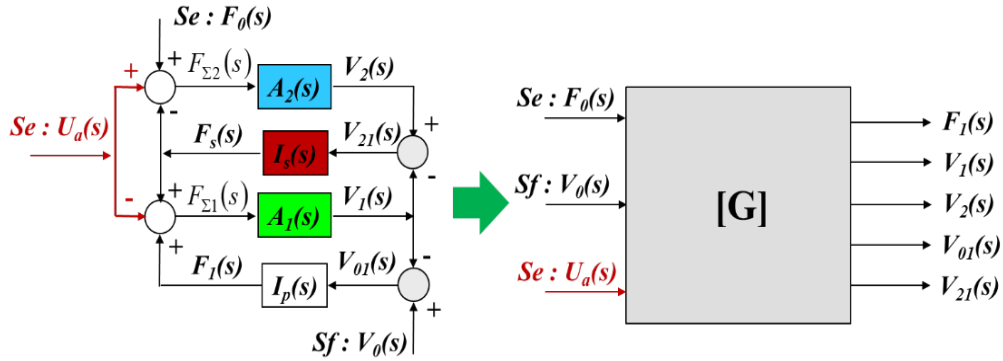


Figure 2.2. Block diagram illustrating the controlled QV.

2.2 Frequency domain study for quarter vehicle model

$$\begin{aligned}
 F_1(s) &= \boxed{G_{11}(s)} F_0(s) + \boxed{G_{12}(s)} V_0(s) + \boxed{G_{13}(s)} U_a(s) \xrightarrow{\text{red}} \text{Road Holding} \\
 V_1(s) &= \boxed{G_{21}(s)} F_0(s) + \boxed{G_{22}(s)} V_0(s) + \boxed{G_{23}(s)} U_a(s) \xrightarrow{\text{green}} \text{Vibrational Comfort} \\
 V_2(s) &= \boxed{G_{31}(s)} F_0(s) + \boxed{G_{32}(s)} V_0(s) + \boxed{G_{33}(s)} U_a(s) \xrightarrow{\text{green}} \text{Vibrational Comfort} \\
 V_{01}(s) &= \boxed{G_{41}(s)} F_0(s) + \boxed{G_{42}(s)} V_0(s) + \boxed{G_{43}(s)} U_a(s) \xrightarrow{\text{blue}} \text{Operating Limits} \\
 V_{21}(s) &= \boxed{G_{51}(s)} F_0(s) + \boxed{G_{52}(s)} V_0(s) + \boxed{G_{53}(s)} U_a(s) \xrightarrow{\text{blue}} \text{Operating Limits}
 \end{aligned}$$

Figure 2.3. Formulation of sensitivity functions between inputs and outputs variables.

According to the diagrams of Figure 2.4 and 2.5, the following transfer functions can be obtained, while assuming $F_0(s) = V_0(s) = 0$:

$$V_2(s) = \frac{s}{m_2 s^2 + b_2 s + k_2} U_a(s) + \frac{b_2 s + k_2}{m_2 s^2 + b_2 s + k_2} V_1(s), \quad (2.7)$$

and

$$\begin{aligned}
 V_1(s) &= -\frac{s}{m_1 s^2 + (b_1 + b_2)s + (k_2 + k_1)} U_a(s) \\
 &+ \frac{b_2 s + k_2}{m_1 s^2 + (b_1 + b_2)s + (k_2 + k_1)} V_2(s).
 \end{aligned} \quad (2.8)$$

From (2.7) and (2.8), the effect of the introduced control effort on the unsprung mass dynamics and sprung mass dynamics could be analyzed using the following two transfer functions respectively:

$$\frac{V_1(s)}{U_a(s)} = -\frac{m_2 s^3}{den(s)}, \quad (2.9)$$

$$\frac{V_2(s)}{U_a(s)} = \frac{s(m_1 s^2 + b_1 s + k_1)}{den(s)}, \quad (2.10)$$

with,

2.2 Frequency domain study for quarter vehicle model

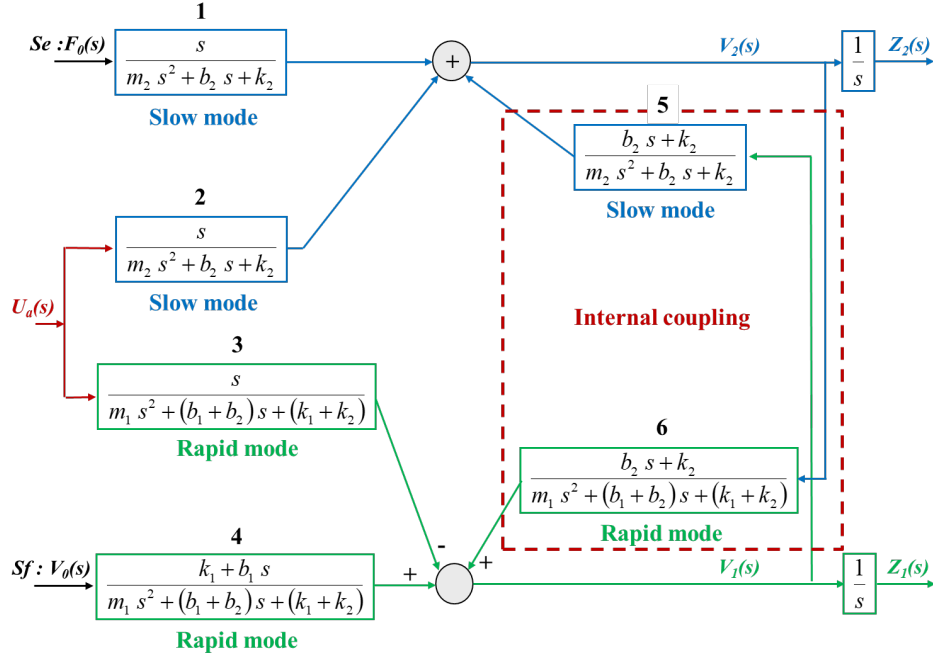


Figure 2.4. Block diagram of different sensitive transfer functions (Velocities).

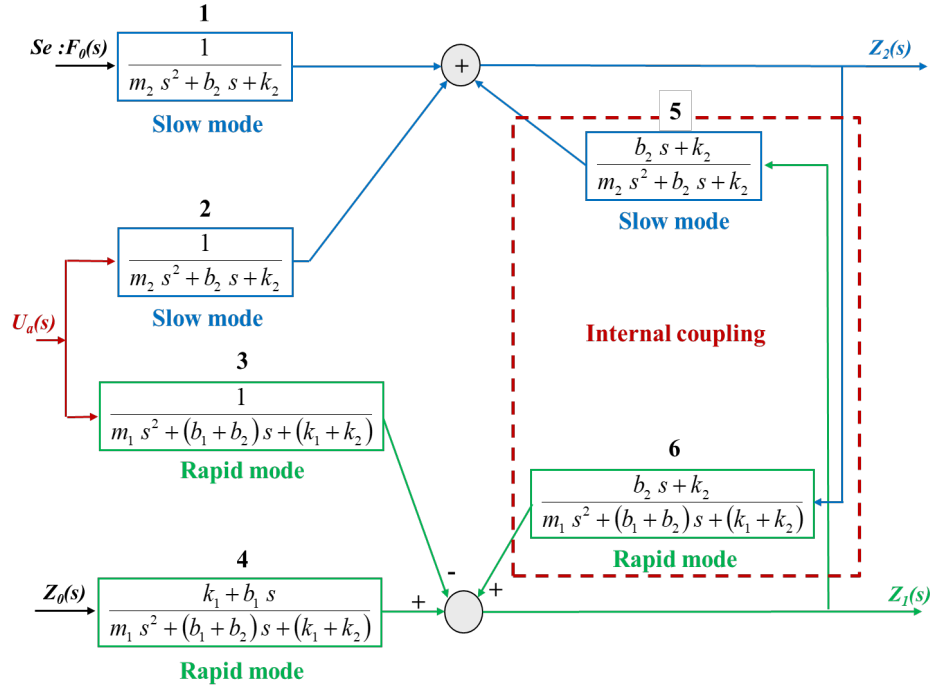


Figure 2.5. Block Diagram of the different sensitive transfer function (Displacements).

$$\begin{aligned} den(s) = & m_1 m_2 s^4 + (m_2(b_1 + b_2) + m_1 b_2) s^3 \\ & + (m_2(k_1 + k_2) + m_1 k_2 + b_1 b_2) s^2 + (b_1 k_2 + k_1 b_2) s + k_1 k_2. \end{aligned} \quad (2.11)$$

The influence of the road and driver disturbances on the quarter vehicle system dynamics could also be analyzed using the following transfer functions:

$$\frac{Z_2(s)}{Z_0(s)} = \frac{(b_1 s + k_1)(b_2 s + k_2)}{den(s)}, \quad (2.12)$$

$$\frac{Z_1(s)}{Z_0(s)} = \frac{(b_1 s + k_1)(m_2 s^2 + b_2 s + k_2)}{den(s)}, \quad (2.13)$$

$$\frac{Z_2(s)}{F_0(s)} = \frac{m_1 s^2 + (b_1 + b_2)s + (k_1 + k_2)}{den(s)}, \quad (2.14)$$

$$\frac{Z_1(s)}{F_0(s)} = \frac{b_2 s + k_2}{den(s)}. \quad (2.15)$$

In order to demonstrate the frequency responses of the transfer functions that appeared in Figure 2.5, a nominal parametric configuration has been considered. Table 2.1 lists the nominal parameters of the quarter vehicle model used for plotting the transfer functions in the frequency domain.

Figure 2.6 shows the bode responses of the numbered transfer function of Figure 2.5. It illustrates the two modes of functionality, namely, the slow mode corresponding to chassis motions or sprung mass motion, and the rapid mode corresponding to the unsprung dynamics or wheel mode. Numerically, for the given parametric configuration, the chassis mode is around 1.22Hz where the wheel mode is approximately 16Hz. These values will change a little bit with the parametric uncertainties of the quarter vehicle model, for front and rear axles as well. However, this characteristic (two modes) usually exists in all touristic vehicles.

2.2 Frequency domain study for quarter vehicle model

Table 2.1. Nominal quarter vehicle parameters.

Parameter	Value	Unit
m_2	200	kg
k_2	12000	N/m
b_2	200	N.s/m
m_1	32	kg
k_1	300000	N/m
b_1	50	N.s/m

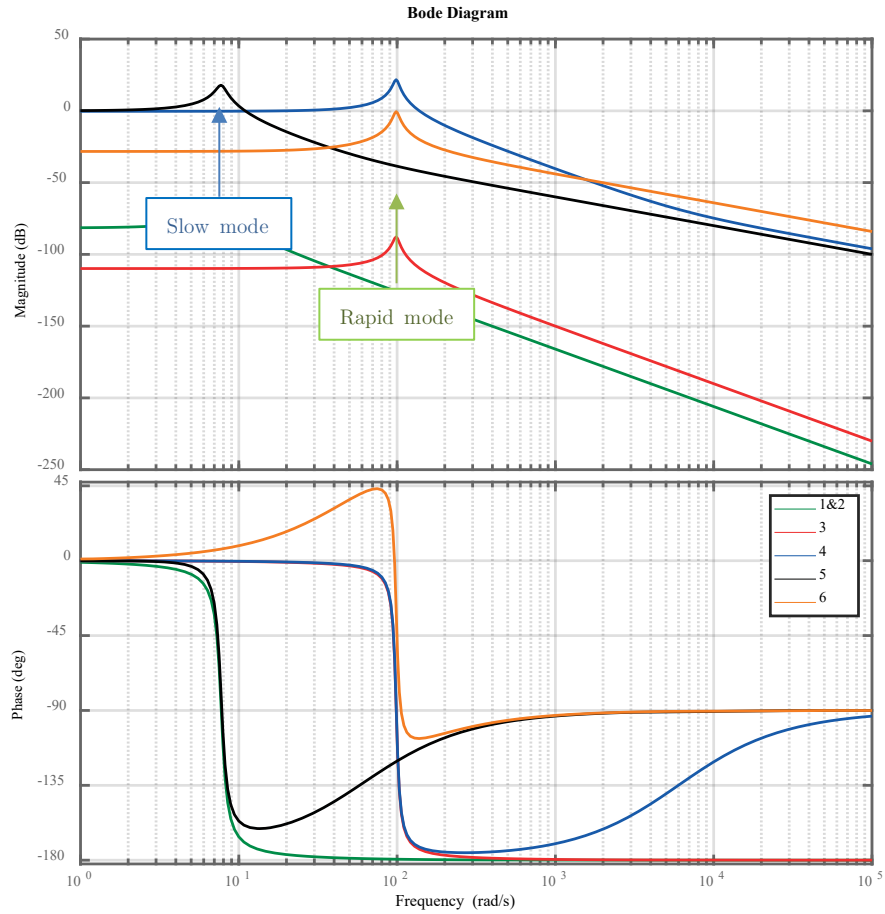


Figure 2.6. Bode responses of the numbered transfer functions as described in Figure 2.5.

2.2.1 Exploitation of the dynamic decoupling for synthesis models

One of the particularities of touristic vehicles is the ability to decouple the dynamics between the chassis mode (around 1 Hz) and the wheel mode (around 15Hz) (Létévé, 2014).

From a mathematical point of view, the dynamics decoupling conditions are as follows:

$$\text{if } k_2 \ll k_1 \text{ and if } b_2 = \sqrt{k_2 m_2}, \quad (2.16)$$

then, the polynomial $den(s)$ of fourth-order in s could be factorized into a product of two polynomial of order 2, such as:

$$den(s) = (m_1 s^2 + (b_1 + b_2)s + k_1)(m_2 s^2 + b_2 s + k_2). \quad (2.17)$$

Thus, the search for the roots of this polynomial becomes easier, such as:

$$\begin{aligned} den(s) &= 0, \\ \implies (s^2 + 2\zeta_1 \omega_{n1} s + \omega_{n1}^2)(s^2 + 2\zeta_2 \omega_{n2} s + \omega_{n2}^2) &= 0, \end{aligned} \quad (2.18)$$

where,

$$\begin{aligned} \omega_{n1} &= \sqrt{\frac{k_1}{m_1}} : \text{the natural frequency of wheel mode;} \\ \zeta_1 &= \frac{(b_1 + b_2)}{2\sqrt{k_1 m_1}} : \text{the damping factor of wheel mode;} \\ \omega_{n2} &= \sqrt{\frac{k_2}{m_2}} : \text{the natural frequency of chassis mode;} \\ \zeta_2 &= \frac{b_2}{2\sqrt{k_2 m_2}} : \text{the damping factor of chassis mode.} \end{aligned} \quad (2.19)$$

It should be noted that according to the condition of (2.16), then (2.14) with $b_2 = \sqrt{k_2 m_2}$, leads to $\zeta_2 = 0.5$.

On the other hand, from a practical point of view, for touristic vehicles, the condition $k_2 \ll k_1$ is always satisfied. Especially, for the light electric vehicle adopted in this study, where the front stiffness of the suspension system is 12000N/m, and the wheel stiffness is 300000N/m. This condition is also met at the rear axle, where the suspension stiffness is 10000N/m, and

the wheel stiffness is 200000N/m. However, concerning the equality related to the value of suspension damping coefficient b_2 , there is no need to be rigorously satisfied. Indeed, for values of ζ_2 that is close to 0.5, the dynamic decoupling could always be applied.

Consequently, for the purpose of the analysis and synthesis, various transfer functions mentioned lately could be simplified, and therefore reduce the complexity of the study. This approach depends on the domain of study as well as on the domain of operation. One example is the sensitivity of the wheel displacement relative to the road perturbations, namely, $T_{10}(s) = Z_1(s)/Z_0(s)$, such that:

$$T_{10}(s) = \frac{Z_1(s)}{Z_0(s)} \approx \frac{1}{\left(\frac{s}{\omega_{n1}}\right)^2 + \frac{2\zeta_1}{\omega_{n1}}s + 1}. \quad (2.20)$$

The second example is the transfer function $T_{20}(s)$, that can be simplified in a range of frequencies of interest (low frequencies) as follows:

$$\forall \omega \ll \omega_{n1}, \quad T_{20}(s) = \frac{Z_2(s)}{Z_0(s)} \approx \frac{k_2 + b_2s}{k_2 + b_2s + m_2(s)^2}. \quad (2.21)$$

Figure 2.7a shows the bode response of the sensitivity transfer function of the chassis dynamics relative to the road disturbances as formulated in (2.12) and its simplified form due to the decoupling as in (2.21). It shows that the simplification form $T_{20}(s)$ is approximately valid in the frequency range of [0-5Hz]. On the other side, Figure 2.7b shows that among a wide range of frequencies, the road disturbances are transmitted without any amplification or attenuation to the vertical movement of the unsprung mass ($Z_1(s)$). Therefore, the dynamics of the unsprung mass (wheel) is negligible compared to that of the chassis dynamics ($Z_2(s)$). Similarly, it could be concluded from the bode response in Figure 2.7b that the simplification form of $T_{10}(s)$ extends over the entire range of frequency of operation of the suspension, which is approximately [0- 30Hz].

Thus, for analysis and synthesis, the 2Dof quarter vehicle model can then be reduced to two linear 1Dof models. One model is relative to the zone of

frequencies [0 - 5Hz] and is associated with the expression (2.21). The other one is associated with the expression (2.20) and related to the [5 - 30Hz] range of frequencies.

Moreover, in the context of vibrational comfort, the following two points could be considered:

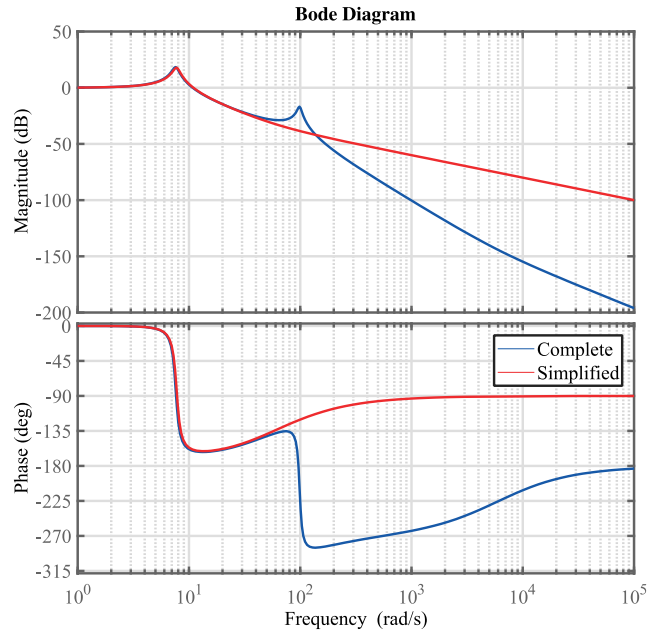
- In the framework of holding chassis and wheel against road perturbations, the performance is to be characterized in the time-domain using the damping factors ζ_1 and ζ_2 . In the frequency domain, the performances are characterized by the values of the resonance factors Q_1 and Q_2 of the transfer functions $T_{10}(s)$ and $T_{20}(s)$, respectively, in which a lower values Q 's reflects better performance.
- The vibration isolation is a filtering process, where it could be represented by the decrease in the gain of the Bode response in the zone of interest [2 -8] Hz, in which the human body is greatly sensitive to vertical vibrations, in addition to the range of frequencies beyond the wheel mode (rapid mode), that is around 15 to 30 Hz.

Taking into account the aforementioned remarks, the establishment of new controllers should be pointed towards one of these ranges. Based on these formalizations, different objectives for vertical dynamics control are assigned, each one related to one region of interest where it should deal with one inherent problematic dilemma related to passive suspension systems.

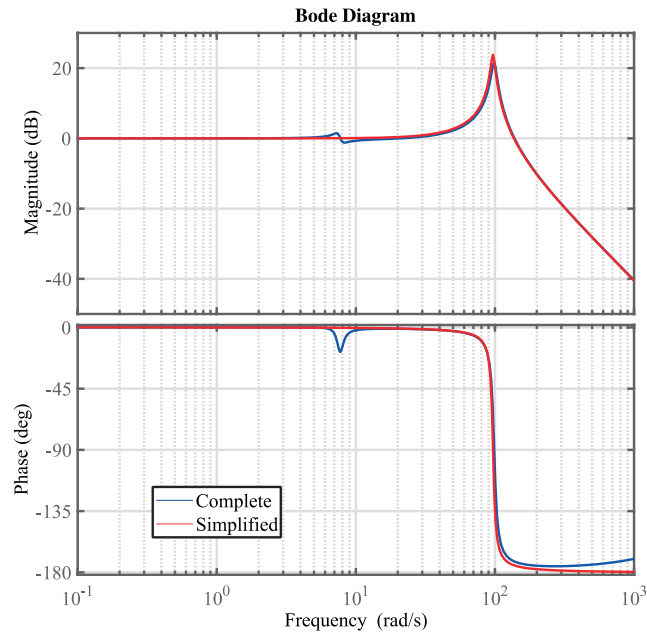
Figure 2.8 shows the analysis model corresponding to each range of interest and domain of study. For road disturbances of low frequencies, the model presented in Figure 2.8a can be used as an analysis model to study the effect of road perturbations on chassis dynamics. However, to analyze the effect of road perturbations on unsprung mass displacement, the model presented in Figure 2.8b based on $T_{10}(s)$ is sufficient. These models should facilitate the study upon reducing the complexity into 1DoF modeling.

In the following upcoming sections, and based on the range of interest, one of these two models should be applied for synthesis where needed.

2.2 Frequency domain study for quarter vehicle model

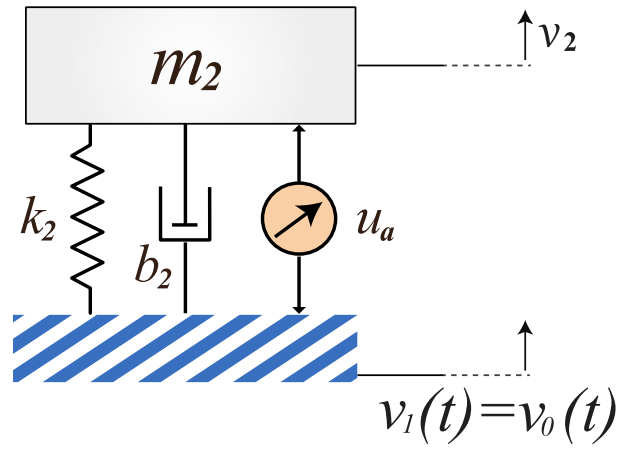


(a)

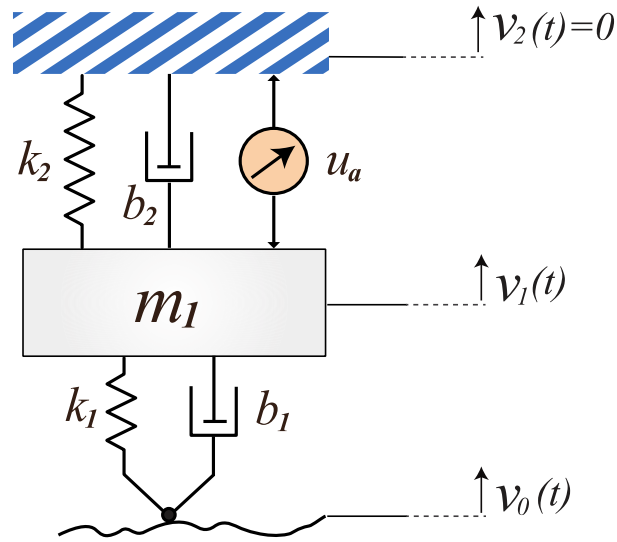


(b)

Figure 2.7. Bode diagram of the transfer functions (a) $T_{20}(s)$ and (b) $T_{10}(s)$.



(a)



(b)

Figure 2.8. Analysis model of quarter vehicle model correspondent to transfer functions (a) $T_{20}(s)$ and (b) $T_{10}(s)$.

2.3 Vehicle's height control

2.3.1 Introduction

Vehicle height adjustment is one of the main features of active suspension systems. The primary objective of this control system is to facilitate the loading and unloading process on the vehicle by adjusting the height of the car body. When the car is at a standstill, raising the body by 5 to 10cm makes the entry and exit easier for the occupants, which provides a comfortable treatment for passengers.

Furthermore, the application of this feature was extended to prove its advantage in reducing death rate fatalities. This function could help to lessen the impending side impact. This is done in combination with vehicles' safety systems and the central driver assistance systems, which use the merged sensor data to identify hazardous situations around the car. At a specific speed of impending side impact, the active suspension system could raise the body up to a few centimeters on the side of impact. This brings the sill into a better position to absorb the impact energy. Deformation of the cabin and the loads acting on the occupants, above all in the chest and abdominal areas, can thus be reduced by up to 50% compared with a lateral collision in which the suspension is not raised (Millikin, 2019).

In this section, a 2nd generation CRONE controller is designed in order to fulfill this objective. The robustly designed controller is synthesized using the simplified quarter vehicle model and then tested on the 2DoF quarter vehicle model, and later on, is applied on the complete 14DoF vehicle model.

2.3.2 Synthesis model

In this section, the study takes into consideration the decoupling analysis discussed in the previous section. Indeed, the assigned objective doesn't need a rapid closed-loop system; thus, the study is focused on low band frequencies. Accordingly, the 1DoF quarter vehicle model could be used as a synthesis model. Besides, under the assumption of a standstill situation, the road profile is considered perfectly even, thus, $z_1(t) = z_0(t) = 0$. Therefore, the 2DoF quarter vehicle model is reduced to the 1DoF model, while considering only the suspension dynamics and the chassis dynamics. Figure 2.9

represents the synthesis model, where the following equation is then formulated to represents the plant's transfer function:

$$P(s) = \frac{Z_2(s)}{U_a(s)} = \frac{1}{m_2 s^2 + b_2 s + k_2} \quad (2.22)$$

Moreover, this transfer function can be written in the following canonical form:

$$P(s) = \frac{Z_2(s)}{U_a(s)} = \frac{P_0}{\left(\frac{s}{\omega_{n2}}\right)^2 + \frac{2\zeta_2}{\omega_{n2}}s + 1} \quad (2.23)$$

where,

$$\begin{aligned} P_0 &= \frac{1}{k_2}, \\ \omega_{n2} &= \sqrt{\frac{k_2}{m_2}}, \\ \zeta_2 &= \frac{b_2}{2\sqrt{k_2 m_2}}. \end{aligned} \quad (2.24)$$

This final form of the transfer function is based on (2.10) while taking into account the decoupling characteristics.

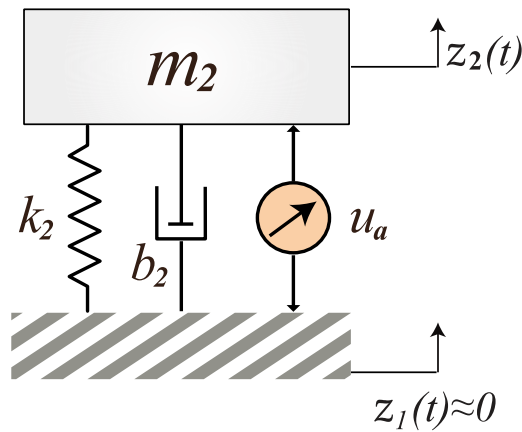


Figure 2.9. Height regulation synthesis model.

2.3.3 Control design methodology

2.3.3.1 Defining parametric uncertainty

Four controllers are implemented, one for each quarter vehicle. However, due to the geometrical symmetry of the chassis about the x-axis, one controller is designed for every axle. According to the assigned objective, each controller is assigned to track the reference height of the chassis $z_{2,ref}(t)$ provided by the supervisor.

In the quarter vehicle synthesis model, three main suspension parameters are considered uncertain. Table 2.2 shows the range of uncertainty of each parameter. These uncertainties caused by the variation of the total mass of the electric vehicle when it is empty (only the driver) or full load (four passengers). For the other suspension parameters, it was assumed that their values have an uncertainty of $\pm 10\%$. Thus, three transfer functions are defined: $P_{i,min}(s)$, $P_{i,med}(s)$, and $P_{i,max}(s)$, in which for front axle $i = 1$, and for rear axle, $i = 2$.

Table 2.2. The variation range of suspension parameters.

Parameter	Front axle (i=1)			Rear axle (i=2)		
	m_2	k_2	b_2	m_2	k_2	b_2
	[kg]	[N/m]	[N.s/m]	[kg]	[N/m]	[N.s/m]
$P_{i,min}$	168	10800	180	68	9000	180
$P_{i,med}$	193	12000	200	118	10000	200
$P_{i,max}$	218	13200	220	168	11000	220

Figure 2.10 illustrates the range of variations of the parameters of the canonical form, more specifically, the natural frequency of the chassis mode ω_{n2} , the damping factor ζ_2 , and the proportional parameter P_0 , for front and rear axles. For this purpose, 10000 samples were considered, where each sample represents a transfer function of random parametric configuration. Using this method, the range of variation (minimum and maximum values) of each term of the canonical transfer function can be extracted from the range of variation listed in Table 2.2. Figure 2.11 and 2.12 show the bode responses of the synthesis models and the effect of the parametric uncertainties, for front and rear axles, respectively.

2.3 Vehicle's height control

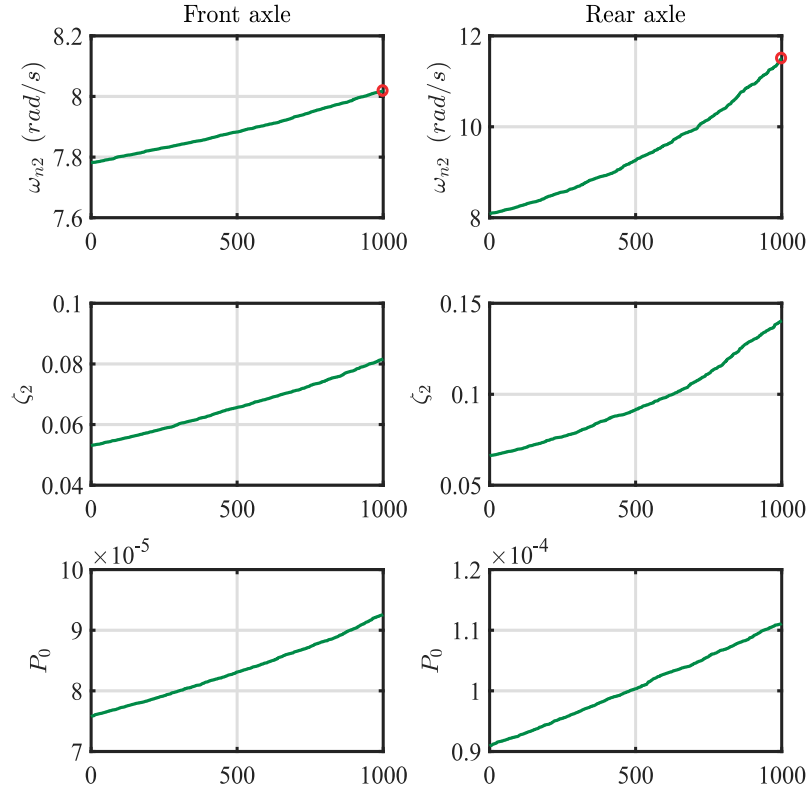


Figure 2.10. Range of variations of the parameters of the canonical form $P(s)$.

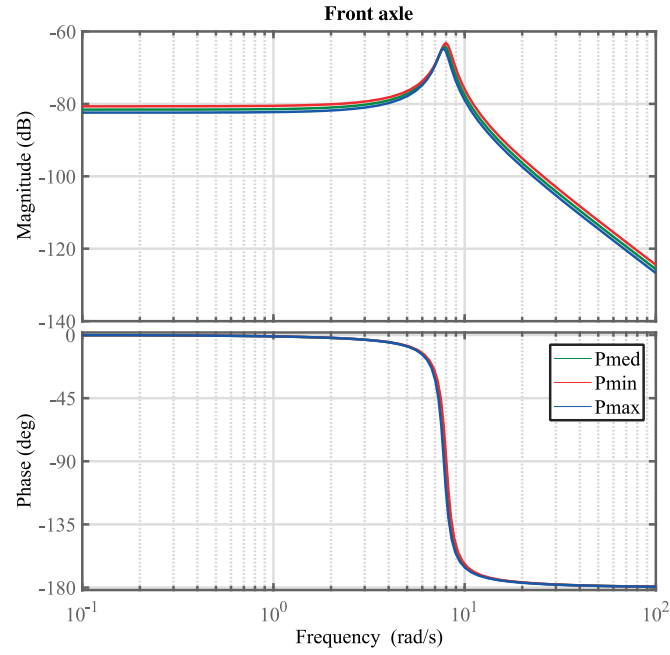


Figure 2.11. Bode response of the front axle synthesis model.

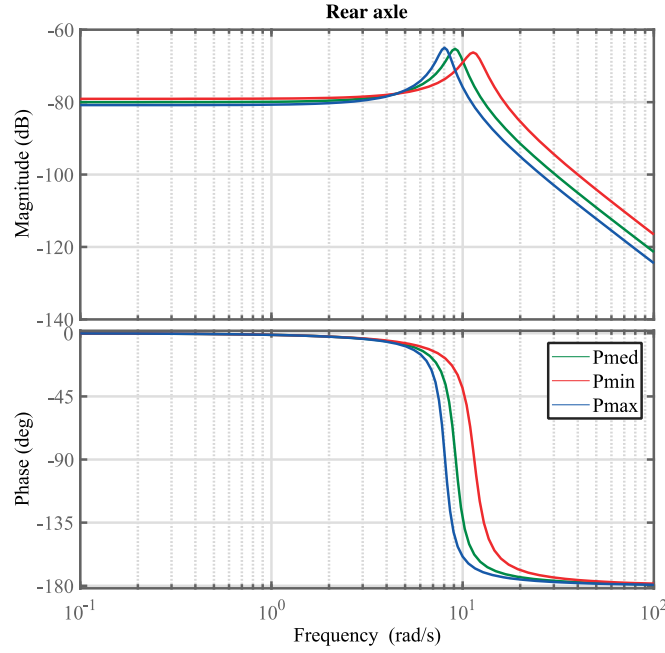


Figure 2.12. Bode response of rear axle synthesis model.

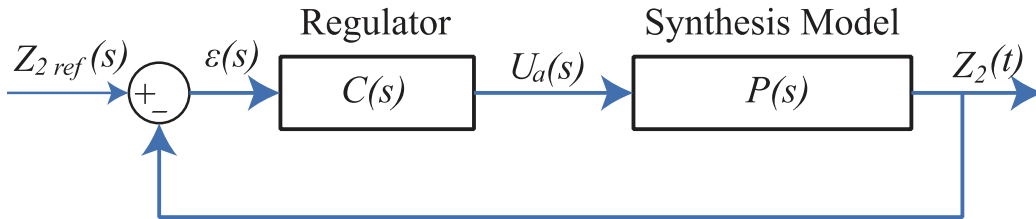


Figure 2.13. Vehicle height regulation's block diagram.

Figure 2.13 represents the unity feedback block diagram of the control methodology, where the $Z_{2ref}(s)$ is the Laplace transformation of the reference value of the car-body position provided by the supervisor and $C(s)$ is the transfer function of the designed controller.

2.3.3.2 Specifications

In this framework, different points are specified for the assigned control strategy and will be listed as follows:

- Rapidity: the crossover frequency of the closed-loop system is to be much less than the natural frequency ω_{n2} .

- Degree of stability: the resonant peak of the complementary sensitivity function is $Q_T \leq 3 \text{ dB}$ that is equivalent to $\min(M_\phi) = 40^\circ$.
- Precision at steady state: the error less than 1%.
- The AW actuator control limit: $\max |u_a| \leq 4000N$.

Particularly here, the “*med*” plants are used as nominal plants in the design process of the two controllers (front and rear axles). Respecting the aforementioned specifications, the following parameters are considered:

$$\omega_{c1} = 1.1 \text{ rad/s} \leq \omega_{n2,nom1}/5, \quad (2.25)$$

$$\omega_{c2} = 1.1 \text{ rad/s} \leq \omega_{n2,nom2}/5, \quad (2.26)$$

$$M_\phi = 45^\circ. \quad (2.27)$$

2.3.3.3 Second Generation CRONE design controller

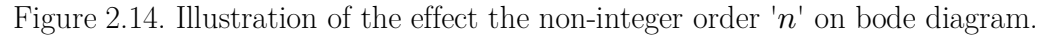
A second-generation CRONE controller can be designed to enforce the following form for the open-loop transfer function:

$$\beta(s) = K \left(\frac{\omega_l}{s} + 1 \right)^{n_l} \left(\frac{1 + \frac{s}{\omega_h}}{1 + \frac{s}{\omega_l}} \right)^n \left(\frac{1}{1 + \frac{s}{\omega_h}} \right)^{n_h}, \quad (2.28)$$

where K , ω_l , and $\omega_h \in \mathbb{R}^+$, and n_l and $n_h \in \mathbb{N}^+$. Integer orders n_l and n_h are set by taking into account the performance specification and the plant magnitude asymptotic behavior at low and high frequencies. This form includes a derivative behavior of order ‘ n ’ around the crossover frequency enabling a phase margin constancy, therefore, a robust performance.

Then, particularly for this study, the transfer function of the CRONE controller ($C(s)$) can be formulated as the following:

$$\begin{aligned} C(s) &= \beta(s)P^{-1}(s) \\ &= K \left(\frac{\omega_l}{s} + 1 \right)^{n_l} \left(\frac{1 + \frac{s}{\omega_h}}{1 + \frac{s}{\omega_l}} \right)^n \left(\frac{1}{1 + \frac{s}{\omega_h}} \right)^{n_h} \frac{\left(\frac{s}{\omega_{n2}} \right)^2 + \frac{2\zeta_2}{\omega_{n2}}s + 1}{P_0}. \end{aligned} \quad (2.29)$$


$$C(s) = C_0 \left(\left(\frac{s}{\omega_{n2}} \right)^2 + \frac{2\zeta_2}{\omega_{n2}} s + 1 \right) \left(\frac{\omega_l}{s} + 1 \right)^{n_l} \left(\frac{1 + \frac{s}{\omega_h}}{1 + \frac{s}{\omega_l}} \right)^{2-m} \left(\frac{1}{1 + \frac{s}{\omega_h}} \right)^{n_h}, \quad (2.30)$$

Finally, the 2nd generation CRONE controller is expressed as the product of two terms, an integer order expression and non-integer order expression, as follows:

where,

$$C_{NE}(s) = \left(\frac{1 + \frac{s}{\omega_h}}{1 + \frac{s}{\omega_l}} \right)^{-m}, \quad \text{where } 0 < m < 1. \quad (2.33)$$

The second step after the selection of the crossover frequency and the phase margin needed is to define the value of n_l , n_h , and n . At low frequencies, and in order to achieve the specified steady-state error, then $n_l = 2$ is adopted. At high frequencies, the objective is to limit the sensibility of control effort to noise measurements, that is, to minimize the gain of the regulator at high frequencies, therefore, we have chosen $n_h = n_p + 1 = 2 + 1 = 3$, where n_p is the order of the controlled plant at high frequencies as shown previously in Figure 2.11 and 2.12.

At medium frequencies, the value of n is computed to attain the specified degree of stability for the closed-loop system. In fact, the calculation of the value of the non-integer order could be done using selected value for phase margin M_ϕ , the factor of the resonance Q_T , module margin M_m , or the damping factor ζ of the system. Here, the value of n is calculated using the assigned value for the phase margin M_ϕ by the following formula:

$$M_\phi = (2 - n)\pi/2, \quad (2.34)$$

then, for $M_\phi = 45^\circ = \frac{\pi}{4} \Rightarrow n = 1.5 \Rightarrow m = 0.5$.

The third step is to determine the values for the transitional frequencies at low and high frequencies, ω_l and ω_h , respectively.

For the front axle, according to Figure 2.11, at $\omega_{c1} = 1.1$ rad/s the uncertainty is approximately gain-like variation. From the rate of decrease of the open-loop magnitude gain 'r' and from the plant magnitude uncertainty, in order to ensure the robustness of the phase margin, the frequency range $[\omega_A, \omega_B]$ needs to cover 0.65 decade, where:

$$r = \log_{10} \frac{\omega_B}{\omega_A} = \left| \frac{-80.59}{-82.32 \ n} \right| = 0.65, \quad (2.35)$$

then,

$$\frac{\omega_B}{\omega_A} = 10^{0.6526} = 4.5. \quad (2.36)$$

As the nominal plant leads to the mean magnitude of the open-loop frequency response around ω_{c1} , then:

$$\begin{aligned}\omega_A &= \omega_{c1}/\sqrt{4.5} = 0.52 \text{ rad/s}, \\ &\text{and} \\ \omega_B &= \omega_{c1} \cdot \sqrt{4.5} = 2.33 \text{ rad/s}.\end{aligned}\tag{2.37}$$

Within the frequency range $[\omega_A, \omega_B]$, the nominal plant phase varies by 1.3° , which confirms the reason for selecting the 2nd generation CRONE controller.

The values of ω_l and ω_h , the corner frequencies, are set using the following formulations:

$$\omega_l = \omega_A/a \text{ and } \omega_h = \omega_B \times b.\tag{2.38}$$

The selection of the values of (a, b) depends on an optimizing methodology of the length of the frequency template as presented in Figure 2.15. Starting from $a = 5$ and $b = 10$, then:

$$\begin{aligned}\omega_l &= 0.52/5 = 0.1038 \text{ rad/s}, \\ &\text{and} \\ \omega_h &= 2.33 \times 10 = 23.3 \text{ rad/s}.\end{aligned}\tag{2.39}$$

Finally, the fractional-order n and gain K of the nominal open-loop transfer function has to ensure the required nominal phase margin M_ϕ and open-loop crossover frequency ω_{c1} . Thus, they are computed by:

$$n = \frac{-\pi + M_\phi + n_h \arctan \frac{\omega_{c1}}{\omega_h} + n_l (\frac{\pi}{2} - \arctan \frac{\omega_{c1}}{\omega_l})}{\arctan \frac{\omega_{c1}}{\omega_h} - \arctan \frac{\omega_{c1}}{\omega_l}},\tag{2.40}$$

and

$$K = \frac{\left(1 + \frac{\omega_{c1}^2}{\omega_h^2}\right)^{\frac{n_h}{2}}}{\left(\frac{\omega_l}{\omega_h}\right)^{\frac{n}{2}} \left(1 + \frac{\omega_l^2}{\omega_{c1}^2}\right)^{\frac{n_l}{2}}}.\tag{2.41}$$

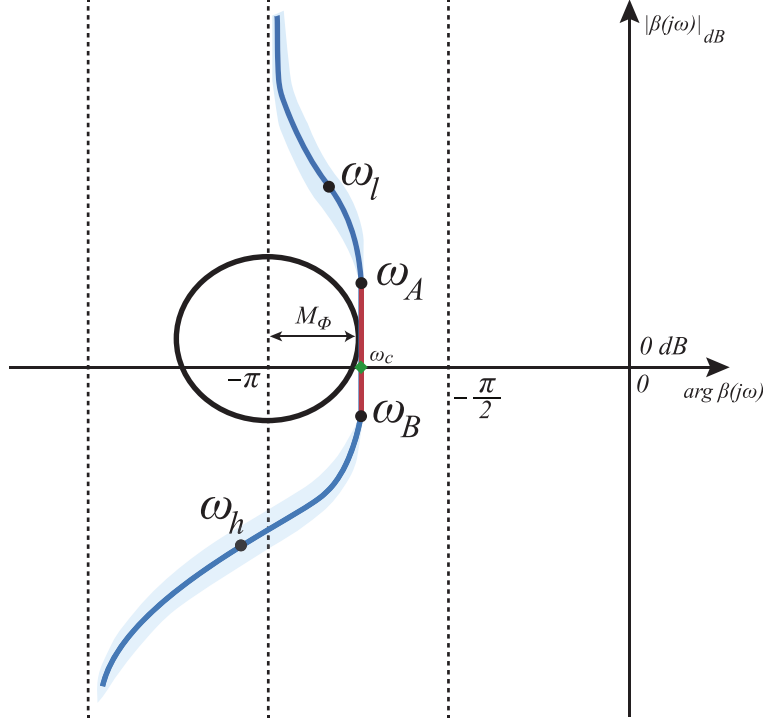


Figure 2.15. Vertical sliding of a frequency template (bold red solid line) ensuring the robustness of phase margin M_ϕ and of resonant peak M_r .

As a result, the nominal phase margin and open-loop gain crossover frequency are ensured with:

$$n = 1.42 \text{ and } K = 46.18. \quad (2.42)$$

Then, the final open-loop transfer function for the front axle is formulated as follows:

$$\beta_1(s) = 46.18 \left(\frac{0.1038}{s} + 1 \right)^2 \left(\frac{1 + \frac{s}{23.3}}{1 + \frac{s}{0.1038}} \right)^{1.42} \left(\frac{1}{1 + \frac{s}{23.3}} \right)^3. \quad (2.43)$$

In the same manner, the open-loop transfer function's parameters are computed for the rear axle plant. According to Figure 2.12, at $\omega_{c2} = 1.1$ rad/s the uncertainty is approximately gain-like variation. From the rate of decrease of the open-loop magnitude gain and from the plant magnitude uncertainty, in order to ensure the robustness of the phase margin, the frequency range $[\omega_A, \omega_B]$ needs to cover 0.68 decade:

$$r = \log_{10} \frac{\omega_B}{\omega_A} = \left| \frac{-80.668}{-78 \ n} \right| = 0.68, \quad (2.44)$$

then,

$$\frac{\omega_B}{\omega_A} = 10^{0.68} = 4.8. \quad (2.45)$$

As the nominal plant leads to the mean magnitude of the open-loop frequency response around ω_{c2} , then:

$$\begin{aligned} \omega_A &= \omega_{c2} / \sqrt{4.8} = 0.5 \text{ rad/s}, \\ &\text{and} \\ \omega_B &= \omega_{c2} \cdot \sqrt{4.8} = 2.4 \text{ rad/s}. \end{aligned} \quad (2.46)$$

Within the frequency range $[\omega_A, \omega_B]$, the nominal plant phase varies by 2.4° , which confirms the reason for selecting the 2nd generation CRONE controller. The values of ω_l and ω_h , the corner frequencies, are set using the following formulations with same values for (a,b), then:

$$\begin{aligned} \omega_l &= 0.52/5 = 0.1 \text{ rad/s}, \\ &\text{and} \\ \omega_h &= 2.33 \times 10 = 24 \text{ rad/s}. \end{aligned} \quad (2.47)$$

According to (2.40) and (2.41), the nominal phase margin and open-loop gain crossover frequency are ensured with:

$$n = 1.42 \text{ and } K = 48.74. \quad (2.48)$$

Then, the final open-loop transfer function for the rear axle is formulated as follows:

$$\beta_2(s) = 48.74 \left(\frac{0.1}{s} + 1 \right)^2 \left(\frac{1 + \frac{s}{24}}{1 + \frac{s}{0.1}} \right)^{1.42} \left(\frac{1}{1 + \frac{s}{24}} \right)^3. \quad (2.49)$$

For the three parametric states of the two plants (front, rear), Figure 2.16 and 2.17 present respectively the open-loop Nichols plots. They clearly show the frequency template tangent to the 3dB contour. The open-loop frequency

responses, as plotted in Figure 2.18 and 2.19, show that the phase margins only vary from 45.3° to 45.1° as the crossover frequency ranges from 1.03 to 1.18 rad/s, for front and rear axle as well. Furthermore, the Nichols chart contours indicate that the resonance peak of $T(s)$ are approximately equal. The band-limitation achieved by ω_l and ω_h permits a good management of the performance/robustness tradeoff.

Figure 2.20 and 2.21 present the closed-loop sensitivity functions for front and rear axles, respectively. They show that:

- The variation on the resonant peak of $T(s)$ is approximately zero.
- The resonant peaks of $S(s)$ are approximately equal.
- At low frequencies, $T(s)$ is close to 0dB, which will result in inaccurate tracking of the reference signal, and $S(s)$ is small, which means desensitization of $T(s)$ versus the plant uncertainty.
- $SG(s)$ decreases for low frequencies (efficient rejection of input disturbances) and $CS(s)$ reaches about 85dB and then decreases (low amplification of noise measurements).

For time-domain simulations, a rational form of the controllers' transfer functions is necessary. The simplest way is to use Oustaloup's method (Oustaloup, 1991b) to replace the band-limited fractional-order integrator of (2.33), using N recursive zeros and poles. As the frequency range $[\omega_l, \omega_h]$ cover three decades, then $N = 4$ is enough to approximate well the fractional-order part ' m '.

Thus, the resulted rational form of the 2nd generation CRONE controllers' transfer functions can be written in the following form:

$$C_1(s) = 665 \left(\frac{193s^2 + 200s + 12e3}{(s/0.1038)^2} \right) (1 + s/23.3)^{-1} \times \frac{(s + 7.99)(s + 2.064)(s + 0.5331)(s + 0.1377)}{(s + 17.58)(s + 4.540)(s + 1.730)(s + 0.3029)}, \quad (2.50)$$

and

$$C_2(s) = 716 \left(\frac{118s^2 + 200s + 10e3}{(s/0.1)^2} \right) (1 + s/24)^{-1} \times \frac{(s + 8.164)(s + 2.075)(s + 0.5273)(s + 0.134)}{(s + 18.06)(s + 4.589)(s + 1.166)(s + 0.2964)}.$$

(2.51)

Figure 2.22 shows the bode response of the rational transfer functions of the two controllers defined by (2.50) and (2.51), for front and rear plants, respectively. These transfer functions are then used in time-domain simulations and applied to the validation model for performance and robustness analysis.

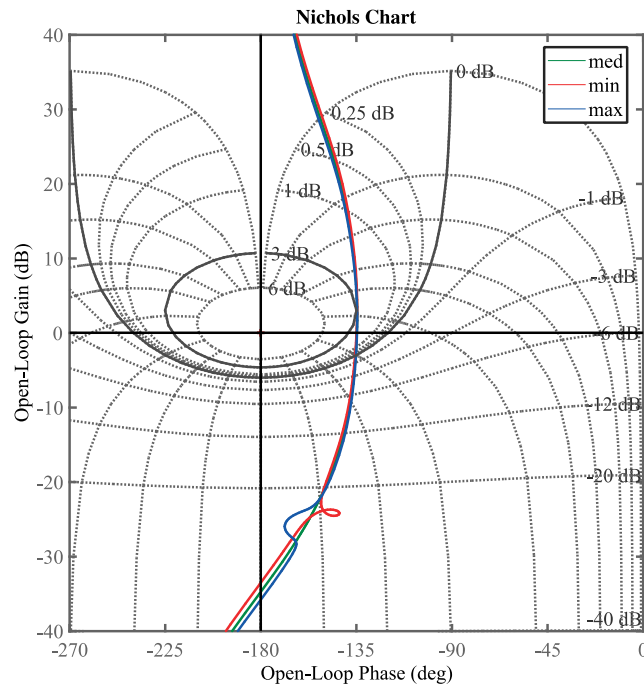


Figure 2.16. Open-loop Nichols plot for the 3 front plants.

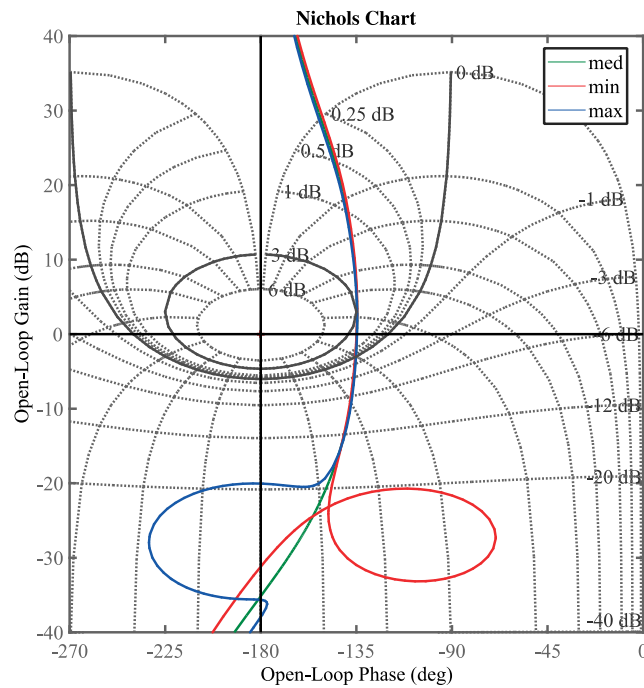


Figure 2.17. Open-loop Nichols plot for the 3 rear plants.

2.3 Vehicle's height control

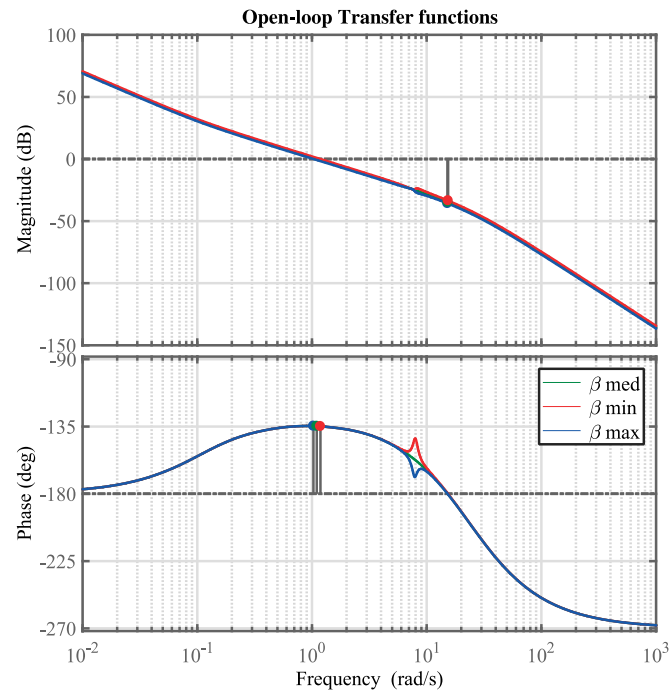


Figure 2.18. Open-loop Nichols plot for the 3 front plants.

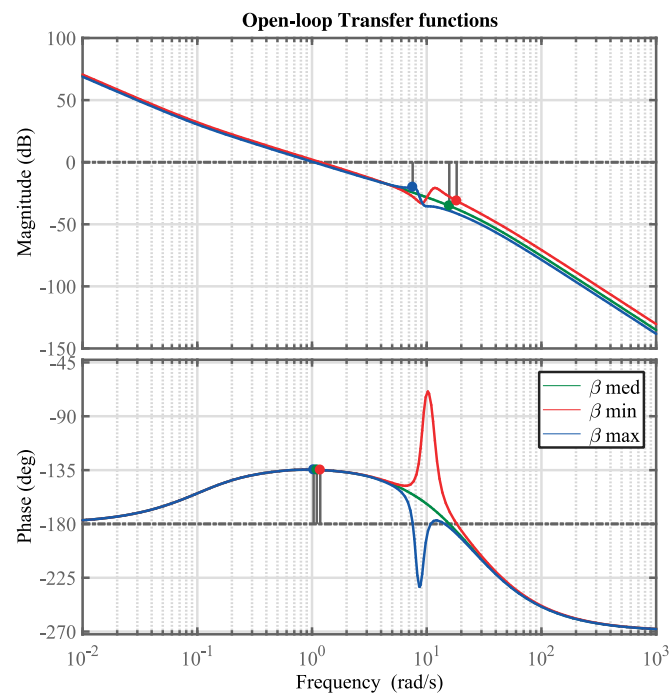


Figure 2.19. Open-loop Nichols plot for the 3 rear plants.

2.3 Vehicle's height control

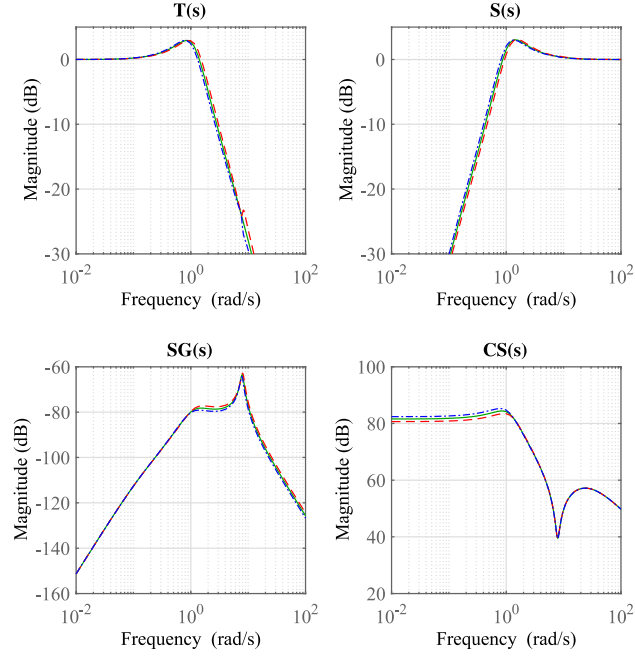


Figure 2.20. Closed-loop sensitivity functions for the 3 **front** plants: P_{nom} (—), P_{min} (---), and P_{max} (-.-).

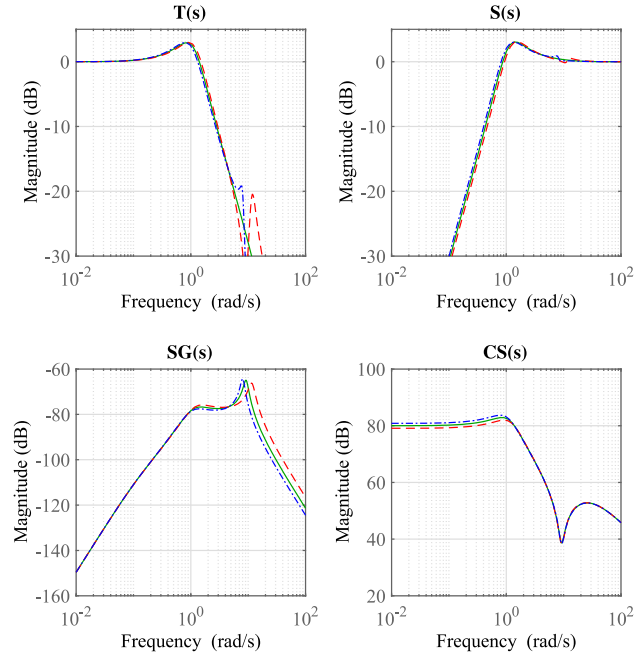


Figure 2.21 Closed-loop sensitivity functions for the 3 **rear** plants: P_{nom} (—), P_{min} (---), and P_{max} (-.-)..

2.3 Vehicle's height control

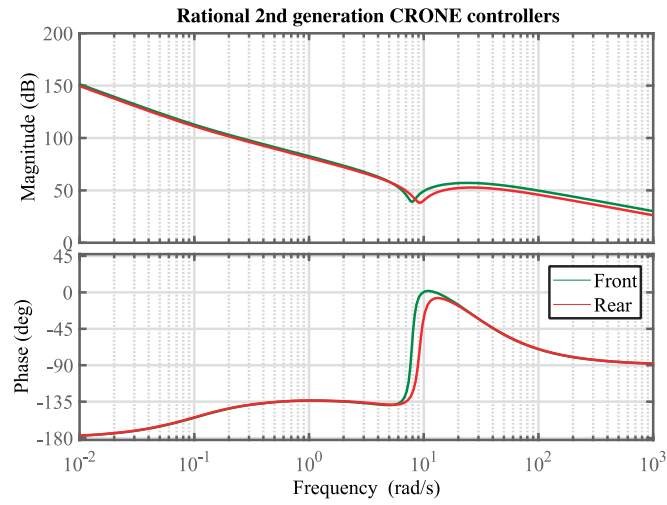


Figure 2.22. Bode plot of rational controllers' transfer functions

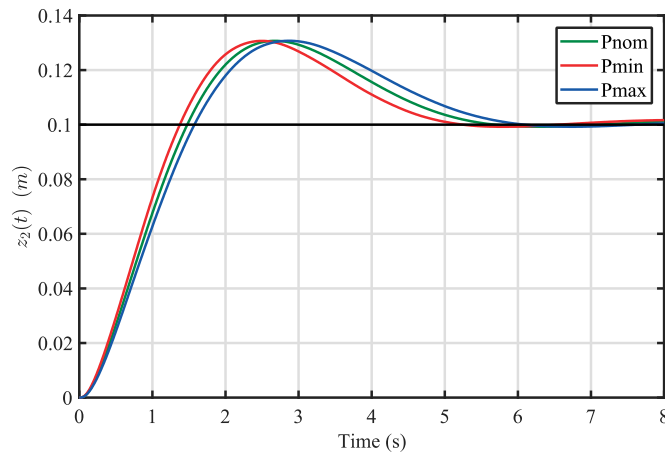


Figure 2.23. Closed-loop step responses for the 3 front plants.

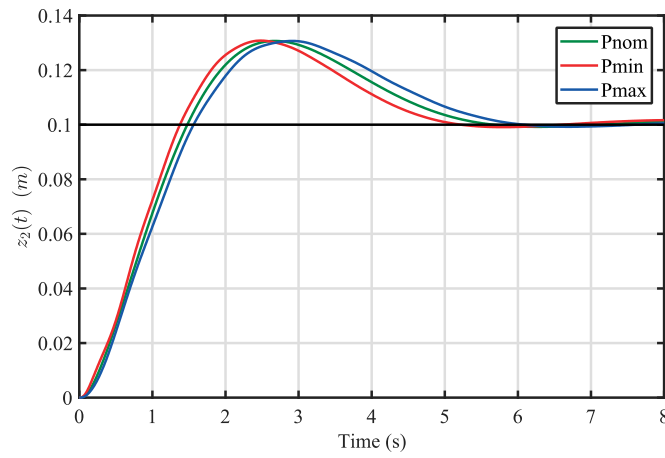


Figure 2.24. Closed-loop step responses for the 3 rear plants.

2.3.4 Time-domain simulations and analysis

The two designed controllers are tested for step responses, at first, for the synthesis models. Figure 2.23 and 2.24 are presented respectively the front and rear step responses of minimal, medium, and maximal systems. They show that for tolerable durations, the tracking of $z_{2ref}(t)$ is efficient. Moreover, the CRONE controllers provide a percentage of overshoot for the response of z_2 (sprung mass displacement) to z_{2ref} that remains almost constant with respect to the plant uncertainties. Besides, all plants have the same damping behavior which reflects the robustness of the damping factor of the closed-loop systems obtained thanks to the CRONE controllers.

In order to validate the designed controller, two test simulations were done on the quarter vehicle model (Figure 2.1), which includes the unsprung mass dynamics as well as the sprung mass dynamics. The two closed-loop systems have given a reference value of 50mm elevation, and the controller should work on tracking the reference robustly versus parametric variations. Each controller is tested on the three plant configurations to examine the robustness of the controllers as well as their performances.

Figure 2.25 shows the simulation results on the validation models for the front and rear axles' suspensions, respectively. It obviously shows the robustness, in both scenarios, of the designed controllers against parametric variation of the plant. All time-domain responses have the same overshoot, steady-state error, and damping behavior. The graphs also plot the effect of the introduced control effort on wheel deformation, where it represents the behavior of the unsprung mass displacements $z_1(t)$.

To extend the benefit of the control strategy, three different scenarios are tested on the full vehicle model. First, the objective is to elevate the center of gravity of the chassis by 5cm. The second scenario is assigned to obtain a reference pitch angle. The final scenario is to elevate the chassis from one side, and thus, obtain an adequate roll angle. In fact, all these scenarios are achieved by means of translational relationship between the car-body reference values and the four vertical positions at each corner ($z_2(t)$).

2.3 Vehicle's height control

Each scenario was tested for three different vehicles' parametric configuration, i.e. empty vehicle (P1), half-loaded vehicle (P2), and fully-loaded vehicle (P3).

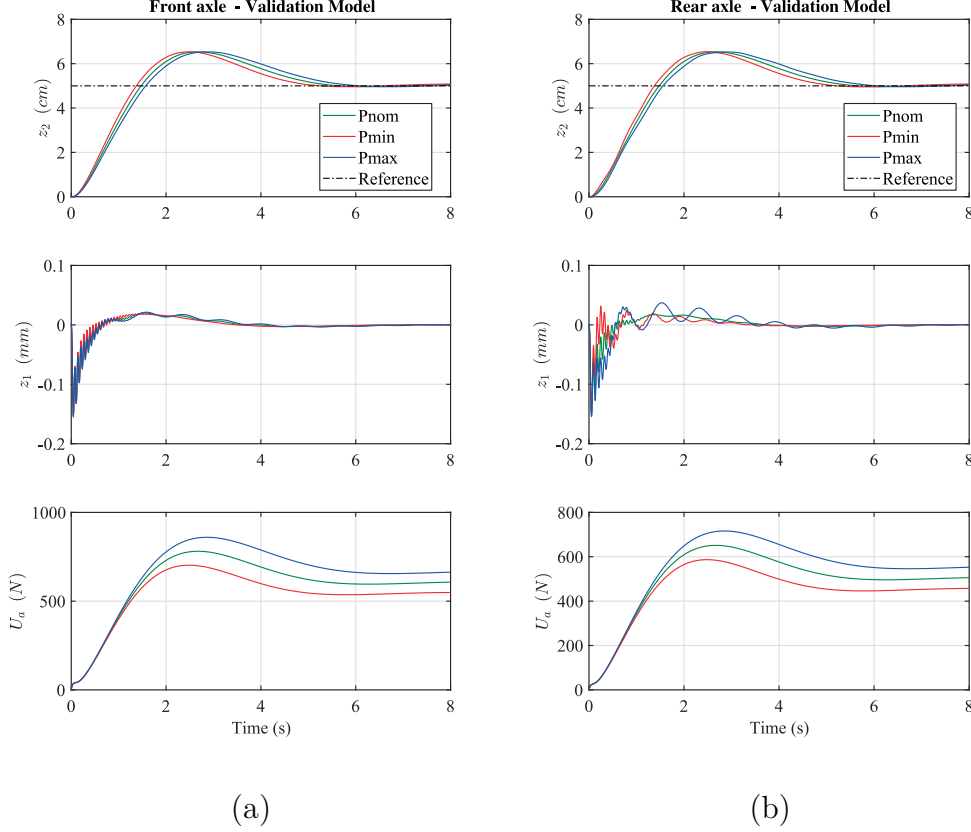


Figure 2.25. Simulation results of the validation model on (a) Front axle and (b) rear axle.

The objective is to examine the robustness of the controllers with car-body dynamics versus masses variations.

Figure 2.26 shows the results of the 3 scenarios. Although of the variation of the total mass of the vehicle, the designed controller provides the same response while varying the height of the chassis, the pitch angle around the y-axis, and the roll angle around the x-axis. The only difference appeared at the height of the center of gravity of the vehicle in the 2nd scenario, which is normal and expected due asymmetry distribution of the mass of the vehicle in the longitudinal direction. Therefore, the CG is initially not at the middle of the chassis length ' L ', then any variation in the pitch angle will vary the value of the height CG.

2.3 Vehicle's height control

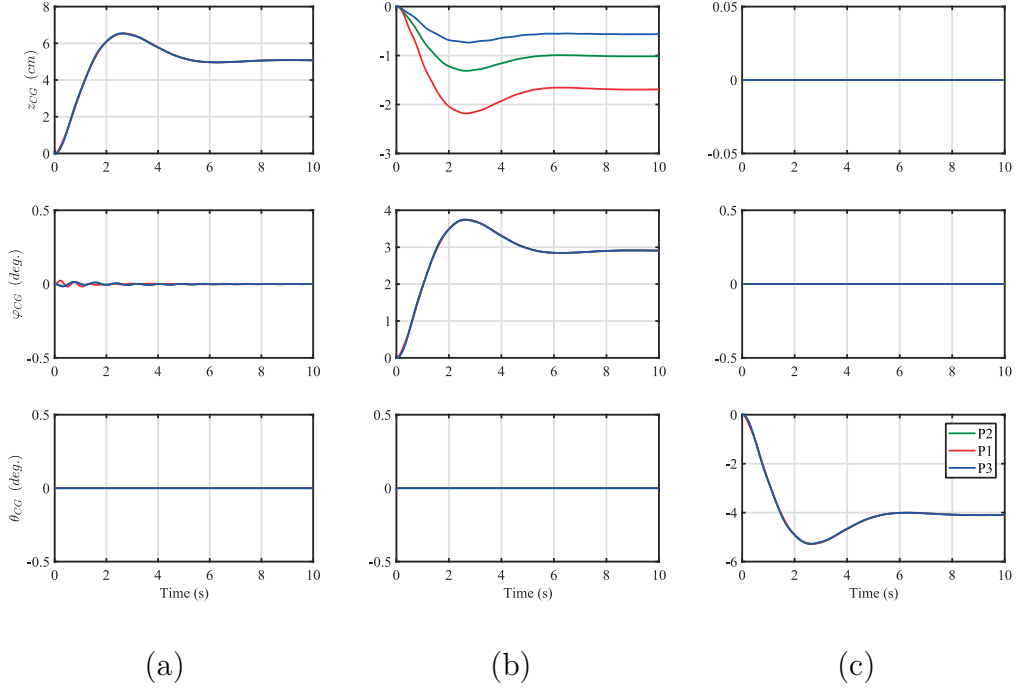


Figure 2.26. Simulation results using the full model of (a) varying height of car-body, (b) attain reference pitch angle, and (c) attain reference roll angle.

2.3.5 Conclusion

The first designated objective was to regulate the height of the chassis. For this purpose, two 2nd generation CRONE controllers are designed for the front axle and rear axle of the vehicle. The frequency and time-domain analysis show the robustness of the designed controller versus parametric variations. Besides, the controllers were able to achieve good tracking reference performance. These controllers proved their ability to regulate the car-body motions when needed. Mainly, these controllers are dedicated to standstill situations for the purpose of exit/enter the vehicle. Thus, it provides more feasibility for occupants, especially for children and passengers with physical disabilities.

Moreover, the control strategy can be considered as an adequate solution for reducing the influence of emergency impending side impact on the vehicle. In fact, it depends mainly on the ability of early detection of such alert and the time response of the controllers, in which it proved that the system could

reach a good elevation in less than 1s, where the objective is no longer tracking a reference at all.

2.4 Fractional-order damping control

2.4.1 Introduction

Active suspension systems are proving their importance in the field of vehicle dynamics. Many studies in the literature show their ability to enhance comfort for passengers (Moreau et al., 2009), vehicle stability (Altet et al., 2003) and driving performance (Termous et al., 2018b) compared to passive systems. However, due to the coupling effects between the suspension dynamics and longitudinal and lateral dynamics (Hamersma and Schalk Els, 2014), active suspension control laws, where the strategy is comfort-oriented, may degrade the performance of braking on rough roads, for example.

Indeed, the active suspension forces introduced by the electric actuator affect the wheel normal forces, which in turn impact the wheel longitudinal contact forces that are directly responsible for the braking, acceleration, and cornering behavior of a vehicle. For this purpose, searching for new design control strategies using suspension control becomes a topic of research nowadays in order to enhance lateral and longitudinal dynamics (Sammier et al., 2003) (Gáspár et al., 2007). In this domain, fractional-order control laws have gained their prevalence where they show their ability in solving different control problems (Moreau et al., 2001).

In this section, the impact of fractional-order control methods has been studied, where we derive optimized different fractional-order (FO) damping control strategies, a comfort-oriented and a road-holding oriented strategy, based on the non-integer derivation of the suspension deflection using the active suspension system introduced in the Active Wheel (Laurent et al., 2000).

The following study represents one of the proposed solutions for the objectives assigned for vertical dynamics control for light electric vehicles. Besides a comfort-oriented control strategy, a road-holding oriented strategy is also proposed where the main purpose is to reduce the variation of the wheel

deflections, thus, improves significantly the lateral and longitudinal dynamics of the vehicle.

Here, the study presents the control strategy and design methodologies. Moreover, frequency-time-domain analysis is done on the level of quarter vehicle models. However, the simulations that reflect real-time scenarios are presented in later chapters while dealing with lateral and longitudinal dynamics on full vehicle validation models.

2.4.2 Suspension model

In general, the vehicle suspension system is required to fulfill a number of functions. These can be stated as follows:

- isolate the vehicle from road surface irregularities;
- control variations in vertical load at the road/tire interface;
- control body motion caused by road inputs, inertia forces, and aerodynamic forces;
- maintain vehicle directional stability during maneuvers.

In fact, the main problem is the conflict between these various aspects of vehicle behavior.

Traditional Suspension

A passive vibration control unit consists of a spring and an energy dissipator. As detailed in previous sections, the suspension system can be modeled as a linear spring and a damper. The expression of the force $f_s(t)$ developed by the suspension is formulated as (2.3) for passive systems:

$$f_s(t) = k_2(z_2(t) - z_1(t)) + b_2(\dot{z}_2(t) - \dot{z}_1(t)), \quad (2.52)$$

The Active Wheel suspension system

The active suspension system embedded in the Active Wheels can be modeled by a spring, an electric actuator that acts as a force generator and a small frictional damping ratio that results from the mechanical links of the system. Thus, the expression of the force developed by the suspension system is then formulated by:

$$f_s(t) = k_2(z_2(t) - z_1(t)) + b_2(\dot{z}_2(t) - \dot{z}_1(t)) + u_a(t). \quad (2.53)$$

The idea is to use the force generator as a continuously controllable damper that develops a force $u_a(t)$ that is proportional to the fractional derivative of the suspension deflection. This force is then written as:

$$u_a(t) = b_a \left(\frac{d}{dt} \right)^n (z_{2i}(t) - z_{1i}(t)), \quad (2.54)$$

With $0 < n < 2$ is the non-integer derivative order, and b_a is a constant gain factor. The Laplace transform of relation (2.54) leads to the following transfer function:

$$U_a(s) = -b_a \frac{1}{s^{1-n}} (V_2(s) - V_1(s)). \quad (2.55)$$

If we neglect the small friction coefficient of the mechanical links in the AW' suspension system, the force $f_s(t)$ developed by the active suspension is then given by:

$$f_s(t) = k_2(z_2 - z_1) + b_a \left(\frac{d}{dt} \right)^n (z_2(t) - z_1(t)). \quad (2.56)$$

The Laplace transform of the vertical dynamics of the quarter vehicle system with fractional-order damping control leads to the following transfer functions:

$$\begin{aligned} V_1(s) = & \frac{(m_2 s^2 + b_2 s + b_a s^n + k_2)(b_1 s + k_1)}{D^n e(s)} V_0(s) \\ & + \frac{s(b_2 + b_a s^n + k_2)}{D^n e(s)} F_0(s), \end{aligned} \quad (2.57)$$

and

$$\begin{aligned} V_2(s) = & \frac{(b_2 s + b_a s^n + k_2)(b_1 s + k_1)}{D^n e(s)} V_0(s) \\ & + \frac{s(m_1 s^2 + (b_2 + b_1)s + b_a s^n + (k_2 + k_1))}{D^n e(s)} F_0(s), \end{aligned} \quad (2.58)$$

with,

$$\begin{aligned}
 D^n e(s) = & m_1 m_2 s^4 + (m_2(b_1 + b_2) + m_1 b_2) s^3 \\
 & + (m_2(k_1 + k_2) + m_1 k_2 + b_1 b_2) s^2 + (k_1 b_2 + b_1 k_2) s \\
 & + k_1 k_2 + b_a(m_1 + m_2) s^{2+n} + b_a b_1 s^{1+n} + b_a k_1 s^n.
 \end{aligned} \tag{2.59}$$

$V_2(s)$, $V_1(s)$, $V_0(s)$, and $F_0(s)$ are the Laplace transform of $\dot{z}_2(t)$, $\dot{z}_1(t)$, $\dot{z}_0(t)$, and $F_0(t)$, respectively.

It should be noticed that for $b_a = 0$ is the case of passive suspension, and when $b_2 = 0$ is the case of active suspension (assumption). Moreover, for the particular case, $n = 1$ and $b_a = b_2$, the active suspension system acts as the passive system.

2.4.3 Control structure

The proposed strategy for the active suspension is shown in Figure 2.27. It consists of a feedback control law used to regulate the suspension deflection versus road input disturbances. Supposing “ b_a ” is constant, the only controlled parameter is the fractional-order “ n ”. The value of n should be chosen according to the selected objectives.

For this purpose, three sensitivity transfer functions were formulated in order to find the optimized value of ‘ n ’, that are:

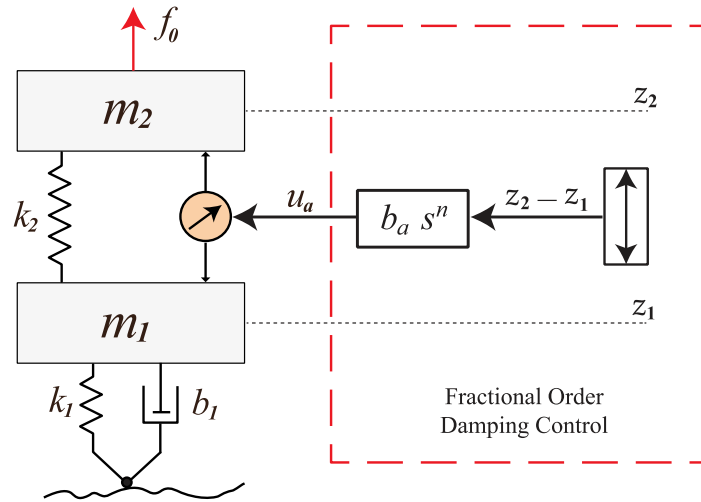


Figure 2.27. Control diagram of the fractional order damping control.

$$H_a(s) = \left. \frac{A_2(s)}{V_0(s)} \right|_{F_0=0} = \left. \frac{sV_2(s)}{V_0(s)} \right|_{F_0=0}, \quad (2.60)$$

where $H_a(s)$ represents the sensitivity of the vehicle's body vertical acceleration to road disturbances. It evaluates the vibration isolation, in which small gains results in better ride comfort.

$$H_{12}(s) = \left. \frac{Z_1(s) - Z_2(s)}{V_0(s)} \right|_{F_0=0}, \quad (2.61)$$

where $H_{12}(s)$ is the sensitivity of suspension deflection to road disturbances.

The final sensitivity function is the one relative to the wheel deflection, $H_{01}(s)$, which plays the role of an indicator for road-holding and a constraint for wheel normal forces variations. This transfer function is formulated as follows:

$$H_{01}(s) = \left. \frac{Z_1(s) - Z_0(s)}{V_0(s)} \right|_{F_0=0}. \quad (2.62)$$

The transfer functions of these three sensitivity functions are easily formulated using the expressions detailed in section 2.2 and (2.57), (2.58), and (2.59). Therefore, they can be written under the following formulations:

$$H_a(s) = \frac{s(b_2s + b_as^n + k_2)(b_1s + k_1)}{D^ne(s)}, \quad (2.63)$$

$$H_{12}(s) = \frac{m_2s(b_1s + k_1)}{D^ne(s)}, \quad (2.64)$$

$$H_{01}(s) = \left(1 - \frac{(m_2s^2 + b_2s + b_as^n + k_2)(b_1s + k_1)}{D^ne(s)} \right) / s. \quad (2.65)$$

Using these sensitivity functions, three criteria expressions are formulated for optimizations purposes and are given as follows:

$$\begin{cases} J_1(n) = J_a(n) = \frac{1}{\eta_1} \int_{\omega_{min}}^{\omega_{max}} |H_a(j\omega)|^2 d\omega \\ J_2(n) = J_{12}(n) = \frac{1}{\eta_2} \int_{\omega_{min}}^{\omega_{max}} |H_{12}(j\omega)|^2 d\omega \\ J_3(n) = J_{01}(n) = \frac{1}{\eta_3} \int_{\omega_{min}}^{\omega_{max}} |H_{01}(j\omega)|^2 d\omega \end{cases}, \quad (2.66)$$

where η_1 , η_2 , and η_3 represent the values of the calculated criteria for the passive suspension system, i.e. $b_a = 0$. The range of integration is considered between $\omega_{min} = 2 \pi 0.1$ rad/s and $\omega_{max} = 2 \pi 30$ rad/s.

According to these criteria, when the value is less than 1, it indicates an improvement over the passive system. The optimal control problem can thus be formulated as finding the minimal values of n for each criterion. Figures 2.28 - 2.31 show the graph plots of the criterion values normalized relative to passive value as a function of the fractional-order n . Minimum values are obtained for front and rear axles, for empty load and full-loaded parametric configurations. Table 2.3 lists the values of n while considering $b_a = 1200$ Ns/m. The suspension control strategy must be changed according to the road state of the surface. In case of a smooth road, the road-holding strategy is then preferred. It is the same case also when a critical braking situation revealed where comfort-oriented strategy is no longer a priority, here the suspension must be switched to road-holding oriented strategy in order to minimize the variation of the wheels' normal forces to reduce the braking distance. These considerations are assigned to the "supervisor", the high-level control unit in the global chassis control, that takes decisions based on all available measurements and estimated variables.

Table 2.3. Optimized values of the damping fractional-order n .

Axle	Load	n		
		J_1	J_2	J_3
Front	Empty load	0.68	1.1	1.69
	Full load	0.7	1.11	1.68
Rear	Empty load	0.64	1.01	1.8
	Full load	0.68	1.06	1.68

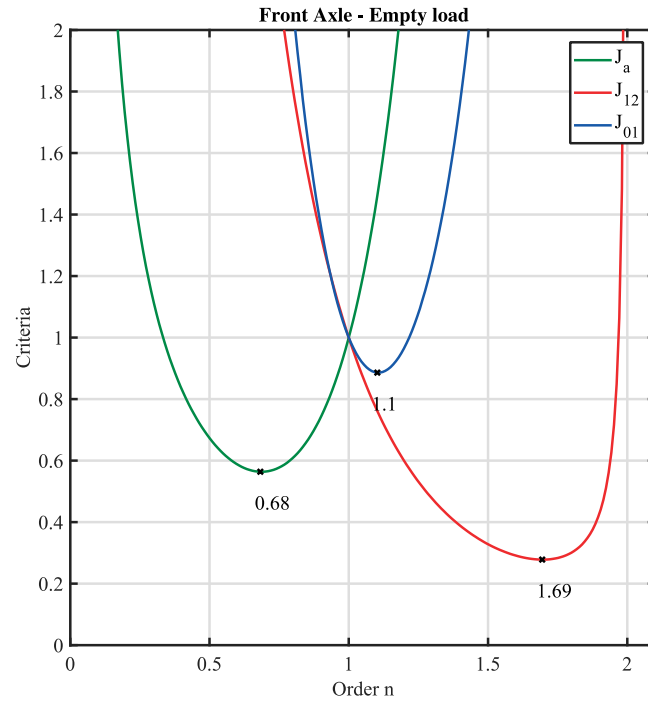


Figure 2.28. Optimized damping order n of front axle for empty vehicle.

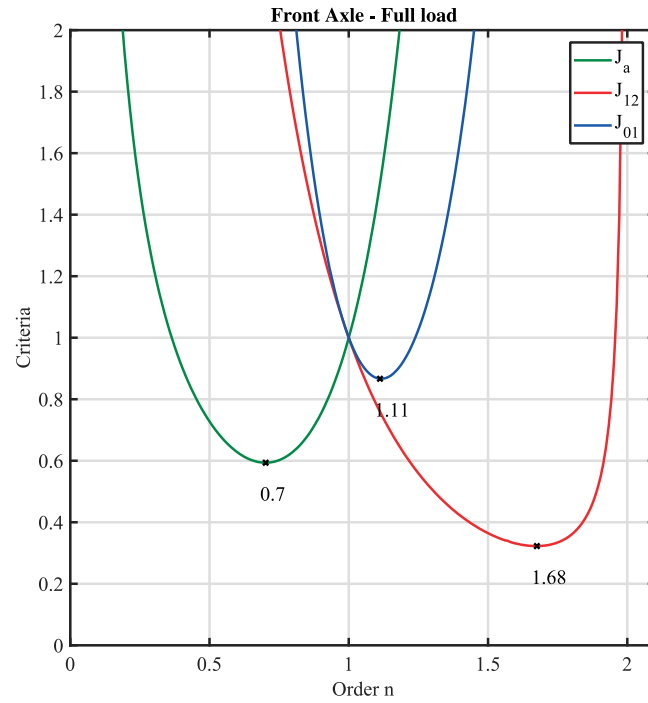


Figure 2.29. Optimized damping order n of front axle for full loaded vehicle.

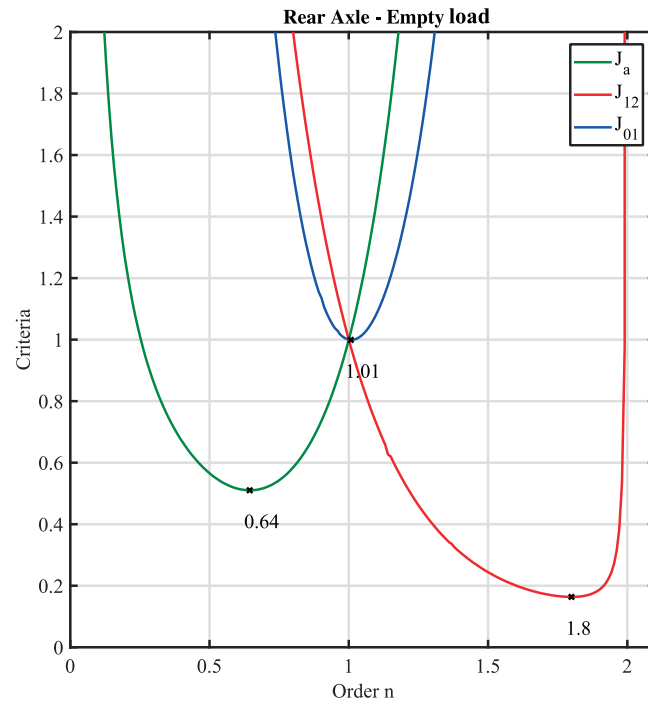


Figure 2.30. Optimized damping order n of rear axle for empty vehicle.

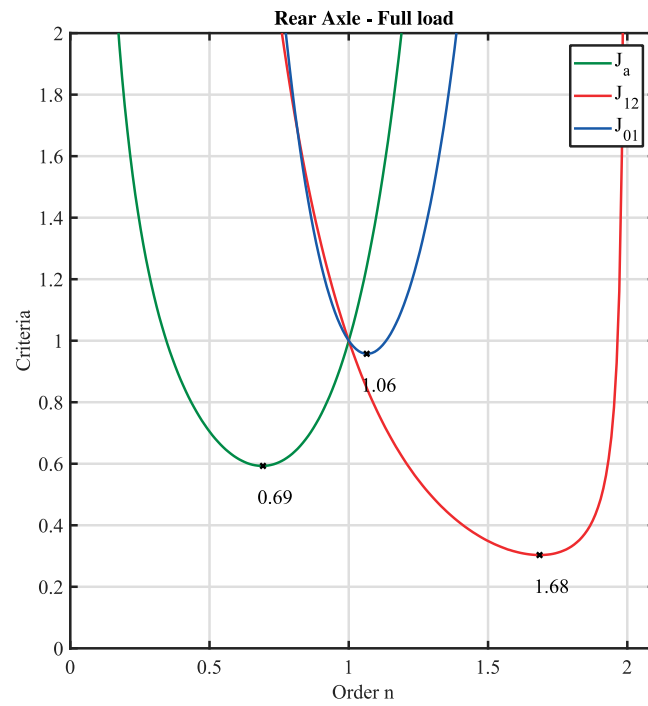


Figure 2.31. Optimized damping order n of rear axle for full loaded vehicle.

2.4.4 Rationalized approach of FO damping control

In order to show the influence of the fractional damping control, several scenarios were done using the quarter vehicle validation model. The scenario was chosen to be a quarter vehicle test rig driven on a rough surface, in which it includes a range of low and high frequencies components so that it affects ride comfort, road holding, and handling.

In this study, two values for n are chosen, and then a comparative study is done. Then, for time-domain simulations, the fractional-order damping control in (2.55) is formalized as a 2nd generation CRONE controller to assure a band-limited derivation of order ‘ n ’ around the crossover frequency enabling a phase margin constancy, and therefore, a robust performance. The controller is expressed as the following:

$$C(s) = C_0 \left(\frac{1 + \frac{s}{\omega_h}}{1 + \frac{s}{\omega_l}} \right)^{1-n}, \quad (2.67)$$

where

$$C_0 = b_a \left(\frac{1 + \left(\frac{\omega_m}{\omega_l} \right)^2}{1 + \left(\frac{\omega_m}{\omega_h} \right)^2} \right)^{\frac{1-n}{2}}. \quad (2.68)$$

Particularly for this study, the central frequency ω_m of the band-limited integrator is selected 1 rad/s. The rate of decrease of the open-loop magnitude gain ‘ r ’ in the frequency range $[\omega_A, \omega_B]$ needs to cover 5 decades, where the range of interest is between 0.1 and 30 Hz.

As the nominal plant leads to the mean magnitude of the open-loop frequency response around ω_m , then:

$$\begin{aligned} \omega_A &= \omega_m / \sqrt{10^5} = 0.0032 \text{ rad/s}, \\ &\text{and} \\ \omega_B &= \omega_m \cdot \sqrt{4.5} = 316.2 \text{ rad/s}. \end{aligned} \quad (2.69)$$

The values of ω_l and ω_h , the corner frequencies, are set using the following formulations:

$$\begin{aligned}\omega_1 &= 0.0032/10 = 0.00032 \text{ rad/s}, \\ \text{and } \omega_h &= 316.2 \times 10 = 3162 \text{ rad/s}.\end{aligned}\tag{2.70}$$

Then fractional part of the 2nd generation CRONE controller should be replaced by a rational transfer function. Thanks to the Oustaloup method, the rational form of the transfer function is obtained for each value of n .

The two values of n are chosen as follows:

$$n_1 = 0.65 \text{ and } n_2 = 1.1.\tag{2.71}$$

Figures 2.32 - 33 show the bode response of the fractional-order damping control $U_a(s)$, compared to the fractional-order 2nd generation CRONE control, and the rational form of the controller used in time-domain simulations, for the two values of n .

It is important to consider the identical responses for all transfer functions in the range of 0.1 - 30 Hz, i.e. the range of interest of frequency for road disturbances. The rational transfer functions were obtained using N recursive zeros and N recursive poles by Oustaloup's method. The 2nd generation CRONE control proved (in the frequency domain) to be an adequate approach for representing the fractional damping control proposed in this section.

Figure 2.34 shows the resulted bode responses of the two sensitivity functions, $H_a(s)$ and $H_{12}(s)$, with the two fractional damping controllers with $n = 0.65$ and $n = 1.1$. In Figure 2.34a, it can be deduced that for $n = 0.65$ the damping control is comfort-oriented strategy, where it attenuates the acceleration response to road disturbances on frequencies greater than 2Hz, especially in the range of interests [4-8Hz]. On the other hand, Figure 2.34b the fractional damping control with order $n = 1.1$ shows a significant attenuation in suspension deflection versus road disturbances on a wide range of frequencies, which is featured prominently at the resonance frequencies of chassis mode and wheel mode. This behavior is eventually granting a road-holding improvement in the time-domain simulations. For this reason, the fractional damping control with order 1.1 could be adopted as a road-holding oriented control strategy.

2.4 Fractional-order damping control

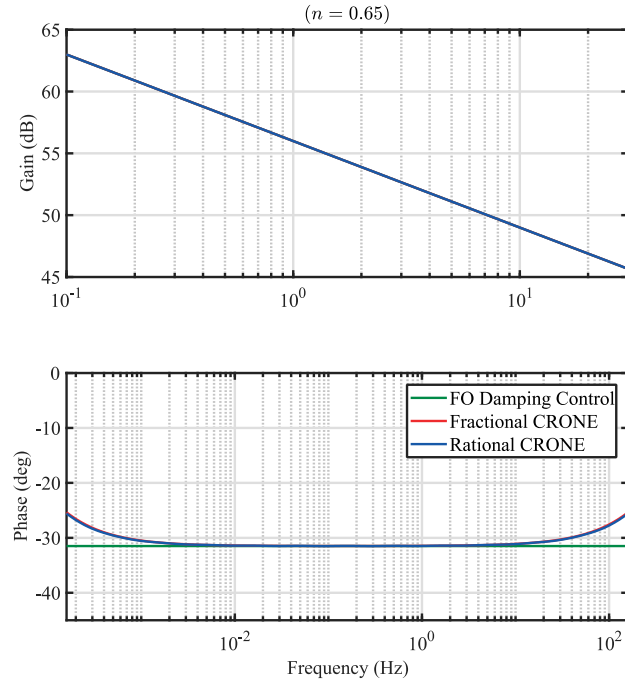


Figure 2.32. FO damping transformation compared to fractional and rational 2nd generation CRONE controller for $n = 0.65$.

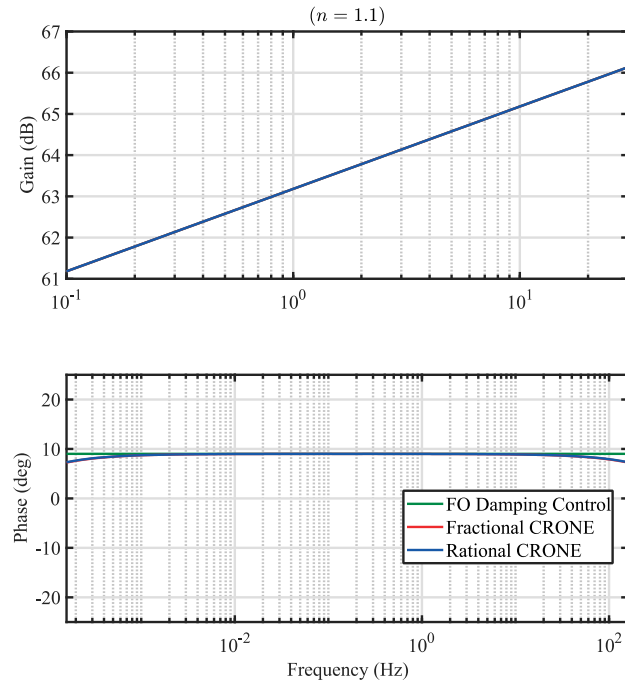


Figure 2.33. FO damping transformation compared to fractional and rational 2nd generation CRONE controller for $n = 1.1$.

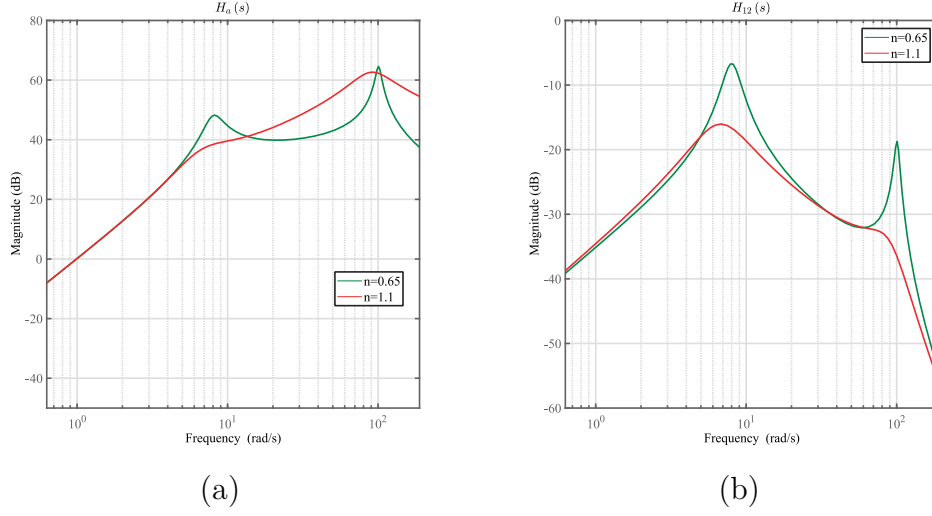


Figure 2.34. Bode response of sensitivity functions: (a) $H_a(s)$ and (b) $H_{12}(s)$, with two fractional damping order $n = 0.65$ and $n = 1.1$.

2.4.5 Time-domain simulations

Using the 2DoF quarter vehicle validation model, two scenarios were done to examine the performance of the fractional-order damping controllers. Each scenario adopts one kind of road disturbances that includes a range of frequencies and specific amplitudes. One parametric configuration is used in all simulations, in which the controlled systems are compared to traditional suspension passive systems of the damping coefficient $b_2 = 1200 \text{ Ns/m}$.

The first scenario uses a sinusoidal profile road disturbance with a sweeping frequency starting from 0.1 to 40 Hz. The amplitude of the sinusoidal form is 1mm. Generally, this scenario is made for testing vibratory isolation of a designed controller. Figure 2.35 represents the results obtained for the two FO damping controllers compared to the passive system.

It is clearly showing that FO damping control with comfort-oriented control have a lower amplitude in terms of vertical accelerations $\ddot{z}_2(t)$ compared to passive and road-holding oriented one. Significantly, the comfort-oriented controller has also much lower control effort values. These results reveal a

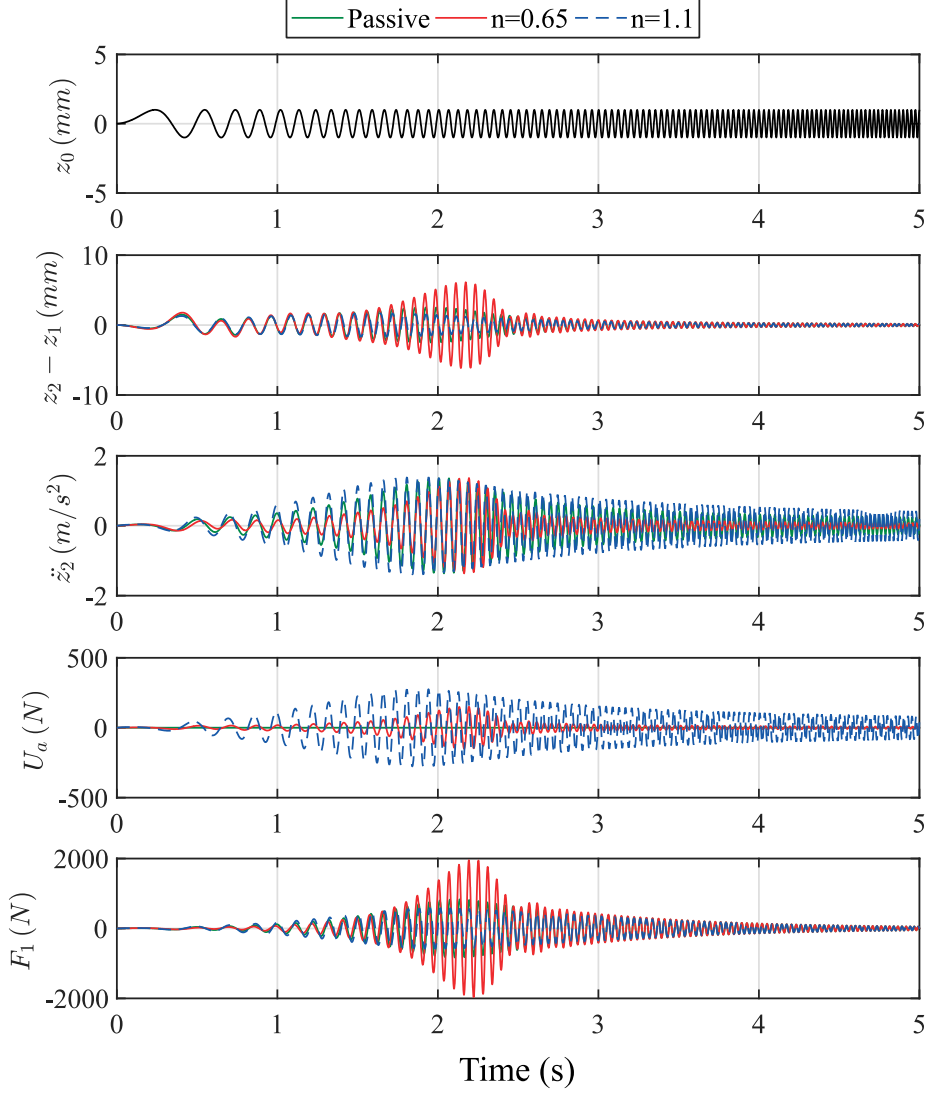


Figure 2.35. Simulation results of fractional damping control compared to passive system with sinus road disturbances of frequency 0.1 to 40Hz of amplitude 1mm.

good performance in vibratory isolations where the main goal is to attenuate the vertical accelerations and thus provide comfort for passengers. This improvement comes at the expense of higher suspension deflections and wheel deflections, which degrades the road-holding performance of the vehicle and may affect the handling process as well.

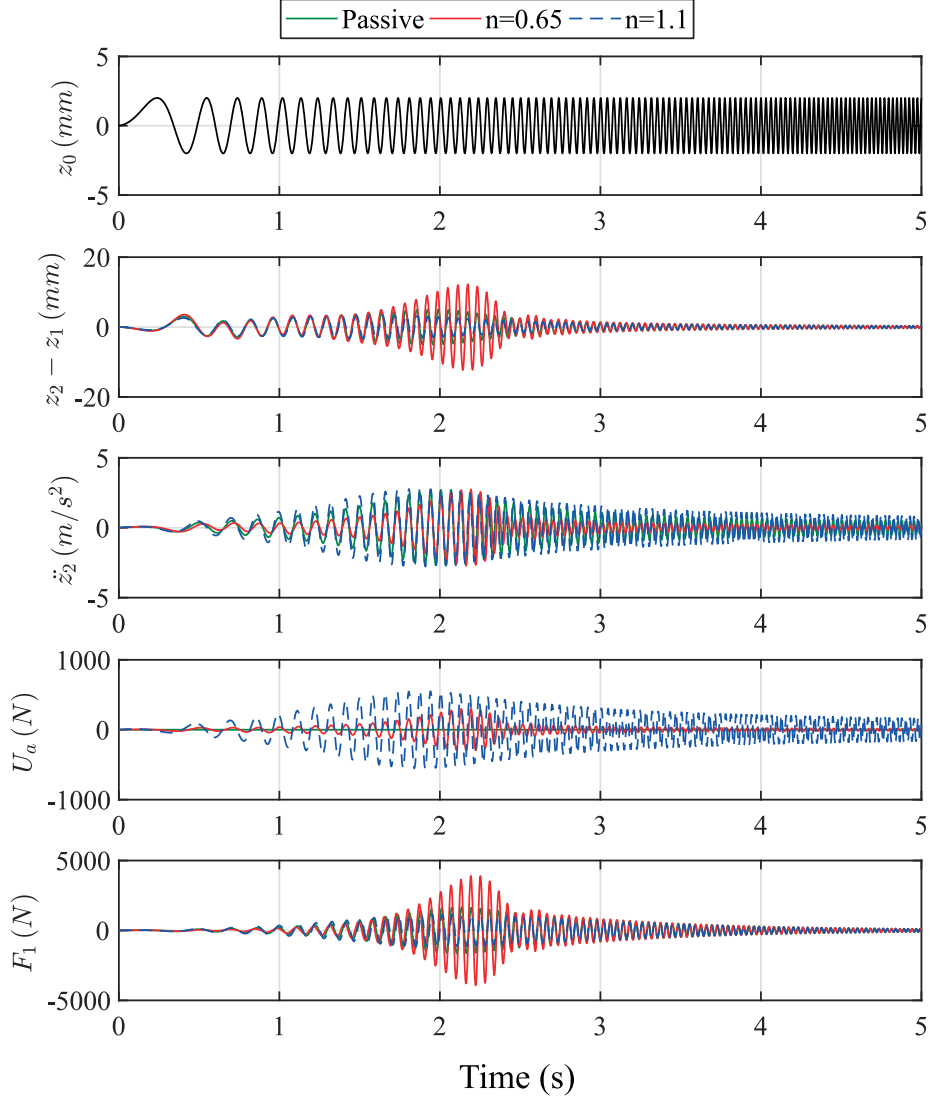


Figure 2.36. Simulation results of fractional damping control compared to passive system with sinus road disturbances of frequency 0.1 to 40Hz of amplitude 2mm.

The results of the second scenario are plotted in Figure 2.36. Here, we increase the amplitude of the sinusoidal profile to 2mm. This test is generally done to test the road-holding performance of control design. Although of high vertical accelerations, the road-holding oriented FO damping controller was able to reduce the suspension deflection amplitudes compared to passive and comfort-oriented systems. This behavior reflects an enhancement in

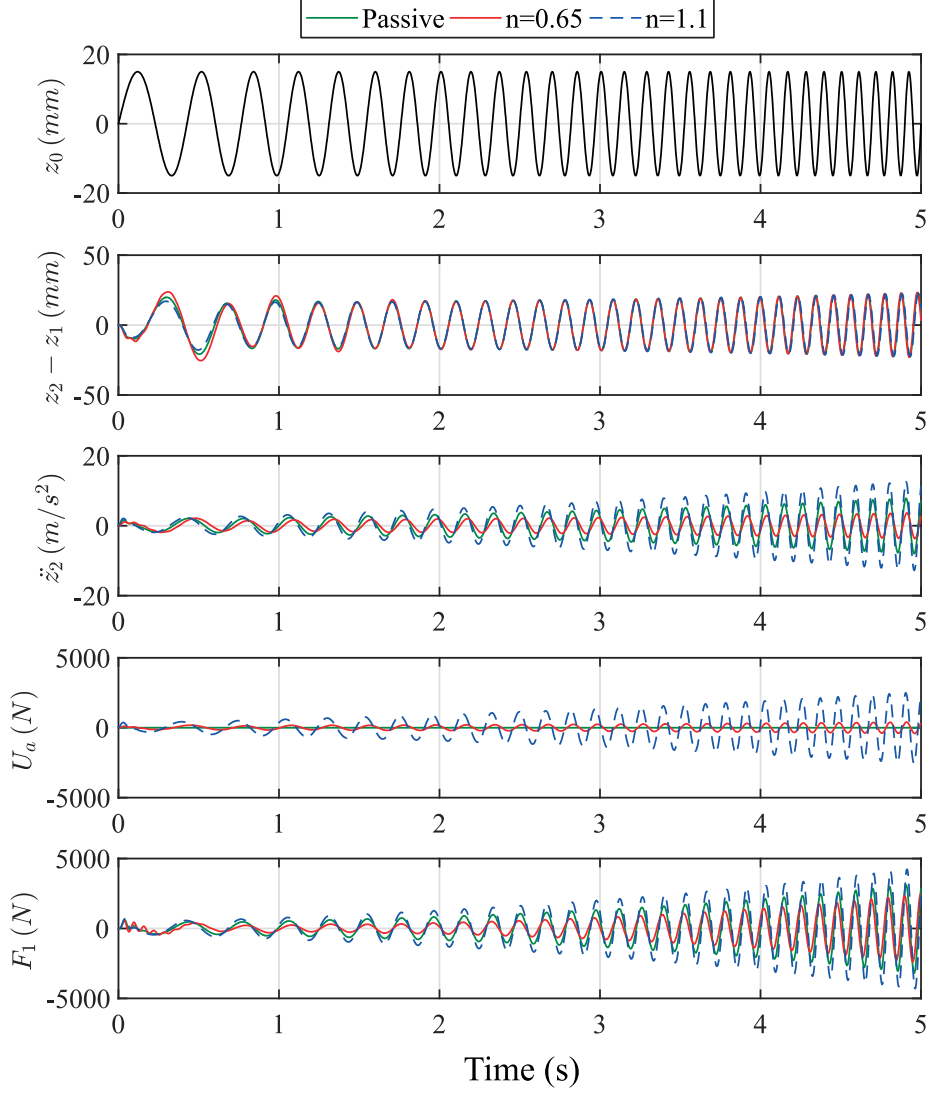


Figure 2.37. Simulation results of fractional damping control compared to passive system with sinus road disturbances of frequency 0.1 to 5.5Hz of amplitude 15mm.

terms of road-holding of the vehicle. Moreover, for $n=1.1$, the system has lower wheel deflections that are an important indication for good handling.

In the third scenario, the sinusoidal profile is now swept between 0.1 to 5.5Hz with an amplitude of 15mm. This scenario is done to examine the comfort performances of a given designed controller. Figure 2.37 shows the results on the dynamics of different variables. At first, the three systems

show approximately the same behavior in terms of suspension deflection. However, the comfort-oriented controller shows a significant attenuation for vertical accelerations compared to passive and road-holding oriented controlled systems. At the same time, the FO damping control of order $n=0.65$ needs lower control efforts. It is worthwhile to mention that in this range of frequencies, the comfort-oriented controller has a better performance of handling compared to other systems where it has a lower variation in wheel deflections as well.

2.4.6 Conclusion

In order to examine the benefits of fractional damping control in rejecting road disturbances, two fractional orders are chosen. According to an optimized strategy, two values have resulted in a specific parametric configuration. The study resulted in two control strategies: a comfort-oriented and a road-holding oriented system. Each control system is related to one value of the fractional-order damping control.

It was shown, in frequency and time-domain simulations, the effectiveness of the comfort-oriented controller in improving comfort performance while it reduces the vertical accelerations versus different ranges of amplitude and frequencies of road disturbances. It proves its ability to isolated vibrations as well compared to other systems, especially the passive systems.

On the other hand, the road-holding FO damping control proves its ability to minimize the variation of suspension deflection against road disturbances compared to the passive systems, and thus, fulfilling the road-holding criterion.

The practical use of these control designs is then to integrates them among other control strategies to improve, for example, braking performance, cornering, lateral stability, etc. These studies will be presented in detail in the next chapters.

2.5 Conclusion

This chapter addresses two main objectives of the active suspension system of an electric vehicle. Using the CRONE CSD methodology, fractional damping control is implemented in two manners: a comfort-oriented

controller and a road-holding oriented controller. The proposed control law could achieve adequate performance in rejecting road disturbances. The experimental results reveal that the presented strategy could provide an important performance as far as a consistent damping non-integer order control is selected. For this purpose, an optimization methodology is adopted for finding the optimized value of the fractional-order of damping control. Hence, the presented method could effectively enhance ride comfort, together with the road-holding and handling of the vehicle.

Moreover, a 2nd generation CRONE control is developed for the control of the vehicle's active suspension system for chassis' height regulation. It was clearly demonstrated that the closed-loop system performance is pretty good enough in varying the car-body mass. The CRONE designs feature significant robustness versus vehicle's parametric variations. This control law is able to vary the height of the chassis successfully for facilitates the exit and entry process to the vehicle. In addition, it could be used for safe manner for reducing the impact of side accidents on the vehicle by elevating the side of impact before the car collision

Chapter 3

Hierarchical Approach for Driver Disturbance Rejection

Contents

3.1	Introduction.....	99
3.2	Hierarchical Approach.....	102
3.3	Vehicle model	105
3.4	Control system design.....	111
3.5	Study requirements	126
3.6	Frequency-domain analysis	134
3.7	Time-domain analysis	138
3.8	Conclusion	149

3.1 Introduction

Road transportation is shifting significantly toward electrification around the globe. The potential to reduce energy consumption and greenhouse emissions are the most important driver for electric mobility. Besides the growing awareness of environmental and population pressures, the innovations market acceptance (Li et al., 2019) and government support (ERTRAC et al., 2017)(European Commission, 2017) results in the advancement of Electric Vehicle (EV) technology. This technology starts to challenge its internal combustion counterparts with large-scale investments and highly coordinated research and development (Ahmad et al., 2018). It becomes essential for meeting the goals of decarbonization and energy security (Paris agreement at COP21 2015 – C40 Committee (COP21, 2015), Madrid COP 25 (Sustainable Innovation Forum, 2019)). Some countries have already made a bold announcement regarding the electrification of mobility that opts to ban diesel vehicles from their cities' center by the next decades (Pereirinha et al., 2018).

Consequently, automobile manufacturers are in the process of launching EVs and a market for electric mobility solutions had been emerged where all-in-wheel devices are expected to play an important role in this new trend. Such vehicles are able to adapt to urban lifestyles, mainly, to contribute to the air quality and noise reduction in urban cities. Since a lighter vehicle means a sharp reduction in energy consumption, a modern solution can contain integrated powertrain suspension located directly inside the wheel. One example of such technology, adopted in this work, is the Active Wheel (AW) developed by Michelin (Fig. 3.1). This advanced technology initiates a new era in road transportation where all essential components have been integrated within the wheel itself: the pneumatic part, a compact traction electric motor with regenerative braking, an electric active suspension system, and the braking system.

The structure of the Active Wheel offers new opportunities in Global Chassis Control (GCC) that rises, recently, to remarkable levels. GCC is the design of cooperative control between the different mechatronic subsystems to enhance vehicle performance, generally: safety, stability, and comfort. While, for example, the (Anti-lock Braking System) ABS optimizes the

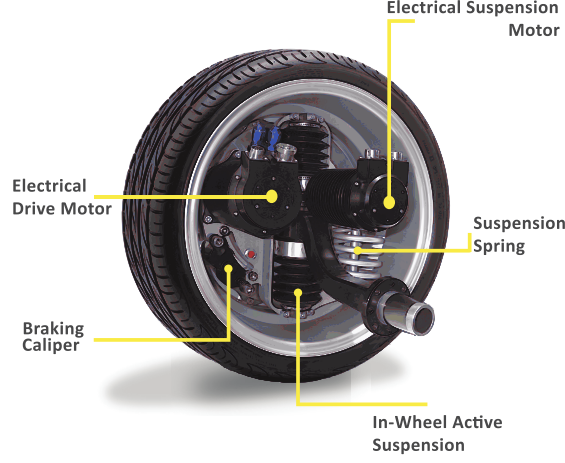


Figure 3.1. Active wheel from Michelin.

braking distance (Benine-Neto et al., 2017; Reif, 2014), (Electronic Stability Program) ESP stabilizes the vehicle along the desired trajectory (Rajamani, 2012b), engine control optimizes both traction torque and emissions (Morand et al., 2013; Rajamani, 2012c), the active suspension systems had proved their ability to control the vertical dynamics of the vehicle in the sense of improving ride quality. Indeed, they can ease the inherent tradeoff in passive systems between comfort and road holding by the integration of actuators between the chassis and wheel mass (Hrovat, 1997; Karnopp, 1983). Although of the high energy consumption of these systems in real applications compared to passive and semi-active systems, it was found that the potential to develop a vibration energy recovery system could achieve an energy balance requirement (Wang et al., 2013). Moreover, the recoverable energy-dependent not only on the driving and road conditions but also on the type of control algorithms (Huang et al., 2011). This fact drives the academic and industrial stakeholders to investigate also control concepts.

In congruence with the global trend and due to its compatibility with the long pursued full electric vehicle, considerable attempts have been done in the past few decades on the development of the control algorithms of active suspension systems (Tseng and Hrovat, 2015). Starting from PID (Li et al., 2018) and intelligent PD controllers (Haddar et al., 2019), to linear Quadratic Regulators LQR (Wu, 2017), and finite-time output feedback controller (Pan and Sun, 2019). However, robust controllers have been also proved their effectiveness to fulfill the suspension control objectives, like H_∞ controllers (Akbari and Lohmann, 2010; Jing et al., 2019; Yu et al., 2018), fuzzy

H_∞ (Li et al., 2012), particularly, for in-wheel motors in electric vehicles (Shao et al., 2019). In addition, nonlinear controllers are also applied in this context, such as backstepping controllers (Lin and Kanellakopoulos, 1997; Sun et al., 2016), adaptive backstepping (Sun et al., 2013), sliding mode controller (Chamseddine et al., 2006; Li et al., 2013), model-free fractional-order sliding mode control (Wang et al., 2018), model predictive controllers (Gohrle et al., 2014), and fuzzy control with wheelbase preview (Zhao et al., 2019).

In this chapter, a hierarchical control strategy, based on two-level controllers (global and local), is proposed for the active suspension system embedded in the AW, where the conventional mechanical suspension has been replaced by a passive spring and a DC electrical motor. In comparison with other force-generating actuators (hydraulic, Hydractive, hydro-pneumatic...), the DC linear characteristics of the AW's suspension system provides an extremely fast response time, low contact friction, high precision and efficiency, good controllability, and less energy consumption (Nguyen et al., 2011). This approach is, in fact, a global solution for the 2nd objective listed in the introduction in the frame of vertical dynamic control of the light electric vehicle. Recalling the main objectives: (1) regulating the height of the center of gravity of the vehicle; (2) holding chassis under driver solicitations; (3) holding chassis against road disturbances; (4) obtain tolerable vibration isolation under road perturbations; finally (5) holding the unsprung mass against road disturbances by reducing the variation of the wheel deflection to enhance vehicle handling.

The present study focuses particularly on the second objective, and then evaluates the ability of the designed controller on satisfying objective (3) and (4). Accordingly, the proposed strategy assumes that the vehicle operates in the “*comfort*” region which represents the majority of the time of use of the vehicle, especially in urban cities, in which the chassis accelerations are within 0.4g. Then, a comfort-oriented approach has been developed using a robust non-integer order controller, namely, the CRONE controller (Sabatier et al., 2015a), to examine the relevant benefits of the fractional-order techniques in the context of suspension control.

We aim from this method to obtain the maximum possible improvement of ride comfort while respecting the road holding and handling criteria. Generally, the ride quality is influenced by two main sets of disturbances. One is caused by the driver upon braking, accelerating, maneuvering, and wind gusts, for example. The other one is the ground input disturbances caused by road roughness that could be classified as shocks (bumps, ...) or vibrations. In fact, improving the performance of such a system can decrease the number of traffic fatalities by preventing physical fatigue of the driver as well as positively influence the driver's subjective impression of the vehicle (Koch and Kloiber, 2014). Furthermore, in line with the innovative advancement in autonomous vehicles, a comfort driving style is highly demanded to overcome motion sickness (Ekchian et al., 2016).

Different test simulations were done to evaluate the performance and robustness of the proposed control approach on a realistic driving scenario using a full nonlinear 14DOF vehicle model. Usually, the strategies implemented to deal with the second objective assumes that the road is perfectly even, which is not the case in reality. Therefore, the simulations will examine the effectiveness of the hierarchical approach in compensating chassis dynamics under driver disturbances, and additionally inspect the ability of the comfort-oriented local controller to reject road disturbances. Evaluations were done using International Standardization (ISO) and well-known indexes regularly used in the context of suspension performance.

3.2 Hierarchical Approach

As mentioned in the general introduction, Advanced Driver-Assistance Systems (ADAS) are implemented nowadays in nearly most of the newly manufactured vehicles (e.g. ABS, ESP, Adaptive Cruise Control (ACC), ...). These systems were designed to operate individually to fulfill its own goal, however, some of these systems are directly or indirectly may affect each other's performance due to the complex coupling between the various vehicle dynamics. Therefore, the absence of any coordination between the actuators may lead to degrading the overall performance of the vehicle regarding handling and safety.

In the frame of GCC, there exists three main architecture in the literature, namely, the centralized control, decentralized control, and control by

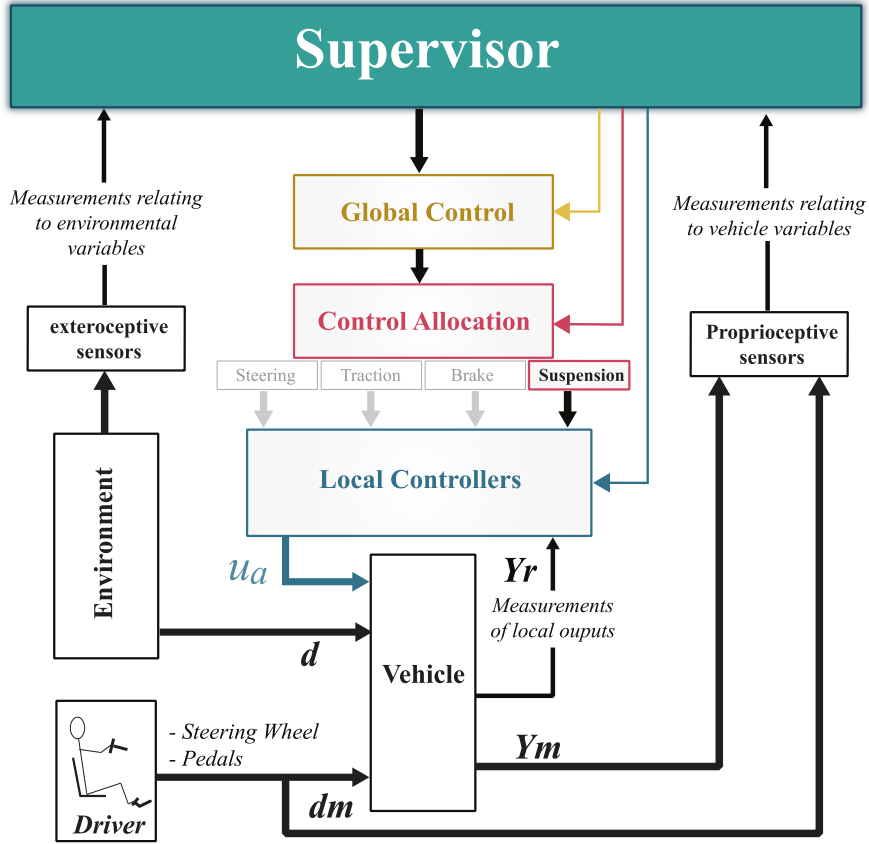


Figure 3.2. Block Diagram of Global Chassis Control.

supervision (Gordon et al., 2003). This study adopts a supervision control strategy, that represents an intermediate structure between the other two ones, by a proposed hierarchical approach for vertical dynamic control of a light electric vehicle. Figure 3.2 illustrates the main four levels of the proposed strategy: Supervisor, Global Control, Control allocation, and Local Control. The supervisor represents the highest level of this hierarchical approach. It receives all available measurements coming from the vehicle itself (sensors, pedals, ...), environment (exteroceptive sensors, camera, LiDAR, ...), and information that could be provided by road infrastructure or by other vehicles (like in autonomous vehicles). All these data are used in the perception of the environment, observation, path planning, motion generation, and last but not least, diagnosis.

One main role of the supervisor is to estimate the domain in which the vehicle is operating. Using the observed or measured values of the lateral (a_y) and longitudinal (a_x) accelerations (Regolin et al., 2019), as well as the

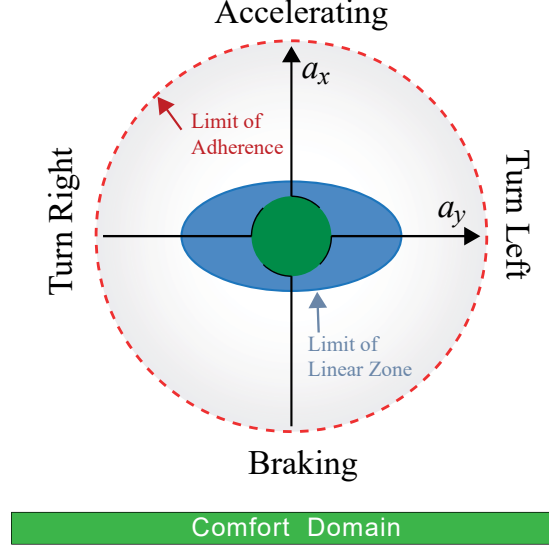


Figure 3.3. Comfort operating domain of a vehicle.

vertical acceleration (a_z), the supervisor thoughtfully allocates the control efforts and references of all active systems. Figure 3.3 illustrates, in an (a_x, a_y) diagram, the main three range of operations. The first one in green, the comfort region, where it is defined by low longitudinal and lateral accelerations that are less than $0.4g$ in absolute value. In this zone, the vertical dynamics of the vehicle has no significant influence on the other dynamics, assuming driving on dry and good roads. The second region (blue), represents the limits of the linear zone of tire model (Pacejka, 2012), and here the suspension system starts to influence the lateral dynamics so that comfort – road holding dilemma should be managed using adapted control strategy. Finally, the active security region (red), which represents the nonlinear zone of the tires where safety is then the priority.

Previously, the hierarchical approach has been introduced and tested in braking phases (Hamrouni et al., 2018), and cornering driving scenarios at moderate constant speeds (Bouvin et al., 2018; Termous et al., 2018a). This study extends the application to control the three main chassis dynamics to compensate for the heave, pitch, and roll motion simultaneously by a global controller. Moreover, the study adopted the 2DOF quarter vehicle model that includes both the sprung and unsprung mass modes, controlled by a local controller, in order to investigate the level of disturbance rejection of road unevenness and vibration isolation. The hierarchical approach is then stated as a validated approach for certain road structures and classes.

3.3 Vehicle model

3.3.1 Validation Model

The simulations for strategy validation are done using a full non-linear car model with 14 degrees of freedom, widely studied in the literature, taking into consideration most of the nonlinearities existing in the vehicle dynamics (Ahmadian and Blanchard, 2007; Connair et al., 1999; Giangiulio, 2006).

3.3.2 Synthesis model

Two main models are synthesized, the first one is related to chassis dynamics for the global controller, and the second one is the quarter vehicle model for the local controllers. Considering the proposed domain of operation (comfort-zone), a simplified model can be used where neglecting some nonlinearities, while taking into account the main fundamental laws of dynamics. The following two subsections describe the synthesis model used for each control design.

3.3.2.1 Chassis Model

Regarding the synthesis model of the chassis of the vehicle, two planes are introduced. The First plane P_1 , is the one that passes through the center of the four unsprung masses (wheels), where the second plane P_0 is the one that passes throughout the four points of contact between the wheel and the road. Thus, in addition to the reference related to the car-body, two references are introduced relative to the unsuspended masses and to the road, R_1 and R_0 , respectively.

Figure 3.4 illustrates the definition of the three planes/references related to the vertical dynamics of the synthesis model. However, for the range of interest of frequency 0 - 5Hz, comfort zone (low frequencies), the three DoF related to heave, pitch, and roll dynamics of the plane P_0 is assumed transferred completely to the plane P_1 . Therefore:

$$v_{z1}(t) = v_{z0}(t), \omega_{\varphi1}(t) = \omega_{\varphi0}(t), \text{ and } \omega_{\theta1}(t) = \omega_{\theta0}(t) \quad (3.1)$$

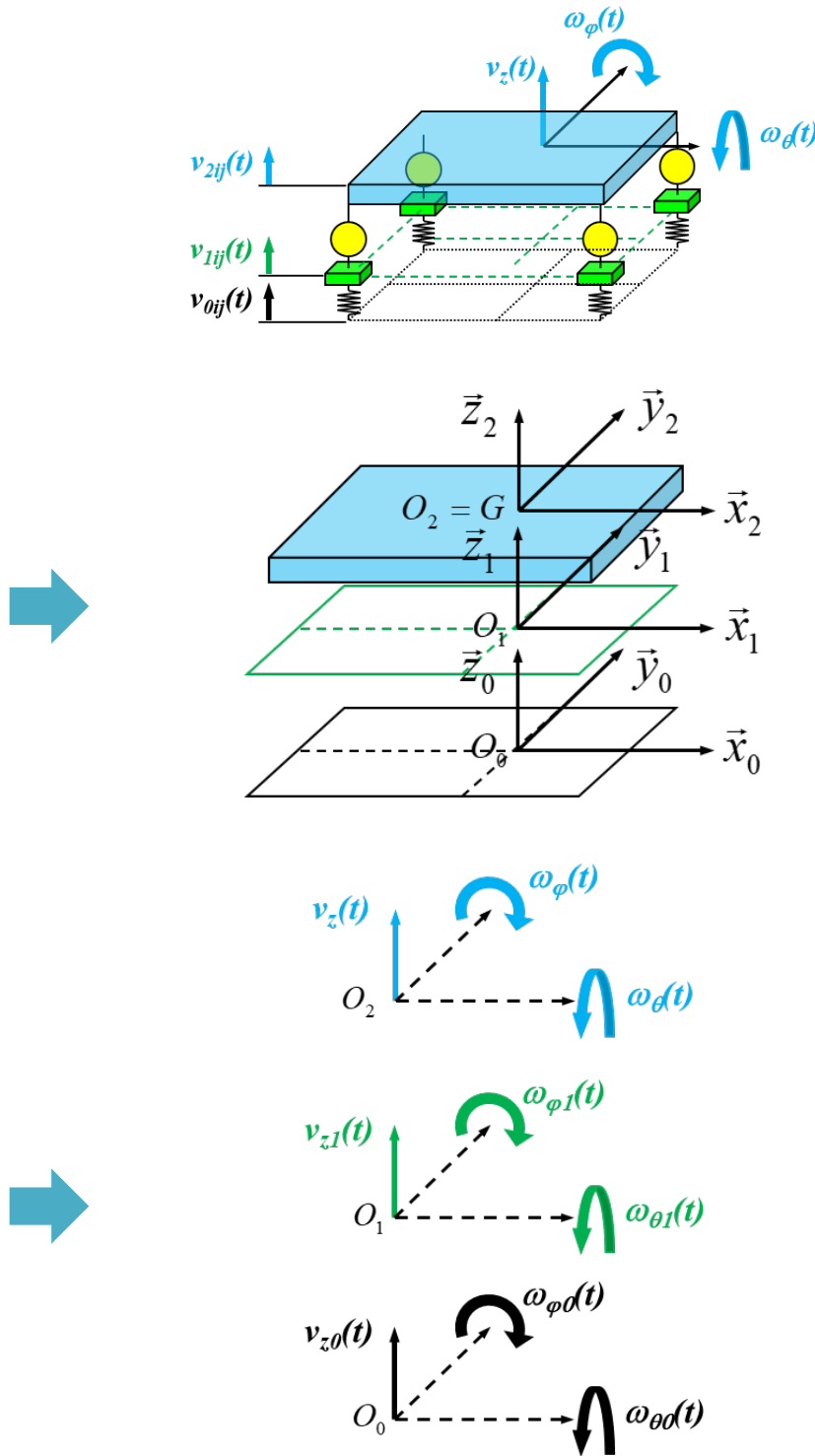


Figure 3.4. Description of the vertical dynamics for obtaining a model for analysis and synthesis.

3.3 Vehicle model

Generally, for the car-body, the application of the fundamental law of dynamics leads to the following three equations of motion:

$$v_z(t) = \frac{1}{M_2} \int_0^t f_{\Sigma z}(\tau) d\tau + v_z(0), \quad (3.2)$$

$$\omega_\varphi(t) = \frac{1}{I_{yy}} \int_0^t C_{\Sigma\varphi}(\tau) d\tau + \omega_\varphi(0), \quad (3.3)$$

$$\omega_\theta(t) = \frac{1}{I_{xx}} \int_0^t C_{\Sigma\theta}(\tau) d\tau + \omega_\theta(0). \quad (3.4)$$

The three variables $v_z(t)$, $\omega_\varphi(t)$, and $\omega_\theta(t)$ represent the velocity of heave displacement of the center of gravity, the angular pitch rate about the y-axis, and the angular roll rate about the x-axis, respectively. The term $f_{\Sigma z}(\tau)$ (N) represents the summation of all forces applied in the vertical direction on the chassis, that is:

$$f_{\Sigma z}(\tau) = \sum_{i=1, j=1}^2 f_{sij}(\tau) + u_z(\tau), \quad (3.5)$$

where,

$$f_{sij}(\tau) = f_{sp,ij}(\tau) + f_{0,ij}(\tau), \quad (3.6)$$

with $f_{sp,ij}(\tau)$ and $f_{0,ij}(\tau)$ represent the passive suspension forces and the load transfer forces at each corner respectively. The term $u_z(\tau)$ is the desired force for heave velocity ($V_z(s)$) regulation, such that:

$$U_z(s) = -C_z(s) V_z(s), \quad (3.7)$$

where $C_z(s)$ represents the transfer function of the heave global controller. $C_{\Sigma\varphi}(\tau)$ (N.m) is the algebraic sum of all external torques applied around the y-axis, and is defined as:

$$\begin{aligned} C_{\Sigma\varphi}(t) &= c_{0\varphi}(t) + c_{s\varphi}(t) + u_\varphi(t) \\ &= f(h_\varphi, M_2, a_x, \dots) + c_{s\varphi}(t) + u_\varphi(t), \end{aligned} \quad (3.8)$$

3.3 Vehicle model

with $c_{0\varphi}(t)$ being the pitch torque induced due to braking, accelerating, etc..., $c_{s\varphi}(t)$ represents the vehicle passive anti-pitch torque, and $u_{\varphi}(t)$ is the active anti-pitch torque provided by the active suspension control efforts, and defined by:

$$u_{\varphi}(t) = u_{FF,\varphi}(t) + u_{FB,\varphi}(t), \quad (3.9)$$

where $u_{FF,\varphi}(t)$ is the feed-forward torque and the $u_{FB,\varphi}(t)$ is the feedback torque that regulates the pitch rate $\Omega_{\varphi}(s)$ using $C_{\varphi}(s)$ transfer function, such that:

$$U_{FB,\varphi}(s) = -C_{\varphi}(s)\Omega_{\varphi}(s). \quad (3.10)$$

Similarly, $C_{\Sigma\theta}(t)$ (N. m) is the algebraic sum of all external torques applied around the x-axis, and is defined as:

$$\begin{aligned} C_{\Sigma\theta}(t) &= c_{0\theta}(t) + c_{s\theta}(t) + u_{\theta}(t) \\ &= f(h_{\theta}, M_2, a_y, \dots) + c_{s\theta}(t) + u_{\theta}(t), \end{aligned} \quad (3.11)$$

with $c_{0\theta}(t)$ being the rolling torque induced due to maneuvering, $c_{s\theta}(t)$ represents the vehicle passive anti-roll torque, and $u_{\theta}(t)$ is the active anti-roll torque provided by the active suspension control efforts, and defined by:

$$u_{\theta}(t) = u_{FF,\theta}(t) + u_{FB,\theta}(t), \quad (3.12)$$

where $u_{FF,\theta}(t)$ is the feed-forward torque and the $u_{FB,\theta}(t)$ is the feedback torque that regulates the roll rate $\Omega_{\theta}(s)$ using $C_{\theta}(s)$ transfer function, such that:

$$U_{FB,\theta}(s) = -C_{\theta}(s)\Omega_{\theta}(s) \quad (3.13)$$

The feedforward control efforts are estimated based on the following two formulas:

$$u_{FF,\varphi}(t) = -h_{\varphi} M_2 \lambda_{\varphi} \tilde{x}_{p\varphi}(t), \quad (3.14)$$

$$u_{FF,\theta}(t) = -h_{\theta} M_2 \lambda_{\theta} \tilde{x}_{p\theta}(t), \quad (3.15)$$

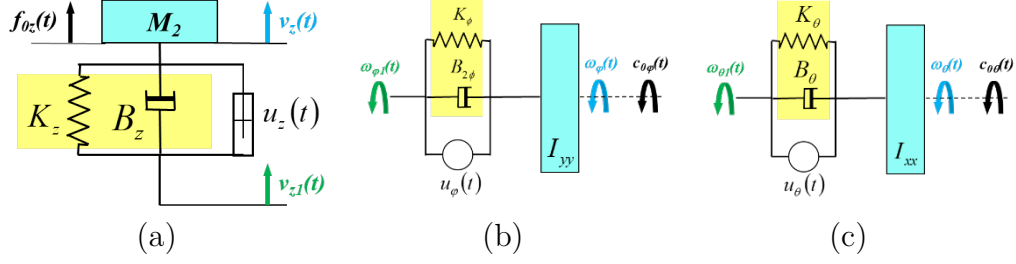


Figure 3.5. Simplified schematics illustrating the car body dynamics: (a) Heave, (b) pitch, and (c) roll motions.

where $\tilde{x}_{p\varphi}(t)$ and $\tilde{x}_{p\theta}(t)$ are the measured displacement of traction/braking pedal and driver steering angle, respectively. The constant values of λ_φ and λ_θ depend on the braking and traction system response, steering system behavior, vehicle geometry, and inertial parameters. The main objective of these feedforward torques is to oppose the driver disturbances, thus, provide fast compensation for chassis dynamics.

Figure 3.5 shows a simplified schematic that illustrate the car body dynamics. In fact, this modeling is used for analysis and control synthesis, where its range of validity is defined by two main assumptions: the frequency range is limited to $[0 \ 5]\text{Hz}$, i.e. the study of low frequency comfort, and the inertia matrix of the body is assumed diagonal, in which the three axes of heave, pitch, and roll are passing through the center of gravity of the chassis.

Accordingly, passive anti-torques and forces can be extracted as follows:

$$F_{sz}(s) = - \left(\frac{k_z}{s} + b_z \right) (V_z(s) - V_{z1}(s)), \quad (3.16)$$

$$C_{s\varphi}(s) = - \left(\frac{k_\varphi}{s} + b_\varphi \right) (\Omega_\varphi(s) - \Omega_{\varphi1}(s)), \quad (3.17)$$

$$C_{s\theta}(s) = - \left(\frac{k_\theta}{s} + b_\theta \right) (\Omega_\theta(s) - \Omega_{\theta1}(s)). \quad (3.18)$$

At equilibrium, with zero initial conditions, three transfer functions can be deduced using (3.2 – 3.4) and (3.16 – 3.18) representing the global chassis dynamics, and are formulated as follows:

$$G_z(s) = \frac{V_z(s)}{U_z(s)} = \frac{s}{M_2 s^2 + b_z s + k_z}, \quad (3.19)$$

$$G_\varphi(s) = \frac{\Omega_\varphi(s)}{U_\varphi(s)} = \frac{s}{I_{yy} s^2 + b_\varphi s + k_\varphi}, \quad (3.20)$$

$$G_\theta(s) = \frac{\Omega_\theta(s)}{U_\theta(s)} = \frac{s}{I_{xx} s^2 + b_\theta s + k_\theta}. \quad (3.21)$$

3.3.2.2 Quarter vehicle model

The vehicle suspension system is modeled using the well-known quarter-model that exists in the literature (Jazar, 2014; Savaresi et al., 2010). Here, the four wheels are assumed decoupled and the suspension dynamics are considered in the frequency range of interest for the vertical dynamics [0 – 30 Hz]. The suspension configuration of the AW is considered as a high bandwidth active suspension system due to the presence of the force generating actuator mounted parallel to the passive spring-damper components (Sun et al., 2015). Assuming that the actuator is ideal, the vertical motion of this system is described by the same equations presented in section 2.2.

At this level, four local regulators are implemented, one for each quarter vehicle. However, due to the geometrical symmetry of the chassis about the x-axis, one controller is designed for every axle. According to the proposed strategy, the objective of each local controller is assigned to regulate the vertical displacement of the chassis $z_{2,ij}(t)$. Denote by $G_i(s)$ the transfer function of the controlled plant, $K_i(s)$ the transfer function of the designed local controller, and the control command law $U_{ij}(s)$ the feedback control input, then:

$$U_{ij}(s) = -K_i(s) \tilde{Z}_{2,ij}(s), \quad (3.22)$$

where $\tilde{Z}_{2,ij}(s)$ is the measured value of the vertical displacement of sprung mass at each corner. Then considering the synthesis model $G_i(s)$ is formulated as:

$$G_i(s) = \frac{Z_{2,ij}(s)}{U_{ij}(s)} = \frac{m_1 s^2 + b_1 s + k_1}{Den_i(s)}, \quad (3.23)$$

where,

$$\begin{aligned}
Den_i(s) = & m_1 m_{2i} s^4 + k_{1i} k_{2i} \\
& + (m_{2i}(b_1 + b_{2i}) + m_1 b_{2i}) s^3 \\
& + (m_{2i}(k_{1i} + k_{2i}) + m_1 k_{2i}) s^2 \\
& + b_1 b_{2i} s^2 + (k_{1i} b_{2i} + b_1 k_{2i}) s.
\end{aligned} \tag{3.24}$$

3.4 Control system design

3.4.1 CRONE control approach

The CRONE (the French acronym for *Commande Robuste d'Ordre Non-Entier*, which means fractional-order robust control) design methodology is a frequency domain approach that has been developed since the 1980s (Oustaloup, 1991a; Sabatier et al., 2015a). It is based on the common unity-feedback configurations where three CRONE control generations have been developed. In these three methods, the open-loop transfer function is defined using fractional order integro-differentiation. One major advantage of the CRONE controller is that the plant uncertainties are taken into account. A direct consequence of these uncertainties is the variation of the stability degree of the controlled system, in other words, the variation of the phase margin of the closed-loop systems, namely, M_ϕ . This implies a different performance of the plant for each set of parameters.

The selection of the CRONE generation depends on the degree of variations of gain or/and phase of the plant due to parametric uncertainties at the desired open-loop gain crossover frequency ω_c (Lanusse et al., 2013). In this contribution, the first-generation CRONE controller is used for both global and local controllers.

3.4.2 Optimization approach of control parameters' selection

The CRONE controller enables the parameterization of the open-loop transfer function with a small number of high-level parameters. Then, the optimization is thus reduced to only the search for the optimal values of these parameters.

The cascade form of the first-generation CRONE controller consists of a proportional constant C_0 , a band-limited fractional-order derivative (m) within two corner frequencies ω_l and ω_h , an integer band-limited integrator of order m_I upper bounded by the frequency ω_I to manage steady-state error, and a low-pass filter of order m_f with a cutoff frequency ω_f to manage the control sensitivity level and reduce noise amplification at high frequencies. Therefore, the general transfer function is formulated as follows:

$$C(s) = C_0 \left(1 + \frac{\omega_I}{s}\right)^{m_I} \left(\frac{1 + s/\omega_l}{1 + s/\omega_h}\right)^m \frac{1}{(1 + s/\omega_f)^{m_f}}. \quad (3.25)$$

The transitional frequencies defined are calculated so that a constant phase is achieved on a frequency range $[\omega_A, \omega_B]$ which covers the frequency range where ω_c could vary due to the plant parametric variation (Sabatier et al., 2015a). Then, the fractional-order m and the gain C_0 are calculated to ensure the required nominal phase margin M_ϕ and open-loop gain cross-over frequency ω_c . In this study, particularly, it was considered that $\omega_I = \omega_l$ and $\omega_f = \omega_h$.

The selection process of the controlled parameters is based on obtaining the highest possible control performance while attaining a reasonable degree of robustness against uncertain parameters. The robustly designed controller should produce a constant open-loop phase in $[\omega_A, \omega_B]$ whose Nichols locus defined by a vertical straight line, so-called the frequency template (Figure 3.6). Ideally, this template ensures the robustness by minimizing the variations of phase margins M_ϕ , modulus margins M_r , and the resonant peaks (Q_s and Q_T) of the sensitivity and the complementary sensitivity functions $S(s)$ and $T(s)$, respectively, where:

$$S(s) = \frac{1}{(1 + \beta(s))}, \quad (3.26)$$

$$T(s) = \beta(s)/(1 + \beta(s)) \quad (3.27)$$

with $\beta(s)$ representing the open-loop transfer function such that $\beta(s) = C(s)G(s)$.

In the frequency domain, the robustness of the designed controller can be assessed by the maximum variation of phase margins ΔM_ϕ or the maximum difference of resonant peaks ($\Delta Q_{T,S}$) with plant uncertainties. On the other side, besides the value of ω_c , the performance of the controller is directly affected by the value ω_l , such that as ω_l increases the steady-state error decreases, whereas the robustness is deteriorated. Same for ω_h , whereas its value increases it provides higher robustness to the system, but it amplifies more the noise effect of the measured signals.

To deal with this tradeoff between performance and robustness, the optimization methodology is then translated to optimize the ‘length’ of the asymptotic phase behavior (or the frequency template) in the Nichols chart. Consequently, reduce the variation of M_ϕ (or ($\Delta Q_{T,S}$)) of the different plants as much as possible.

3.4.3 Performance specifications

The specifications of the global controller and the local controllers are as follows:

- For the stability degree, the resonant peak of the complementary sensitivity function is $Q_T \leq 3 \text{ dB}$ that is equivalent to $\min(M_\phi) = 40^\circ$.
- For the rapidity of the closed-loop system, the widest possible bandwidth while taking into consideration the actuator limits, noise amplification, and plant frequency response.
- For the precision at steady state, the relative error lower than 1%.
- The AW actuator control limit: $\max|u_a| \leq 4000N$.

3.4.4 Global controller design

All parameters of the three controlled plants related to chassis dynamics presented in (3.16 - 3.18) are considered uncertain. The range of uncertainty of each parameter is listed in Table 3.1. Figure 3.7 shows the plants bode responses of the extremum plants. It can be easily deduced that the plants’ variations are mostly gain-like only at high frequencies ($\omega \geq 30 \text{ rad/s}$). Therefore, in this range, the first-generation CRONE controller can be used to control the three plants.

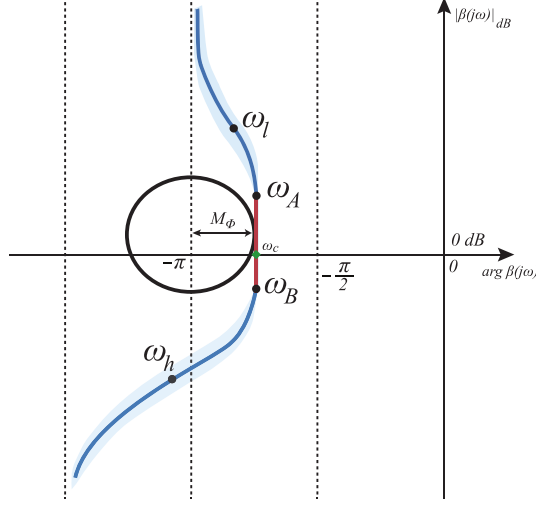


Figure 3.6. Frequency template in the open loop Nichols plot.

Table 3.1. Uncertain parameters of global transfer functions.

Parameter	Range	Unit
M_2	472–772	kg
k_z	39600–48400	N/m
k_φ	41600–48020	N/m
k_θ	19960–24400	N/m
b_θ	363–444	$N \cdot s/m$
b_φ	800–891	$N \cdot s/m$
b_z	720–880	$N \cdot s/m$
I_{xx}	225–400	$kg \cdot m^2$
I_{yy}	400–750	$kg \cdot m^2$

For control synthesis, the “*max*” plants are used as nominal plants in the design process, that is:

$$G_{z,nom}(s) = \frac{s}{772 s^2 + 880s + 48400}, \quad (3.28)$$

$$G_{\varphi,nom}(s) = \frac{s}{750 s^2 + 891s + 48020}, \quad (3.29)$$

$$G_{\theta,nom}(s) = \frac{s}{400 s^2 + 444s + 24400}. \quad (3.30)$$

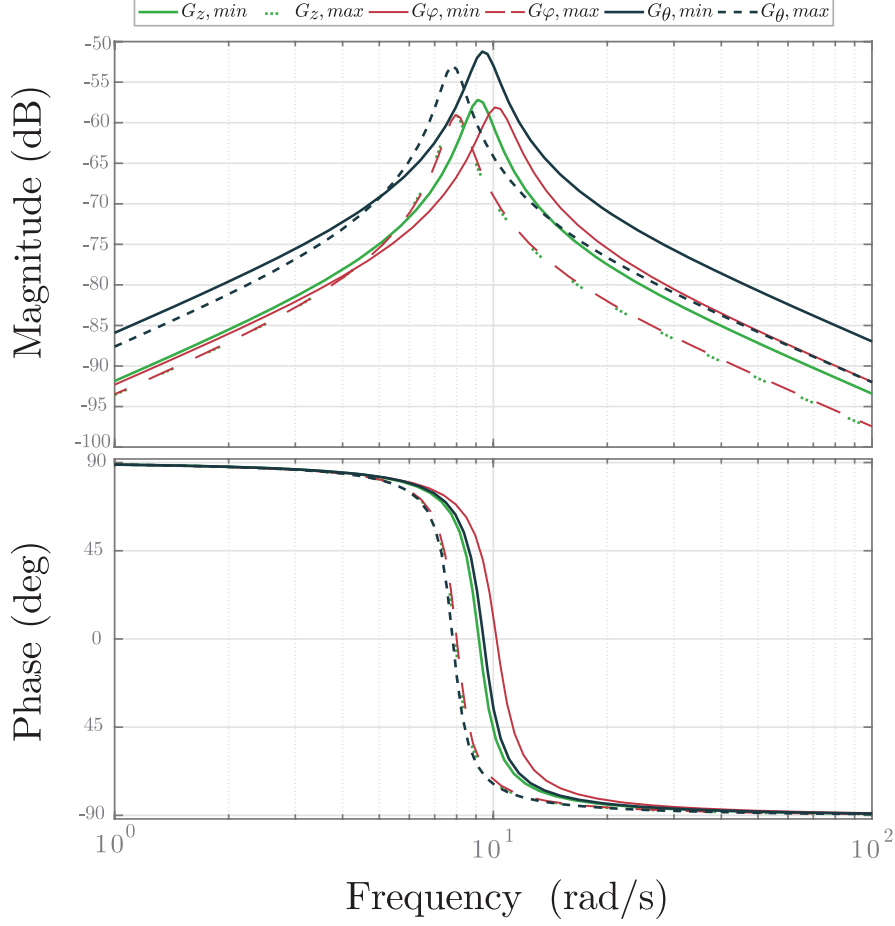


Figure 3.7. Bode responses of global plants' transfer functions.

The open-loop transfer functions for the three systems are defined as follows:

$$\begin{aligned}\beta_z(s) &= C_z(s)G_{z,nom}(s), \\ \beta_\varphi(s) &= C_\varphi(s)G_{\varphi,nom}(s), \\ \beta_\theta(s) &= C_\theta(s)G_{\theta,nom}(s).\end{aligned}\tag{3.31}$$

According to (Sabatier et al., 2015a), the control algorithm starts at the selection of the desired crossover frequencies of the open-loop transfer functions, namely, $\omega_{z,c}$, $\omega_{\varphi,c}$, and $\omega_{\theta,c}$. Respecting the aforementioned specifications, the upper limits of crossover frequencies are indicated taking into account the active wheel suspension actuator limit in addition to the noise measurement specifications, that is:

- Control input related to measurement noise is less than **10%**.
- The noise level for heave motion is $\max(N_z) \leq 2cm/s$, and for pitch and roll motion $\max(N_\varphi, N_\theta) \leq 1.5^\circ/s$.

To translate these specifications to the frequency domain criterion, the following input sensitivity function $CS(s)$ is considered, where:

$$CS(s) = C(s)/(1 + \beta(s)). \quad (3.32)$$

The magnitude $|CS(j\omega)|$ is computed using the following:

$$|CS_z(j\omega)| = \left| \frac{U_{z,FB}(j\omega)}{N_z(j\omega)} \right| \leq \left| \frac{10\% \times (4 \times 4000)}{0.02} \right| = 80e3 N.s/m, \quad (3.33)$$

and

$$\begin{aligned} |CS_\varphi(j\omega)| &= |CS_\theta(j\omega)| = \left| \frac{U_{\varphi,FB}(j\omega)}{N_\varphi(j\omega)} \right| \\ &\leq \left| \frac{10\% \times (4 \times 4000)}{1.5 \times \pi/180} \right| = 61e3 N.m.s/rad. \end{aligned} \quad (3.34)$$

Knowing that at high frequencies ω_{HF} , $|CS(j\omega_{HF})| \approx |C(j\omega_{HF})|$, and considering a proportional controller $C(s) = C_p$, then it is easy to compute the upper bound of the cross over frequency of each closed-loop system. Given that the open-loop gain at the crossover frequency ω_c is unity, that is:

$$|\beta(j\omega_c)| = |CS(j\omega_c) G(j\omega_c)| = |C_p G(j\omega_c)| = 1, \quad (3.35)$$

then,

$$C_{pz} = 80e3 \Rightarrow \omega_{z,c} \leq 105 rad/s, \quad (3.36)$$

$$C_{p\varphi} = 61e3 \Rightarrow \omega_{\varphi,c} \leq 83 rad/s, \quad (3.37)$$

$$C_{p\theta} = 61e3 \Rightarrow \omega_{\theta,c} \leq 154 rad/s. \quad (3.38)$$

To reduce complexity, one value is chosen for the three crossover frequencies satisfying (3.28 – 3.30), then $\omega_c = 80$ rad/s.

In fact, the controlled plants have very similar behavior in the frequency domain (Figure 3.7). For this reason, one control parametric configuration can be used for the three controllers, except the value of C_0 that is adapted according to the controlled plant to obtain the desired crossover frequency of each open-loop transfer function. The value of the fractional-order derivation m is chosen so that $M_\phi = 45^\circ$, where $m_l = 2$ and $m_f = 1$. Then, the first-generation CRONE control parameters are computed and the resulted fractional-order controllers are as follow:

$$C_z(s) = 357120 \times C_E(s) C_{NE}(s), \quad (3.39)$$

$$C_\varphi(s) = 347920 \times C_E(s) C_{NE}(s), \quad (3.40)$$

$$C_\theta(s) = 185200 \times C_E(s) C_{NE}(s), \quad (3.41)$$

where,

$$C_E(s) = \left(\frac{1 + s/2}{s/2} \right) (1 + s/1702)^{-1}, \quad (3.42)$$

and

$$C_{NE}(s) = \left(\frac{1 + s/2}{1 + s/1702} \right)^{-0.47}. \quad (3.43)$$

Finally, for time-domain simulations, the fractional part of the controller ($C_{NE}(s)$) should be replaced by another rational transfer function. Thanks to Oustaloup's Method (Oustaloup et al., 2000), the rational form of the controller transfer function is obtained. Using N recursive zeros and N recursive poles, the band-limited fractional-order derivation is replaced as follows:

$$\left(\frac{1 + s/2}{1 + s/1702} \right)^{-0.47} \rightarrow \prod_{N=1}^5 \left(\frac{1 + s/\omega_{ze_N}}{1 + s/\omega_{po_N}} \right), \quad (3.44)$$

where, 5, 20, 78, 304, and 1187 rad/s are the values of zeros, and 3, 10, 41, 160, and 625 rad/s are the values of poles.

Figure 3.8 shows the bode responses of the designed global controllers. Figure 3.9 shows the open-loop bode plots for the nominal plants of three

3.4 Control system design

global systems. The consistency between the three plants is expected due to the adopted design strategy in which all global controllers used to have the same cross-over frequency, stability margins, and phase behavior.

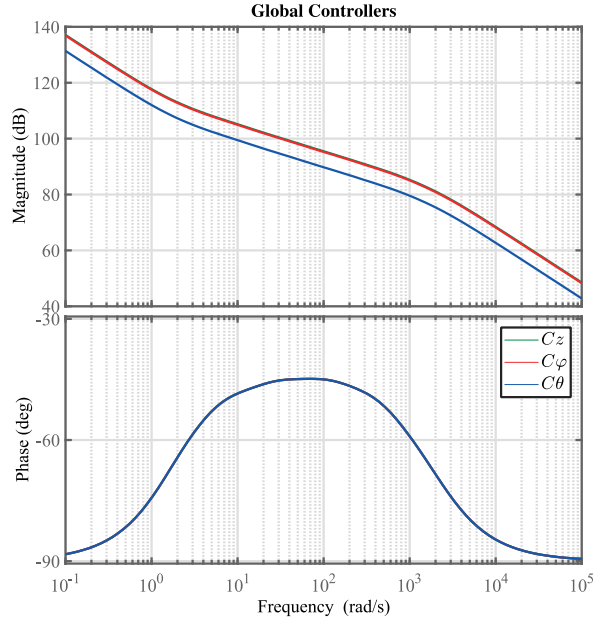


Figure 3.8. Bode responses of global controllers' transfer functions.

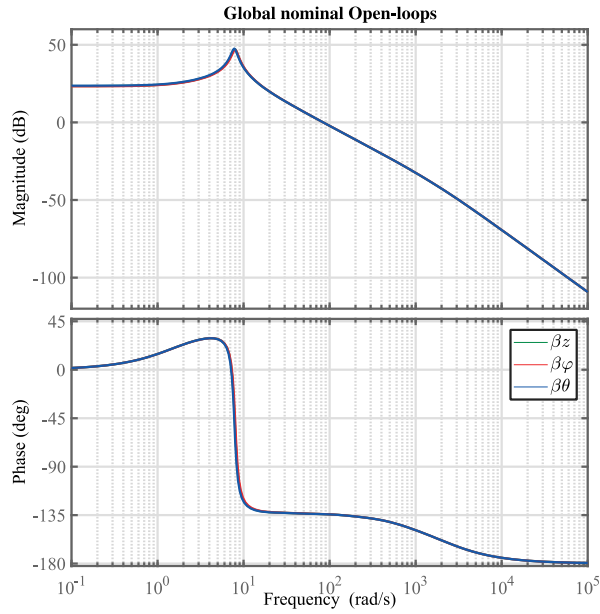


Figure 3.9. Bode responses of global nominal open-loops.

3.4.5 Local control design

In the quarter vehicle synthesis model, three main suspension parameters are considered uncertain. Table 3.2 shows the range of uncertainty of each parameter, thus, three transfer functions are defined: $G_{i,min}(s)$, $G_{i,med}(s)$, and $G_{i,max}(s)$.

Figure 3.10 shows the bode responses of the local synthesis models and the effect of the parametric uncertainties. It is clear that the uncertainty leads to higher variation for the rear local plant in comparison to the front one. Also, it is shown that both plants have an asymptotic phase behavior in the frequency range between the resonance and anti-resonance frequency. This behavior imposes a lower and upper bound for the rapidity (ω_c) of the closed-loop system.

Table 3.2. Range of variation of suspension parameters.

Parameter	Front axle (i=1)			Rear axle (i=2)		
	m_2	k_2	b_2	m_2	k_2	b_2
	[kg]	[N/m]	[N.s/m]	[kg]	[N/m]	[N.s/m]
$G_{i,min}$	168	10800	180	68	9000	180
$G_{i,med}$	193	12000	200	118	10000	200
$G_{i,max}$	218	13200	220	168	11000	220

Similar to global controller design, and considering the specifications, a first-generation CRONE controller is designed for every axle. Here, the “*med*” plants are used as nominal plants in the design process. The crossover frequencies of the open-loop transfer functions are selected, namely, $\omega_{c1} = 50 \text{ rad/s}$ and $\omega_{c2} = 40 \text{ rad/s}$, for front and rear controllers respectively, where the variation is approximately gain-like only. Taking into account the required phase margin ($M_\phi = 45^\circ$) and the value of the crossover frequencies, then the obtained control parameters for front and rear axle controllers are listed in Table 3.3.

Thus, the fractional-order local CRONE controllers are:

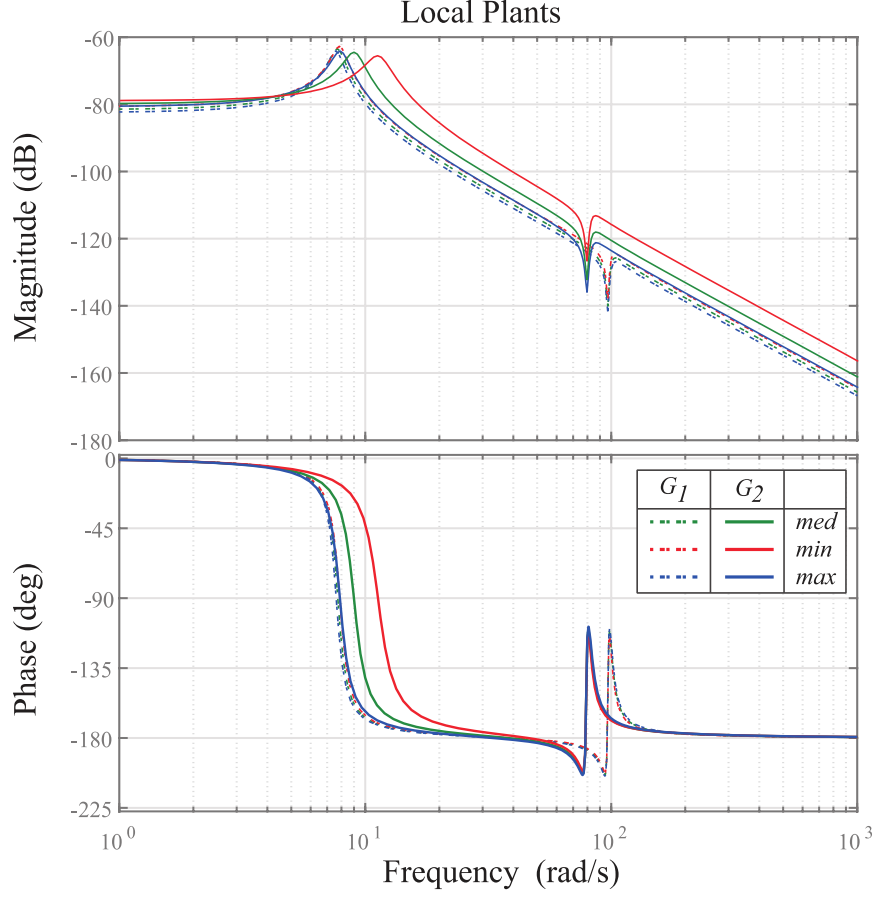


Figure 3.10. Bode responses of local plants.

$$K_1(s) = 83028 \left(1 + \frac{2.79}{s}\right) \left(\frac{1 + s/2.79}{1 + s/897}\right)^{0.62} \frac{1}{(1 + s/897)}, \quad (3.45)$$

$$K_2(s) = 33591 \left(1 + \frac{2}{s}\right) \left(\frac{1 + s/2}{1 + s/1610}\right)^{0.58} \frac{1}{(1 + s/1610)}. \quad (3.46)$$

Again, the band-limited fractional-order derivation is replaced by 5 recursive zeros and 5 recursive poles for each as follow:

$$\left(\frac{1 + s/2.79}{1 + s/897}\right)^{0.62} \rightarrow \prod_{N=1}^5 \left(\frac{1 + s/\omega_{ze_N}}{1 + s/\omega_{po_N}}\right), \quad (3.47)$$

3.4 Control system design

where the values of zeros are: 3.5, 11, 35, 110, and 352 rad/s, and the values of poles are: 7.1, 22.5, 71.5, 227, and 720 rad/s. While for the rear axle controller:

$$\left(\frac{1 + s/2}{1 + s/1610} \right)^{0.58} \rightarrow \prod_{N=1}^5 \left(\frac{1 + s/\omega_{ze_N}}{1 + s/\omega_{po_N}} \right), \quad (3.48)$$

where the values of zeros are: 2.6, 10, 38.4, 146, and 559 rad/s, and the values of poles are: 5.7, 22, 83.4, 318, and 1215 rad/s.

Figure 3.11 shows the bode response of both controllers designed and Figure 3.12 shows the open-loop bode response for the nominal plants of two axles.

Table 3.3. Control parameters of the local crone controllers.

Front Control Parameters	Value	Rear Control Parameters	Value
m_l, m_f	1	m_l, m_f	1
m	0.62	m	0.58
C_0	83028	C_0	33591
ω_l	2.79 rad/s	ω_l	2 rad/s
ω_h	897 rad/s	ω_h	1610 rad/s

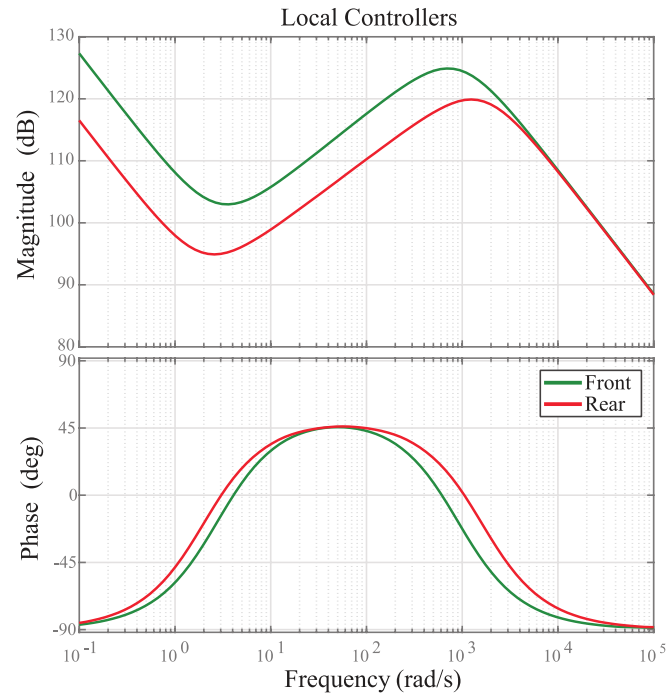


Figure 3.11. Bode response of local controllers.

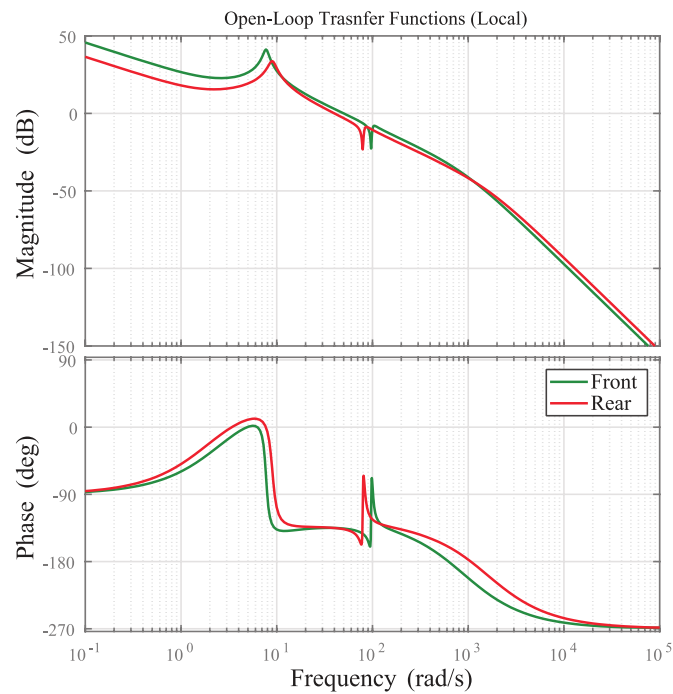


Figure 3.12. Bode response of open-loop transfer functions of local controllers.

3.4.6 Control Allocation

Once the desired global control efforts are determined, a new repartition is applied to assure the passage of the different efforts to the four suspensions. The relations that enable the transition of $u_z(t)$, $u_\varphi(t)$, and $u_\theta(s)$ to the AW actuators are described in this section.

Recalling the global objective of the hierarchical approach: to compensate chassis dynamics under driver disturbances, then the input variable references are given by:

$$v_{z_{ref}}(t) = \omega_{\varphi_{ref}}(t) = \omega_{\theta_{ref}}(t) = 0. \quad (3.49)$$

Assuming that the pitch and roll angles have small values and the chassis is infinitely rigid, the relation between the global control efforts and the four suspension forces can be formulated as follows:

$$f_{s11}(t) + f_{s12}(t) + f_{s21}(t) + f_{s22}(t) = u_z(t), \quad (3.50)$$

$$b(f_{s21}(t) + f_{s22}(t)) - a(f_{s11}(t) + f_{s12}(t)) = u_\varphi(t), \quad (3.51)$$

$$c(f_{s21}(t) - f_{s22}(t)) - c(f_{s11}(t) - f_{s12}(t)) = u_\theta(t). \quad (3.52)$$

However, in order to establish a direct relationship between the forces $f_{sij}(t)$ and the chassis dynamics, it is necessary to add a fourth relation. Therefore, the Roll Stiffness Distribution (RSD) factor $\alpha_{RSD}(t)$ (Abe, 1994) was used. This factor is important for the stability of the vehicles during maneuvers. Since the track width of the front and rear axles are equal, then α_{RSD} is given by:

$$\alpha_{RSD}(t) = \frac{c(f_{s12}(t) - f_{s11}(t))}{c(f_{s21}(t) - f_{s22}(t)) - c(f_{s11}(t) - f_{s12}(t))}. \quad (3.53)$$

Considering (3.48), then the expression of α_{RSD} is formulated as follows:

$$\alpha_{RSD}(t) u_\theta(t) = c(f_{s12}(t) - f_{s11}(t)). \quad (3.54)$$

Therefore, the relations (3.50)–(3.54) can be written under the following matrix form:

$$\begin{bmatrix} 1 & 1 & 1 & 1 \\ -a & -a & b & b \\ -c & c & c & -c \\ -c & c & 0 & 0 \end{bmatrix} \begin{pmatrix} f_{s11} \\ f_{s12} \\ f_{s21} \\ f_{s22} \end{pmatrix} = \begin{pmatrix} u_z \\ u_\varphi \\ u_\theta \\ \alpha_{RSD} \ u_\theta \end{pmatrix}. \quad (3.55)$$

Thus, using the inverse of (3.52), the desired values of the four suspensions $\bar{f}_{s,ij}(t)$ can be computed as follows:

$$\begin{pmatrix} \bar{f}_{s11} \\ \bar{f}_{s12} \\ \bar{f}_{s21} \\ \bar{f}_{s22} \end{pmatrix} = \begin{bmatrix} \frac{b}{2L} & \frac{-1}{2L} & 0 & \frac{-1}{2c} \\ \frac{b}{2L} & -\frac{1}{2L} & 0 & \frac{1}{2c} \\ \frac{a}{2L} & \frac{1}{2L} & \frac{1}{2c} & \frac{-1}{2c} \\ \frac{a}{2L} & \frac{1}{2L} & -\frac{1}{2c} & \frac{1}{2c} \end{bmatrix} \begin{pmatrix} u_z \\ u_\varphi \\ u_\theta \\ \alpha_{RSD} \ u_\theta \end{pmatrix}. \quad (3.56)$$

Finally, the overall control input of the active suspension system is then expressed by the algebraic sum of the local control efforts of local controllers ($u_{ij}(t)$), the desired force of the global controller ($\bar{f}_{s,ij}(t)$), and the estimated force of the passive suspension elements ($\hat{f}_{sp,ij}$), that is:

$$u_{a,ij}(t) = u_{ij}(t) + \bar{f}_{s,ij}(t) + \hat{f}_{sp,ij}(t) \quad (3.57)$$

Figure 3.13 illustrates the overall schematics of the hierarchical approach. Finally, the development of the proposed control algorithm requires various feedback values of the vehicle states variables, including the sprung mass displacements and the main chassis dynamics. Plenty of methods have been proposed for this purpose and experimental validation is reported in (Hashemi et al., 2017; Viehweger et al., 2020). In this study, it is assumed that all these variables can be measured or estimated accurately.

In fact, after the global references of the control efforts are perfectly known, then three strategies could be conceived while taking into consideration the technology of the used actuator that is the DC electric motor. These strategies can be listed as follows:

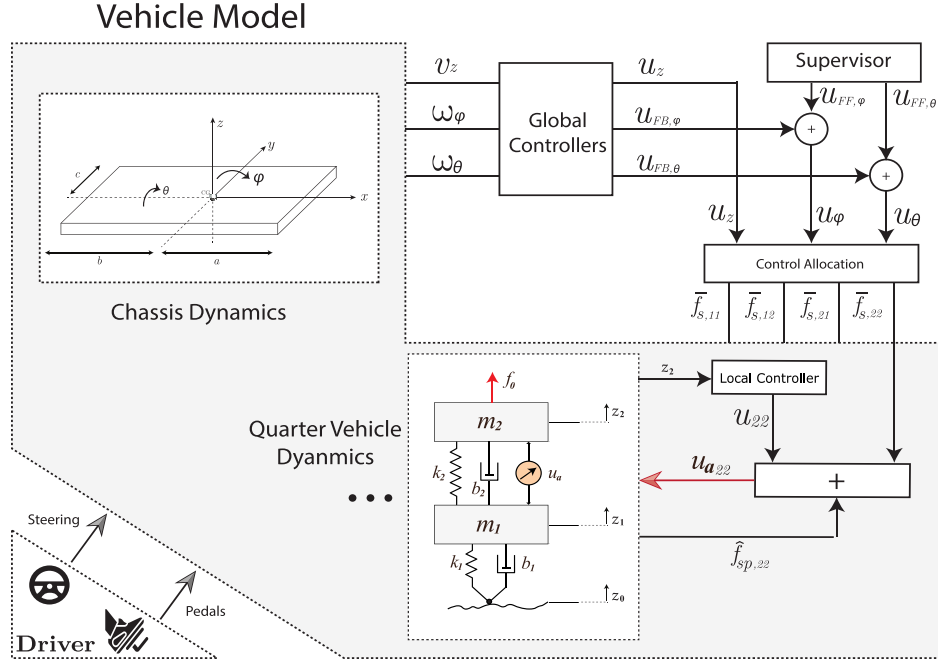


Figure 3.13. Schematic illustration for the hierarchical approach.

- **Direct control order:** apply the inversion law Force - Current of the electric suspension actuator to obtain the value of the reference current. Then introduce the reference current to the electric motor directly.
- **Current regulation (closed-loop control):** same for the first strategy but with a closed-loop control system to regulate the current provided to the electric actuator to track the reference value of the computed current.
- **Current and/or sprung mass regulation:** like the previous strategy but with the ability for adding an additional closed-loop system for sprung mass regulation combined with regulation of the current electric suspension actuator.

In this study, it is assumed that the actuator is ideal, that is perfectly providing the reference values obtained from the hierarchical approach combined with the part for sprung mass regulations.

3.5 Study requirements

3.5.1 Disturbance model

In order to evaluate the performance of the designed suspension local controller, the quarter models are subjected to different road disturbances. In the context of vehicle ride comfort and handling, the suspension system is disturbed by two main road inputs that are mainly classified as shock and vibrations (Hrovat, 1997). Shocks are discrete events of relatively short duration and high intensity that caused large suspension deflections, where vibrations are typically specified as random processes that consist of high-frequency components. Both types have a major influence on ride comfort and safety of the vehicle. In general, a well-designed controlled suspension must perform adequately in a wide range of shock and vibration environments.

3.5.1.1 Random road profiles

Beside driver disturbances, if the vibration induced by power and transmission systems is ignored, the unevenness of the road surface is the most important factor affecting the passenger ride comfort. In simulations, the random road profile is generated according to the International Standard Organization ISO 8608 (ISO-8608, 2011) where eight road roughness categories labeled from A to H are defined by the single-sided power spectral density PSD in the space-frequency (cycles/m) domain. The roughness profile of the road surface can be defined using the following equation:

$$G_d(\Omega) = G_d(\Omega_0) \cdot \left(\frac{\Omega}{\Omega_0} \right)^{-w}, \quad (3.58)$$

where $\Omega_0 = 1 \text{ rad/m}$ is the conventional value of angular spatial frequency, and $G_d(\Omega_0)$ is a constant derived from consistent tables found on the basis of the considered road class (Agostinacchio et al., 2014; Andr n, 2006; ISO-8608, 2011; Pan et al., 2017; Tyan et al., 2009). In this study, an artificial road profile is generated using a stochastic representation as a function of PSD of vertical displacements. Then, the road profile can be described by the following expression (Agostinacchio et al., 2014):

$$\begin{aligned}
z_0(x) &= \sum_{i=0}^{N_i} A_i \sin(\Omega_i \cdot x + \phi_i) \\
&= \sum_{i=0}^{N_i} \sqrt{2 \cdot \Delta\Omega \cdot G_d(\Omega_i)} \cdot \sin(\Omega_i \cdot x + \phi_i),
\end{aligned} \tag{3.59}$$

where A_i is the amplitude, ϕ_i is the random phase angle that follows a uniform probabilistic distribution within $[0 - 2\pi]$, x is the abscissa variable within the range $0 \rightarrow L_0$, and L_0 is the length of the road profile. $\Delta\Omega$ is the step size of the PSD bounded by two lower and upper angular spatial frequencies $\Omega_1 = 0.04 \text{ rad/m}$ and $\Omega_N = 10 \text{ rad/m}$ respectively, in order to cover an appropriate band of speeds of the passing vehicle. Table 3.4 lists the values of $G_d(\Omega_0)$ of some road classes while adopting $w = 2$ in (3.58).

Table 3.4. ISO 8608 values of $G_d(\Omega_0)$ related to some road class.

$G_d(\Omega_0) \times 10^{-6} (m^3)$			
Road class	Lower limit	Geometric Mean	Upper limit
A	-	1	2
B	2	4	8
C	8	16	32
$\Omega_0 = 1 \text{ rad/m}$			

3.5.1.2 Singular disturbance: Bump

In order to provide a realistic framework regarding shock road disturbances, a pronounced bump on smooth road is introduced. A widely used simple model for the vertical road displacement of a singular disturbance event is expressed by the following:

$$z_0(t) = \begin{cases} h_b \left(1 - \cos \left(\frac{2\pi v_x}{L_b} t \right) \right), & \text{for } 0 \leq t \leq \frac{L}{v_x} \\ 0, & \text{else} \end{cases} \tag{3.60}$$

where h_b represents half of the bump height, L_b represents the bump length and v_x represents the passing-vehicle's velocity.

3.5.2 Benchmark systems

Different suspension systems are used as performance benchmarks for the designed local active suspension control system. In this section, one parameter configuration for quarter vehicle model is adopted for all the systems presented, in which $m_2 = 218 \text{ kg}$, $k_2 = 12e3 \text{ N/m}$, $k_1 = 3e5 \text{ N/m}$, $b_1 = 50 \text{ N.s/m}$, and $m_1 = 32 \text{ kg}$.

Based on the frequency response of $Z_2(s)/Z_0(s)$ and $Z_1(s)/Z_0(s)$, the sensitivity transfer functions of the sprung mass and unsprung mass motion relative to road disturbance, respectively, the value of b_2 (damping factor) is adapted to get:

- a) A passive suspension system (PSc) acting as a baseline for the minimal behavior needed to ride comfort where the body factor resonance Q_2 of $|Z_2(s)/Z_0(s)|$ should not exceed 2, ($Q_2 \leq 2$). Then $b_{2c} = 1040 \text{ N.s/m}$.
- b) A passive suspension system (PSr) that represents the lower-limit performance needed for the unsprung mass dynamic, where the unsprung factor resonance Q_1 of $|Z_1(s)/Z_0(s)|$ should not exceeds 3, ($Q_1 \leq 3$). Then, for $b_{2r} = 975 \text{ Ns/m}$, minimal security is ensured.

In fact, the use of these systems is a rule of thumb methodology adopted by the PSA (Peugeot Citroën Associates) group to evaluate any newly designed strategies at the very first stage (Hamrouni et al., 2019).

- c) The third benchmark system is a system based on (PSr) with an optimized Skyhook controller (Sh), such that:

$$U_{Sh}(s) = -C_{Sh}(s) V_2(s), \quad (3.61)$$

where $V_2(s)$ is the Laplace transform of the velocity of the vertical displacement of the chassis ($\dot{z}_2(t)$). The transfer function $C_{Sh}(s)$ consists of a simple damping coefficient ' b_{sh} ' multiplied by a low pass filter with a well-selected cut-off frequency to limit unsprung damping factor. The selection of b_{sh} is based on an optimized strategy used in (Hamrouni et al., 2019). Then, obtained transfer function of $C_{Sh}(s)$ is as follows:

$$C_{sh}(s) = \frac{b_{SH}}{1 + \frac{s}{\omega_{Sh}}} = \frac{2225}{1 + \frac{s}{63}}. \quad (3.62)$$

Figure 3.14 shows the frequency response of the benchmark systems. We observe that, for the assumed parameters, the considered PSc system has similar dynamic behavior of PSr system at the wheel-mode frequency, (close Q_1 values). Therefore, in the evaluation section, only the PSc passive system will be considered for comparison.

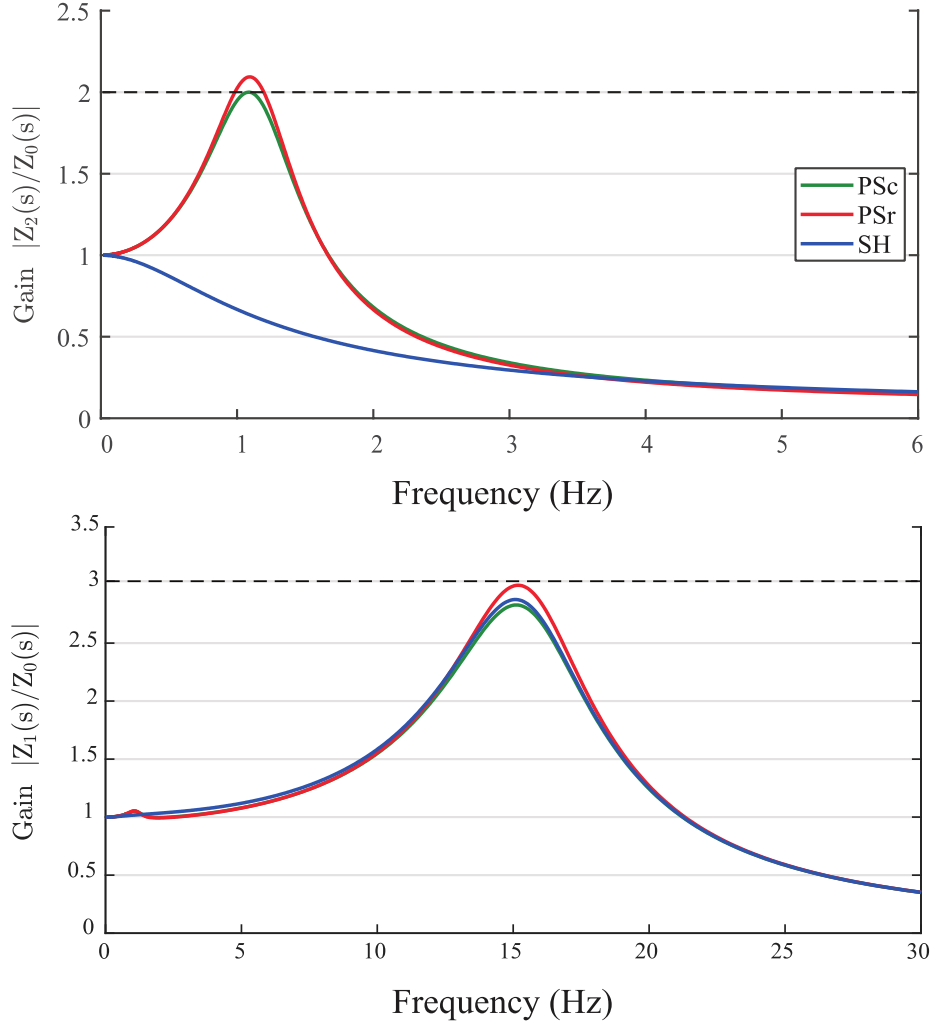


Figure 3.14. Frequency response of benchmark systems.

Finally, for the sake of comparing the performance, a PID controller is designed. In order to get a fair comparison, two main criteria are taken into account: the PID controller should have the same rapidity and stability margin as the designed CRONE controller. Since the chosen parametric configuration is for the front axle, therefore, the selected crossover frequency of the open-loop transfer function with the PID controller is $\omega_{c,PID} = 50 \text{ rad/s}$. Moreover, the integration and the low pass filter transitional frequencies are supposed to be equal to that of the $K_1(s)$. Then, the transfer function of the PID controller is written as follows:

$$K_{1,PID}(s) = 167690 \left(\frac{1 + s/2.79}{s/2.79} \right) \frac{1 + s/16.8}{1 + s/148.25} (1 + s/895)^{-1}. \quad (3.63)$$

The rest control parameters of the PID are chosen in order to have the open-loop transfer function tangent to 3dB contour in the Nichols chart, the same as the CRONE controller. In the same manner, a PID controller is also designed for the rear axle, and the resulting transfer function is formulated as follows:

$$K_{2,PID}(s) = 6991.6 \left(\frac{1 + s/2}{s/2} \right) \frac{1 + s/14.6}{1 + s/109.5} (1 + s/1610)^{-1}. \quad (3.64)$$

Figure 3.15. shows the bode responses of the CRONE controllers compared to the PID controllers for front and rear axles.

Figure 3.16 shows the Nichols chart of the open-loop transfer function for the nominal plants with the two controllers. It can be seen that both controllers intersect the 0dB at the same frequency and are tangent to 3dB contour (same phase margins).

3.5 Study requirements

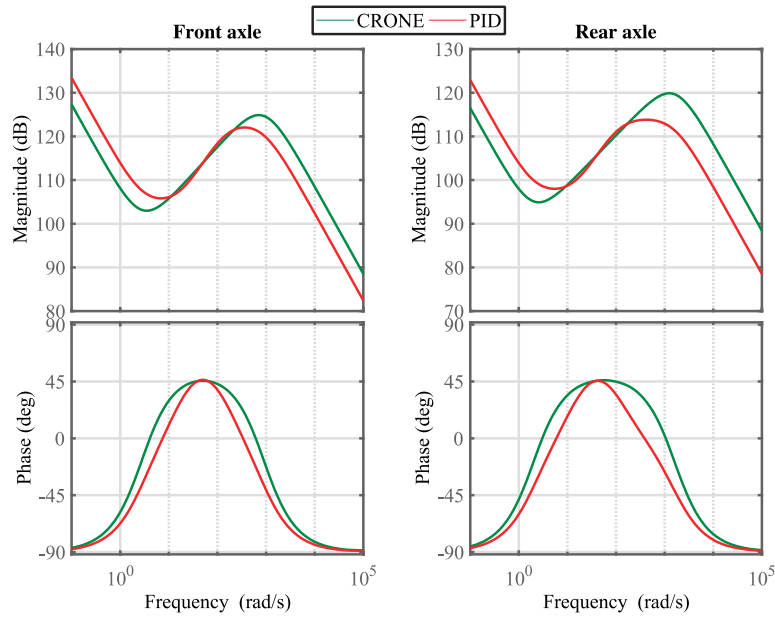


Figure 3.15. Bode responses of local CRONE and PID controllers.

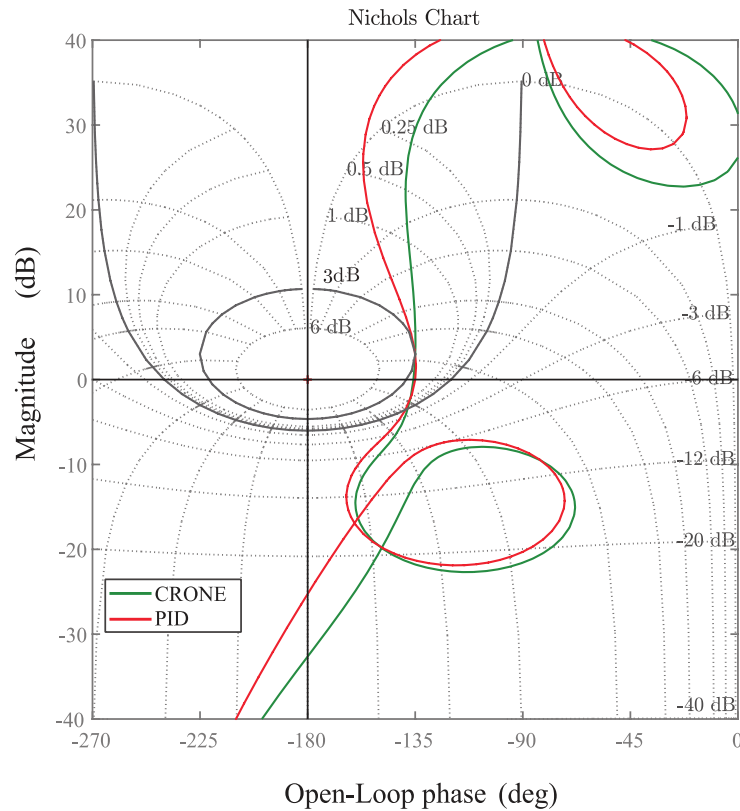


Figure 3.16. Nichols chart of open-loop transfer functions of local systems with PID and CRONE controllers.

3.5.3 Evaluation Indexes

Various methods are used to evaluate the performance of the proposed control law with respect to the nominal benchmark systems. In general, in academic and industrial applications, there are two main aspects of interest: The comfort and road-holding characteristics.

- Ride comfort is primarily associated with low vertical accelerations $\ddot{z}_2(t)$. For this reason, the root means square (RMS) value of the vertical chassis acceleration is considered as a measure for ride comfort. However, human comfort depends also on the frequency of the vertical acceleration, as well as its direction, location, and duration, especially, in the frequency range [4–8 Hz] where the human sensitivity for vertical vibrations is distinctive (Standard, 1997). For this reason, ISO 2631 specifies a method to assess ride comfort through weighting the value of the vertical acceleration by a shaping filter $W_c(s)$ that emphasizes the comfort relevant frequency range (Zuo and Nayfeh, 2003). A good approximation for the frequency weighting curve of ISO 2631-1 can be described as follows (Koch and Kloiber, 2014):

$$W_c(s) = \frac{10^2(0.9 s^4 + 11 s^3 + 114 s^2 + 55 s + 55)}{s^5 + 93 s^4 + 10^3(\frac{1}{4} s^3 + 26 s^2 + 81 s + 80)}. \quad (3.65)$$

Figure 3.17 shows the bode response of $W_c(s)$, in which it presents a bandlimited filter for frequencies in the range of interest [4 - 8] Hz. Furthermore, the maximum value of the vertical acceleration is also calculated which is indicative in singular disturbance events.

- The suspension deflection $|z_2(t) - z_1(t)|$ is limited to 9cm in the AW suspension system. Moreover, the RMS value of suspension deflection is also considered to analyze road holding.

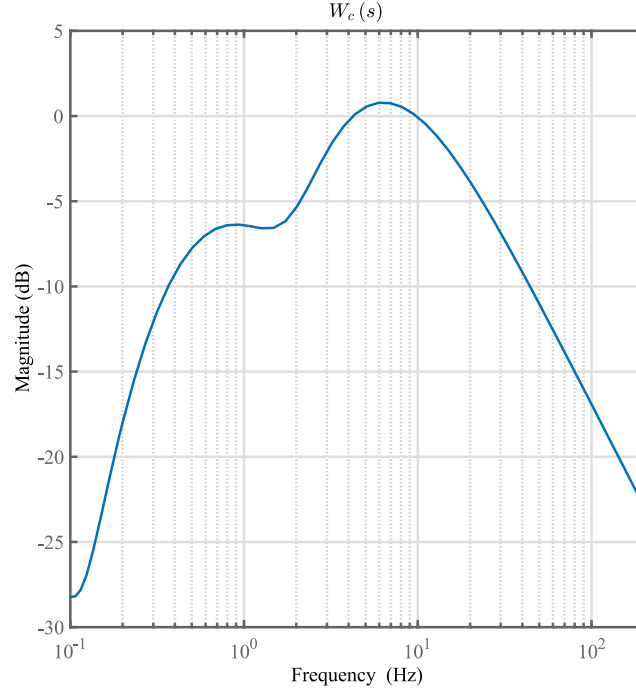


Figure 3.17. Bode response of $W_c(s)$ transfer function.

- The dynamic wheel load's RMS value represents a good index to evaluate ride safety to ensure the contact between the tire and the road. Thus, the transfer of longitudinal and lateral forces is guaranteed so that the driver can control the vehicle by steering, braking, etc... For this reason, the following formula is adopted:

$$\max(\|F_{dyn}\|_{rms}) \leq \frac{F_{stat}}{3} \leq \frac{(m_2 + m_1)g}{3}, \quad (3.66)$$

where F_{dyn} is the wheel deflection, and F_{stat} is the static wheel load. This is derived from the 3σ - rule where F_{dyn} would remain within $\pm F_{stat}$ for 99.7% of the time (Mitschke and Wallentowitz, 2014).

- The peak and the RMS value of the actuator's forces is also considered. Additionally, power consumption is also taken into consideration to compare the active systems, and the following relation has been selected (Marzbanrad et al., 2004):

$$P_w(t) = [-b_2(\dot{z}_2 - \dot{z}_1) + u_a(t)] (\dot{z}_2 - \dot{z}_1). \quad (3.67)$$

3.6 Frequency-domain analysis

In order to assess the robustness of the designed controllers, the Nichols charts of the open-loop transfer functions are plotted for global controllers with extremum plants as shown in Figure 3.18. It clearly shows the frequency template that is tangent to 3dB contour, which reflects the robustness of each controller against the parametric variation. Thus, the variation in the stability margins is approximately zero.

Figure 3.19 and Figure 3.20 show the Nichols charts for the front and rear open-loop transfer functions with CRONE and PID local controllers, respectively. The designed CRONE controller is matching the specification where the open-loop transfer functions are tangent to the 3dB contour ensuring high stability against parametric variations, in contrast to the PID controller, especially for rear plants. Numerically, the resulted maximum variations in

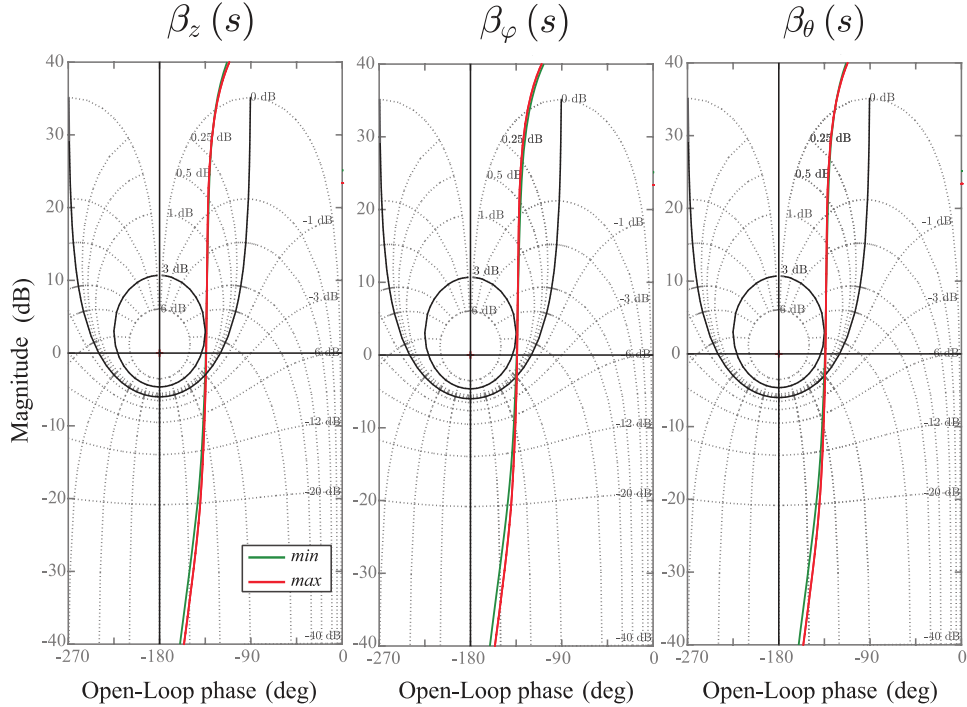


Figure 3.18. Nichols chart for global open-loop transfer functions.

the peak response of the complementary sensitivity functions $T(s)$ are as follows: for front axle $\max(\Delta Q_T) = 0.02dB$ with CRONE controller where for PID is $0.27dB$, and for the rear axle, $\max(\Delta Q_T) = 0.1dB$ with CRONE controller while with PID is $0.43dB$. Therefore, although of high uncertainty in the suspension parameters, the designed CRONE controller shows its robustness in general, and particularly compared to PID.

Regarding the performance of the local controllers, Figure 3.21 and Figure 3.22 show respectively the frequency responses of the sensitivity of the sprung mass acceleration and suspension deflection to road disturbance for nominal plants. It is obvious that the controlled plants are able to attain high attenuation for the sprung mass acceleration for a wide range of frequencies compared to the PSc system, especially in the range of interest ($\leq 8Hz$). However, this improvement comes at the expense of a degradation at the resonance wheel-mode frequency. It can be observed in Figure 3.22 the high gain at $f \approx 15Hz$ for the controlled systems compared to the passive and Skyhook systems. This fact will be translated to high variation for wheel deflection in case of high frequency road disturbances, and consequently less able to handle the vehicle by the driver. Moreover, at low frequencies ($\leq 1Hz$), the controlled systems are mostly not attenuating the suspension deflection comparing to other systems, which will reflect a higher values suspension deflection in the time-domain. In contrast, the Skyhook system keeps the damping behavior of the PSc system at wheel-mode frequencies, but it has less vertical acceleration attenuation. However, it effectively eliminates the effect of the resonance behavior at the chassis-mode frequency (around 1.5 Hz).

It should be noted that the difference in magnitudes at high frequencies appeared in Figure 3.21 is due to the difference in the damping coefficient of the suspension systems. For Active Wheel, as mentioned earlier, the damping coefficient has a very low value that results only from the mechanical parts used in such a system, where no shock absorber is used in this structure. Therefore, the high gain at wheel mode frequency shown in Figure 3.22 is not only due to the closed-loop system but also because of the small value of the damping coefficient of the suspension system.

3.6 Frequency-domain analysis

Although this analysis is done on one parametric configuration of the quarter vehicle, it could be applied to other configurations in which they share the same characteristics and no significant changes could be detected.

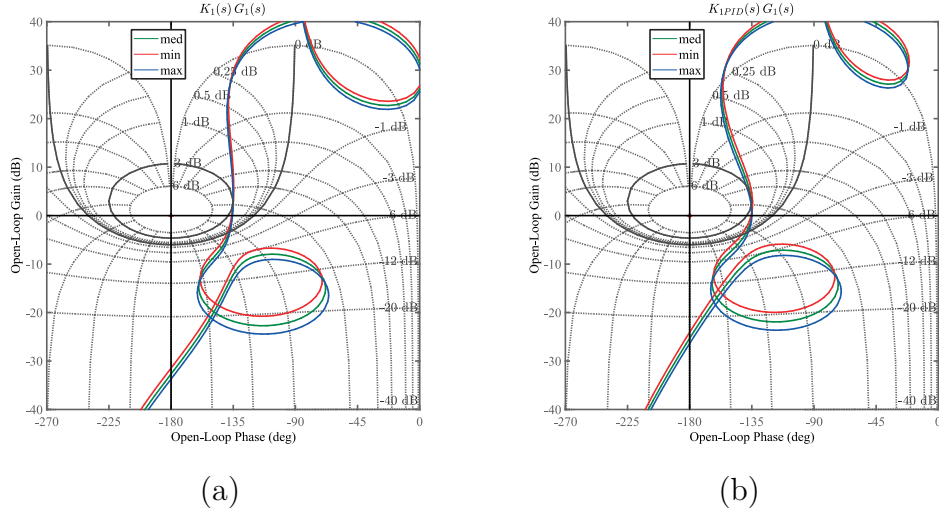


Figure 3.19. Nichols chart of the open-loop transfer function of front plants with (a) CRONE and (b) PID controllers.

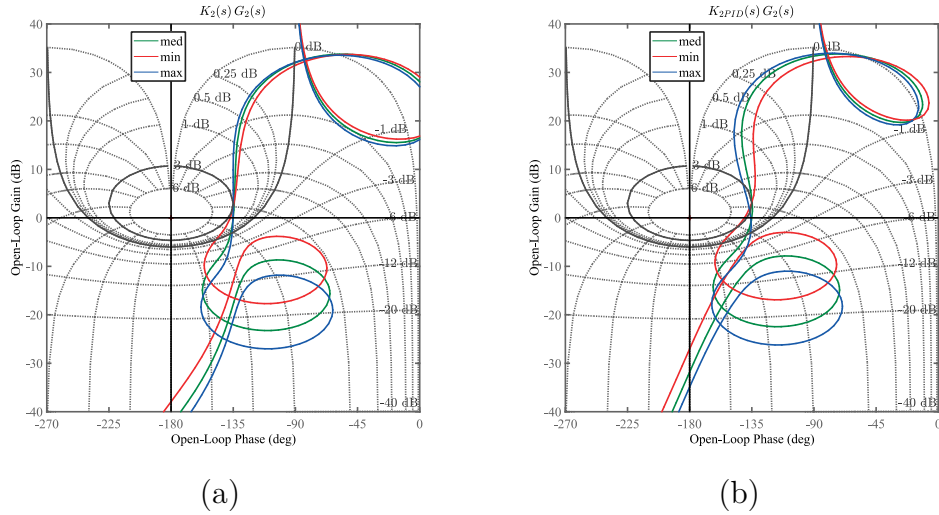


Figure 3.20. Nichols chart of the open-loop transfer function of front plants with (a) CRONE and (b) PID controllers.

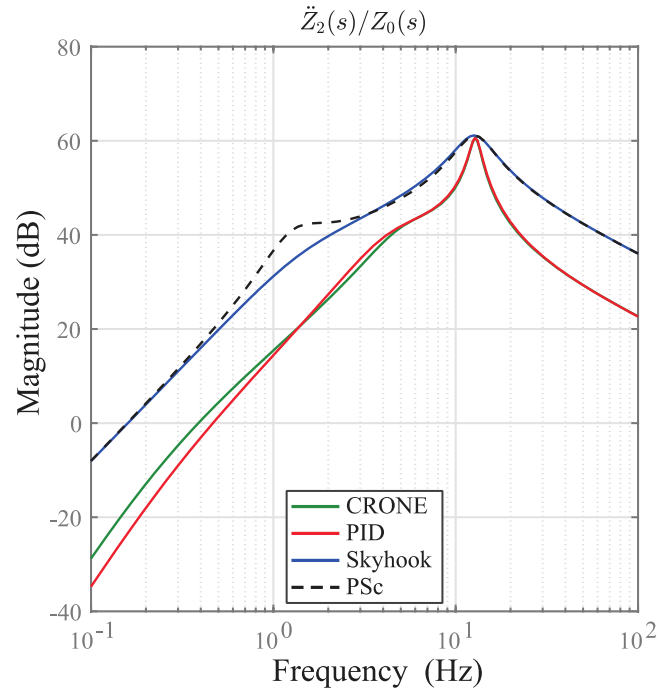


Figure 3.21. Sensitivity transfer functions of the sprung mass acceleration relative to road disturbances.

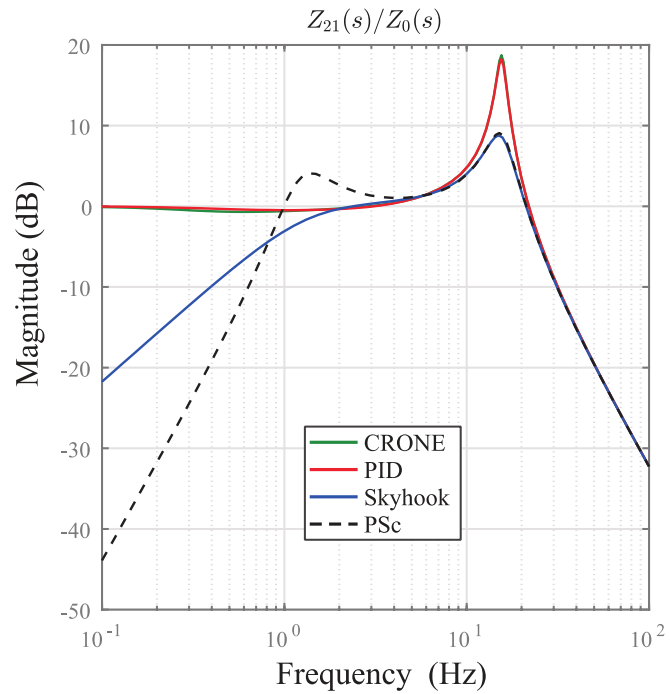


Figure 3.22. Sensitivity transfer functions of the suspension deflection relative to road disturbances.

3.7 Time-domain analysis

The simulations are divided into two subsections: one for testing the limits of the designed local controller in rejection of road disturbances, where the quarter vehicle used is for the front axle with the parametric configuration of section 3.5.2. The second one is to test the performance of the full vehicle model in rejecting driver disturbance. The parameters of the vehicle used are also here different from the nominal values in order to examine the robustness of the controller as well as its performance ($M = 820\text{kg}$, $b = 6/5\text{m}$, $a = 4/5\text{m}$, $k_{1,1} = 3e5\text{ N/m}$, $k_{1,2} = 2e5\text{ N/m}$, $b_1 = 50$, $m_1 = 32\text{ kg}$, $c = 0.71\text{m}$, $k_{2,1} = 12e3\text{ N/m}$, $k_{2,2} = 10e3\text{ N/m}$, $h_\theta = h_\varphi = 0.5\text{m}$, and $b_2 = 200\text{ Ns/m}$ for the controlled system).

3.7.1 Rejection of road disturbances

3.7.1.1 Singular event disturbance

An isolated bump is employed in this simulation as described in (3.5.1.2). The vehicle is passing over a bump, of a height of 10cm and length 1m, at a speed of 10km/h. Figure 3.23 shows the performance of the controlled system compared to the passive and Skyhook system. The CRONE and PID control show a high reduction in vertical acceleration which reveals an important improvement of ride comfort, however, they exceed the suspension deflection limits. Numerically, Table 3.5 lists the RMS values and maximums that evaluate the performance of the controlled systems relative to the passive system in percentage. It is obvious that the CRONE controller gains more comfort improvement compared to Skyhook and PID controlled systems. It can be concluded from the results obtained that the Skyhook controlled system could be an adequate solution for this kind of singular event road disturbances unless the height of the bump doesn't exceed the limits of the suspension deflection ($\leq 9\text{cm}$), where the designed controller provides more ride comfort for passengers, especially that the wheel deflection is within the admissible limits.

Practically, this simulation is not enough for analyzing the performance of the proposed strategy on singular disturbances. A holistic study should be done on the effect of all characteristics of the road profile. A comfort-oriented active suspension control strategy could be an adequate solution for

3.7 Time-domain analysis

road profiles like in Highways, national roads, or secondary roads. Moreover, it will be adopted also for singular obstacles that lead to acceptable suspension deflections, where a threshold value should be predefined. The decision of what control algorithm should be applied is based on the detected obstacles' characteristics like its geometry, speed of passing vehicle, and its power spectral density (PSD), for example.

For this reason, the study of the effect of such characteristics should be done and strategies could be implemented based on a holistic analysis. This work is probably one of the author's concerns for future studies.

Table 3.5. Simulation results for the controlled systems with bump road profiles.

Quantity	Bump		
	SH	CRONE	PID
$ \ddot{z}_2 _{rms}$	1.778	0.3	0.338
	+30%	+88.1%	+86.76%
$ \ddot{z}_{2,comf} _{rms}$	1.24	0.246	0.277
	+20.56%	+84.2%	+82.23%
$max(\ddot{z}_2)$	5.73	0.97	1.05
	+24.12%	+87%	+86%
$ z_2 - z_1 _{rms}$	0.024	0.029	0.0288
	+27.7%	+11.8%	+11%
$max(z_2 - z_1)$	0.068	0.0967	0.0973
	+20%	-14.2%	-14.9%
$\ F_{dyn}\ _{rms}$	451	264	271
	+0.48%	+53.4%	+51.6%
P_w	141.48	207	208
$\ u_a\ _{rms}$	225	383	392
$max(u_a) (N)$	648	1321	1360

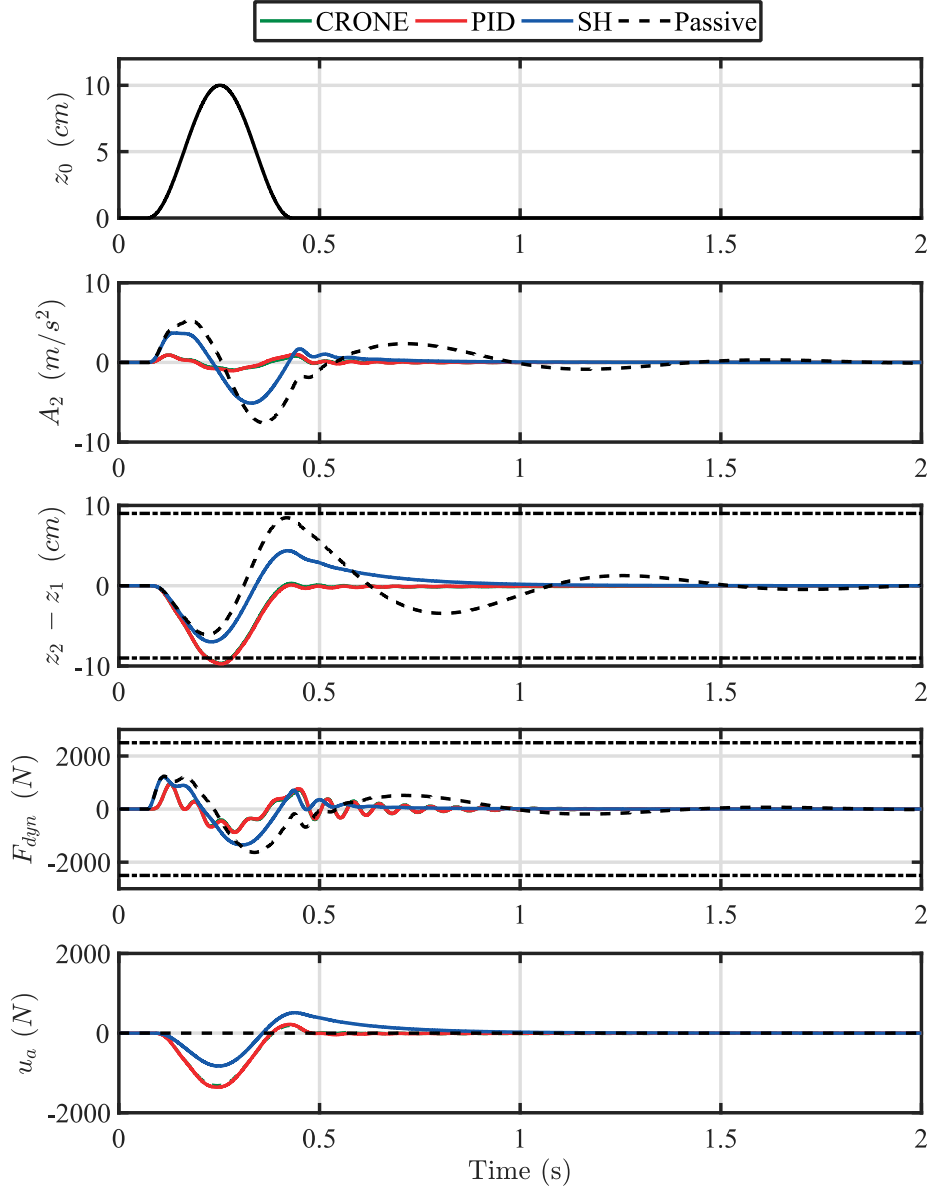


Figure 3.23. Simulation results of road bump.

3.7.1.2 Random road disturbance

In this test simulation, two road classes are employed where the vehicle is driven on a road of class A (Very good - $\max(|z_0|) = 1.5\text{cm}$) and class A-B (Good - $\max(|z_0|) = 2.5\text{cm}$) of a length of 250m. Figure 3.24 displays the

3.7 Time-domain analysis

road profiles used and their PSD graph. The road class A (green) is generated by $G_{d,A}(\Omega_0) = 1$ and $G_{d,A-B}(\Omega_0) = 2$ for road class A-B.

Figure 3.25 and Figure 3.26 show the performance of the CRONE controller compared to PSc system with road class A and A-B, respectively, where the variable $A_2(t)$ represents the vertical acceleration of the sprung mass. Table 3.6 and Table 3.7 lists the numerical results of the controlled quarter vehicle systems driven in road class A and A-B, respectively. The numerical results showed that the designed comfort-oriented local controller can improve ride comfort significantly by reducing $A_2(t)$ up to 47 – 50 % relative to PSc system, while respecting road holding critical limits formulated in section 3.5.3. The degradations in the performance of the dynamic wheel load F_{dyn} are acceptable in these scenarios where the RMS values are still

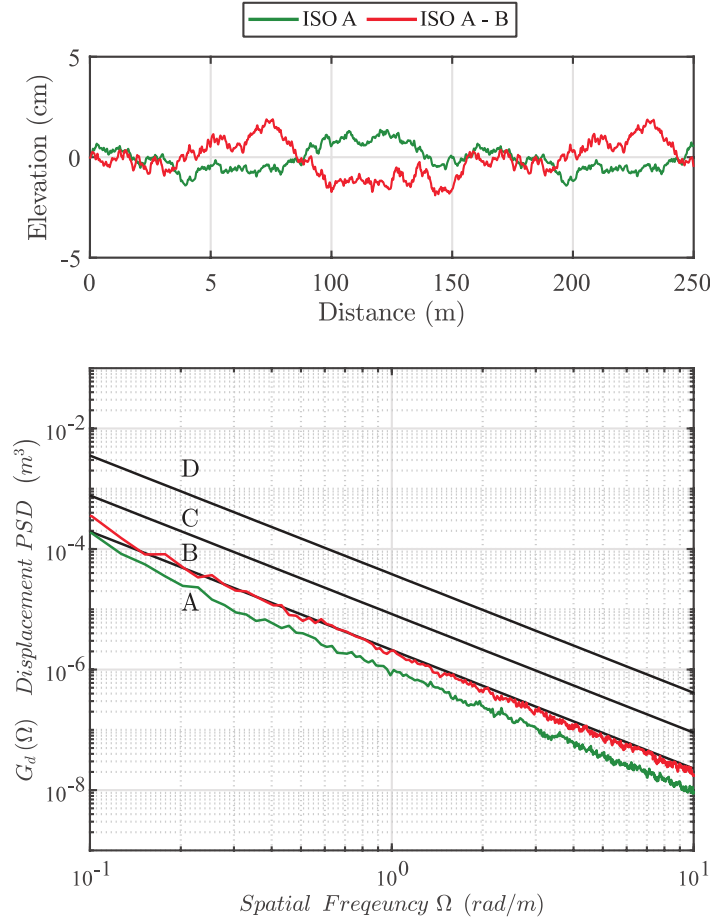


Figure 3.24. ISO road profiles and their PSD graphs.

3.7 Time-domain analysis

less than the limit ($F_{stat}/3 = 250 * g/3 = 817.5$). However, it is clear that for rougher road profiles (class $\geq B$), the RMS value of the wheel load dynamics could increase and exceed the limits, and as a result, the comfort-oriented controller could then affect the handling performance of the vehicle. The Skyhook system provides more safety margins but at the expense of low comfort improvement. These results are consistent with the frequency domain analysis where in frequencies range $[4 - 8 \text{ Hz}]$, the controlled systems have a significant attenuation in contrast to the Skyhook controller. In terms of power consumption, PID and CRONE have very close values with an advantage for the latter in the desired actuator forces. The obtained results give the preference for the CRONE controller in terms of robustness and performance for random road rejection testing scenarios.

Table 3.6. Simulation results for the controlled systems with class A roads.

	Profile 1 (Road Class A)		
	Sh	CRONE	PID
$ \ddot{z}_2 _{rms}$	0.5	0.262	0.27
	5.1%	50.5%	49.1%
$ \ddot{z}_{2,comf} _{rms}$	0.417	0.212	0.218
	0.9%	49.5%	48.2%
$max(\ddot{z}_2)$	1.5	0.855	0.72
	10.6%	49.2%	48.2%
$ z_2 - z_1 _{rms}$	0.0028	0.006	0.006
	11.8%	-93.9%	-96.6%
$max(z_2 - z_1)$	0.0088	0.0157	0.0159
	12.5%	-55.8%	-57.7%
$\ F_{dyn}\ $	328.3	515	503
	-1.5%	-59.3%	-55.5%
P_w	6	21.8	21.88
$\ u_a\ _{rms}$	31.3	76.3	78.3
$max(u_a)$	89.2	194.4	202.5
(%) relative to the PSc system			

3.7 Time-domain analysis

Table 3.7. Simulation results for the controlled systems with class A-B roads.

	Profile 2 (Road Class A-B)		
	Sh	CRONE	PID
$ \ddot{z}_2 _{rms}$	0.73	0.4	0.41
	3.7%	47.2%	46%
$ \ddot{z}_{2,comf} _{rms}$	0.611	0.325	0.332
	0.35%	47%	45.8%
$max(\ddot{z}_2)$	2.4	1.524	1.544
	4.6%	39.5%	38.7%
$ z_2 - z_1 _{rms}$	0.004	0.00892	0.009
	6.3%	-112%	-115%
$max(z_2 - z_1)$	0.011	0.0219	0.0223
	9.56%	-82.9%	-86.4%
$\ F_{dyn}\ $	470.6	788.261	767.7
	-1.8%	-70.5%	-66%
P_w	12.5	57.342	57.124
$\ u_a\ _{rms}$	43.7	109.8	113
$max(u_a)$	116	263	280
(%) relative to PSc system			

3.7 Time-domain analysis

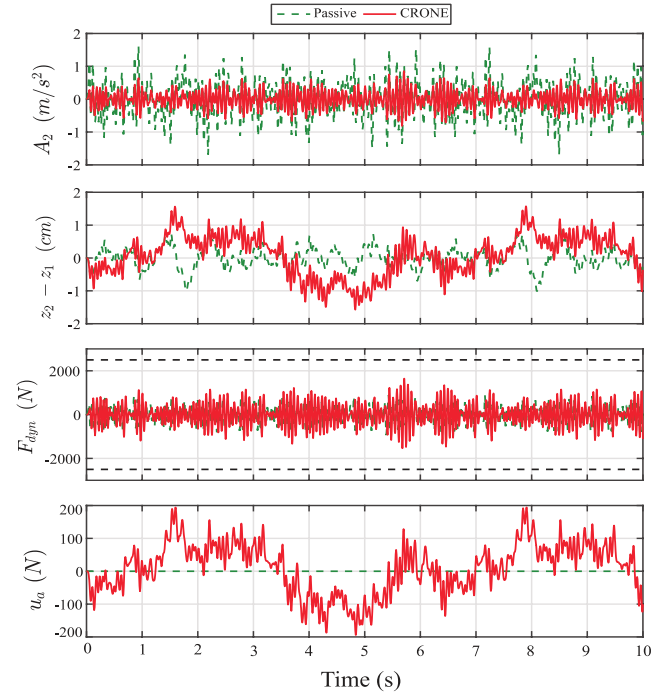


Figure 3.25. Simulation results of CRONE controller with road class A.

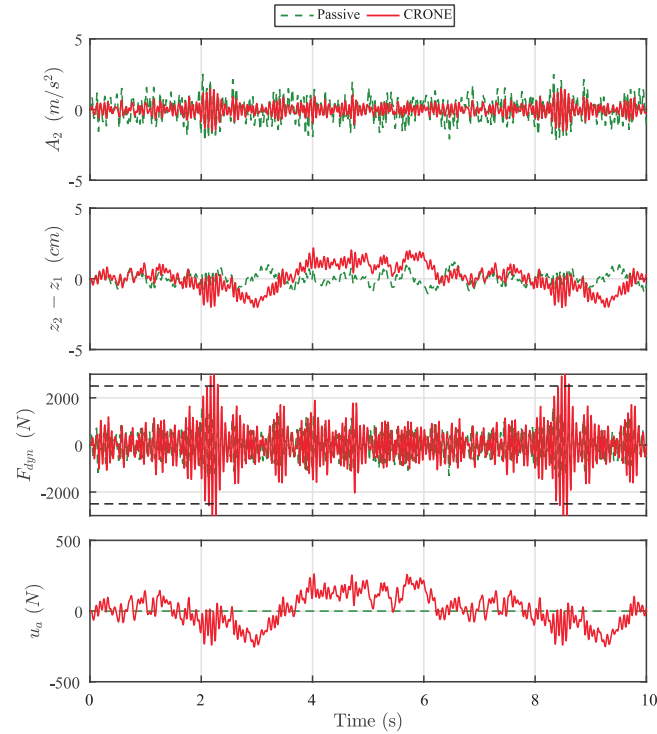


Figure 3.26. Simulation results of CRONE controller with road class A-B.

3.7.2 Driver Disturbance Rejection Scenario

The adopted driving scenario consists of two phases, the vehicle starts at an initial speed at 90km/h then the driver starts to slow down the vehicle until it reaches a speed of around 55km/h . In the second phase, at $t = 5.5\text{s}$, the driver introduces a positive steering input to turn left the vehicle. Figure 3.27 shows the steering input profile, the introduced braking/motor torques, the values of a_y and a_x , and the vehicle trajectory. It should be noted that the resulted values of the longitudinal and lateral accelerations are within the limits ($0.4g$), which means that the vehicle is operating in the comfort zone, which is the region of interest in this study.

Figure 3.28-30 display the chassis dynamics of the four systems: Passive system, system with only CRONE local controllers (LC), the system with CRONE global and local controllers without feedforward (GC+LC), system with CRONE global controller with feedforward control efforts only (GC+FF), and finally system with all components (All, i.e. GC+LC+FF). Primarily, the controlled systems prove their ability to highly compensate for the chassis dynamics. However, the plots reveal the advantage of the global controller and the feedforward control efforts. Obviously, the controlled system, where all control efforts elements are included, has better performance in compensating chassis dynamics. Table 3.8 shows the RMS values of different variables for all possible control configurations. The complete hierarchical approach proves its advantage in reducing pitch and roll accelerations, as well as sprung mass acceleration. On the other hand, in Figure 3.31, systems without local controller achieved better suspension deflection values that reflect more road-holding safety margins. However, this improvement achieved at the expense of less vibration isolation, where higher acceleration values are obtained.

Table 3.8. Simulation results of the driving scenario.

Variable (RMS)	System					
	PSc	LC	GC	GC+LC	GC+FF	All
$\ddot{z}_{CG}(\text{m/s}^2)$ $\div 10^3$	2.55	0.7	0.26	0.29	0.164	0.156
$\ddot{\varphi}_{CG}(\text{°/s}^2)$	1.35	0.17	0.06	0.05	0.036	0.0296
$\ddot{\theta}_{CG}(\text{°/s}^2)$	4.7	0.375	0.123	0.098	0.039	0.031
$U_a(N)$	0	1050	1007.6	1049.4	1049.3	1060

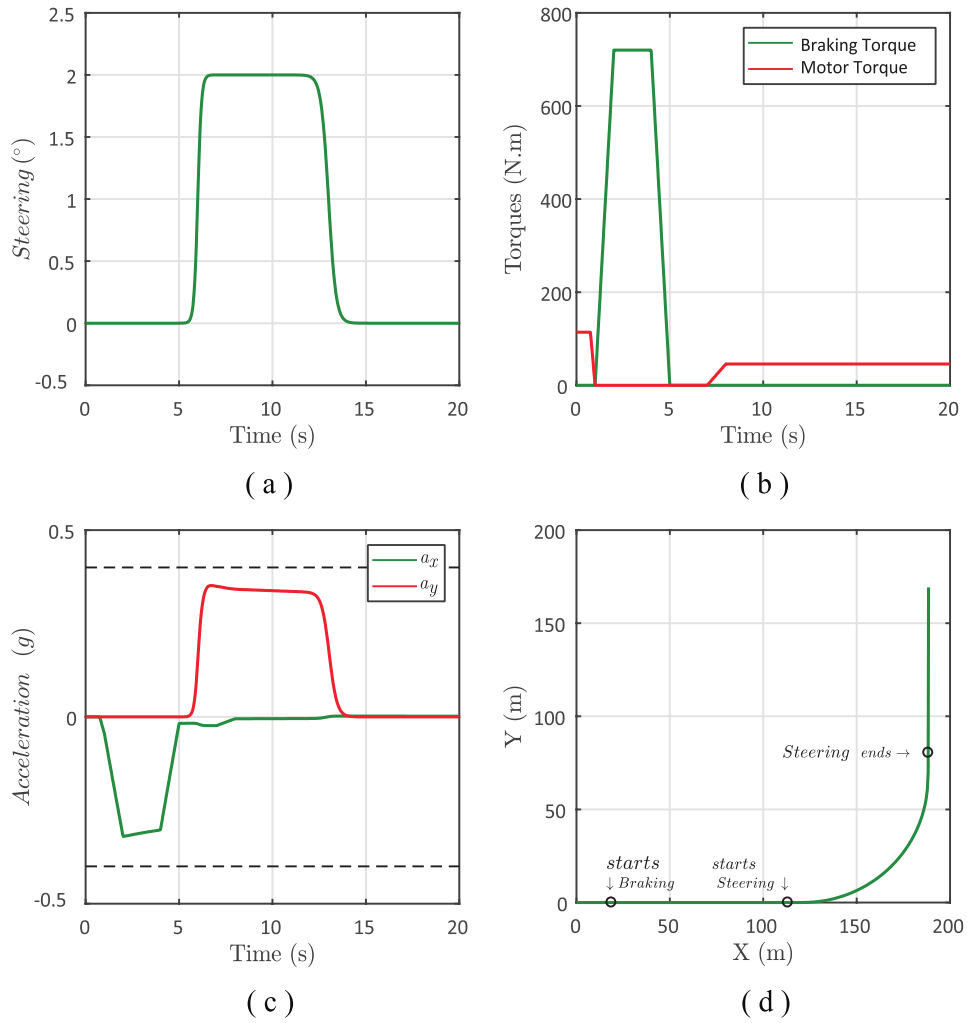


Figure 3.27. Driving scenario variables: (a) Steering profile, (b) introduced brake/motor torques, (c) resulted longitudinal and lateral accelerations, and (d) vehicle trajectory.

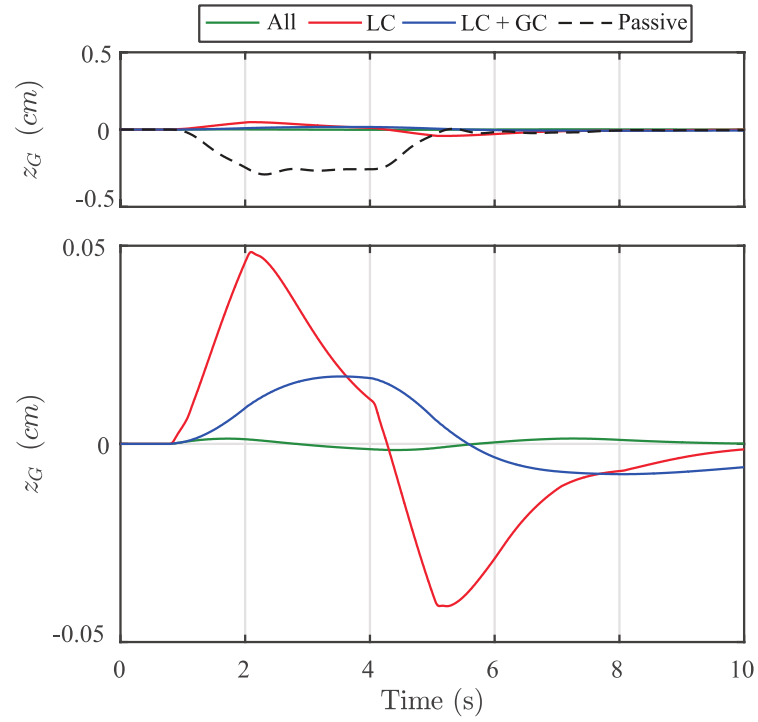


Figure 3.28. Simulation results of the vertical dynamics of CG.

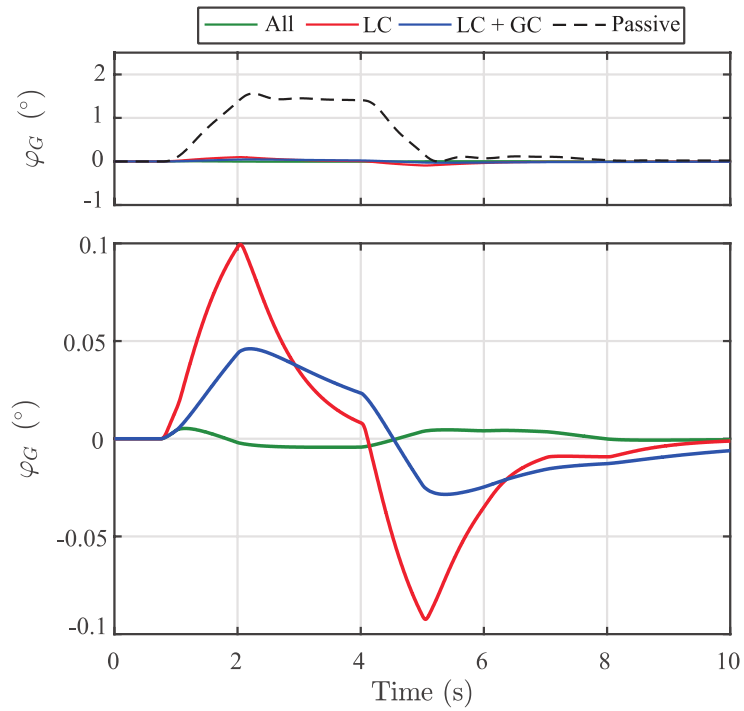


Figure 3.29. Simulation results of pitch motion of the chassis.

3.7 Time-domain analysis

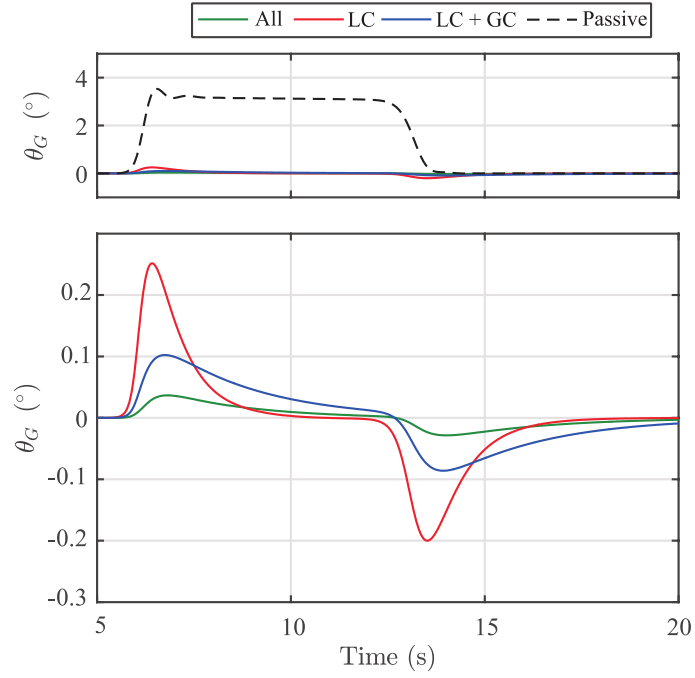


Figure 3.30. Simulation results of roll motion of the chassis.

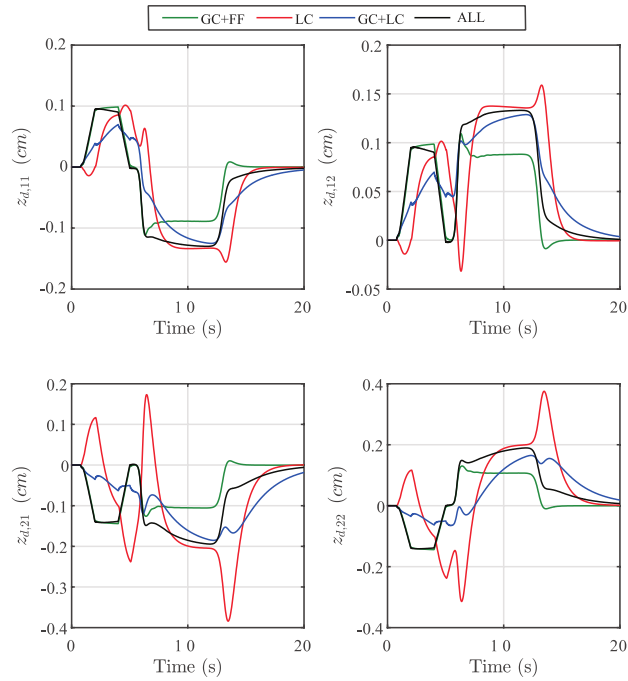


Figure 3.31. Simulation results of suspension deflections for different controlled systems.

3.8 Conclusion

Based on the hierarchical control approach, two-level controllers are presented for the AW suspension system. The systems are controlled using the first-generation CRONE controllers while taking into account the vehicles' parametric uncertainties. The main objective of the proposed approach is to reject the driver disturbances in light electric vehicles. In the range of interest of the study, the simulation results show the effectiveness of the strategy to enhance ride comfort and respecting the road holding/handling specifications. The combination of two-level controller permits to maximize the benefit of the embedded active suspension actuator in the AW. The controller shows its ability to fulfill the needed performance and robustness against the parametric variation of the vehicle. Consequently, it is shown that the local controller is able to deal with road disturbances of the A-B class. It is able to operate in a safe region without any significant effect on handling performances.

The extension of this work, in the framework of Global Chassis Control, is to implement other robust controllers that deal with the remaining objectives listed in the introduction, e.g. rejecting singular events and uneven road profiles (higher than B classes), and design road-holding oriented suspension controllers. The switching algorithm between the different designed controllers should be based on various sensing data given to the supervisor. Moreover, another control strategy should be implemented to deal with critical situations where the vehicle will operate outside the comfort region. The supervisor will then switch to the controller (e.g. road holding oriented controller, ...) that is most convenient to the vehicle and to the environment/road situation.

Chapter 4

Study and control of the ABS function

Contents

4.1	Introduction.....	152
4.2	Modeling	154
4.3	Control system design.....	167
4.4	Performance analysis.....	180
4.5	Effect of Vertical dynamics on the ABS control system.....	189
4.6	Conclusion	201

4.1 Introduction

The safety of modern vehicles can be attributed to a wide range of complex systems that aim to prevent loss of lives, whether it assists the driver in an active sense or simply provides passive protection. However, the effectiveness of the braking system of the vehicle has always been one of the primary factors that can save occupant's lives.

The anti-lock brake system (ABS) is considered as a landmark invention of braking systems. As shown in the general introduction, the yaw stability control (YSC), electronic stability program (ESP), and automatic emergency brake (AEB) are gradually invented and integrated into various braking systems. The continuous integration of these new features and improvement of the braking system had been greatly improved safety performance and ride comfort (Ahn et al., 2009).

Several ABS strategies and control methodologies are available today. State-of-the-art control strategies, such as sliding mode, gain scheduling and fuzzy logic control, finds its use in ABS research as software implemented simulation models (Aly et al., 2011). However, the operation of ABS on rough road is a relatively new research area that is yet to be fully understood. The ability of ABS to perform on rough terrains is deteriorated by fluctuations in wheel speeds and by the fluctuation of vertical loading in the tire. It was found that the variation in the wheel speeds, due to terrain excitations, could partially explain why ABS does not perform as well on rough terrains, as on smooth terrains (Penny and Els, 2016). Braking on rough terrains causes the tires to lose contact with the terrain momentarily and the contact patch of the tires also varies, reducing a vehicle's ability to perform a stable emergency maneuver (van der Merwe et al., 2018).

A scientific explanation as to why braking distance on rough terrains is much larger than on smooth terrains, is identified by Hamersma and Els (2014) that state that the rough surface of the terrain causes body roll and pitch motions in the vehicle which in-turn causes large fluctuations in wheel loads. This decreases the longitudinal forces on the tires because of the vertical force variations, thus, increasing the braking distance.

In the literature, investigations have been done on improving the braking performance of ABS on rough terrain, through altering the stiffness and damping settings of a vehicle's suspension (Hamersma and Els, 2014). Numerous tests with different suspension characteristic combinations were performed and it was found that the braking distance enhancement could be significant.

Since longitudinal braking force generation is heavily dependent on vertical load, the rough terrain braking problem can essentially be improved with adequate suspension control (Niemz and Winner, 2006; Reul and Winner, 2009). Further advances in this control strategy can be carried out using continuous damping along with an accommodating ABS algorithm. This study aims to develop a simulation model and a test platform to conduct further research into the rough road ABS braking problem.

At first, a 3rd generation CRONE controller is designed to maximize the efficiency of the braking system on AW. The study takes into consideration the road adhesion variations, vehicle mass variation, and vehicle velocity variations. Various testing scenarios were implemented on a quarter vehicle model while comparing the designed controller with the uncontrolled system in addition to a PID and 1st generation CRONE controllers. The final objective of this system is to reduce the braking distances while taking into consideration system limitations and noise measurement criterion.

Then, the half-vehicle model is depicted to study the effect of the load transfer disturbance on the performance of the ABS controller. By the end, the road disturbances were taken into account, and some testing scenarios made to find out its effect on the ABS performance. In order to minimize the performance deterioration, the fractional-order damping controllers introduced in Chapter 2, are also implemented to test for its influence on the overall system, in its different scenarios, i.e. comfort-oriented and road holding oriented controllers.

The work done in the frame of the ABS controller was based on the previous study presented in (Benine-Neto et al., 2017), where it didn't consider the vertical dynamics. The contribution here is the adaptation of the designed controller and the analysis of the effect of the vertical dynamics on the closed-loop system's performance.

4.2 Modeling

Throughout this chapter, the following notation convention of the different physical variables is adopted as follows:

$$X(t) = X^e + x(t), \quad (4.1)$$

where:

- $X(t)$ represents the physical magnitude of the variable in the absolute reference;
- X^e defines the reference value (constant) fixed by the stationary regime (equilibrium) around which the study of the dynamic behavior is carried out;
- $x(t)$ is the small variations in the physical quantity $X(t)$ around its equilibrium value X^e .

Thus, all the notations in lower case are considered as variations and all physical variables without capital letter notations are variables whose reference are zero. Finally, the Laplace transform of the variation $x(t)$ is noted as $X(s) = TF\{x(t)\}$.

4.2.1 Schematization and configuration

As the vehicle is considered moving in a straight line, particularly in this chapter, the transverse and yaw dynamics can be neglected. In addition, the vehicle is assumed to be perfectly symmetrical along the longitudinal axis, thus, a bicycle model could be considered in order to represent the longitudinal dynamics (Figure 4.1a) where needed. At first, the subject focuses only on half of the front axle, that is to say, that we consider a quarter model of the front vehicle (Figure 4.1b).

As the Electro-mechanical braking system (EMB) is considered in this study, Figure 4.2 shows an overview and the block diagram of the EMB actuator. As a brand-new form of braking, it completely abandons the traditional hydraulic braking system. Instead, it is powered by electric energy. It uses wires to transfer energy and data cables to transfer signals. It drives brake pads to clamp the friction plate by motor and related enforce

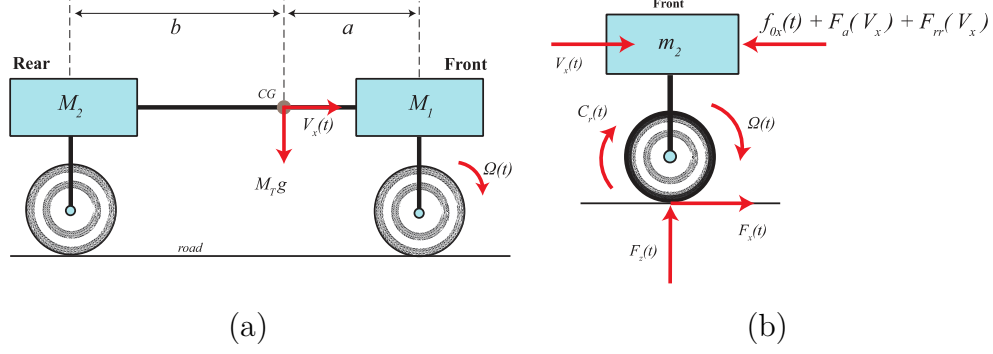


Figure 4.1. Schematization and configuration: longitudinal bicycle models (a) and front vehicle quarter (b).

mechanism, ultimately stopping the wheel. EMB has become the developing direction of the braking system due to its' high-efficiency, high braking performance, being environmentally friendly and easily integrated. The EMB system is composed of a controller and an actuator. As one of the key parts of the EMB system, the performance of its actuator influences the brake of the vehicle directly (Zhuo et al., 2017).

Although there are numerous EMB actuator schemes, they are composed of some basic models: drive module, enforce module, motion conversion module and sensor module. The Drive module, as the core of EMB, means the drive motor. Recently, Brush DC Motor (BDC), Brushless DC Motor (BLDC), Torque Motor and Switched Reluctance Motor (SR) are widely used. Enforce module includes reducer and other enforcement mechanisms. The commonly used reducers are cylindrical gear reducer, bevel gear reducer, planetary gear reducer, and worm reducer. The main enforce mechanisms are wedge mechanism, hinge mechanism, lever mechanism, cam mechanism, and crank slider mechanism. Motion conversion module plays the role of converting the rotational motion of drive motor to transitional motion, its main implementations are spiral drive mechanism, rack and pinion mechanism, crank slider mechanism and cam mechanism. The sensor module is mainly used in the control of the EMB actuator and it is required to provide higher sensitivity, as well as a lower price. In the classic three closed-loop control system, clamping force, motor speed, and motor current signal are essential. Correspondingly, a pressure sensor, a speed sensor, and a current sensor are required (Zhuo et al., 2017).

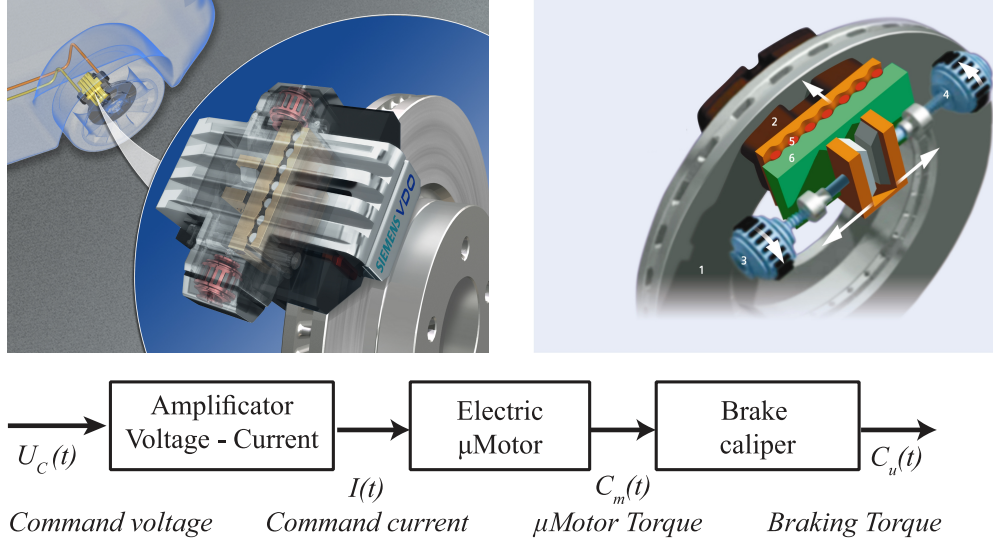


Figure 4.2. Functional diagram of the EMB actuator.

4.2.2 Dynamic equations

The equation describing the longitudinal dynamics of the quarter vehicle model using Bond-Graph approach is given by:

$$V_x(t) = \frac{1}{m} \int_0^t F_\Sigma(\tau) d\tau + V_x(0), \quad (4.2)$$

where the algebraic sum of the external forces $F_\Sigma(t)$ applied to the mass $m = m_1 + m_2$ (m total mass of the quarter of the vehicle considered, m_1 unsprung mass and m_2 sprung mass) is given by:

$$F_\Sigma(t) = F_x(t) - f_{0x}(t) - F_a(V_x) - F_{rr}(V_x), \quad (4.3)$$

with $F_x(t)$ is the longitudinal force developed by the tire, $f_{0x}(t)$ is the longitudinal gust of wind (variation) modeled by a force applied to the center of gravity CG , and $F_a(V_x)$ is the resistance aerodynamics whose expression is given by:

$$F_a(V_x) = \frac{1}{2} \rho S_x C_x V_x^2(t), \quad (4.4)$$

with ρ is the air density, S_x represents the projected area of a quarter of the vehicle in the longitudinal direction, and C_x corresponds to the aerodynamic drag coefficient.

Moreover, $F_{rr}(V_x)$ is the result of the rolling resistance expressed at the center of gravity CG of the quarter vehicle, and is expressed by:

$$F_{rr}(V_x) = (\lambda_0 + \lambda_2 V_x^2(t)) m g, \quad (4.5)$$

where λ_0 and λ_2 are two positive constants.

In the same manner, the dynamics of rotation of the wheel is described by:

$$\Omega(t) = \frac{1}{J_r} \int_0^t C_\Sigma(\tau) d\tau + \Omega(0), \quad (4.6)$$

where the algebraic sum of the external couples $C_\Sigma(t)$ applied to the inertia J_r is given by:

$$C_\Sigma(t) = C_r(t) - r_0 F_x(t) - C_{fv}(t), \quad (4.7)$$

with J_r is the inertia of the wheel, $\Omega(t)$ represents the absolute rotation speed of the wheel, r_0 is its radius under load, $C_r(t)$ represents the torque applied to the wheel by the traction motor (positive torque) or by the braking actuator (torque negative), and $C_{fv}(t)$ is the resulting viscous friction torque given by:

$$C_{fv}(t) = b_r \Omega(t), \quad (4.8)$$

where b_r is a viscous coefficient of friction.

In this study, the tire model used is the Pacejka model (Pacejka, 2012). The inputs and outputs for this model are described in Figure 4.3, in which the inputs are:

- The wheel vertical normal force $F_z(t)$,

- the sideslip wheel angle $\delta_p(t)$, which is considered null in this study (straight-line motion),
- the road adhesion μ ,
- the wheel slip rate $T(Vx(t), \Omega(t))$.

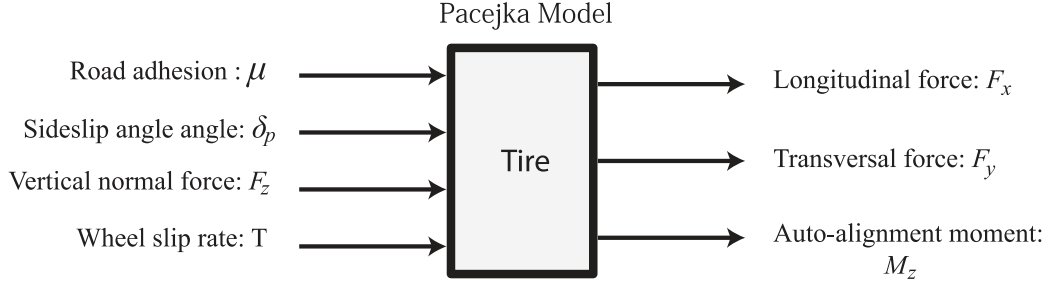


Figure 4.3. Black box model of the tire.

More precisely, the relationship between the wheel slip rate $T(t)$ and the longitudinal wheel forces (also called the magic formula in literature), is given by:

$$F_x(t) = \mu D_x \sin \left[C_x \arctan \left(B_x \left[(1 - E_x) T(t) + \frac{E_x}{B_x} \arctan(B_x T(t)) \right] \right) \right], \quad (4.9)$$

where the parameters B_x , C_x , D_x , and E_x depend on the characteristics of the tire used and on the value of the normal force $F_z(t)$.

In addition, the road adhesion μ is considered to be an uncertain parameter that could vary between 0.1 (icy-ground) and 1 (dry-ground). In the same way, the static component of the normal force is uncertain because it is equal to the weight distributed on each wheel, the uncertainty is linked to the mass $m = m_1 + m_2$ varying between unloaded and loaded vehicle, i.e.:

$$F_z^e = m g, \quad (4.10)$$

The expression of the slip rate $T(Vx(t), \Omega(t))$ depends on the acceleration ($T_{acc}(Vx(t), \Omega(t))$) or braking ($T_{fre}(Vx(t), \Omega(t))$), as:

$$T(t) = \begin{cases} \Omega(t)r_0 - V_x(t) \geq 0, \text{ then } T_{acc}(t) = \frac{\Omega(t) r_0 - V_x(t)}{\Omega(t) r_0} \geq 0 \\ \Omega(t)r_0 - V_x(t) < 0, \text{ then } T_{fre}(t) = \frac{\Omega(t) r_0 - V_x(t)}{V_x(t)} < 0 \end{cases} . \quad (4.11)$$

Finally, in the framework of this study, the dynamics of the EMB actuator is considered negligible, then the relationship between the control voltage input $u_c(t)$ and the braking control torque $c_u(t)$ applied to the wheel is formulated as follows:

$$c_u(t) = K u_c(t) , \quad (4.12)$$

where $K = 125 \text{ Nm/V}$ and $\max|U_c| = 12\text{V}$.

4.2.3 Model Linearization

In accordance with the remark made at the beginning of section 4.2, the following notations are used:

$$\left\{ \begin{array}{l} V_x(t) = V_x^e + v_x(t) \\ \Omega(t) = \Omega^e + \omega(t) \\ T(t) = T^e + \tau(t) \\ F_x(t) = F_x^e + f_x(t) \\ F_a(t) = F_a^e + f_a(t) \\ F_{rr}(t) = F_{rr}^e + f_{rr}(t) \\ C_{fv}(t) = C_{fv}^e + c_{fv}(t) \\ C_r(t) = C_m^e + c_u(t) \end{array} \right. . \quad (4.13)$$

4.2.3.1 Tire linearization

The first hypothesis of the linearization process supposed that the equilibrium point leads to a slip rate T^e belonging to the interval $[-10\%, +10\%]$, that is related to the linear operating zone of the tire (see Figure 4.4). In this case, the longitudinal force $F_x(t)$ is written in the form:

$$F_x(t) = F_x^e + f_x(t), \quad (4.14)$$

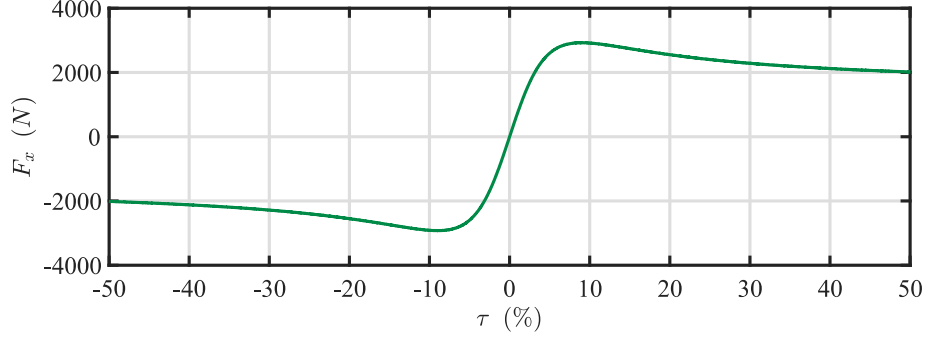


Figure 4.4. Longitudinal forces as function of tire slip rate according to Pacejka model.

$$\text{with} \quad F_x^e = p_x T^e, \quad (4.15)$$

$$\text{and} \quad f_x(t) = p_x \tau(t), \quad (4.16)$$

where, p_x is the slope of the tangents to the curve $(T(t), F_x(t))$, such that:

$$\begin{aligned} p_x &= \left. \frac{\partial F_x}{\partial T} \right|_{T=T^e} \\ &= \mu [BCD]_x \frac{\left[1 - E_x + \frac{E_x}{1 + B_x^2 T^{e2}} \right]}{1 + B_x^2 \cdot \left[(1 - E_x) T^e + \frac{E_x}{B_x} \arctan(B_x T^e) \right]^2} \\ &\quad \times \cos \left[C_x \arctan \left(B_x \left[(1 - E_x) T^e + \frac{E_x}{B_x} \arctan(B_x T^e) \right] \right) \right]. \end{aligned} \quad (4.17)$$

However, in the indicated linear region of operation, the values of p_x is formulated as follows:

$$p_x = \mu [BCD]_x. \quad (4.18)$$

The value of $[BCD]_x$ depends on different parameters and characteristics of the tires and is studied in detail in later sections.

Regarding the linearization for the slip rate variable, it is important to distinguish between the two phases, acceleration and deceleration. For acceleration, we have:

$$T_{acc}(V_x(t), \Omega(t)) = T_{acc}^e + \eta_{acc} \omega(t) + \mu_{acc} v_x(t) \quad (4.19)$$

with,

$$\begin{cases} T_{acc}^e = 1 - \frac{V_x^e}{r_0 \Omega^e} \geq 0 \\ \eta_{acc} = \left. \frac{\partial T_{acc}}{\partial \Omega} \right|_{\substack{V_x=V_x^e \\ \Omega=\Omega^e}} = \frac{V_x^e}{r_0 \Omega^{e2}} = cste > 0 \\ \mu_{acc} = \left. \frac{\partial T_{acc}}{\partial V_x} \right|_{\substack{V_x=V_x^e \\ \Omega=\Omega^e}} = - \frac{1}{r_0 \Omega^e} = cste < 0 \end{cases}, \quad (4.20)$$

where for the braking phases, we have:

$$T_{fre}(V_x(t), \Omega(t)) = T_{fre}^e + \eta_{fre} \omega(t) + \mu_{fre} v_x(t), \quad (4.21)$$

with,

$$\begin{cases} T_{fre}^e = \frac{r_0 \Omega^e}{V_x^e} - 1 < 0 \\ \eta_{fre} = \left. \frac{\partial T_{fre}}{\partial \Omega} \right|_{\substack{V_x=V_x^e \\ \Omega=\Omega^e}} = \frac{r_0}{V_x^e} = cste > 0 \\ \mu_{fre} = \left. \frac{\partial T_{fre}}{\partial V_x} \right|_{\substack{V_x=V_x^e \\ \Omega=\Omega^e}} = - \frac{r_0 \Omega^e}{V_x^{e2}} = cste < 0 \end{cases}. \quad (4.22)$$

In resume, after linearization, the longitudinal force $F_x(t)$ is written as follows:

- in acceleration:

$$\begin{cases} F_x(t) = F_x^e + f_x(t) \\ F_x^e = p_x T^e \\ f_x(t) = p_x \eta_{acc} \omega(t) + p_x \mu_{acc} v_x(t) \end{cases}, \quad (4.23)$$

- in braking:

$$\begin{cases} F_x(t) = F_x^e + f_x(t) \\ F_x^e = p_x T^e \\ f_x(t) = p_x \eta_{fre} \omega(t) + p_x \mu_{fre} v_x(t) \end{cases}. \quad (4.24)$$

4.2.3.2 Linearization of the aerodynamic resistance

The linearization of the expression (4.4) related to the aerodynamic resistance force $F_a(V_x)$ can be formulated as follows:

$$F_a(V_x(t)) = F_a^e + f_a(v_x(t)), \quad (4.25)$$

where,

$$F_a^e = F_a(V_x^e), \quad (4.26)$$

and,

$$f_a(v_x(t)) = b_a v_x(t), \quad (4.27)$$

with,

$$\begin{cases} F_a^e = \frac{1}{2} \rho S_x C_x V_x^{e2} = cste \\ b_a = \left. \frac{\partial F_a}{\partial V_x} \right|_{V_x=V_x^e} = \rho S_x C_x V_x^e = cste \end{cases}. \quad (4.28)$$

The parameter b_a here is related to the viscous aerodynamic friction coefficient (in Ns/m) that depends mainly on the speed of the vehicle $V_x^e = V_{x0}$ (in m/s).

4.2.3.3 Linearization of rolling resistance force

In the same manner, the linearization of the expression (4.5) related to the rolling resistance force $F_{rr}(V_x)$ can be formulated as follows:

$$F_{rr}(V_x(t)) = F_{rr}^e + f_{rr}(v_x(t)), \quad (4.29)$$

where,

$$F_{rr}^e = F_{rr}(V_x^e), \quad (4.30)$$

and,

$$f_{rr}(v_x(t)) = b_{rr} v_x(t), \quad (4.31)$$

with,

$$\begin{cases} F_{rr}^e = (\lambda_0 + \lambda_2 V_x^{e2}) m g = cste \\ b_{rr} = \left. \frac{\partial F_{rr}}{\partial V_x} \right|_{V_x=V_x^e} = 2 \lambda_2 m g V_x^e = cste \end{cases}, \quad (4.32)$$

where, b_{rr} is coherent with a viscous coefficient of friction (Ns/m) depending on the speed of the vehicle $V_x^e = V_{x0}$ (m/s) and the mass m of the quarter vehicle.

4.2.3.4 Equilibrium values and initial conditions

Considering the assumption of small variations and taking into account the previous equations development, (4.2) and (4.6) are rewritten in the following form, respectively:

$$m \dot{v}_x(t) = F_x^e + f_x(t) - f_{0x}(t) - F_a^e - f_a(t) - F_{rr}^e - f_{rr}(t), \quad (4.33)$$

$$J_r \dot{\omega}(t) = C_m^e + c_u(t) - r_0 F_x^e - r_0 f_x(t) - C_{fv}^e - c_{fv}(t). \quad (4.34)$$

At the point of equilibrium, in steady-state speed $V_x^e = V_{x0} = 50, 70$, or 90km/h , all variations are zero. The relationships (4.33) and (4.34) then can be reduced to:

$$\begin{cases} 0 = F_x^e - F_a^e - F_{rr}^e \\ 0 = C_m^e - r_0 F_x^e - C_{fv}^e \end{cases}. \quad (4.35)$$

The numerical expression of each variable at the equilibrium point is done in accordance with the different steps presented using the block diagram of Figure 4.5 where the starting point is from the selection of the speed V_{x0} . Thus, the magnitude of which the expression is determined in Step N-1 is given to a step N to determine the following expression, etc.

Therefore, we get the following ordered steps:

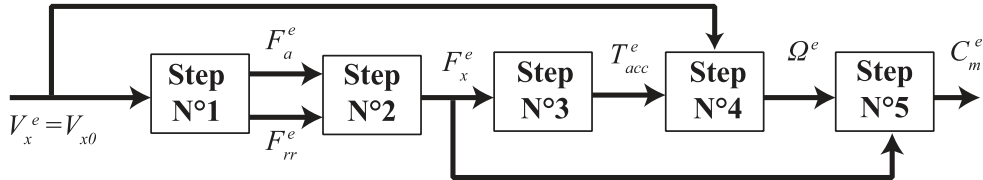


Figure 4.5. Overview of the steps necessary to determine the variables at equilibrium state.

$$\left\{ \begin{array}{l} 0 - V_x^e = V_{x0} \quad [m/s] \\ 1 - F_a^e = \frac{1}{2} \rho S_x C_x V_x^{e2}, \text{ and } F_{rr}^e = (\lambda_0 + \lambda_2 V_x^{e2}) mg [N] \\ 2 - F_x^e = F_a^e + F_{rr}^e \quad [N] \\ 3 - T_{acc}^e = \frac{1}{[BCD]_x} F_x^e \quad [\%] \\ 4 - \Omega^e = \frac{1}{r_0} \left(\frac{V_x^e}{1 - (T_{acc}^e/100)} \right) \quad [rad/s] \\ 5 - C_m^e = r_0 F_x^e + b_r \Omega^e \quad [Nm] \end{array} \right. . \quad (4.36)$$

4.2.4 Synthesis model

The designed controller is based on the frequency response of the plant; therefore, a linearized model of the plant dynamics is required. The linearization process during the braking phase around an operating point is adopted and it could be defined by the following state-space representation:

$$\begin{cases} \dot{\underline{x}} = A \underline{x} + B u \\ y = C \underline{x} + D u \end{cases} , \quad (4.37)$$

with,

$$\underline{x} = \begin{pmatrix} x_1 = v_x(t) \\ x_2 = \omega(t) \end{pmatrix} , \quad u = \begin{pmatrix} f_{0x} \\ u_c(t) \end{pmatrix} \quad \text{and} \quad y = \omega(t), \quad (4.38)$$

which leads to the transfer function $G(s)$ that is given by:

$$G(s) = \left. \frac{\Omega(s)}{U_c(s)} \right|_{f_{0x}=0, b_m=0} , \quad (4.39)$$

where $\Omega(s) = \mathcal{L}\{\omega(t)\}$ and $U_c(s) = \mathcal{L}\{u_c(t)\}$, and taking into consideration the parametric uncertainty of the plant, and in the absence of the noise measurements, $b_m = 0$, and neglecting the gust wind forces, $f_{x0} = 0$.

The obtained linearized longitudinal dynamics is described by:

$$m \dot{v}_x(t) = f_x(t) - f_a(t) - f_{rr}(t) - f_{x0}. \quad (4.40)$$

Concerning the wheel dynamics, the angular acceleration $\dot{\Omega}^e$ can be computed for a constant slip rate T_{opt} and a given longitudinal velocity V_x^e , by the following formula:

$$\dot{\Omega}(t) = \frac{T_{opt} + 1}{r_0} \dot{V}_x(t). \quad (4.41)$$

For braking phases, the wheel traction torque is considered null, $C_m = 0$, then the corresponding control effort is computed as:

$$U_c^e = -\frac{J_r \Omega^e - r_0 F_x^e - b_r \Omega^e}{K}. \quad (4.42)$$

Finally, linearizing (4.6) around a given optimal slip rate T_{opt} , we get:

$$J_r \dot{\omega}(t) = -K u_c(t) - r_0 p_x \tau(t) - b_r \omega(t). \quad (4.43)$$

Based on (4.41) and (4.43), the state-space matrix's parameters are obtained as follows:

$$A = \begin{bmatrix} -\frac{\frac{\Omega^e r_0 p_x}{V_x^{e2}} + \frac{\rho C_x S_x V_x^e}{2} + 2V_x^e g \lambda_2 m}{m} & \frac{r_0 p_x}{V_x^e m} \\ \frac{\Omega^e r_0^2 p_x}{J_r V_x^{e2}} & -\frac{b_r + \frac{r_0^2 p_x}{V_x^e}}{J_r} \end{bmatrix}, \quad (4.44)$$

$$B = \begin{bmatrix} -\frac{1}{m} & 0 \\ 0 & -\frac{K}{J_r} \end{bmatrix}, \quad C = [0 \ 1], \text{ and } D = 0.$$

The transfer function $G(s)$ can be thus obtained as follows:

$$G(s) = \frac{-K \left(\frac{s}{J_r} + \frac{2\Omega^e r_0 p_x + \rho C_x S_x V_x^{e3} + 4V_x^{e3} g \lambda_2 m}{2J_r V_x^{e2} m} \right)}{s^2 + ps + q}, \quad (4.45)$$

where,

$$p = \frac{b_r}{J_r} + 2V_x^e g \lambda_2 + \frac{r_0^2 p_x}{J_r V_x^e} + \frac{\rho C_x S_x V_x^e}{2m} + \frac{\Omega^e r_0 p_x}{V_x^{e2} m}, \quad (4.46)$$

and,

$$q = \frac{(\rho C_x S_x + 4g \lambda_2 m)(r_0^2 p_x + V_x^e b_r)}{2J_r m} + \frac{\Omega^e r_0 p_x b_r}{J_r V_x^{e2} m}. \quad (4.47)$$

4.2.5 Modeling of the reference

The generation of the reference inputs to the control process is composed of a pre-compensation part which is defined by the voltage control input reference $u_{ref}(t)$ and the generation of the reference value of the angular velocities of the wheel $\omega_{ref}(t)$.

In fact, the variation of the values of $u_{ref}(t)$ is the image of the driver's desired braking torques. Thus, from the measured values $x_p(t)$ of the position of the braking pedal (from 0 to 12cm), the reference voltage can be calculated (from 0 to 12V), as follows:

$$u_{ref}(t) = K_p x_p(t), \quad (4.48)$$

where $K_p = 100\text{V/m}$.

On the other hand, the values of the reference of the wheel desired angular velocity $\omega_{ref}(t)$ could be computed in the following manner: the estimated value of the wheel slip rate can be defined as the following formula depending on the estimated or a measured value of the wheel angular and longitudinal velocity, as follows:

$$\hat{T}_{fre}(t) = \frac{\hat{\Omega}(t) r_0}{\hat{V}_x(t)} - 1 < 0 \Leftrightarrow \hat{\Omega}(t) r_0 < \hat{V}_x(t). \quad (4.49)$$

Here, two cases are defined in order to obtain the reference value of the angular wheel velocity:

- If $\hat{T}_{fre}(t) > \hat{T}_{opt}$, then $\omega_{ref}(t)$ is taken as:

$$\Omega_{ref}(t) = \hat{\Omega}(t). \quad (4.50)$$

where \hat{T}_{opt} is selected according to the tire response curve, and represents the optimal slip rate, e.g. 8%, 10%. This value generally depends on the tire characteristics and the values of the available grip/adhesion.

- Otherwise, if $\hat{T}_{fre}(t) \leq \hat{T}_{opt}$, then:

$$\Omega_{ref}(t) = (1 + T_{opt}) \frac{\hat{V}_x(t)}{r_0}. \quad (4.51)$$

4.3 Control system design

4.3.1 Strategy

The control scheme for the ABS is presented in Figure 4.6. The block *Regulator* indicates the designed controller (CRONE). The signal $b_m(t)$ represents the noise on the measurement of the wheel angular velocity, $\Omega(t)$. The term $U_{ref}(s)$ represents the reference voltage that is proportional to the displacement of the braking pedal as illustrated in (4.48). The values $\Omega_{ref}(s)$ are generated in the *Generation of references* block as explained in (4.50) and (4.51). The block *Vehicle*, particularly, in this section represents the quarter vehicle validation model.

The ABS strategy is consisting of two main phases. At regular braking conditions, in which no critical situation or sliding process may occur, the ABS is deactivated (inactive), and therefore $\Omega_{ref}(t) = \Omega_{mes}(t)$. In this case, the error is null and the feedback controller has no effect at all, that is $U_{fb} = 0$. Thus, the only input to the plant, in this case, is the feedforward part, $U_{ff}(t)$.

The ABS system becomes active when there is a risk of wheel locking. This situation, practically, is detected when the estimated slip rate $T(t) < T_{opt}$ (braking phase). Then, the reference signal is given as:

$$\Omega_{ref}(t) = \frac{(1 + T_{opt})V_x(t)}{r_0} , \quad (4.52)$$

where it differs from the $\Omega_{mes}(t)$, and therefore the error is no longer zero, and the feedback loop starts to counteracts the feedforward signal provided by the driver.

In order to deactivate the ABS, two conditions must be met simultaneously:

- $T(t) \geq T_{opt}$, which ensures a safe situation in which the tire forces are not saturated anymore.
- A decrease in the value of $x_p(t)$, which indicates the driver's intention to reduce or bring to an end of the braking action (braking pedal release).

It should be noted that some previous works found in the literature (Nyandoro et al., 2011; Tang et al., 2013) prefer to formulate the control strategy as a regulation of the slip rate dynamics. However, one major drawback of such strategies is in switching in the controller structure derived from the ABS active or inactive modes. Hence, it requires treating the

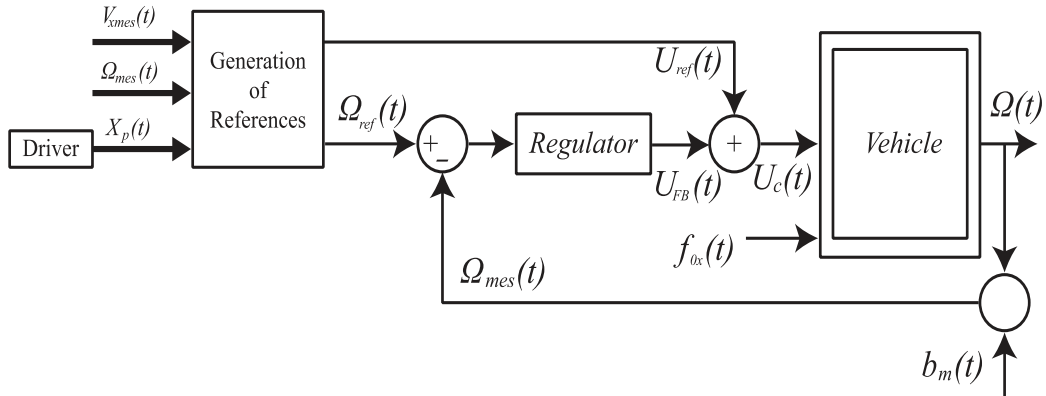


Figure 4.6. Control schema for ABS control loop.

problem with hybrid-system tools to ensure stability and performance under these commutations. The presented strategy proposed by (Benine-Neto et al., 2017) consists of tracking a reference wheel speed. The activation of the ABS changes the reference-generator model, thus avoiding commutations on the feedback loop, and providing the same results as a slip rate regulation. The overall strategy for ABS is illustrated in Figure 4.7.

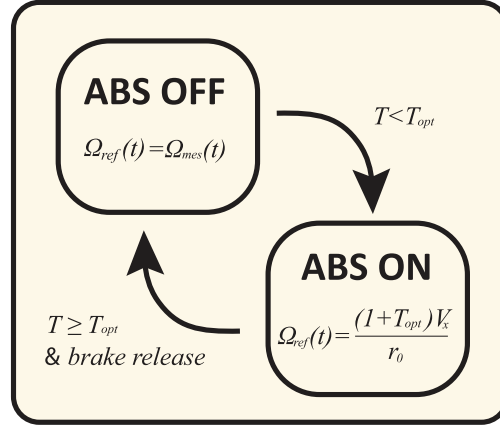


Figure 4.7. Reference generator for wheel angular velocity (flow chart).

4.3.2 Control specifications

Several specifications should be taken into account before launching the design process. Regarding the controller, the following specifications are required:

- Control input related to noise measurement is less than 15% of the greatest measurement voltage.
- A Nominal overshoot of step response related to reference signal: about 30%.

As mentioned before, the range of the control input is $U_c(t) \in [0 - 12]V$. The noise level of $\Omega(t)$ corresponds to 2% sensor range, that is $\max(b_m(t)) = 2 \text{ rad/s}$.

In order to translate these specifications into frequency-domain terms, following equations associated with Figure 4.6 are introduced:

$$\Omega(s) = -T(s)b_m(s) + GS(s)U_{ff}(s) + T(s)\Omega_{ref}(s), \quad (4.53)$$

$$\epsilon(s) = -S(s)b_m(s) - GS(s)U_{ff}(s) + S(s)\Omega_{ref}(s), \quad (4.54)$$

$$U_{FB}(s) = -CS(s)b_m(s) - T(s)U_{ff}(s) + CS(s)\Omega_{ref}(s), \quad (4.55)$$

with $C(s)$ representing the transfer function of the controller, and other transfer functions were previously introduced in detail in Chapter 1.

According to the maximum control effort available and the indicated measurement noise percentage related to it, an upper boundary limit is calculated for the closed-loop cutoff frequency, so-called ω_{cg} . Depending on the formulation of the control sensitivity function $CS(s)$, we get the following:

$$\left| \frac{U_{FB}(j\omega)}{b_m(j\omega)} \right| = |CS(j\omega)| \leq \left| \frac{0.15 \times 12V}{2rad/s} \right| = 0.89Vs/rad. \quad (4.56)$$

Taking advantage of the fact that at high frequencies ω_{HF} , the frequency response of the control sensitivity functions is very close to that of the controller's transfer function, that is:

$$|CS(j\omega_{HF})| \approx |C(j\omega_{HF})| \leq \frac{0.89Vs}{rad}, \quad (4.57)$$

and, at the open-loop gain crossover frequency ω_{cg} , we have:

$$\beta(s) = |C(j\omega_{cg})G(j\omega_{cg})| = 1, \quad (4.58)$$

then, one can consider a proportional controller such that $C(s) = C_p \leq 0.89Vs/rad$, and can compute the upper bound of ω_{cg} using (4.58) by:

$$|G_{nom}(j\omega_{cg})| \leq \frac{1}{C_p} = 1.12 \text{ rad/sV}. \quad (4.59)$$

Therefore, depending on the frequency response of the nominal plant proposed, the upper bound limit is computed so that the inequality (4.59) is satisfied.

Finally, regarding the allowed overshoot, it can be represented as the peak gain of the complementary sensitivity function $T(s)$, which will be denoted

as resonant gain M_{r0} for the nominal plant. The $M_{r0} = 3dB$ corresponds to an overshoot of about 30%.

4.3.3 Plant definition

Three main parameters have the influence on the frequency response of the system transfer function $G(s)$, that are more explicitly: V_x^e , that determines the values of Ω^e through (4.51); m , that appears explicitly on the coefficient of the plant transfer function (4.45); and finally μ^e that affects the value of p_x according to (4.17) that in turn also appears in (4.45). It is worth noting that these three parameters are obtained after considering the linearized model about a trajectory of constant slip rate, namely T_{opt} . The range of variations of these parameters as assumed in this study are listed in Table 4.1.

In order to analyze the effect of the parametric uncertainty on the frequency response of the controlled plant $G(s)$, a study should be made to find how the variation of road adhesion and vehicle's mass affects the variation of the value of p_x .

Two main approaches are applicable to calculate the variation of p_x . The first approach is to assume that p_x corresponds to the slope of the tangent to the curve (T, F_x) at the origin. In this case, the values can be computed by the following algorithm for each value of m and μ :

$$p_x = \mu [BCD] , \quad (4.60)$$

where $[BCD]$ is an expression related to the Pacejka tire model, and it depends on the micro parameters of the model, and is formulated as:

Table 4.1. Range of variation of uncertain parameters of the ABS control plant.

Parameter	Range	Unit
V_x^e	15 – 30	m/s
μ^e	0.5 – 1	-
m	200 – 250	kg

$$[BCD] = (b3 \times Z^2 + b4 \times Z)e^{-b5 \times Z}, \quad (4.61)$$

where $b3$, $b4$, and $b5$ are three models' parameters and are equal to 23.9, 242, and 0, respectively. Here, Z represents the vertical wheel contact force F_z in kN, that is:

$$Z = F_z/1000 = m \times g/1000, \quad (4.62)$$

where g is the gravity constant. It should be noted that the value of F_z here is assumed constant in which it represents the static load of the vehicle.

The second approach to calculate the variation of p_x is what adopted here in this study. A numerical function is implemented to calculate the slope of the tangent at a predefined value of slip rate, T_{opt} . The function, based on two values of slip rates nearly around T_{opt} , calculates the slope of the tangent drawn between these two points as illustrated in Figure 4.8.

In fact, the range of variation of p_x is highly depending on the value of T_{opt} . According to the used Pacejka tire model, and after analyzing the different response of F_x as a function of mass variation and road adhesion variations, the range of uncertainty of p_x is obtained. Figure 4.9 plots the variation of p_x as a function of 5000 samples of bounded random values of wheel contact static force F_z , and road adhesion μ . The green points represent the calculated values of p_x at each given sample (F_z, μ) . A random process is used to select random numbers from a predefined range of variations for

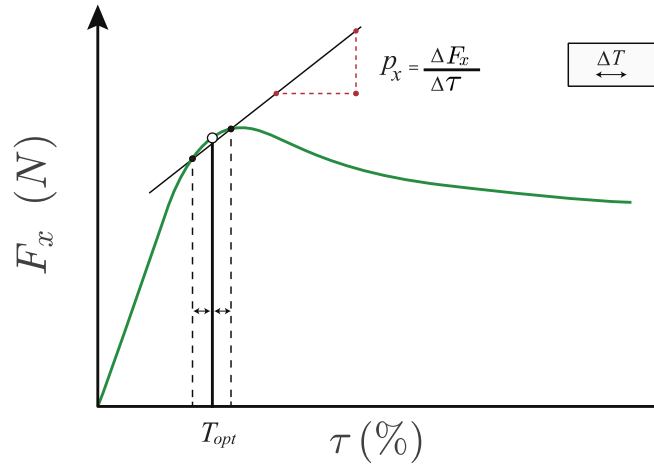


Figure 4.8. Second approach of calculating p_x .

4.3 Control system design

each parameter. The red contour represents the sorted samples (in terms of magnitude) in which it reveals the overall behavior of the variation of this parameter and indicates the extremums of such variations. The minimum and the maximum value are described by two dashed black lines as shown in Figure 4.9. It should be noted that these results are obtained at the wheel slip rate value of 7%.

However, each given value of slip rate results in a different range of variations of p_x . For this reason, for study and control design, it is critical to indicate the value of T_{opt} precisely. Table 4.2 lists the variations of the tire-force slope coefficient p_x as a function of specified values of slip rates.

Table 4.2. Range of variation of p_x as function the chosen of slip rate.

Wheel slip rate value T in %		Range of variation of p_x
7%	→	3200 – 6838
7.5%	→	2260 – 4590
8%	→	1355 – 2942
8.9%	→	95 – 810
$m \in [200 - 250]\text{kg}$ and $\mu \in [0.5 - 1]$		

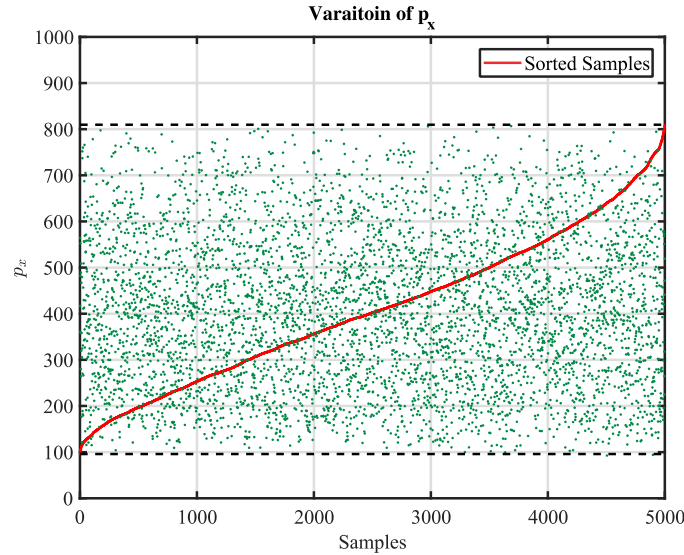


Figure 4.9. Variation of p_x as function of random samples of F_z and μ .

In this study, although the maximum values at which tire-force slope is in the range of 8.5-9%, the optimal value is considered $T_{opt} = 8\%$ in order to avoid fast switching between positive and negative values of p_x . For this reason, the values are chosen just behind the maximum value. As a result, in addition to the specified range of variations for m , V_x^e , and μ , the range of variation of p_x is then [1355- 2942].

Knowing that all the parameters of the plant transfer function $G(s)$ are now defined, then the frequency responses of the plant against uncertainties can be studied.

In order to analyze the influence of the parametric uncertainties on the frequency responses of the plant $G(s)$, 50 random plants were computed and plotted as shown in Figure 4.10 (yellow). As a result, three main plants were considered: $G_{nom}(s)$, $G_{min}(s)$, and $G_{max}(s)$. Figure 4.10 shows the responses of these plants, where their parametric configurations are detailed in Table 4.3.

Table 4.3. Parametric variation of $G(s)$.

Plant	V_x^e [m/s]	μ^e	m [kg]
G_{nom}	25	1	250
G_{min}	30	0.5	250
G_{max}	15	1	200

4.3.4 CRONE controller

The selection of the generation of CRONE controller, as illustrated in Chapter 1, depends mainly on the magnitude and phase behavior of the controlled nominal plant around the selected crossover frequency. Therefore, the cross over frequency should be assigned.

According to the previous section, the nominal plant's transfer function thus could be obtained and formulated as follows:

$$G_{nom}(s) = \frac{31250s + 16610}{250s^2 + 2567s + 149.2}. \quad (4.63)$$

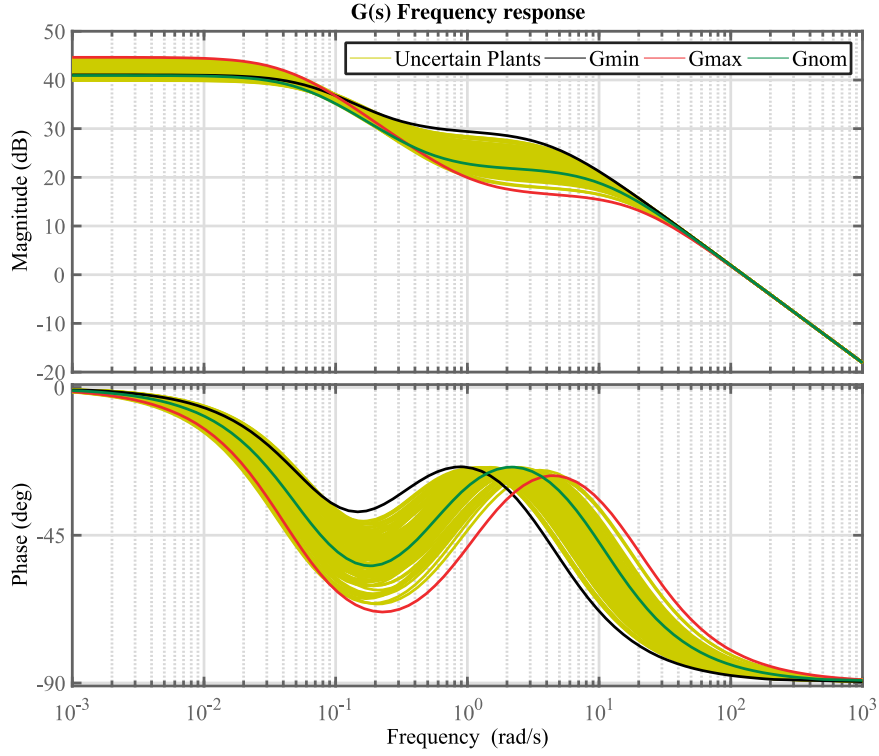


Figure 4.10. Bode diagrams of $G(s)$; $G_{nom}(s)$, $G_{min}(s)$, $G_{max}(s)$, and the yellow lines representing the variations of magnitude and phase for each frequency considering all parametric variations.

Taking into consideration the specifications of section 4.3.2, then the crossover frequency ω_{cg} can be easily now calculated. Based on the frequency response and the control sensitivity specifications, thus the upper bound for the crossover frequency is:

$$\omega_{cg} \leq 113 \text{ rad/s.} \quad (4.64)$$

Consequently, the third generation must be used since there are high variations of gain and phase of the plant due to parametric uncertainties at the desired open-loop gain crossover frequency ω_{cg} , as shown in Figure 4.10. The usage of this generation should provide more robust performance for the controller versus parametric variations. However, it is impossible to attain an ideal robustly controller with all these variations, therefore, the process

is directed to find the optimized controller for the robustness/performance tradeoff.

The open-loop transfer function with the 3rd generation CRONE controller is defined by an integrator of complex fractional-order $n = a + bi \in \mathbb{C}_i$, such that:

$$\beta(s) = \Re_{/i} \left(\frac{\omega_u}{s} \right)^n. \quad (4.65)$$

Its real part determines the phase location at ω_{cg} , such that $\text{Arg}\{\beta(j\omega_{cg})\} = -a\pi/2$, and its imaginary part determines the angle with the vertical of the Generalised template on the Nichols chart, as shown in Figure 4.11.

Figure 4.11 also shows various Nichols' magnitude contours. The closed-loop resonant gain M_{r0} corresponds to the value of the contour that is tangent to the nominal open-loop plot. Plant uncertainties are modeled by the ellipses around each frequency ω , causing an increase on the closed-loop resonant gain M_{rmax1} for the perturbed plants, as illustrated in Figure 4.11a. By choosing an adequate direction of the generalized template it is possible to minimize the effect of the plant uncertainties on the closed-loop resonant gain, as shown by the optimal template in Figure 4.11b.

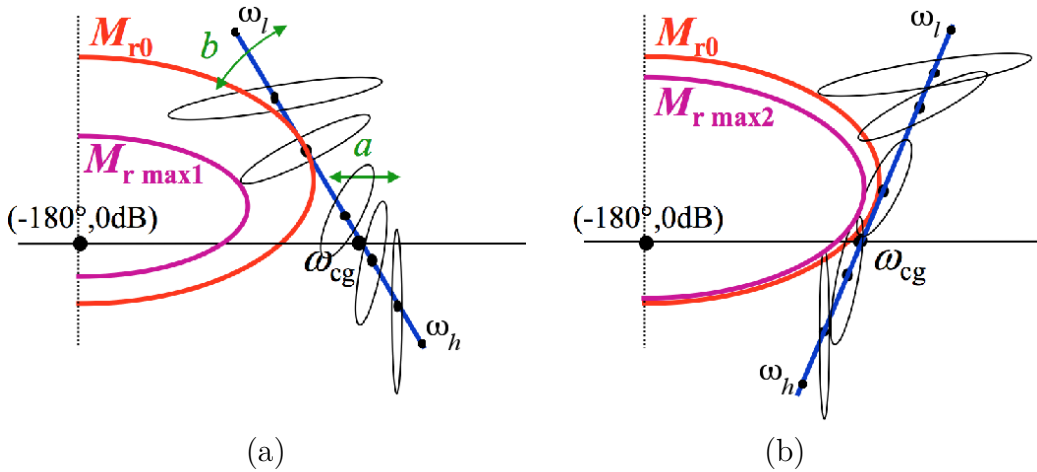


Figure 4.11. Generalized (a) and optimal (b) templates of open-loop for 3rd generation CRONE controller.

Hence, the 3rd generation CRONE controller design consists of an optimization to minimize the M_r variations computed by a robustness-oriented cost function defined by:

$$J = \sup_{\omega, G} |T(j\omega)| - M_{r0} \quad , \quad (4.66)$$

while taking into consideration the constraints based on the sensitivity functions, where $T(j\omega)$ here represents the complementary transfer function.

Four independent high-level parameters are optimized: ω_l , ω_h , resonant frequency ω_r , and open-loop gain at ω_r , namely Y_r which corresponds to the gain at the tangent point to the Nichols contour grid M_{r0} . The real and imaginary parts of the complex non-integer order a and b , depending on Y_r . Considering the bandwidth limitation in (4.56) and including integral and low pass effects, the open-loop becomes as follows:

$$\beta(s) = K \left(\frac{\omega_l}{s} + 1 \right)^{n_l} \left(\frac{1 + \frac{s}{\omega_h}}{1 + \frac{s}{\omega_l}} \right)^a \left(\Re_{/i} \left[\left(C_0 \frac{1 + \frac{s}{\omega_h}}{1 + \frac{s}{\omega_l}} \right)^{ib} \right] \right)^{-sign(b)} \left(1 + \frac{s}{\omega_h} \right)^{-n_h} \quad , \quad (4.67)$$

where,

$$C_0 = \left(\frac{1 + \left(\frac{\omega_r}{\omega_l} \right)^2}{1 + \left(\frac{\omega_r}{\omega_h} \right)^2} \right)^{\frac{1}{2}} \quad , \quad (4.68)$$

with n_l and $n_h \in \mathbb{N}^+$.

The values of n_l and n_h are selected considering the assigned specification and the frequency response of the controlled plant. Thus, for the proposed electro-mechanical ABS controller, it is chosen $n_l = 2$ in order to track ramp inputs (linear variation of $\Omega_{ref}(t)$). Then, in order to obtain better filtering of measurement noise, and considering the specified overshoot for a step response (30%), i.e. $|T(j\omega_r)_{nom}| \approx 3dB$, the order of low pass filter is chosen as $n_h = 2$.

The tuning parameters a , b , ω_l , and ω_h are used to shape the nominal open-loop frequency response. One aim of this loop shaping is to move the frequency uncertainty domains away from the critical point $(-\pi, 0)$. According to (Sabatier et al., 2015a), each parameter acts mainly on one shape feature of the nominal open-loop transfer function and thus can be optimized easily.

As the plant uncertainty is taken into account by the least conservative method, a nonlinear optimization method must be used to find the optimal values of the independent parameters. As the performance of the closed-loop system is as important as its stability degree of robustness, in order to manage precisely the performance related to tracking, regulation, and control effort level, while minimizing the cost function (4.66), the 3rd generation CRONE controller considers also 5 frequency-domain inequality constraints that have to be fulfilled for all the plants (with all parametric variations) and for every $\omega \in \mathbb{R}^+$:

$$\inf_G |T(j\omega)| \geq T_1(\omega), \quad (4.69)$$

$$\sup_G |T(j\omega)| \leq T_u(\omega), \quad (4.70)$$

$$\sup_G |S(j\omega)| \leq S_u(\omega), \quad (4.71)$$

$$\sup_G |CS(j\omega)| \leq CS_u(\omega), \quad (4.72)$$

$$\sup_G |GS(j\omega)| \leq GS_u(\omega). \quad (4.73)$$

Briefly from (Sabatier et al., 2015b), the bounds T_1 and T_u can be used to avoid the sluggishness of the response to a step variation, and could limit the lower value of the crossover frequency and the highest value of the resonant peak M_r . Then, S_u permits the limitation of the effect of the output disturbances by limiting the resonant peak of $|S(j\omega)|$, that could be addressed also by the lower value of the modulus margin M_m . Moreover, the bound CS_u is a boundary on the control effort sensitivity function and can be used to limit the control effort $u(t)$ with respect to measurement noise $b_m(t)$ and output disturbances. It should be noted that usually the

closed-loop bandwidth is usually limited by taking into account this constraint as in this study. Finally, bound GS_u is also useful in the case of the control of low-damped modes of the plant by limiting the effect of the disturbance $d_u(t)$, and thus ensuring the accuracy of the control loop.

The optimization is achieved by MATLAB using the CRONE toolbox. The main purpose of this toolbox is to calculate the CRONE controller transfer function based on the plant transfer function as well as the parametric uncertainties of the system. The toolbox can specify which generation is the most suitable to answer the user specifications and it can deliver the controller transfer function in a rational form after applying the Oustaloup's approximation. For interested authors, they can refer to the following references for more information concerning the toolbox and its characteristics (Lanusse et al., 2016, 2013; Malti et al., 2012, 2011; Malti and Victor, 2015; Oustaloup et al., 2002).

The resulting open-loop parameters of the CRONE controller, $C_{ABS}(s)$, are listed in Table 4.4. The resulting open-loop crossover frequency $\omega_{cg} = 90$ rad/s, satisfying the specifications of (4.64). Figure 4.12 shows a comparison between the fractional and the rational form of the controller's transfer function $C_{ABS}(s)$.

Table 4.4. Open-loop parameters of the 3rd generation CRONE controller.

Open-loop parameter	value
ω_l	55 rad/s
ω_h	165 rad/s
ω_r	55 rad/s
Y_r	5.5
a	0.4
b	0.8

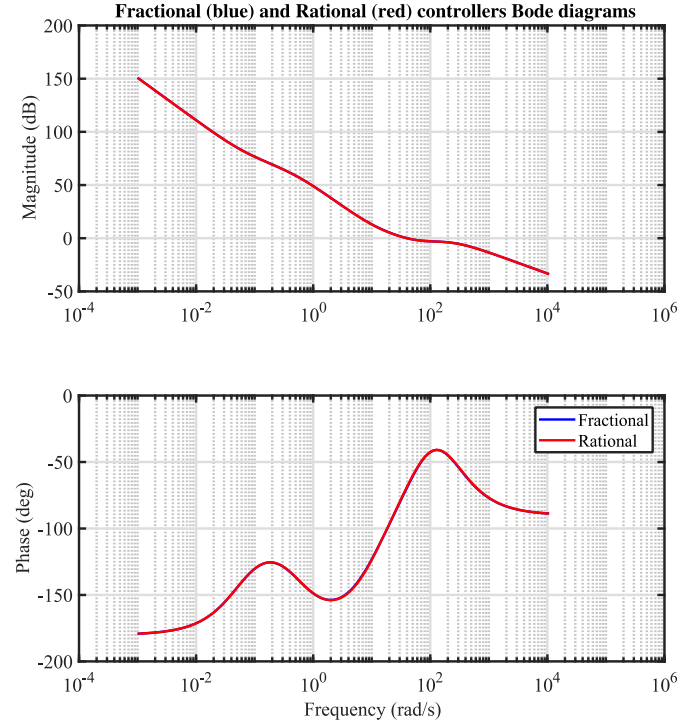


Figure 4.12. Bode response of the fractional and rational from of the controller $C_{ABS}(s)$ (toolbox).

4.4 Performance analysis

4.4.1 Frequency domain

Figure 4.13 shows the Bode response of the open-loop transfer function with the CRONE controller. It is shown that the cross over frequency varies between 88 - 90 rad/s versus plants' parametric variations. On the other hand, the phase margins vary in the range of 49 - 57 °. Figure 4.14 shows the Nichols diagram of the open-loop plants. It can be shown that the nominal transfer function (in green) is tangent to the 3dB Nichols magnitude contour, according to the design requirement at the open-loop gain Y_r .

The constraints imposed on the sensitivity function for the design of the controllers are represented with the dashed black lines in Figure 4.15 which also shows the magnitude of each sensitivity function considering the uncertain plants with the designed controller. Table 4.5 shows the maximum gain

4.4 Performance analysis

of each sensitivity function considering the perturbed plants. Since all of them satisfy the assigned constraints, then robustness is ensured.

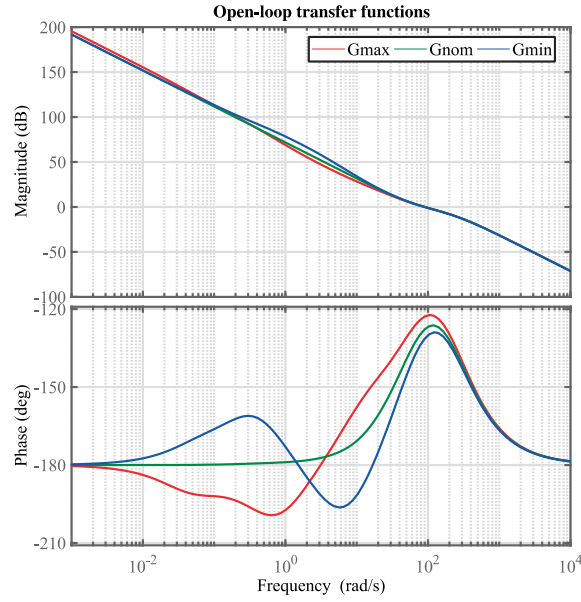


Figure 4.13. Bode response of open-loop transfer functions with CRONE controller.

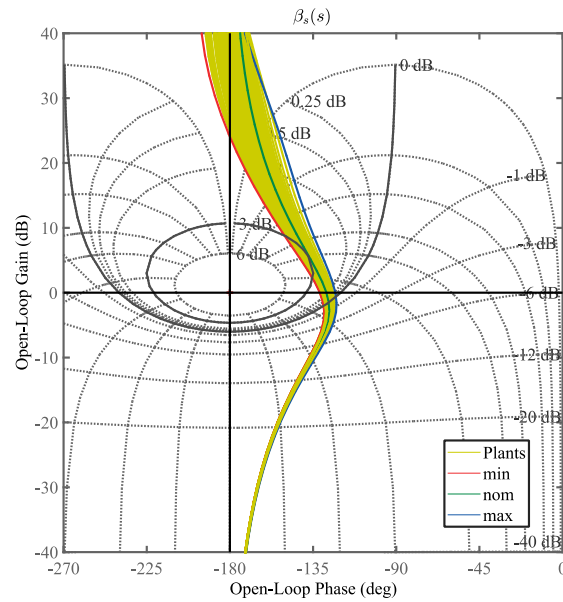


Figure 4.14. Nichols diagram for the open-loop transfer functions.

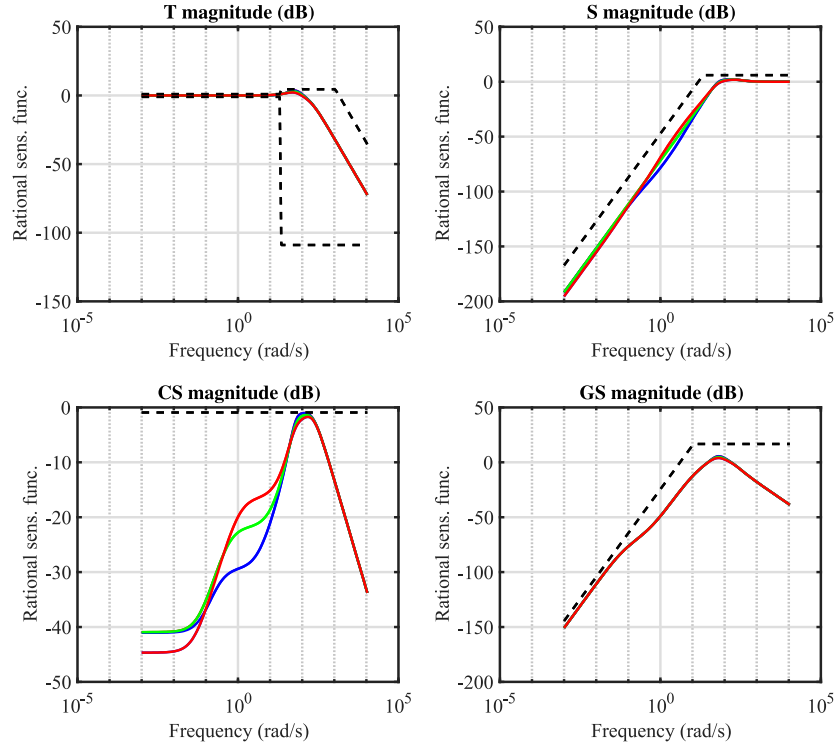


Figure 4.15. Frequency responses of sensitivity functions.

Table 4.5. Maximum gain in dB of sensitivity functions for perturbed $G(s)$.

	$T(s)$	$S(s)$	$CS(s)$	$GS(s)$
CRONE	3.6dB	2.3dB	-1dB	5.6dB

4.4.2 Time domain analysis

In order to evaluate the performance of the designed ABS controller, several testing scenarios were done. The quarter vehicle validation model used for testing is the one described in 4.2.2 while considering a different parametric configuration from that of nominal one to examine the robustness of the controller versus mass variations.

For comparison reason, two more controllers are designed, a first-generation crone controller, $C_{1ABS}(s)$ and a PID controller, $C_{PID}(s)$. Both controllers

are designed to have the same crossover frequency (Iso-rapidity) and the same stability margin with the nominal plant $G_{nom}(s)$. Figure 4.16 shows the bode response of the controllers compared to the designed third-generation CRONE controller. Figure 4.17 plots the Bode response on the open-loop transfer functions of the nominal plants with the three controllers. It can be seen that all of them have the same crossover frequency and stability phase margin.

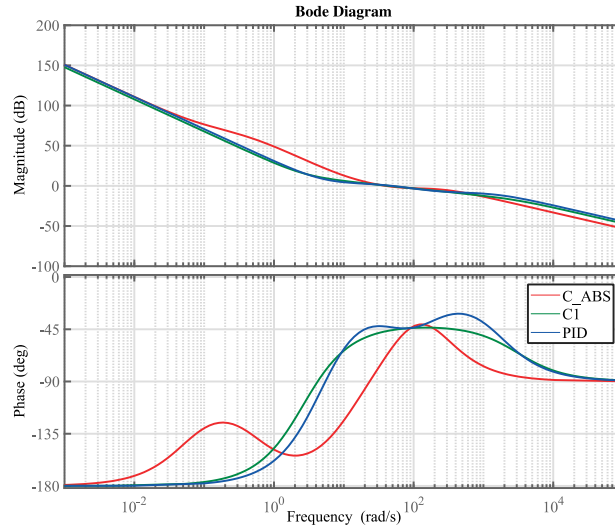


Figure 4.16. Bode response of the controllers' transfer function.

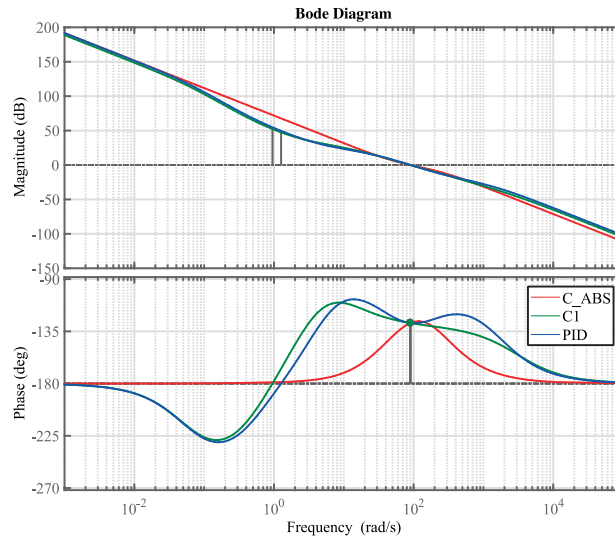


Figure 4.17. Bode response of the open-loop nominal transfer functions with controllers.

The first scenario (A) is a vehicle moving with an initial velocity of $V_x^e(t = 0) = 30m/s$, driven on a dry and even road ($\mu = 1$). The driver starts to slow down the vehicle by pressing the braking pedal slowly. The driver input has a steady-state position that corresponds to $U_c = 10V$.

Figure 4.18 shows the vehicle longitudinal and angular velocities of the different systems. The uncontrolled vehicle shows the worst braking performance, as it presents the highest braking distance (distance till $V_x = 0.5m/s$), which confirms the importance of ABS control. In fact, it can be seen that the ABS controllers prevent the wheels from locking. At $t = 2.3s$, the wheel slip rate, shown in Figure 4.19, becomes smaller than the T_{opt} , and therefore the ABS is activated. All controllers manage to satisfactorily track the wheel reference angular velocity. The corresponding control inputs are plotted in Figure 4.20. Up to 2.3s, only the feed-forward term is present, but once the ABS is activated, the feedback term counteracts in order to track $\Omega_{ref}(t)$, avoiding wheel locking-up.

It is also interesting to consider the influence of the measurement noise on the control input. For this reason, the power spectrum density is plotted for each control effort for every controller, as shown in Figure 4.21. It is clear that the 3rd generation CRONE controller designed has a lower PSD magnitude compared to other controllers. Such behavior can be explained by the high gains on the open-loop Bode response of other controller compared to the $C_{ABS}(s)$ (Figure 4.16). This filtering properties in high frequencies for the 3rd generation controller causes less agitation on the control input.

In this sense, such an advantage does not seem significant in the braking performance, where the braking distances are almost very close to each other, i.e. 50.69, 50.67, and 50.66m for PID, C_{1ABS} , and C_{ABS} , respectively. Nevertheless, it is very important mainly for two reasons (Benine-Neto et al., 2017): Firstly, it reduces the energy consumption of the actuator and increases its life-time; Secondly, if such control input agitation level, as for other PID controller, for example, is acceptable, then the CRONE 3rd generation design allows the use of lower quality (noisier) wheel speed sensors, which may be cheaper.

4.4 Performance analysis

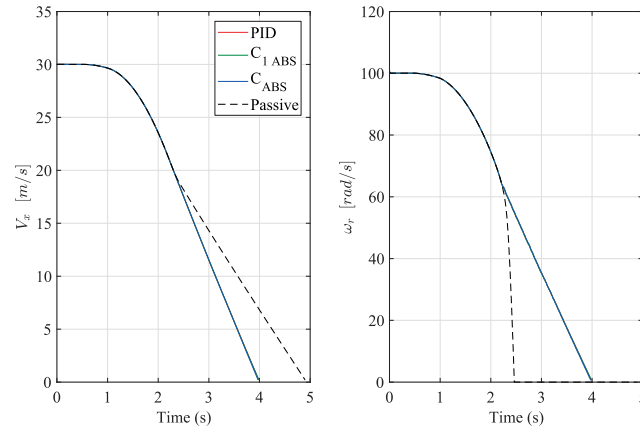


Figure 4.18. Longitudinal velocity and wheel angular velocity of the quarter car in braking scenario (A).

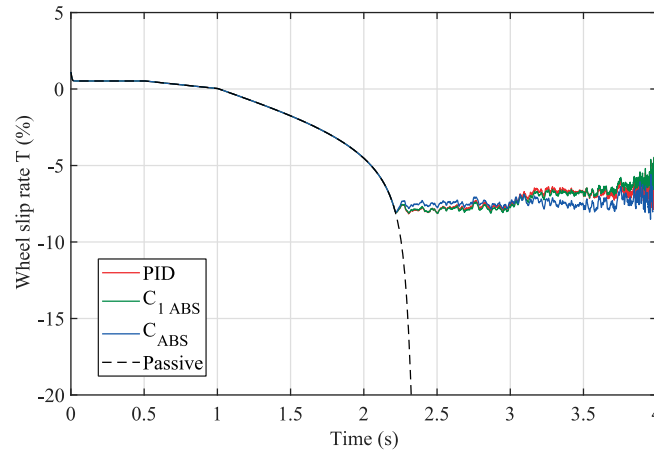


Figure 4.19. Slip rate of the quarter car in Scenario (A).

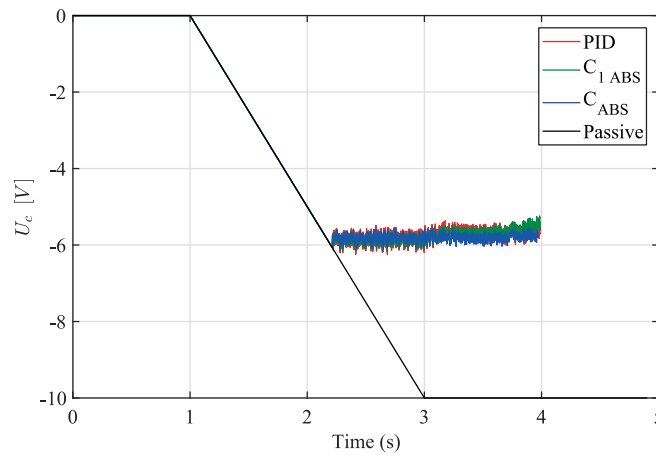


Figure 4.20. Control input for the quarter car in braking scenario (A).

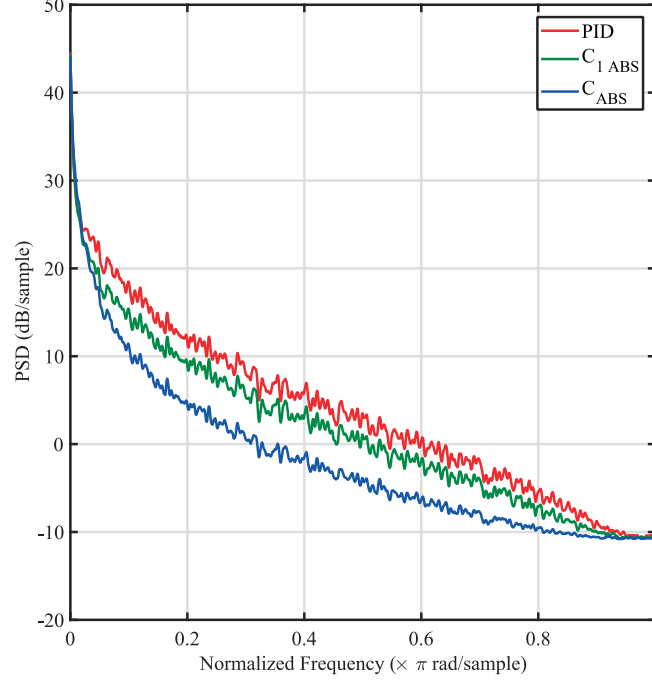


Figure 4.21. Power spectrum density of control efforts in braking scenario (A).

In order to examine the robustness of the controllers in the time domain against road adhesion variations, a second scenario is simulated. The second scenario (B) presents an emergency braking, where the driver input has a steady-state position corresponding to $U_c = 12V$ (full pedal displacement). The road adhesion is degraded from 1(dry) to 0.5 (wet) at $t = 2.5s$, i.e. $\mu = 0.5, \forall t > 2.5s$. All other parameters are the same as in scenario (A).

The braking distance are respectively 45.86, 45.79, and 45.65m for PID, C_{1ABS} , and C_{ABS} , respectively. The wheel is locked due to high braking pressure at 1.5s for the uncontrolled system. As shown in Figure 4.22, the controlled systems show a good performance in preventing wheel blocking. Moreover, at $t = 2.5s$ the controlled systems prove their ability to adapt to the variations on the road adhesion. As shown in Figure 4.23, all controllers responded to the adhesion variation at $t = 2.5s$, and in few milliseconds, they could track the references angular wheel velocities again. Figure 4.24 plot the control inputs for the different controllers.

As for scenario (A), in this scenario, the PSD graph for the control efforts are plotted in Figure 4.25. It clearly shows the advantage of the designed 3rd generation CRONE controller over the other controllers in the frame of power consumption.

The simulations done in this section takes into consideration only the longitudinal dynamics of the quarter vehicle model while neglecting the vertical dynamics. However, it is highly critical to consider the suspension dynamics and its effect on the performance of the ABS controller in cases where the load transfer is introduced, and more importantly, when the road is no longer even. Thus, the effect of load transfer is taken into consideration on the half-vehicle model, and road disturbances are then introduced on the quarter vehicle model. As a result, the ABS controller faces a new challenge of robustness and performance against high variations on the wheel contact vertical forces, denoted by F_z [N].

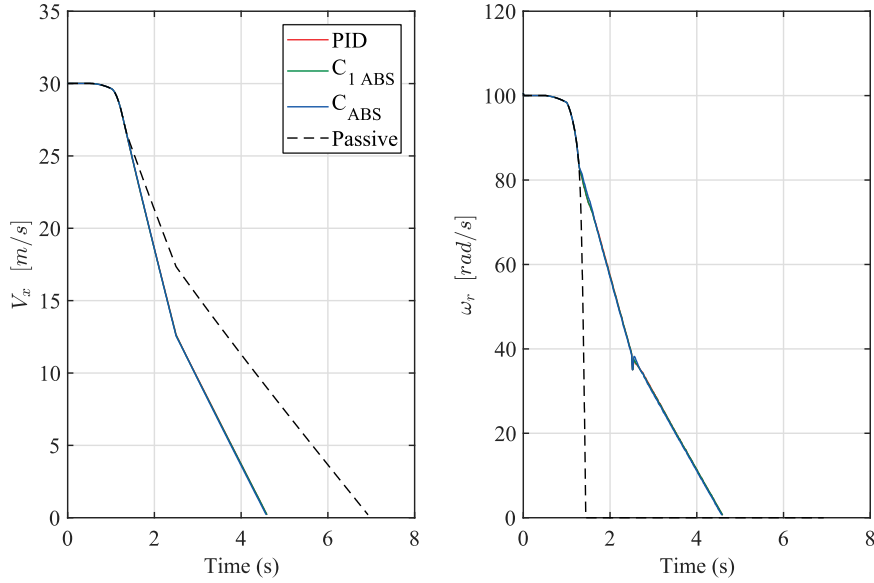


Figure 4.22. Longitudinal velocity and wheel angular velocity of quarter car in braking scenario (B).

4.4 Performance analysis

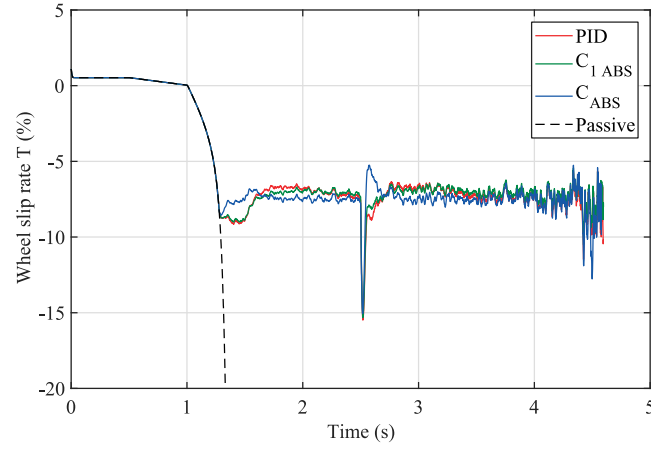


Figure 4.23. Slip rates of quarter car in braking scenario (B).

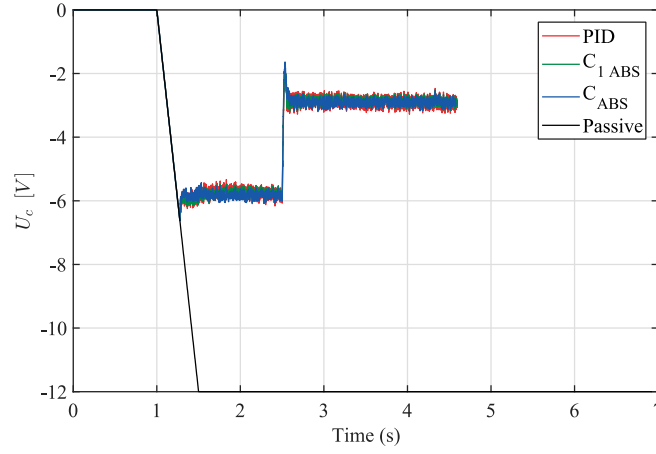


Figure 4.24. Control input for the quarter car in braking scenario (B).

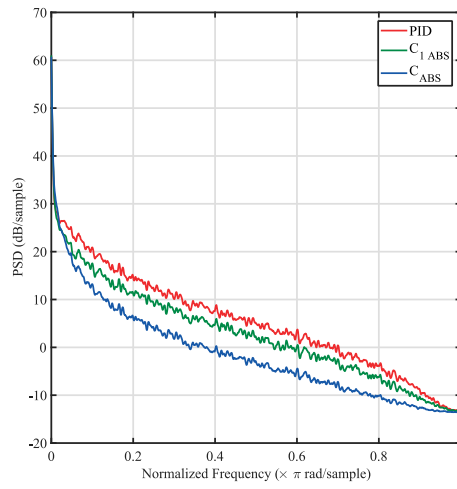


Figure 4.25. Power spectrum density of control efforts in braking scenario (B).

4.5 Effect of Vertical dynamics on the ABS control system

4.5.1 Introduction

Many theories and design methods for ABS and active suspension systems have been proposed individually over the years. As introduced in the last sections, the ABS system manipulates the braking of automobiles in order to prevent uncontrollable skidding in accidents as a result of locked-up wheels. It can provide directional stability and shortens the braking distance (Lin and Ting, 2007).

On the other hand, active suspension systems must be able to guarantee the ride comfort of passengers. Hence, in the design of active suspensions, the improvement of ride quality is a major control objective to be emphasized. In this framework, many control designs schemes were developed for both a quarter-car and a half-car active suspension system (Fialho and Balas, 2002; Huang et al., 2010; Lin and Huang, 2004), which aimed to improve the tradeoff between the ride quality of passenger comfort and the utilization of suspension travel.

The purpose of this section is to take advantage of the designed ABS controller combined with the active suspension system using the fractional damping control to further reduce vehicle braking time and stopping distance. During the braking process, if the vertical normal force is increased (this situation is equivalent to an increase of the weight of a car, driver disturbances, ...), the friction force between the car and road surface is increased to help the vehicle to stop in a shorter distance. As normal force cannot be increased naturally, active suspensions should, therefore, be the tool employed to achieve that adjustment of the normal force. With the choice of an appropriate integrated algorithm, the vertical normal force can be adjusted with the braking torque in order to achieve a reduction of braking time and stopping distance.

However, one main important cases in which the performance of the ABS control is degraded is when driving over rough terrain (Hamersma and Schalk Els, 2014; Kaldas et al., 2011; Sanchez-Torres et al., 2013). Not only

is the effective rolling radius is changing due to undulations in the road surface, but the vertical and torsional dynamics of the wheel may be excited to such an extent that contact between the tire and the road is lost or that the tire starts oscillating. The tire oscillation has a significant effect on the performance of an ABS system (Adcox et al., 2012).

As stated in (Hamersma and Schalk Els, 2014), the situation is further complicated by the so-called run-in effect of tire force generation. Gillespie (Gillespie, 1992) describes the run-in effect stating that a tire's response to a step input is not instantaneous. The lag is related to the rotation of the tire, typically taking between one-half and one full revolution of the wheel to reach the steady-state force condition. A varying vertical load on the tire, as is the case when driving over a rough road, thus further complicates the optimum application of ABS. When the wheel load increases, the size of the contact patch is increased with rubber that is not deformed. The 'new' rubber has to deform before it generates a significant longitudinal force, which lags the increase in vertical load. In contrast, when the wheel load decreases, the contact patch area decreases and the force generated is decreased instantaneously. Furthermore, due to the low damping present in the tire, natural frequencies may be excited due to the terrain input and the periodic braking input from the ABS. The net effect of this process is a reduction in the brake force and increased stopping distances (Breuer and Bill, 2008).

Therefore, due to this coupling effect between the suspension dynamics and the braking system (Hamersma and Schalk Els, 2014), active suspension control laws, where the strategy is comfort-oriented, may degrade the performance of braking on rough roads. Indeed, the active suspension forces introduced by the electric actuator affect the wheel normal forces, which in turn impact the wheel longitudinal contact forces that are directly responsible for the braking behavior of a vehicle. For this reason, a convenient combination between ABS control and Fractional-order damping control is proposed to minimize the effect of road roughness on the performance of the braking system of the vehicle.

4.5.2 Dynamic model

In this study, the half vehicle model is adopted, representing the motion of the two-wheeled car model, as shown in Figure 4.26. There are four

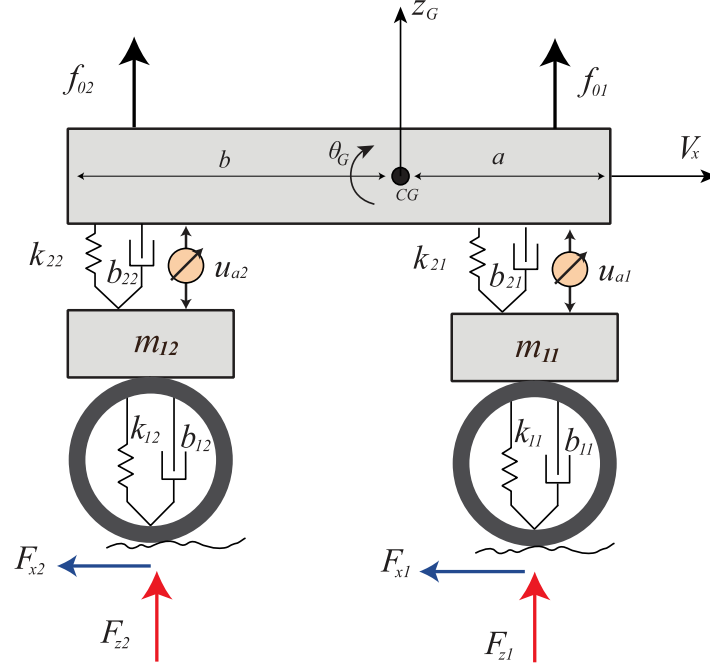


Figure 4.26. Half-car model.

equations to derive a linear model for the vertical dynamics and three equations to derive a nonlinear model for the longitudinal dynamics.

The only difference here in this study is the addition of the vertical dynamics of the quarter vehicle model, and the chassis dynamics, i.e. heave and pitch motion. Moreover, the vertical wheel normal forces F_z are no longer static, and it includes wheel dynamics. Thus, it is formulated as follows:

$$F_{zi}(t) = m_i g + f_{1i}(t), \quad (4.74)$$

where $i = 1$ for front axle $i = 2$ for the rear axle. The dynamic force $f_{1i}(t)$ is formulated as in (2.2) in chapter 1. The forces f_{0i} represented in Figure 4.26 are the front and rear load shift due to the longitudinal acceleration or deceleration, formulated as:

$$f_{01} = \frac{h + z_G}{(a + b)} M a_x(t), \quad (4.75)$$

and

$$f_{02} = -\frac{h + z_G}{(a + b)} M a_x(t). \quad (4.76)$$

The heave and pitch motion of the chassis could be calculated using the dynamics of the front and rear sprung masses, by:

$$\begin{aligned} z_{21} &= z_G - a \sin(\theta_G), \\ z_{22} &= z_G + b \sin(\theta_G). \end{aligned} \quad (4.77)$$

Supposing that θ_G has a small value, and using the inverse of (4.77), we get the following relation:

$$\begin{pmatrix} z_G \\ \theta_G \end{pmatrix} = \begin{pmatrix} 1 & -a \\ 1 & b \end{pmatrix}^{-1} \begin{pmatrix} z_{21} \\ z_{22} \end{pmatrix}. \quad (4.78)$$

4.5.3 Control structure

For purpose of comparing the performance and analyzing the different effects of the vertical dynamics characteristics, the fractional-order damping control discussed in Chapter 2 is introduced and for ABS control the 3rd generation CRONE controller designed in the previous section is adopted here as it demonstrated the best performances among the three controllers studied.

4.5.4 Testing simulations

In order to test the influence of the vertical dynamics of the vehicle on the ABS control process, different scenarios should be done, each one to analyze one variable at a time. All simulations are done using the same scenario made in the previous sections where a vehicle starting at an initial speed of $V_x(t = 0) = 30m/s$. Two kinds of disturbances are taken into account to excite the vertical dynamics, the driver disturbance and road irregularities, each one using its convenient vehicle model.

4.5.4.1 Driver disturbance

Passive suspension

At first, two simulations were done to compare the system's performance with and without vertical dynamics. At this stage, the road is taken perfectly

even so that we study the effect of the load shift only. Here, the ABS system is deactivated during all the simulation time.

Figure 4.27a shows the wheel slip rate behaviors of the two systems for front and rear axles. Figure 4.27b plots the vehicle longitudinal velocity where it shows that the two systems have identical dynamics except for a small duration around $t = 3s$. In Figure 4.28a and b, the wheel normal forces and the longitudinal forces are plotted respectively. Due to the variation of the load transfer at each axle, it influences the wheel contact forces, and as a result, we could observe the difference between the two systems in the values of the longitudinal forces at each wheel. As a result, the braking difference of these systems is recorded as 64.41 and 64.74m, for a system without and with the suspension system, respectively.

Passive suspension with ABS Control

We consider the previous scenario, with an ABS controller implemented at each wheel. The braking distance is respectively, 54.92 and 55.44m for the system without and with the suspension system. Figure 4.29 shows the wheel slip rate response and the longitudinal velocities of the vehicle, in which the latter shows a little bit difference between the two systems that explain the difference found in the braking distances. Figure 4.30 shows the wheel normal forces and the longitudinal forces, in which it describes the effect of the variation of the load transfer on the vehicle.

In both testing scenarios, it was concluded that the introduction of the vertical dynamics degraded the overall performance of the braking system. Although of the increase in the longitudinal forces on the front axle for the systems with a suspension due to load transfer, but we can see the high reduction on the rear longitudinal forces on both cases. These variations lead to obtaining a degradation on the value of the stopping distances. It should be noted that these responses may highly depend on the tire characteristics and the testing scenario. However, this conclusion could be generalized due to its consistency with several studies found in the literature.

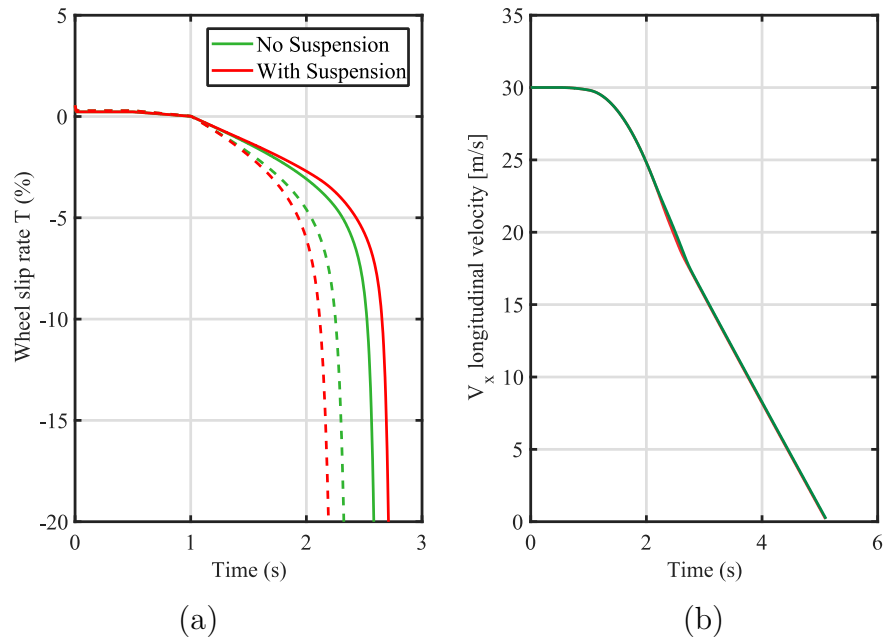


Figure 4.27. Braking performance of the system with and without vertical dynamics: (a) wheel slip rate and (b) the vehicle longitudinal velocity, front axle (—) and rear axle (- -).

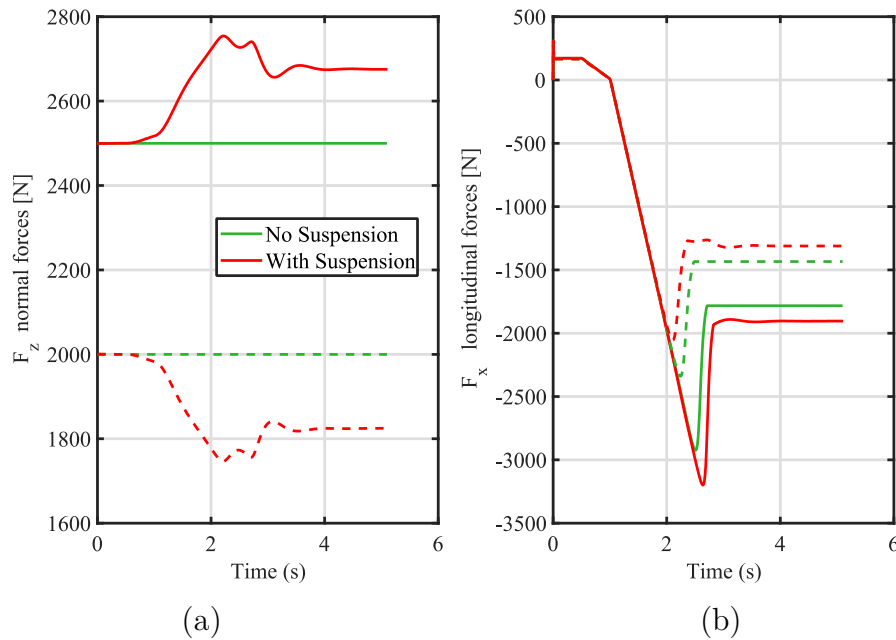


Figure 4.28. Braking performance of the system with and without vertical dynamics: front axle (—) and rear axle (- -).

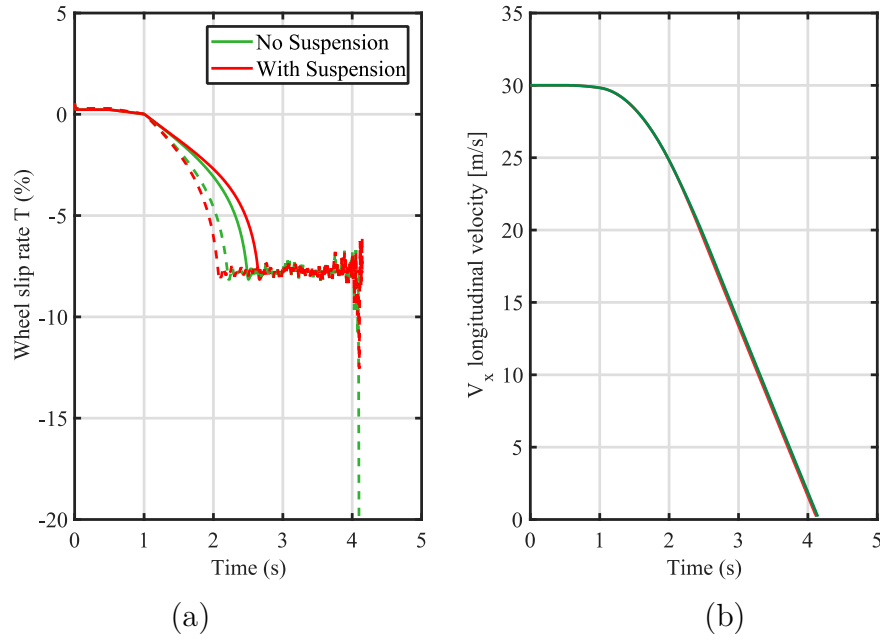


Figure 4.29. Braking performance of ABS controlled systems with and without vertical dynamics: (a) wheel slip rate and (b) the vehicle longitudinal velocity, front axle (—) and rear axle (- -).

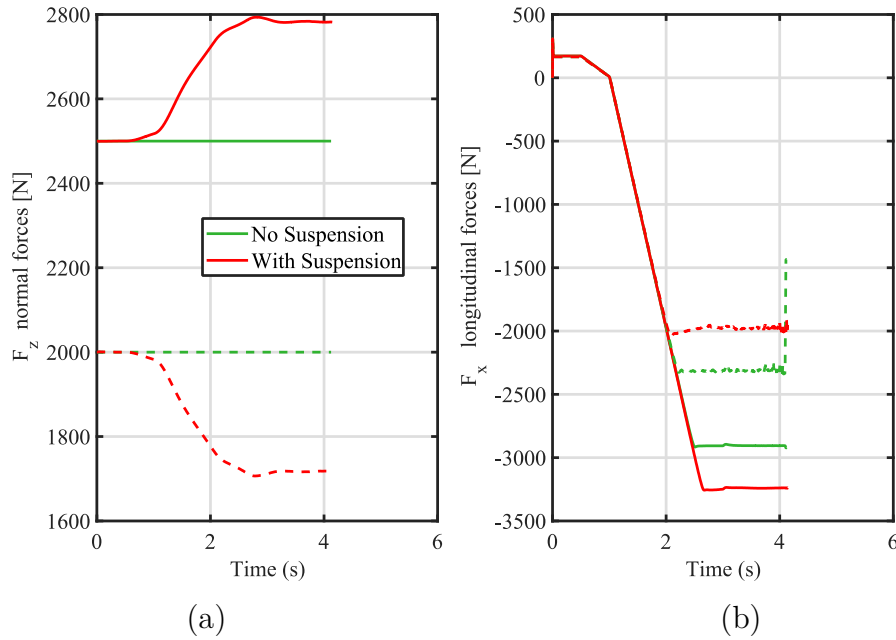


Figure 4.30. Braking performance of ABS controlled systems with and without vertical dynamics: front axle (—) and rear axle (- -).

Controlled suspension With ABS system

Two more simulations were done, one with a passive suspension system and controlled ABS and another one with a controlled suspension system and ABS controller. The second system was tested for three fractional-order damping configurations as described in Chapter 2, i.e. $n = 0.65$, $n = 1.1$, and $n = 1.4$. The braking distances of these simulations gave very close values that are around 55.44m.

4.5.4.2 Road disturbances

Many testing simulations were done taking into consideration road roughness. The results of these simulations are listed in 6 different tables. Tables 4.6 4.7, and 4.8 present the results on the front axle quarter vehicle model, while Tables 4.9, 4.10, and 4.11 correspond to the rear axle quarter vehicle model. Tables 4.6 and 4.9 are for the braking distance without an ABS control system, Tables 4.7 and 4.10 are for systems with ABS control system with $T_{opt} = 8\%$, and finally Tables 4.8 and 4.11 are for systems with ABS control system but with $T_{opt} = 7\%$, where (A) means a normal braking scenario and (B) is an emergency braking scenario.

The overall performance leads to the following conclusions:

- The results confirm the deteriorative effect of the road unevenness on the braking performance where higher stopping distances were observed in all tested configurations.
- They also confirm the ability of the designed ABS control strategy in reducing braking time and distances, and thus attain more safety for passengers and pedestrians, in different configurations.
- The passive suspension system effect becomes more significant in emergency braking scenarios on systems with ABS controllers, thus, necessitating more future attention. It should be noted that this effect is more indicative on heavier vehicles, in which for front axle it recorded up to 55cm difference compared to the rear axle quarter vehicle model in which the maximum difference was few centimeters.
- The convenient selection of the optimal value of the wheel slip rate plays an important role where all the braking distances obtained with

$T_{opt} = 8\%$ were less than those obtained with of $T_{opt} = 7\%$, more specifically, they were 0.6m smaller on average.

- The FO damping control shows an advantage in reducing the braking distance where $n = 1.1$, compared to other fractional-orders and even compared to the passive suspension system.

For further analysis of the key role of FO damping control for this enhancement in braking distance, three selected scenarios were plotted, where Figure 4.31 and 4.32 show the wheel contact forces and longitudinal forces respectively. The results were shown for a quarter vehicle model controlled with the designed ABS control while considering a fractional damping control with $n = 0.65$ (comfort-oriented), $n = 1.1$ (road holding oriented), and a system without vertical dynamics (no suspension).

The road-holding oriented FO damping control was able to reduce the variation of the wheel normal contact forces, thus, the variation of the longitudinal forces F_x , as illustrated in Figure 4.31 and 4.32, respectively. The RMS values of these forces relative to the system without vertical dynamics are listed in Table 4.12. It shows a reduction of 8.5% and 7% for $n = 1.1$ compared to passive system, and 38% and 34% compared to $n = 0.65$, in the RMS values of F_z and F_x respectively.

4.5.5 Conclusion

The test simulations on the quarter vehicle model show that rough terrain excitation further contributes to dynamic tire effects such as loss of vertical contact and poor contact patch generation that leads to reduced longitudinal force generation.

It is concluded that the combined use of the ABS control and a convenient active suspension control can be a useful approach in the research of ABS braking on rough terrains. Moreover, the effect of load shifting is studied on the ABS control on the half-vehicle model. The results show a degradation in the performance of the ABS control due to the variation of wheel normal contact forces at the front and rear axles. In this sense, the fractional-order damping control seems not efficient in improving braking performance in even road scenarios.

4.5 Effect of Vertical dynamics on the ABS control system

Table 4.6. Braking distances of systems without ABS control (front axle model).

Braking Distance [m]					
No ABS	Without Suspension	Passive Suspension	Fractional-order Damping Controlled Suspension		
			n=0.65	n=1.1	n=1.4
(A)	61.42	61.74	61.47	61.84	62
(B)	55.48	55.64	55.75	55.59	55.71

Table 4.7. Braking distances of systems with ABS control (front axle model)
with $T_{opt} = 8\%$.

Braking Distance [m]					
ABS ($T_{opt} = 8\%$)	Without Suspension	Passive Suspension	Fractional-order Damping Controlled Suspension		
			n=0.65	n=1.1	n=1.4
(A)	53.56	54.11	54.34	54.08	54.55
(B)	39.24	40.04	40.76	40	40.69

Table 4.8. Braking distances of systems with ABS control (front axle model)
with $T_{opt} = 7\%$.

Braking Distance [m]					
ABS ($T_{opt} = 7\%$)	Without Suspension	Passive Suspension	Fractional-order Damping Controlled Suspension		
			n=0.65	n=1.1	n=1.4
(A)	53.86	54.15	54.73	54.08	54.94
(B)	39.81	40.64	41.47	40.58	41.15

4.5 Effect of Vertical dynamics on the ABS control system

Table 4.9. Braking distances of systems without ABS control (rear axle model).

Braking Distance [m]					
No ABS	Without Suspension	Passive Suspension	Fractional-order Damping Controlled Suspension		
			n=0.65	n=1.1	n=1.4
(A)	57.99	58.39	58.72	58.24	58.37
(B)	53.59	53.65	53.78	53.64	54.06

Table 4.10. Braking distances of systems with ABS control (rear axle model)
with $T_{opt} = 8\%$.

Braking Distance [m]					
ABS ($T_{opt} = 8\%$)	Without Suspension	Passive Suspension	Fractional-order Damping Controlled Suspension		
			n=0.65	n=1.1	n=1.4
(A)	49.34	49.85	50.35	49.78	50.28
(B)	37.92	38.51	39.04	38.47	39.03

Table 4.11. Braking distances of systems with ABS control (rear axle model)
with $T_{opt} = 7\%$.

Braking Distance [m]					
ABS ($T_{opt} = 7\%$)	Without Suspension	Passive Suspension	Fractional-order Damping Controlled Suspension		
			n=0.65	n=1.1	n=1.4
(A)	49.77	50.34	50.86	50.28	50.75
(B)	38.63	39.23	39.78	39.2	39.88

4.5 Effect of Vertical dynamics on the ABS control system

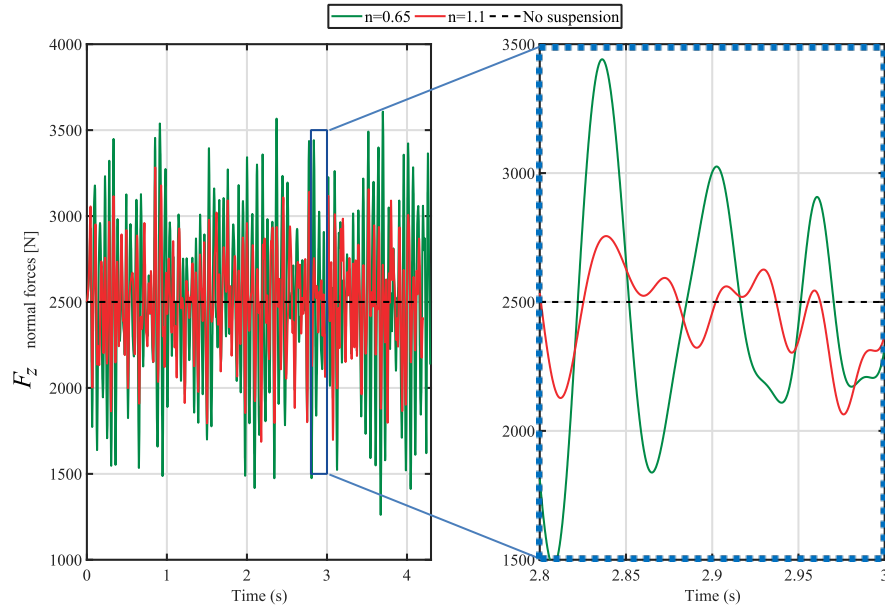


Figure 4.31. Wheel contact forces with ABS control and FO damping control.

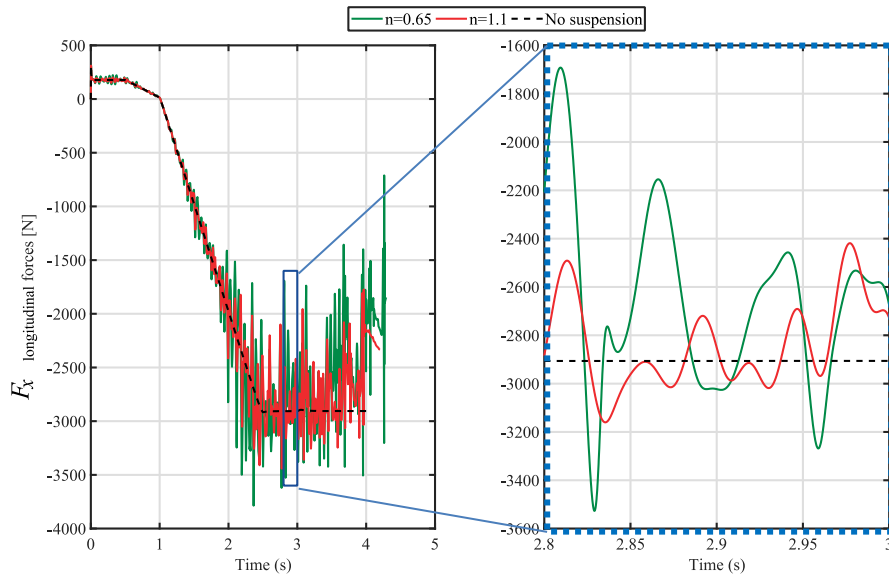


Figure 4.32. Longitudinal forces with ABS control and FO damping control.

Table 4.12. RMS values for wheel forces with FO damping controllers.

RMS	Passive	$n = 0.65$	$n = 1.1$
F_z [N]	305	454	280
F_x [N]	262	363	240

4.6 Conclusion

Many factors could affect vehicle's safety in road traffic situations. One main factor is the wet or slippery road surfaces and the abrupt reaction of the driver. In such hazardous driving conditions, it is possible for the wheels of a vehicle to lock up under high braking torque. As a result, the vehicle can become uncontrollable or may go into a slip or leave the road. Here, the antilock braking control system detects the tendency of the wheels to lock up under braking and regulate the braking pressure conveniently to prevent the wheels from locking up and the vehicle, thus, remains steerable. As a consequence, the vehicle can be braked or stopped quickly and safely.

For this reason, a 3rd generation CRONE controller was designed in order to track a reference value for the wheel angular velocity that attain enhanced braking performance. In the framework of the quarter vehicle model, the controller designed proves its ability in tracking the generated reference, and thus, reducing the braking distance. Besides model parametric variations, the designed controller shows its robustness against high road adhesion variations. Moreover, the simulation results show the 3rd generation CRONE controller was less sensitive to noise measurement compared to a 1st generation CRONE and PID controller.

However, due to the coupling effect between the vertical and longitudinal dynamics, the influence of load shifting and wheel fluctuations due to road excitations were studied. Road input excitation deteriorates braking performance which results in longer stopping distances due to a number of suspensions and tire contributing factors, in addition to the vehicle's body motions such as heave and pitch that are excited by rough road or driver input. It was shown that the rough terrain braking problem can essentially be improved with suitable fractional-order damping suspension control.

This study can be extended to include another suspension control algorithm that might improve the braking performance. Moreover, investigation of the role of ABS in stabilizing the vehicle during maneuvering is to be considered later on. In fact, the system should also be able to ensure that handling stability and steerability are maintained.

Chapter 5

Vehicle Stability Control

Contents

5.1	Introduction.....	204
5.2	Vehicle model.....	205
5.3	Yaw rate regulation by corrective yaw moment	213
5.4	Yaw rate regulation by active steering.....	223
5.5	Lateral position Control.....	234
5.6	Effect of the Vertical dynamics on the lateral stability control	242
5.7	Conclusion	248

5.1 Introduction

Many active systems have been widely used in automotive vehicles in order to increase safety and avoid accidents. For light electric vehicles, it is essential to give importance for lateral stability during a maneuver. The two most famous active systems that are used to provide lateral stability are the anti-lock braking systems (ABS) (Benine-Neto et al., 2017) and the Electronic Stability Program (ESP).

Several studies exist in the literature dealing with yaw rate regulation, and could be divided into three categories: regulation with an active steering system that provides additional steering angle (Benine-Neto et al., 2010), regulation with differential braking to create the needed moment around the z-axis of the chassis (Wang et al., 2011), and finally a coordination control strategy that combine both active systems to improve stability and safety for vehicles (Termous et al., 2018b). These objectives were achieved using a different kind of controllers that used to regulate the yaw motion. Starting from the very simple methods using PID controller (Deur et al., 2010), to the sliding mode controller (Tchamna and Youn, 2013), the H_∞ controller (LIAN et al., 2015), the backstepping (Zhou and Liu, 2010), model predictive control (MPC) (Xu et al., 2020), and many others.

In this chapter, the study is focused on yaw motion control, and the objective is to enhance the performance of the lateral dynamics of the vehicle. This can be achieved by introducing a well-designed controller that could help the driver, through additional yaw moment, to avoid skidding out of the trajectory when a sudden change of road adhesion occurs, the side wind force is applied to the vehicle, or upon emergency maneuvering. In fact, the yaw moment can be provided by two main actuators: the braking actuator and the steering actuator. For this purpose, two controllers were designed individually, in the sense of regulating yaw rate dynamics. The study was aimed at examining the performance of each controller at a time, the future work was assigned to implement adequate coordination between these active systems for an optimized performance of the vehicle's stability. However, since enhancing the vehicle's stability doesn't lead always to the best lateral position for a vehicle, another controller was designed to track a generated reference for the lateral position.

The efficiency of each controller can be analyzed by its effectiveness in regulating the yaw rate or lateral position of the vehicle to its reference against disturbances, and its robustness against uncertain parameters of the vehicle. Starting from the velocity of the vehicle to the total mass, and last but not least the road adhesion that has the biggest influence on steering performance (Monot et al., 2017).

Finally, since most studies on lateral stability don't take into consideration the effect of the vertical dynamics on the lateral control, our purpose in this study is to highlight the effect of the vertical dynamics of the chassis on the performance of the designed lateral controllers.

5.2 Vehicle model

In this section, all the notations in lower case are considered as variations and all physical variables without capital letter notations are variables whose reference are zero. Finally, the Laplace transform of the variation $x(t)$ is noted as $X(s) = TF\{x(t)\}$.

5.2.1 Schematization and configuration

In this study, the Four-wheel vehicle model (FWVM) was used, commonly called the two tracks model as seen in Figure 5.1, and it is widely addressed in the literature to study the transversal vehicle behavior (Rajamani, 2012b).

The first remark concerning this model is that the steering input angle introduced by the driver, β_v , is considered less than 10° . Moreover, the width of both axles is considered equal, that is the vehicle is symmetric with respect to the x-axis. Regarding the active systems, all used actuators are assumed ideal, that is all control efforts designed are introduced directly to the vehicle model where the actuator dynamics were neglected.

The chosen vehicle velocities are considered constant in this study, assuming the vehicle is equipped with active cruise control. The value of this speed is selected around 50km/h. Some test scenarios could consider a speed higher than 50km/h to analyze the effect of high velocities on the stability of the designed controller.

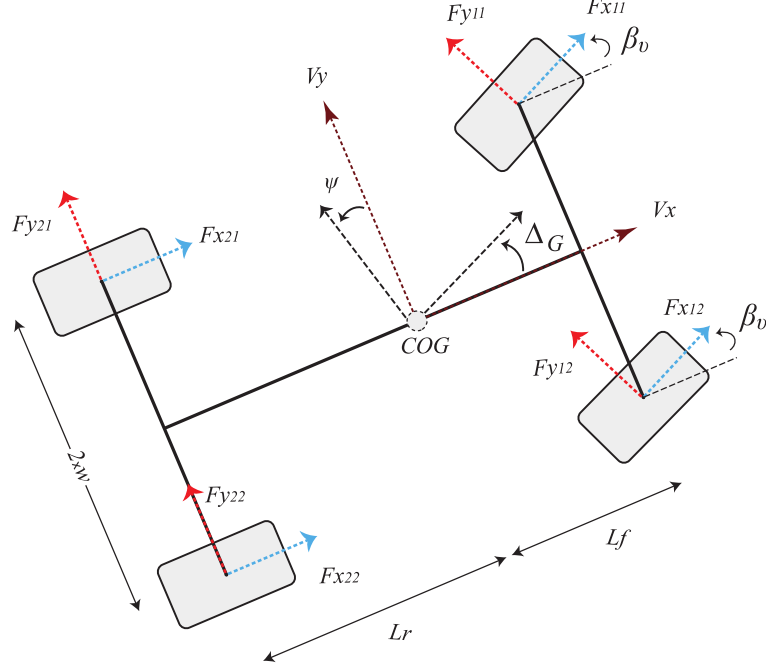


Figure 5.1. Four-wheel model schematization.

5.2.2 Dynamic equations

The main equation describing the yaw motion of the lateral model is given by:

$$\begin{aligned}
 I_z \ddot{\psi} = & w \left(\cos \beta_v (F_{x12} - F_{x11}) + \sin \beta_v (F_{y11} - F_{y12}) \right) \\
 & + L_f \left(\sin \beta_v (F_{x11} + F_{x12}) + \cos \beta_v (F_{y12} + F_{y11}) \right) \\
 & - L_r (F_{y22} + F_{y21}) - w (F_{x21} - F_{x22}) + M_{res},
 \end{aligned} \tag{5.1}$$

where I_z is the moment of inertia, M_{res} represents the resistance moment about the z-axis, and F_x and F_y are respectively the longitudinal and the transversal forces applied on the tires. The variable β_v represents the steering angle introduced by the driver, Δ_G is the sideslip angle at the CG, and w , L_f and L_r are the chassis' dimensions as illustrated in Figure 5.1.

The equation representing the lateral acceleration a_y , in the vehicle frame of reference, is given by:

$$a_y = \dot{V}_y + V_x \dot{\psi}, \tag{5.2}$$

where V_x represents the longitudinal speed of the vehicle, $\dot{\psi}$ represents the yaw rate, and V_y is the lateral speed. The variable \dot{V}_y can be expressed by the following equation:

$$\begin{aligned} M\dot{V}_y = & -M\dot{\psi}V_x - f_{y0} + \sin\beta_v(F_{x12} + F_{x11}) \\ & + F_{y22} + F_{y21} + \cos\beta_v(F_{y12} + F_{y11}), \end{aligned} \quad (5.3)$$

where f_{y0} represents the side wind gust applied on the center of gravity of the vehicle. The tire forces are generated according to the well-known Pacejka Model (Pacejka, 2012), where more than 30 empirical parameters are needed to fully describe the experimental measurements. The calculation of these forces depends mainly on the value of the road adherence μ , the tire ground contact forces F_z , and Δ_p the tire's sideslip angle. The sideslip angle at the center of gravity of the vehicle can be described by:

$$\Delta_G = \frac{V_y}{V_x}. \quad (5.4)$$

The inputs and outputs of the tire model are described in Figure 5.2, in which the inputs are:

- The wheel vertical normal force $F_z(t)$,
- The tire's sideslip wheel angle $\Delta_p(t)$,
- the road adhesion μ ,
- the wheel slip rate $T(Vx(t), \Omega(t))$.

More precisely, the relationship between $\Delta_p(t)$ and the lateral wheel forces are given, according to the magic formula, by:

$$F_y(t) = \mu D_y \sin \left[C_y \arctan \left(B_y \left[(1 - E_y) \Delta_p(t) + \frac{E_y}{B_y} \arctan (B_y \Delta_p(t)) \right] \right) \right], \quad (5.5)$$

where the parameters B_y , C_y , D_y , and E_y depend mainly on the characteristics of the tire used and on the value of the normal force $F_z(t)$.

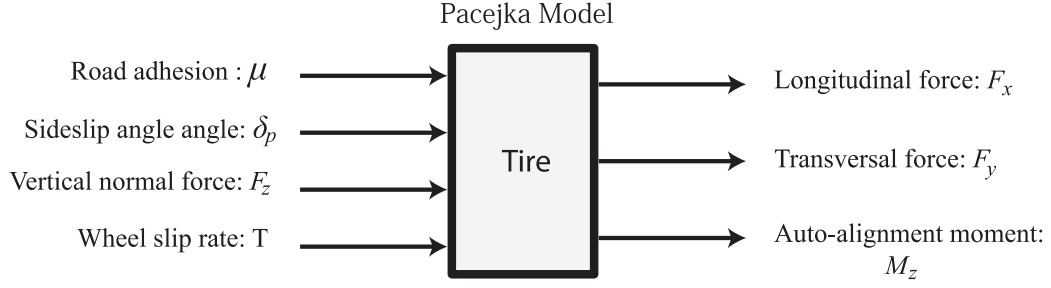


Figure 5.2. Black box model of the tire.

The wheel sideslip angle dynamic is formulated for each wheel as follows:

$$\begin{aligned}
 \Delta_{p12} &= \beta_v - \arctan\left(\frac{\dot{y} + L_f \dot{\psi}}{\dot{x} + w \dot{\psi}}\right), \\
 \Delta_{p11} &= \beta_v - \arctan\left(\frac{\dot{y} + L_f \dot{\psi}}{\dot{x} - w \dot{\psi}}\right), \\
 \Delta_{p22} &= -\arctan\left(\frac{\dot{y} - L_r \dot{\psi}}{\dot{x} + w \dot{\psi}}\right), \\
 \Delta_{p21} &= -\arctan\left(\frac{\dot{y} - L_r \dot{\psi}}{\dot{x} - w \dot{\psi}}\right).
 \end{aligned} \tag{5.6}$$

5.2.3 Equation of the trajectory

The trajectory of the vehicle is defined by the coordinates $X_G(t)$ and $Y_G(t)$ of the center of gravity CG in the absolute reference frame of the vehicle (R_0).

The coordinates $X_G(t)$ and $Y_G(t)$ are obtained by integrating the components $\dot{x}_G(t)$ and $\dot{y}_G(t)$, the speeds of the center of gravity, defined in the absolute frame of reference R_0 , that is:

$$\vec{V}_{G/R_0} = V_{x0} \vec{x} + V_y(t) \vec{y} = \left[\frac{d\vec{OG}}{dt} \right]_{R_0} = \left[\frac{d}{dt} (X_G(t) \vec{x}_0 + Y_G(t) \vec{y}_0) \right]_{R_0}, \tag{5.7}$$

or, after derivation,

$$\vec{V}_{G/R_0} = \dot{x}_G(t) \vec{x}_0 + \dot{y}_G(t) \vec{y}_0 = V_{x0} \vec{x} + V_y(t) \vec{y}, \quad (5.8)$$

in which the following relationships could be extracted as:

$$\begin{cases} \vec{x} = \cos \Psi(t) \vec{x}_0 + \sin \Psi(t) \vec{y}_0 \\ \vec{y} = -\sin \Psi(t) \vec{x}_0 + \cos \Psi(t) \vec{y}_0 \end{cases}, \quad (5.9)$$

and in the form,

$$\begin{cases} \dot{x}_G(t) = V_{x0} \cos \Psi(t) - V_y(t) \sin \Psi(t) \\ \dot{y}_G(t) = V_{x0} \sin \Psi(t) + V_y(t) \cos \Psi(t) \end{cases}, \quad (5.10)$$

Finally, by introducing the sideslip angle at CG, $\Delta_G(t)$, and by integrating the relation (5.10), we obtain the following:

$$\begin{cases} X_G(t) = \int_0^t (V_{x0} \cos \Psi(\tau) - V_y(\tau) \sin \Psi(\tau)) d\tau + X_{G0} = x_G(t) + X_{G0} \\ Y_G(t) = \int_0^t (V_{x0} \sin \Psi(\tau) + V_y(\tau) \cos \Psi(\tau)) d\tau + Y_{G0} = y_G(t) + Y_{G0} \end{cases}, \quad (5.11)$$

where X_{G0} and Y_{G0} are the initial values for the position of the center of gravity of the vehicle.

5.2.4 Model Linearization

The design of the frequency-based controllers is based on the frequency response of the plant; therefore, the vehicle model should be linearized around some operating points. Starting from the major nonlinear variable, the lateral forces F_y represented in Figure 5.3 shows that the values of the lateral forces have linear behavior when Δ_p is in the range of $[-1.5^\circ, 1.5^\circ]$. Thus, at this operating area, the lateral forces can be calculated by:

$$F_y(t) = c_y \Delta_p(t), \quad (5.12)$$

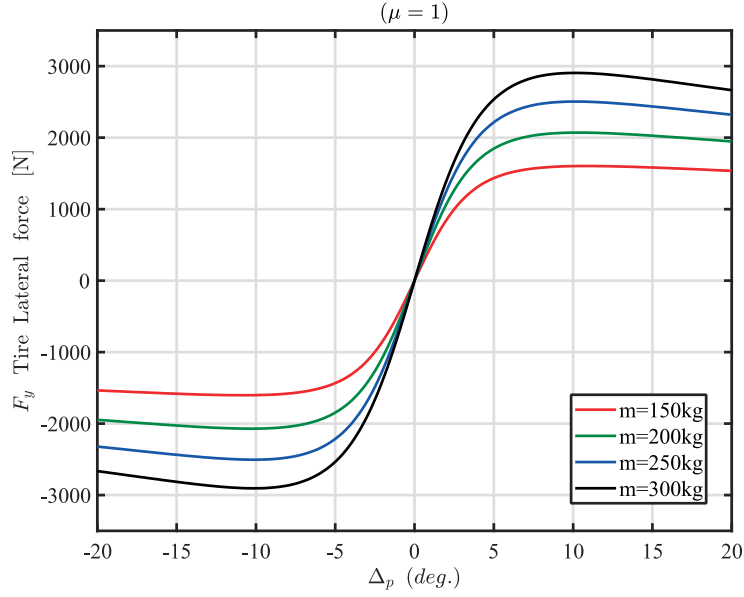


Figure 5.3. Lateral forces as function of wheel sideslip angle.

where c_y represents the cornering stiffness that supposed to be constant for a given adhesion coefficient and a total vehicle mass. The computation process of this parameter is exactly the same as for the longitudinal stiffness p_x that was obtained and illustrated in Chapter 4.

Moreover, the following assumptions were taken into account:

- The value of the steering angle (at the vehicle's wheels level) is less 5° , then we consider $\cos \beta_v \approx 1$ and $\sin \beta_v \approx 0$.
- The vehicle is equipped with a cruise control system and the ESP is short and rapid in order not to influence the longitudinal speed, therefore the value of the longitudinal speed is considered constant and denoted by V_{x0} .
- The vehicle is considered to be symmetric with respect to the x-axis of the chassis, thus at equilibrium, the longitudinal forces F_x that are at the same axle, are considered to be equal ($F_{x11} = F_{x12}$ and $F_{x21} = F_{x22}$).
- The tire sideslip angles at the same axle are equal.

Therefore, at equilibrium, the variables representing the lateral dynamics could be simplified and formulated by the following equations:

$$I_z \ddot{\psi} = L_f(f_{y,11} + f_{y,12}) - L_r(f_{y,21} + f_{y,22}) + u_z, \quad (5.13)$$

$$M \dot{v}_y = f_{y,11} + f_{y,12} + f_{y,21} + f_{y,22} + f_{y0} - MV_{x0} \dot{\psi}, \quad (5.14)$$

$$\begin{aligned} \Delta_{p,11} &= \Delta_{p,12} = \beta_v - \Delta_G - L_f \frac{\dot{\psi}}{V_{x0}}, \\ \Delta_{p,21} &= \Delta_{p,22} = -\Delta_G + L_r \frac{\dot{\psi}}{V_{x0}}, \\ &\text{with } \Delta_G = v_y/V_{x0}. \end{aligned} \quad (5.15)$$

The variable $u_z(t)$ represents the variation of the yaw torque control introduced by the designed controllers that would be generated by additive braking torques applied on the tires.

5.2.5 State-space representation

The state-space representation of the linearized lateral model is then established and can be described by:

$$\begin{cases} \dot{x}(t) = Ax(t) + Bu(t) \\ y(t) = Cx(t) + Du(t) \end{cases}, \quad (5.16)$$

where,

$$x(t) = \begin{pmatrix} x_1 = \dot{\psi}(t) \\ x_2 = \Delta_G(t) = v_y/V_{x0} \end{pmatrix}, \quad u(t) = \begin{pmatrix} f_{0y}(t) \\ u_z(t) \\ \beta(t) \end{pmatrix}, \quad (5.17)$$

$$A = \begin{bmatrix} -2 \frac{L_f^2 c_{yf} + L_r^2 c_{yr}}{I_z V_{x0}} & \frac{-2PDE}{I_z} \\ \frac{-2}{MV_{x0}^2} PDE - 1 & \frac{-2}{MV_{x0}} (c_{yf} + c_{yr}) \end{bmatrix}, \quad (5.18)$$

$$B = \begin{bmatrix} 0 & \frac{1}{I_z} & \frac{2L_f c_{yf}}{I_z} \\ \frac{1}{MV_{x0}} & 0 & \frac{2c_{yf}}{MV_{x0}} \end{bmatrix}, \quad C = [1 \quad 0], \quad D = 0,$$

with $PDE = L_f c_{yf} - L_r c_{yr}$, where c_{yf} and c_{yr} are the front and rear corner stiffness, respectively. The synthesis model used for the design of the controllers in the frequency-domain is represented by the transfer function $G_1(s)$, and can be written in the following canonical form:

$$G_1(s) = \left. \frac{\dot{\Psi}(s)}{U_z(s)} \right|_{f_{y0}=\beta_v=0} = \frac{K_0(1 + s/\omega_z)}{1 + \frac{2\zeta}{\omega_n}s + \left(\frac{s}{\omega_n}\right)^2}, \quad (5.19)$$

where,

$$\begin{aligned} K_0 &= V_{x0}(c_{yf} + c_{yr}) / (2c_{yf}c_{yr}L^2 - MV_{x0}PDE), \\ \omega_z &= 2(c_{yf} + c_{yr}) / MV_{x0}, \\ \omega_n &= ((4c_{yf}c_{yr}L^2 - 2MV_{x0}^2PDE) / I_z MV_{x0}^2)^{1/2}, \\ \zeta &= \frac{((c_{yf} + c_{yr})/M + (L_f^2 c_{yf} + L_r^2 c_{yr})/I_z)}{\omega_n V_{x0}}. \end{aligned} \quad (5.20)$$

The transfer function $G_1(s)$ is dependent on three main parameters: the longitudinal speed V_{x0} , the road adhesion μ that is included in the c_{yf} and c_{yr} coefficients, and the total mass of the vehicle M . The value of the front and rear wheelbase L_f and L_r , and the yaw inertia I_z are directly related to the value of M , where they are changing according to its value.

5.2.6 Uncertain Plants

The range of variation of each uncertain parameter is shown in Table 5.1. According to these variations, three plants were selected and named as: the nominal plant, minimum plant, and maximum plant, where the nominal plant corresponds to the normal driving conditions. Figure 5.4 shows the influence of the uncertainty in the frequency domain. It should be noted that these variations correspond to a light electric vehicle parametric configuration in two conditions: an empty vehicle (only driver) and a fully-loaded vehicle (five passengers). The study considers a wide range of road adhesion variation, where $\mu = 0.1$ corresponds to an icy road surface and $\mu = 1$ to a dry road surface.

5.3 Yaw rate regulation by corrective yaw moment

Table 5.1. Parametric variations of $G_1(s)$.

Plant	V_{x0}	μ	M	I_z	L_f	L_r
	km/h		kg	kg.m ²	m	m
G_{1nom}	50	1	600	360	2/3	4/3
G_{1min}	45	1	900	420	8/9	10/9
G_{1max}	55	0.1	600	360	2/3	4/3

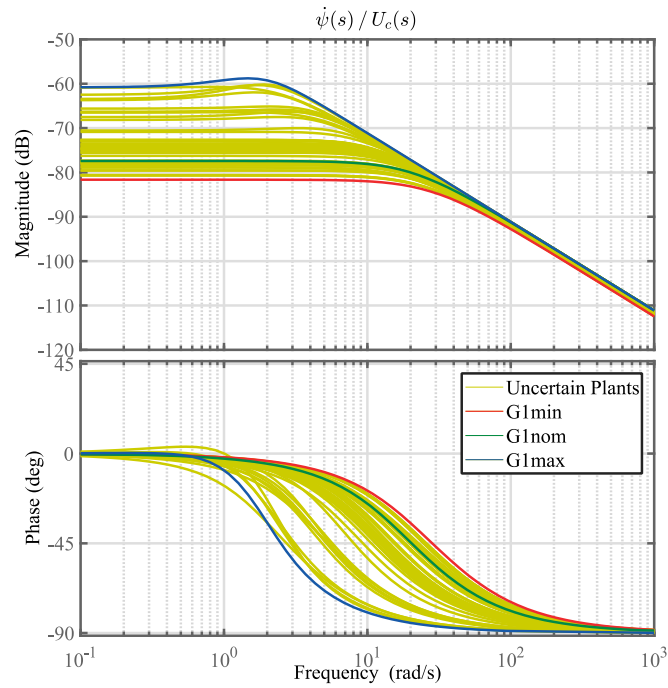


Figure 5.4. Bode responses of uncertain plants of $G_1(s)$.

5.3 Yaw rate regulation by corrective yaw moment

In this section, the design of the 3rd generation CRONE controller and the PID controller are detailed. In order to have a fair comparison between the two controllers, they should be designed so that the rapidity and stability margin are identical for both controllers for the nominal plant chosen. Both controllers are designed to track the yaw rate reference generated by a supervisor based on the steering profile introduced by the driver. The

evaluation is done in terms of robustness and performance against disturbance rejection and parametric variations.

5.3.1 Specifications

Several specifications are required for the controllers:

- The control input related to the measurement noise is less than 10% of the greatest value of the control input.
- The nominal overshoot of the step response related to the reference signal is about 30%.

Denote by M_{r0} the value of the closed-loop resonant gain of the contour that is tangent to the nominal open-loop transfer function on Nichols chart. Thus, the stability could be granted by fixing the value of M_{r0} that is chosen to specify a value of 3dB for the nominal plant. Therefore, it ensures a phase margin greater than 40° and therefore, satisfying stability.

Figure 5.5 shows the control scheme for the yaw rate regulation using braking torques. In order to export these specifications in the frequency domain, the following functional equations associated with Figure 5.5 are introduced.

$$\begin{aligned}\dot{\Psi}(s) &= T(s) \left(\dot{\Psi}_{ref}(s) - N_m(s) \right), \\ \varepsilon(s) &= S(s) \left(\dot{\Psi}_{ref}(s) - N_m(s) \right), \\ U_z(s) &= CS(s) \left(\dot{\Psi}_{ref}(s) - N_m(s) \right).\end{aligned}\tag{5.21}$$

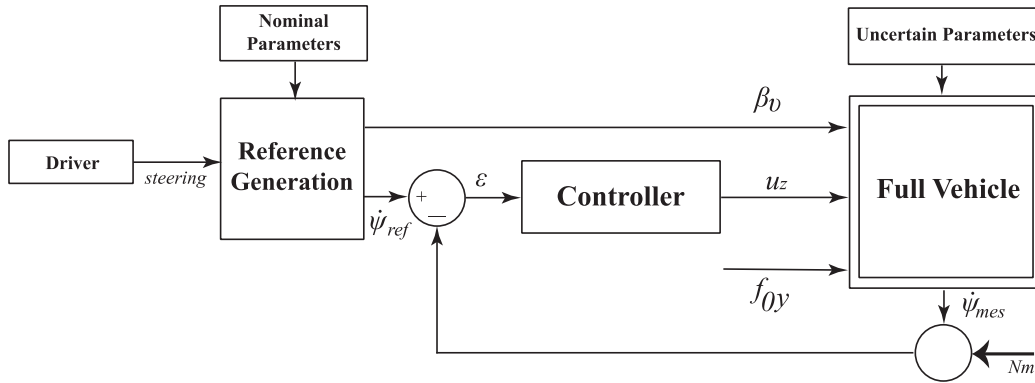


Figure 5.5. Block diagram for yaw rate regulation by braking torque.

The open-loop crossover frequency, denoted by ω_u , is chosen so that the sensitivity of the input control to the noise measurement (N_m) is less than 10%. Meaning that:

$$\left| \frac{U_z(j\omega)}{N_m(j\omega)} \right| = CS(j\omega) \leq \left| \frac{10\%U_{z\max}}{N_{m0}} \right|, \quad (5.22)$$

where N_{m0} is the maximum magnitude of the sensor noise measurements that is usually specified in the sensor's datasheet. Knowing that the Maximum control input is 3000Nm, and the noise level of yaw rate is considered 1% of the sensor range (1 rad/s), then:

$$|CS(j\omega)| \leq \left| \frac{0.1 \times 3000}{0.01} \right| = 3e4 \text{ N.m.s/rad}. \quad (5.23)$$

Thus, for high frequencies ω_{HF} , $|CS(j\omega)| \approx |C(j\omega_{HF})| \leq 3e4 \text{ Nms/rad}$. Knowing that $|C(j\omega_u)G_{1nom}(j\omega_u)| = 1$, and considering the controller as a proportional controller C_0 , then it is easy to calculate an upper bound for the crossover frequency ω_u . In this study and for the nominal conditions, $\omega_{u,max} = 82 \text{ rad/s}$. To manage the performances related to tracking, regulation, and control effort, the sensitivity functions must fulfill the following inequality constraints for all parametric states of the plant.

To limit the highest resonant peak:

$$\forall \omega \in \mathbb{R}^+: |T(j\omega)| < T_{max} = 6 \text{ dB}. \quad (5.24)$$

To limit the lowest modulus margin:

$$\forall \omega \in \mathbb{R}^+: |S(j\omega)| < S_{max} = 6 \text{ dB}. \quad (5.25)$$

To limit the control effort:

$$\forall \omega \in \mathbb{R}^+: |CS(j\omega)| < CS_{max} = 85.5 \text{ dB}. \quad (5.26)$$

To improve the input disturbance rejection:

$$\forall \omega \in \mathbb{R}^+: |GS(j\omega)| < GS_{max} = -68 \text{ dB}. \quad (5.27)$$

5.3.2 CRONE Controller

In this study, the third generation CRONE controller must be used because of the presence of high variation of gain and phase about the desired open-loop crossover frequency ω_u . The same methodology used in Chapter 4 is applied here to design the 3rd generation CRONE controller $C_1(s)$.

For good tracking for ramp inputs references and better filtering of measurements noise, it is chosen $n_l = 2$ and $n_h = 2$, respectively. Using the CRONE Toolbox, the remaining parameters are calculated as follows: $\omega_r = \omega_0 = 10\text{rad/s}$, $Y_r = 7$, $\omega_1 = 25\text{rad/s}$, $a_0 = 0.345$, and $b_0 = 2.4$. The resulting open-loop crossover frequency is $\omega_u = 19.2 \text{ rad/s}$ for the nominal plant.

One of the main seeking objectives while designing the parametric configuration of the CRONE controller is to choose the smallest possible crossover frequency that satisfies all the aforementioned criteria. This concept explains the small value of ω_u obtained compared to the maximum allowable value of ω_u . In fact, this option has several advantages related to noise measurement rejection at high frequencies, sensors selection, and facilitates the work of the actuators that inevitably have inherent limits on its dynamics.

5.3.3 PID Controller

The PID controller was designed so that we get identical ω_u as for the CRONE controller. The obtained PID controller has the following cascade form:

$$C_{PID}(s) = C_{0PID} \left(\frac{1 + s/\omega_i}{s/\omega_i} \right)^2 \frac{1 + s/\omega_b}{1 + s/\omega_h} (1 + s/\omega_f)^{-1}, \quad (5.28)$$

where C_{0PID} is a proportional gain and ω_i is the integral transitional frequency. The parameters of the phase-lead compensator are chosen in order to have the nominal open-loop transfer function tangent to the 3dB contour on Nichols chart, and finally, a low pass filter is added with a cutoff frequency ω_f . The resulting PID controller parameters are: $C_{0PID} = 3.6e5$, $\omega_i = 2.4\text{rad/s}$, $\omega_f = 192\text{rad/s}$, $\omega_b = 75\text{rad/s}$, and $\omega_h = 0.5\text{rad/s}$.

5.3.4 Frequency-domain analysis

Figure 5.6 shows the Bode plot responses of the transfer functions of the two controllers, and Figure 5.7 plots the Bode response of the nominal open-loop transfer functions with the two controllers. Figure 5.8 and 5.9 show the Nichols chart of the open-loop transfer functions for the three uncertain plants with CRONE and PID controllers, respectively. It can be seen that the nominal open-loop transfer function for both controllers (in green) is tangent to the 3dB contour.

The fact that the 3rd generation CRONE controller can bring more phase-lead after ω_u than the PID controller, provides more robustness against uncertain parameters. It is obvious that the variation of M_r is smaller for the CRONE controller compared to the PID controller. Moreover, it can be noticed that the variation of the phase margin M_ϕ is also small compared to that of the PID controller. Numerically, with the CRONE controller, the cross over frequency varies between 12.8 and 26.6rad/s versus plants' parametric variations, while with the PID it varies between 14.2 and 23rad/s. On the other hand, the phase margins vary in the range 48.4 - 72.2° with the CRONE controller, while with PID it varies between 3.92 - 53.4°.

The constraints imposed on the sensitivity functions for the design of the controllers are represented with the dashed black lines in Figures 5.10 and 5.11, for CRONE and PID controller, respectively. They also show the magnitude of each sensitivity function considering the uncertain plants with the designed controller. Table 5.2 shows the maximum gain of each sensitivity function considering the perturbed plants. Since all of them satisfy the assigned constraints with CRONE controller, then robustness is ensured, in contrast to the case of PID controller.

Table 5.2. Maximum gain in dB of sensitivity functions for perturbed $G1(s)$.

	$T(s)$	$S(s)$	$CS(s)$	$GS(s)$
$C_1(s)$	5.9dB	2.4dB	85.5dB	-74dB
$C_{1PID}(s)$	23.4dB	23.3dB	102dB	-55dB

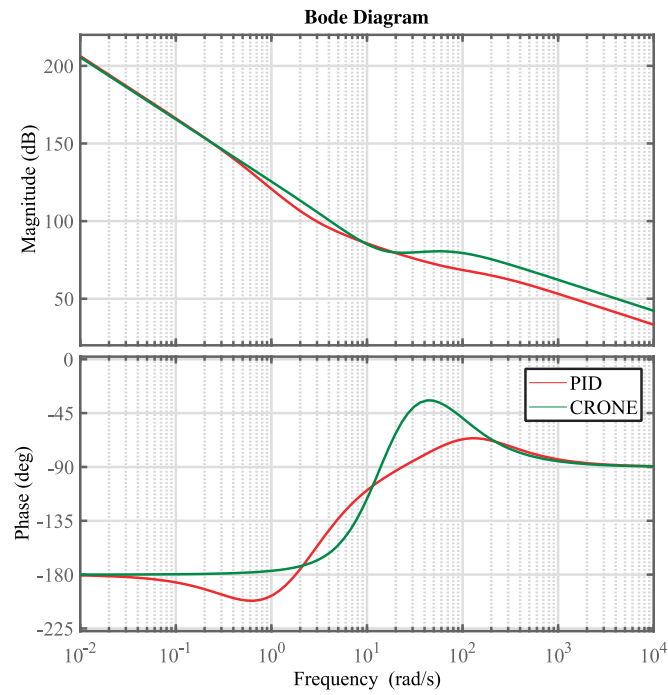


Figure 5.6. Bode plot for designed controllers of $G_1(s)$ plant.

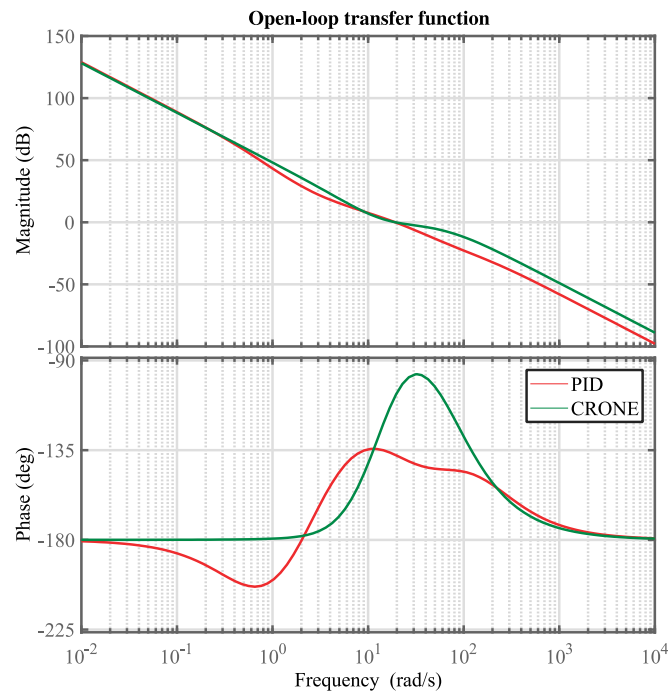


Figure 5.7. Bode response of the nominal open-loop transfer function.

5.3 Yaw rate regulation by corrective yaw moment

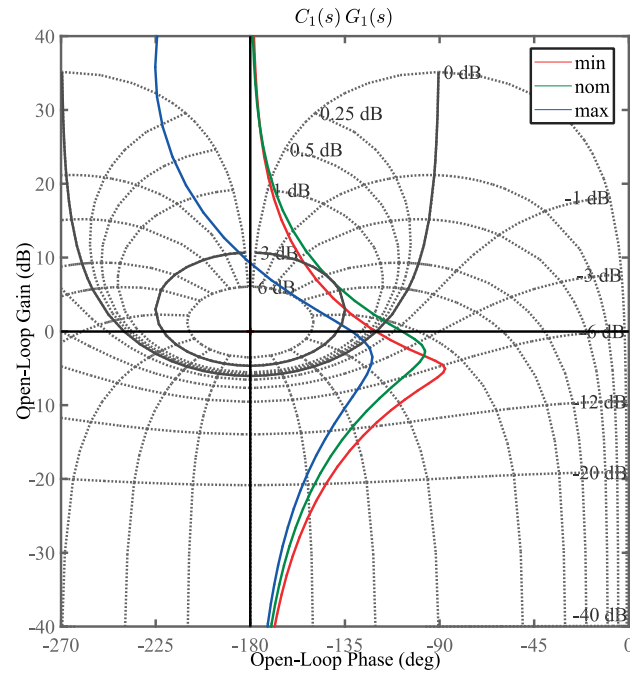


Figure 5.8. Nichols chart for open-loop transfer functions with CRONE controller $C_1(s)$.

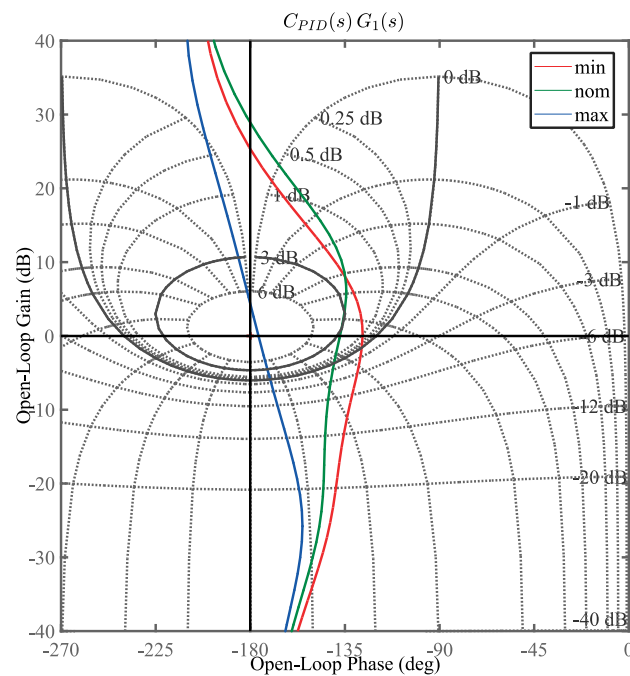


Figure 5.9. Nichols chart for open-loop transfer functions with PID controller.

5.3 Yaw rate regulation by corrective yaw moment

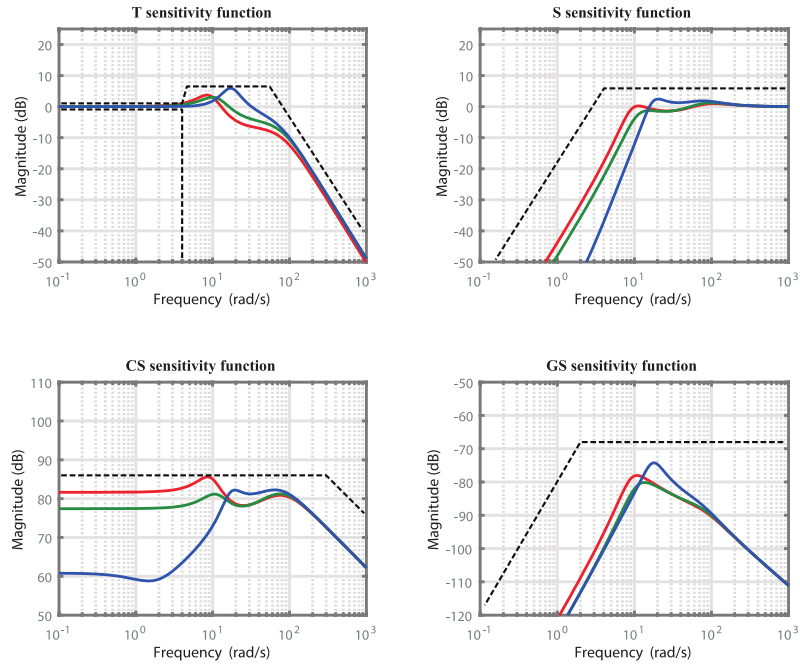


Figure 5.10. Frequency responses of sensitivity functions with $C_1(s)$.

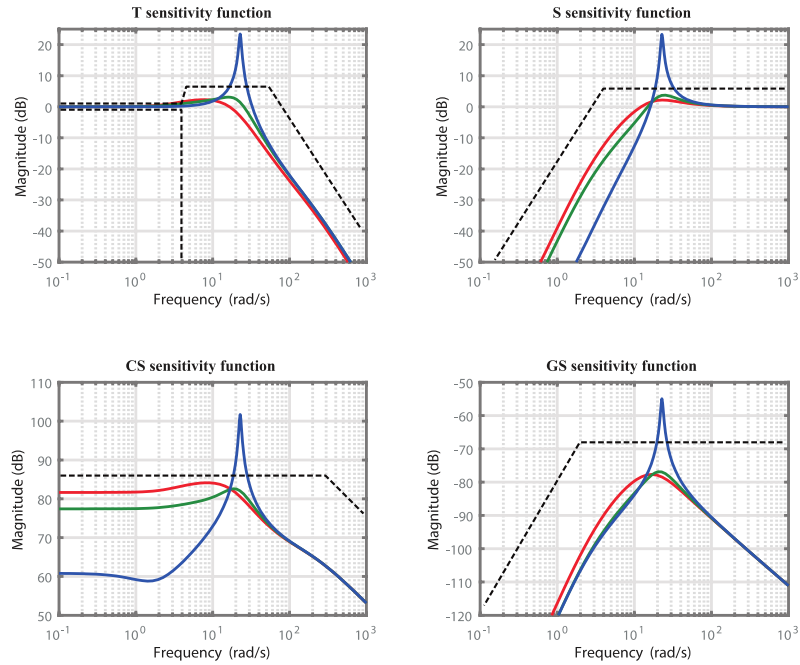


Figure 5.11. Frequency responses of sensitivity functions with $C_{1PID}(s)$.

5.3.5 Test simulations

In order to evaluate the performance of the designed controller in stabilizing the vehicle, several testing scenarios were done. Particularly here, only the lateral and longitudinal dynamics were considered while neglecting the vertical dynamics of the vehicle. Later on, the effect of the vertical dynamics on the lateral stability is studied separately in the next sections.

The first scenario (A) consists of a vehicle driven at an initial speed of 55km/h, on dry and even road. The vehicle parameters are considered different from their nominal values to examine the robustness of the controllers against vehicle's parametric variations. The electric vehicle goes through a sudden change lane maneuver whose steering profile plotted in Figure 5.12. The lane change starts at $t=0.5$ s, during the maneuver and about $t=0.7$ s, the vehicle goes through an ice patch ($\mu = 0.1$) and lasts for 1.5s. The maneuver finishes at $t=2$ s.

Figure 5.13 shows a comparison of the different yaw motions. Although of low vehicle speed adopted in this scenario, the uncontrolled system shows a high deviation from the generated reference of yaw rate. The CRONE controller shows a more stable performance where we can see smaller peak oscillations around the reference ($t=1.25$ s to $t=2.5$ s) compared to the performance of the PID controller that reveals a tendency to lose stability.

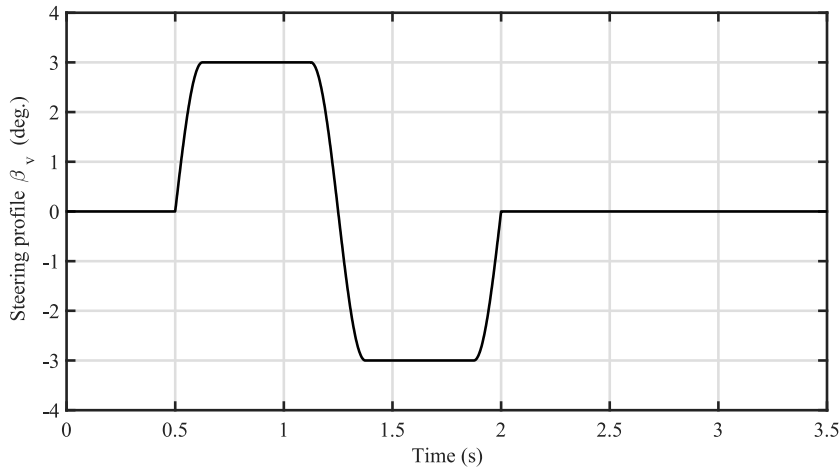


Figure 5.12. Steering profile of scenario (A).

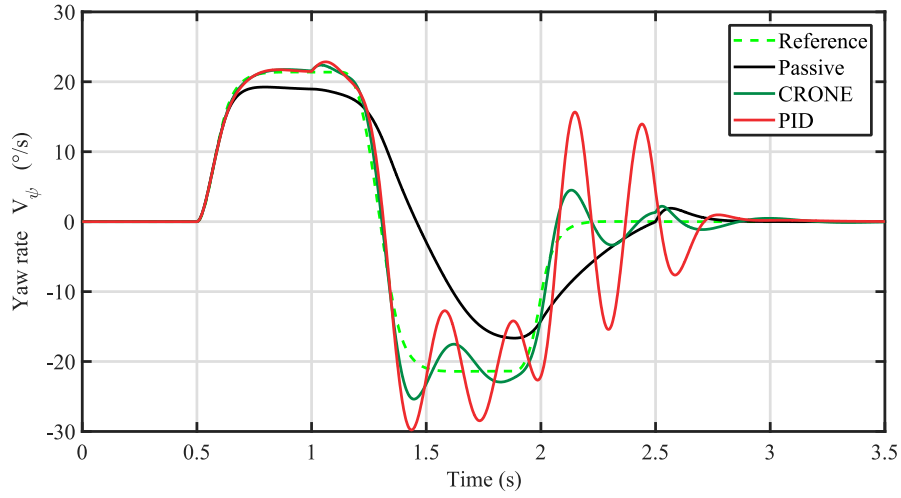


Figure 5.13. Yaw rate motions of scenario (A).

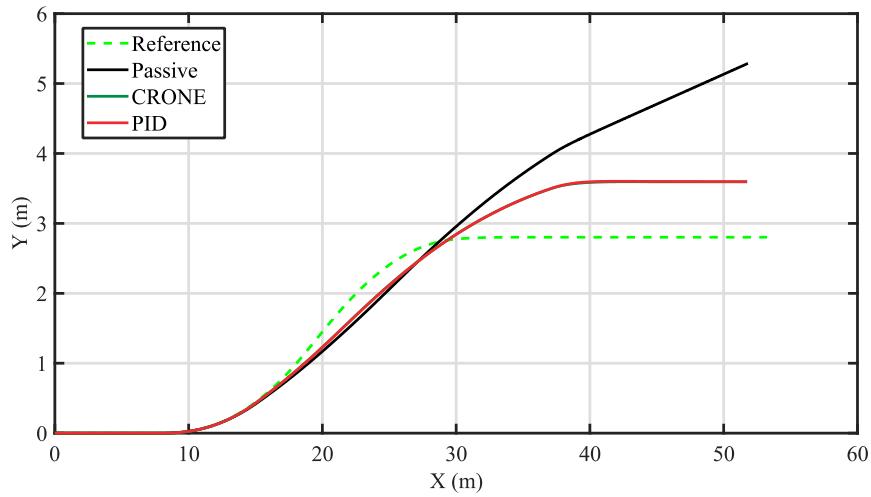


Figure 5.14. Vehicle trajectories of scenario (A).

Although both controllers have consistent trajectory response, as shown in Figure 5.14, the CRONE controller demanded less control effort for yaw rate reference tracking as shown in Figure 5.15. In fact, the steady-state error in Figure 5.14 between the reference trajectory and the controlled system trajectories is understandable and expected since the control objective is to track the yaw rate reference and not the lateral position of the reference model. For this purpose, another controller is needed in which it uses steering control to track the reference values of the lateral position of the vehicle, and this point will be discussed in later sections.

Numerically, the maximum values of $U_c(t)$ are 1771 and 2565Nm for CRONE and PID, respectively. Moreover, the RMS values of $U_c(t)$ were recorded 445 and 880Nm for CRONE and PID respectively. These results reflect the robustness of the designed 3rd generation CRONE controller against parametric variation, mainly, the road adhesion, compared to the PID controller.

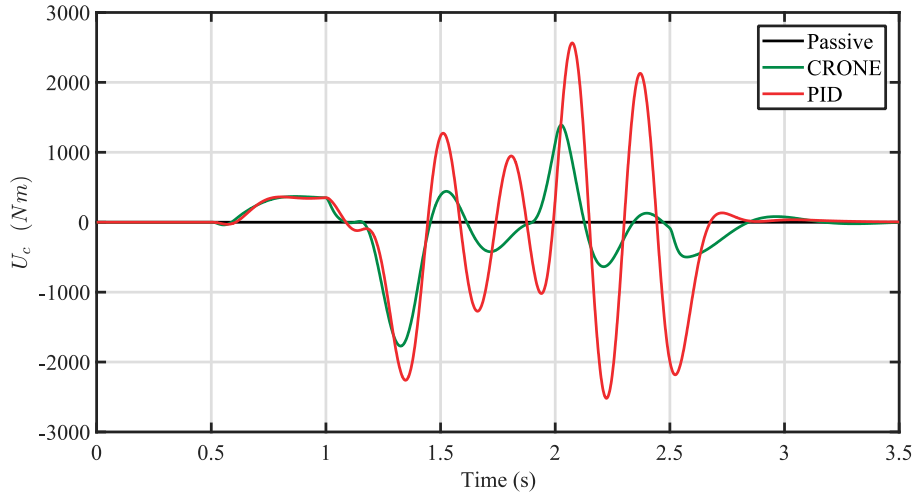


Figure 5.15. Yaw moment control efforts of scenario (A).

5.4 Yaw rate regulation by active steering

5.4.1 Introduction

In some scenarios, the drivers may not be capable to maintain vehicle's stability when they want to turn the vehicle, where might easily skid and spin out, possibly resulting in a road accident. The main reason is that the nominal yaw rate motion during turning is difficult to be achieved in the presence of external disturbances and parametric variations.

As shown in the previous sections that the vehicle's stability is highly enhanced with braking torques, for modern vehicles, the yaw rate can also be controlled by adjusting the steering angle with an active front steering (AFS) system. In addition to the steering wheel mechanism, an electromechanical actuator (usually a geared DC motor) is installed on the steering column, which can provide a superposition angle to the steering wheel angle

to adjust the actual steering angle. The yaw rate can then be corrected via proper control of the active front steering (AFS) actuator. In order to guarantee the vehicle's yaw stability with the AFS system, the objective of the vehicle yaw rate controller is to determine an appropriate front steering angle for the AFS-actuator to adjust yaw rate dynamics (Wong et al., 2019).

5.4.2 Synthesis model

Taking advantage of the previous illustration and models' equations, and using the state-space representation of the lateral dynamics of the electric vehicle, the synthesis model for the active steering control can be formulated while taking into consideration the third input of vector 'B' in (5.18), that is the steering input $u_\beta(t)$.

Therefore, the model used for control design in the frequency-domain is represented by the transfer function $G_2(s)$ and can be written as follows:

$$G_2(s) = \left. \frac{\dot{\Psi}(s)}{U_\beta(s)} \right|_{f_{y0}=0}, = \frac{K_{02} \left(1 + \frac{s}{\omega_{z2}} \right)}{1 + \frac{2\zeta_2}{\omega_{n2}} s + \left(\frac{s}{\omega_{n2}} \right)^2}, \quad (5.29)$$

where,

$$\begin{aligned} K_{02} &= \frac{-PDE + L_f V_{x0} b_y}{q I_z M V_{x0}}, & \omega_{z2} &= -\frac{PDE}{L_f V_{x0} M} + \frac{b_y}{M}, \\ \omega_{n2} &= \sqrt{q}, & \zeta_2 &= \frac{\left(\frac{b_z}{I_z} + \frac{b_y}{M} \right)}{2\sqrt{q}}. \end{aligned} \quad (5.30)$$

with,

$$\begin{aligned} A_x &= \frac{PDE}{M V_{x0}} + V_{x0}, & q &= \frac{b_z b_y}{I_z M} - \frac{PDE A_x}{I_z V_{x0}}, \\ b_z &= \frac{L_f^2 c_{yf} + L_r^2 c_{yr}}{V_{x0}}, & b_y &= \frac{c_{yf} + c_{yr}}{V_{x0}}. \end{aligned} \quad (5.31)$$

5.4 Yaw rate regulation by active steering

The range of variation of each uncertain parameter is shown in Table 5.3. According to these variations, three plants were chosen and named: the medium plant G_{2med} , minimum plant G_{2min} , and maximum plant G_{2max} . Figure 5.16 shows the influence of the uncertainty in the frequency domain, in addition to the frequency response of the three perturbed plants.

Table 5.3. Parametric uncertainties of $G_2(s)$.

	M [kg]	V_{x0} [m/s ²]	μ
G_{2med}	750	50	0.6
G_{2min}	600	55	0.35
G_{2max}	900	45	1

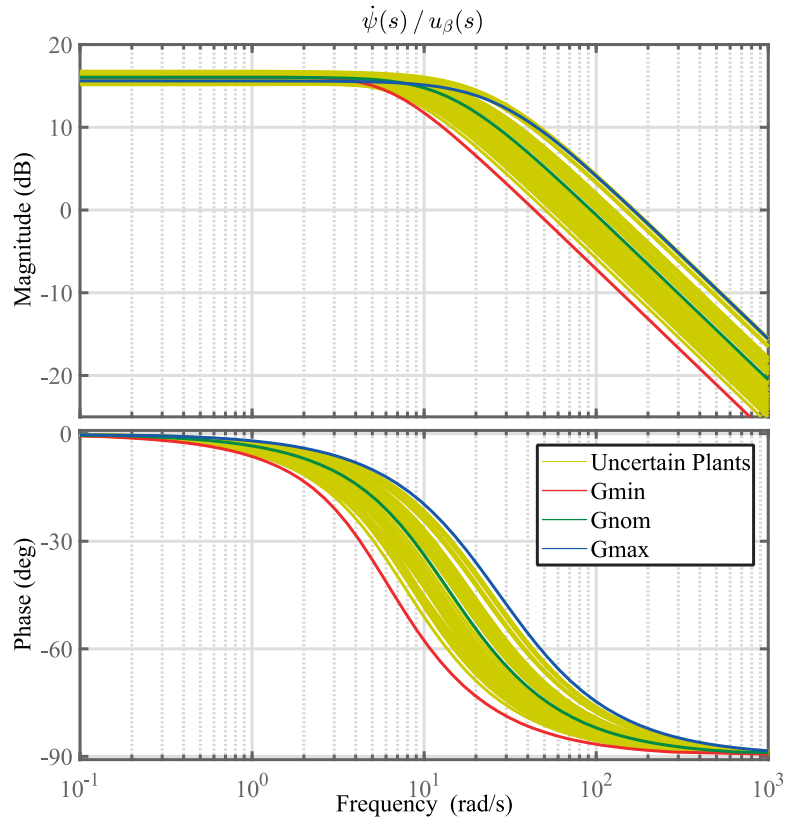


Figure 5.16. Bode responses of uncertain plants of $G_2(s)$.

5.4.3 Control Design

5.4.3.1 Specifications

Several specifications are required for the controllers:

- Control input related to measurement noise less than 10% of the greatest value of the control input.
- The nominal overshoot of step response related to the reference signal is about 30%.
- Use the smallest possible value ω_c .
- Maximum limit of introduced steering effort is $\max|u_\beta| < 10^\circ$.

Figure 5.17 shows the control scheme for the yaw rate regulation using active steering.

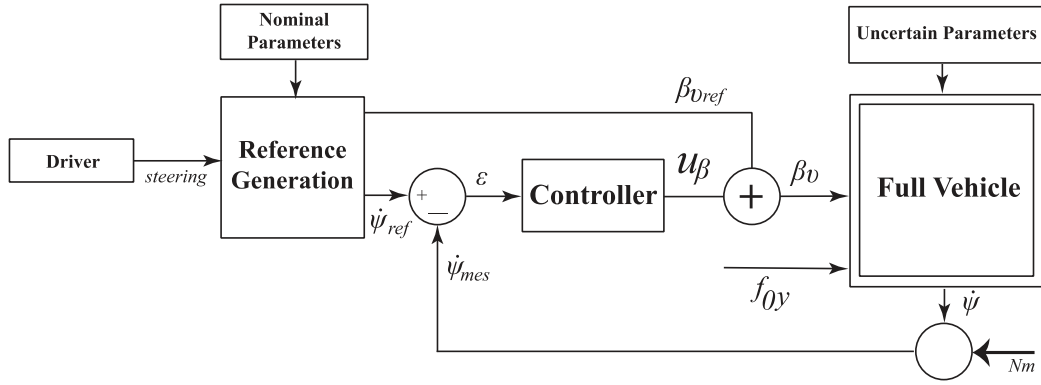


Figure 5.17. Functional diagram of yaw rate regulation by active steering.

The open-loop crossover frequency ω_u is chosen so that the sensitivity of the input control to noise measurement (N_m) is less than 10%. Meaning that:

$$\left| \frac{U_\beta(j\omega)}{N_m(j\omega)} \right| = CS(j\omega) \leq \left| \frac{10\% U_{\beta max}}{N_{m0}} \right|. \quad (5.32)$$

The maximum control input considered in this study is $\max(|u_\beta|) = 10^\circ$, and the maximum noise level of yaw rate $\dot{\psi}(t)$ is considered around $N_{m0} = 0.01 \text{ rad/s}$, that corresponds to 1% of sensor range (1 rad/s). Thus, the control input sensitivity can be formulated as the following:

$$|CS(j\omega)| \leq \left| \frac{0.1 \times 10 \times \frac{\pi}{180}}{0.01} \right| = 1.8s. \quad (5.33)$$

Thus, for high frequencies ω_{HF} , $|CS(j\omega)| \approx |C(j\omega_{HF})| \leq 1.8s$. Knowing that $|C(j\omega_u)G_{2nom}(j\omega_u)| = 1$, and considering the controller as a proportional controller C_0 , then it is easy to calculate the maximum value of ω_u . In this study and for the nominal conditions, the upper bound for the cross-over frequency is obtained as $\omega_{u,max} = 164rad/s$. To manage the performances related to tracking, regulation and control effort, the sensitivity functions must fulfill the following inequality constraints for all the parametric states of the plant.

To limit the highest resonant peak:

$$\forall \omega \in \mathbb{R}^+: |T(j\omega)| < T_{max} = 3.5dB. \quad (5.34)$$

To limit the lowest modulus margin:

$$\forall \omega \in \mathbb{R}^+: |S(j\omega)| < S_{max} = 6dB. \quad (5.35)$$

To limit the control effort:

$$\forall \omega \in \mathbb{R}^+: |CS(j\omega)| < CS_{max} = 4.8 \text{ dB}. \quad (5.36)$$

To improve the input disturbance rejection:

$$\forall \omega \in \mathbb{R}^+: |GS(j\omega)| < GS_{max} = 10dB. \quad (5.37)$$

5.4.3.2 CRONE Controller

According to the frequency response of the plant model, the third generation CRONE controller must be used because of the presence of high variation of gain and phase about the desired open-loop crossover frequency ω_u . It should be noted that the ‘med’ plant is used as a nominal plant for control synthesis. Using the same methodology described in Chapter 4, the 3rd generation CRONE controller $C_2(s)$ was designed.

In order to obtain a good tracking for ramp inputs references and better filtering of measurements noise, it was chosen $n_l = 2$ and $n_h = 2$ respectively. Using the CRONE Toolbox, the rest parameters are calculated as follows: $\omega_r = 80 \text{ rad/s}$, $\omega_0 = 5 \text{ rad/s}$, $Yr = 1.2$, $\omega_1 = 500 \text{ rad/s}$, $a0 = 1.43$, and $b0 = -0.48$. The resulting open-loop crossover frequency is $\omega_u = 88.6 \text{ rad/s}$ for the nominal plant.

5.4.3.3 PID Controller

The PID controller was designed so we get identical ω_u , and in the same methodology illustrated in section 5.3.3. The obtained PID control parameters are: $C_{0PID} = 1.51$, $\omega_i = 7.38 \text{ rad/s}$, $\omega_f = 177 \text{ rad/s}$, $\omega_b = 126.7 \text{ rad/s}$, and $\omega_h = 62 \text{ rad/s}$.

5.4.3.4 Frequency analysis

Figure 5.18 and 5.19 show the Bode plot of the two controllers and of the response of the open-loop transfer functions with the two controllers, respectively. Figure 5.20 and 5.21 show the Nichols chart of the open-loop transfer function for the three uncertain plants for both controllers.

The Nichols chart of the 3rd generation CRONE controller shows more robustness against uncertain parameters compared to the PID controller. It is obvious that the variation of the M_r is smaller for the CRONE controller compared to the PID controller. Moreover, it can be noticed that the variation of the phase margin M_ϕ is also small compared to that of the PID controller. Numerically, with the CRONE controller, the crossover frequency varies between 52.7 and 127 rad/s versus plants' parametric variations, while with PID it varies between 53 and 125 rad/s. On the other hand, the phase margins vary in the range 40 - 42.8° with the CRONE controller, while with PID it varies between 41.2 - 46°.

The constraints imposed on the sensitivity function for the design of the controllers are represented with the dashed black lines in Figure 5.22 and 5.23, with CRONE and PID respectively, in addition to the magnitude of each sensitivity function considering the uncertain plants with the designed controller. Table 5.4 shows the maximum gain of each sensitivity function considering the perturbed plants.

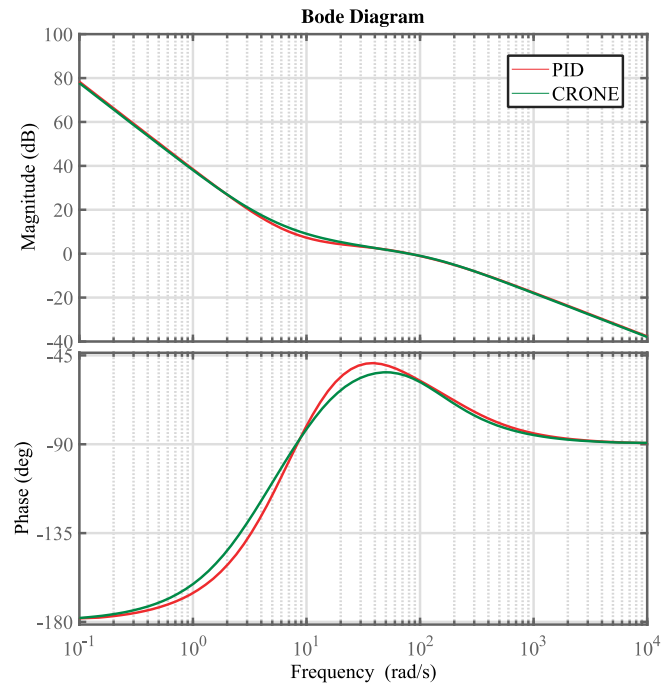


Figure 5.18. Bode plot for designed controllers of $G_2(s)$ plant.

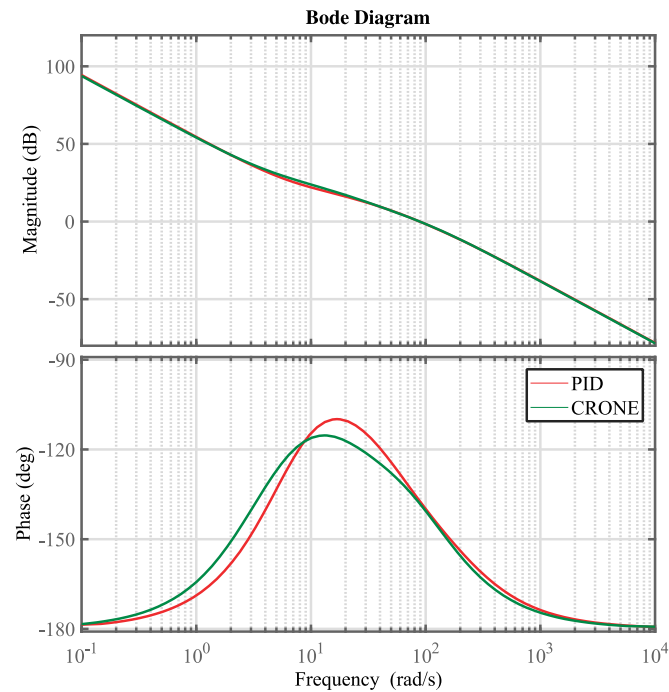


Figure 5.19. Bode response of the nominal open-loop transfer function of active steering systems.

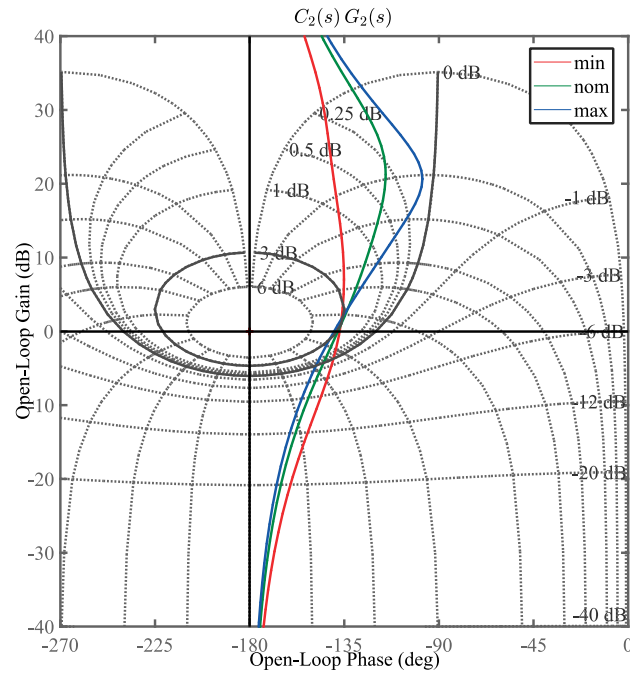


Figure 5.20. Nichols chart for open-loop transfer functions with CRONE controller $C_2(s)$.

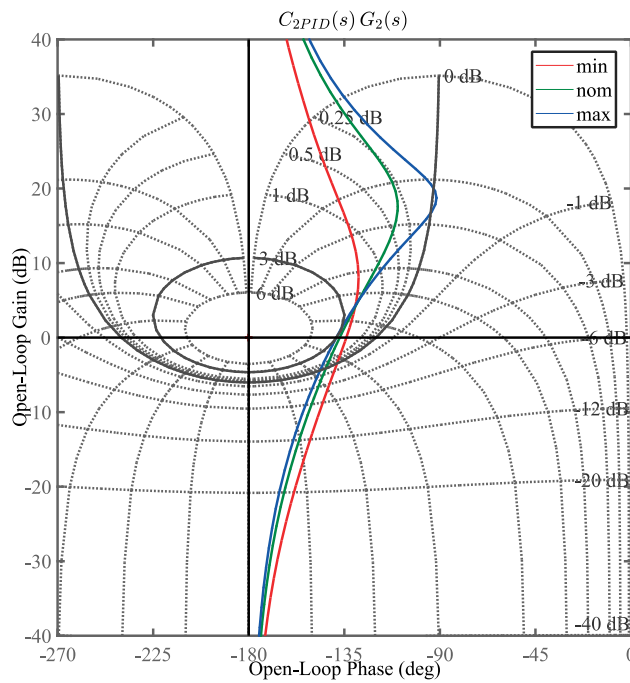


Figure 5.21. Nichols chart for open-loop transfer functions with $C_{2PID}(s)$.

5.4 Yaw rate regulation by active steering

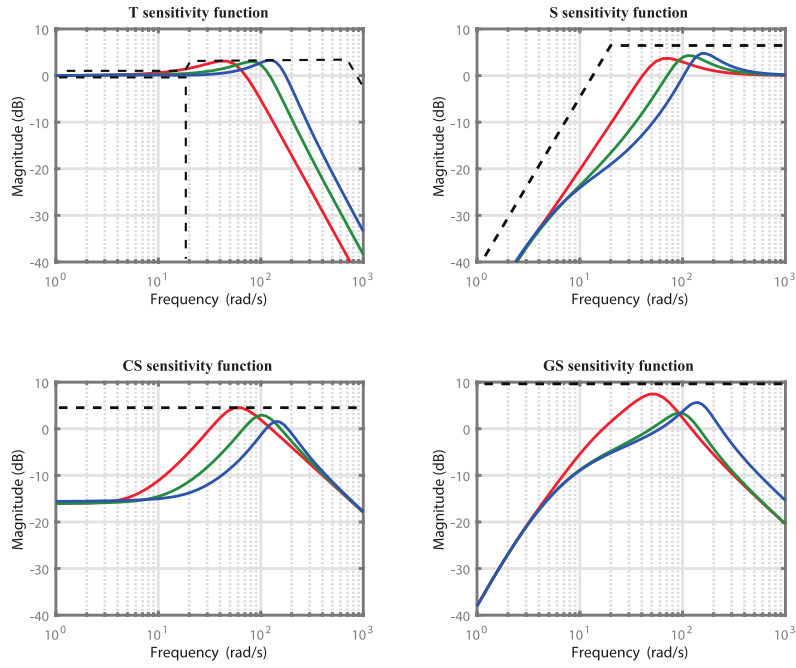


Figure 5.22. Frequency responses of sensitivity functions with $C_2(s)$.

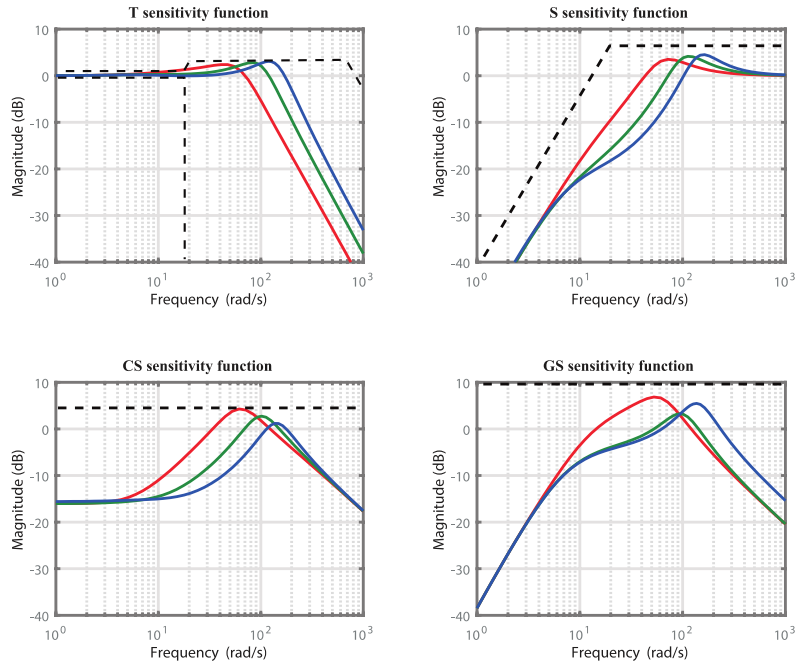


Figure 5.23. Frequency responses of sensitivity functions with $C_{2PID}(s)$.

Table 5.4. Maximum gain in dB of sensitivity functions for perturbed $G_2(s)$.

	$T(s)$	$S(s)$	$CS(s)$	$GS(s)$
$C_2(s)$	3.2 dB	4.8dB	4.5dB	7.4dB
$C_{2PID}(s)$	3.05dB	4.52dB	4.28dB	6.84dB

5.4.4 Simulation results

The scenario (A) simulated in section 5.4 is also adopted here. The only difference is that the road adhesion dropped down from $\mu = 1$ (dry road) to $\mu = 0.5$ (wet road). The simulation compares three systems: an uncontrolled system, a system controlled by $C_{2PID}(s)$, and a system controlled by the 3rd generation CRONE controller $C_2(s)$.

Figure 5.24 shows the yaw motion response of the different systems. It shows that both designed controllers were able to track the generated yaw rate reference, unlike the uncontrolled system that performs far from the reference. The main reason for this deviation for the passive system caused by the low road adhesion introduced. The additive steering angle $u_\beta(t)$ provided by the controllers, as shown in Figure 5.25, allows the vehicle to perform around the generated reference. Figure 5.26 plots the vehicle trajectories where it reflects the enhancement of the controlled system compared to the passive one.

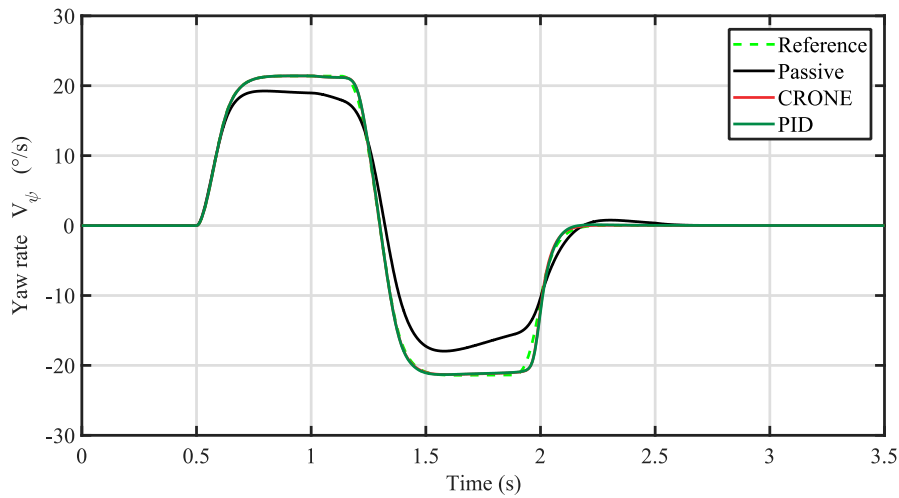


Figure 5.24. Yaw rate motions with active steering control.

5.4 Yaw rate regulation by active steering

In fact, this controller is applicable for a reasonable road adhesion. This means that for lower road adhesion ($\mu < 0.35$), this control strategy is no longer effective. In order for the steering dynamics to influence the vehicle dynamics needs a tolerable amount of grip. This is not the case when the road adhesion is very low, in which the grip is no longer enough for traction and steering at the same time.

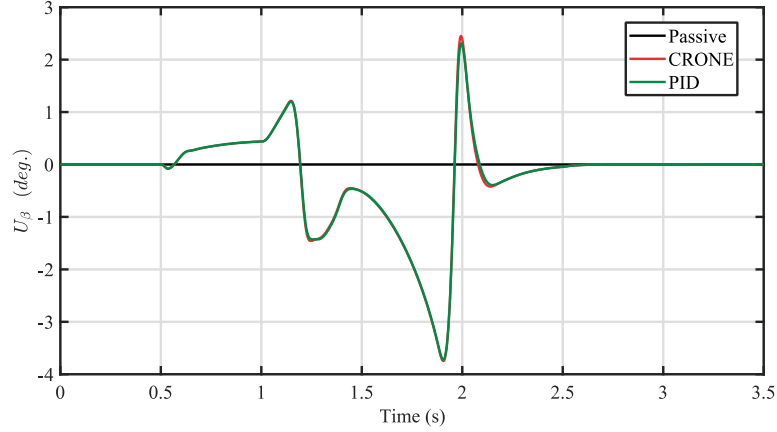


Figure 5.25. Control active steering angle.

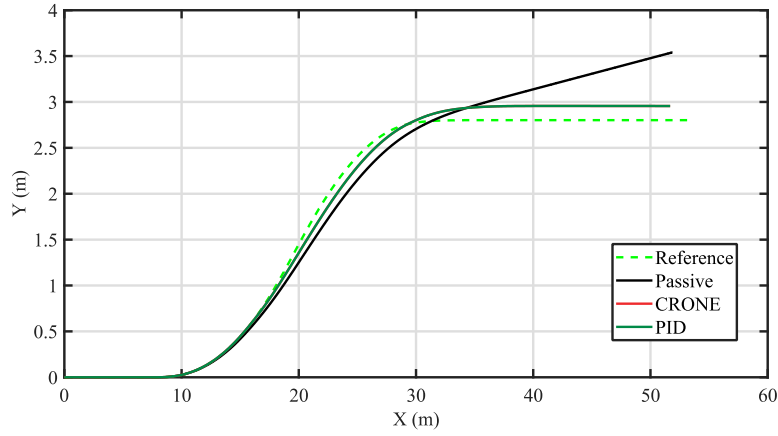


Figure 5.26. Vehicle trajectories with active systems compared to passive and reference models.

For this reason, for future studies when control coordination will be implemented, this kind of controllers (yaw rate regulation using active steering) should be deactivated when a specified threshold is exceeded. In this situation, the yaw rate (or sideslip) regulation by differential braking torques is more efficient.

5.5 Lateral position Control

5.5.1 Introduction

The objective of this study is to control the lateral position $Y_G(t)$ of the center of gravity of the vehicle to track a reference lateral position Y_{Gref} generated by a nominal model whose parametric state does not vary, unlike the validation model which present parametric uncertainties.

The previous stability control shows a good performance in tracking yaw rate reference, and therefore, an important enhancement in stability and safety using introduced braking torques or active steering angle. However, it was shown that the trajectories of the active systems, although they address vehicle stability, they can't perfectly attain the best trajectory. In some situations, it went 1m far from the generated reference trajectory. This result could be critical in real scenarios and a controller for the lateral position is then needed to ensure the vehicle's safety. The designed controller is addressed individually, in which the study neglects the other controllers introduced in previous sections.

5.5.2 Synthesis model

Following the same modeling process detailed in section 5.2, the synthesis model for lateral position regulation can be formulated with the help of the previous synthesis models and state-space representation in section 5.2.5.

Assuming that the longitudinal velocity is constant and that the equilibrium of the lateral position is 0, the lateral dynamics of the vehicle can be formulated as follows:

$$\dot{y}_G(t) = V_{x0}\psi(t) + v_y(t) \quad . \quad (5.38)$$

Then, the synthesis model or the plant transfer function $G_3(s)$ related to lateral position control can be obtained using the following:

$$G_3(s) = \frac{Y_G(s)}{U_\beta(s)} = \frac{1}{s} \left(V_{x0} \frac{G_2(s)}{s} + \frac{V_y(s)}{U_\beta(s)} \right) \quad . \quad (5.39)$$

The transfer function $V_y(s)/U_{\beta(s)}$ can be easily deduced from the state-space representation in 5.2.5 when considering the third input of $u(t)$, that is $u_{\beta}(s)$, and the second variable of the state variable $x(t)$ which is the side-slip angle $\Delta_G(t)$. Knowing that $\Delta_G(s) = V_y(s)/V_{x0}$, then:

$$\frac{V_y(s)}{U_{\beta}(s)} = \frac{\Delta_G(s)}{U_{\beta}(s)} \cdot V_{x0} . \quad (5.40)$$

Finally, the transfer function can be expressed as follows:

$$G_3(s) = \frac{Y_G(s)}{U_{\beta}(s)} = \left(\frac{\omega_3}{s}\right)^2 \left(\frac{1 + \frac{2\zeta'_3}{\omega'_{n3}} s + \left(\frac{s}{\omega'_{n3}}\right)^2}{1 + \frac{2\zeta_3}{\omega_{n3}} s + \left(\frac{s}{\omega_{n3}}\right)^2} \right) , \quad (5.41)$$

where,

$$\left\{ \begin{array}{l} \omega_{n3} = \omega_{n2} \\ \zeta_3 = \zeta_2 \\ \omega_3 = \sqrt{\frac{d_0}{q}} \\ \zeta'_3 = \frac{d_1}{2\sqrt{d_0 d_2}} \\ \omega'_{n3} = \sqrt{\frac{d_0}{d_2}} \end{array} \right. , \quad (5.42)$$

with,

$$\left\{ \begin{array}{l} d_0 = \frac{V_{x0} b_y L_f c_{yf} - PDE \ c_{yf}}{M \ I_z} \\ d_1 = \frac{b_z V_{x0} c_{yf} - PDE \ L_f \ c_{yf}}{M \ I_z \ V_{x0}} \\ d_2 = c_{yf}/M \end{array} \right. . \quad (5.43)$$

5.5.3 Uncertain Plants of $G_3(s)$

The range of variation of each uncertain parameter is similar to what shown in Table 5.3 since it uses the same actuator (steering) for regulation. According to these variations, three plants were chosen and named as: the medium plant, minimum plant, and maximum plant. Figure 5.27 shows the influence of the uncertainty in the frequency domain.

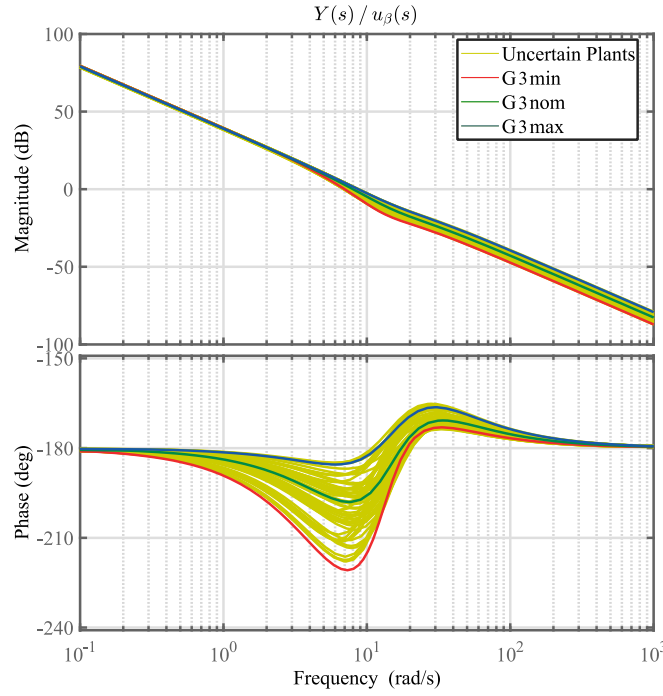


Figure 5.27. Bode responses of uncertain plants of $G_3(s)$.

5.5.4 Control design

Figure 5.28 shows the control scheme for the lateral position regulation using the active steering control input $u_y(t)$. The open-loop crossover frequency is chosen to be less than 10 rad/s. For this reason, the third generation CRONE controller must be used. It should be noted that the ‘*med*’ plant is used as a nominal plant for control synthesis. Following the same process of the previous methodology, the parameters of the 3rd generation CRONE controller $C_3(s)$ are calculated.

For $n_l = 3$ and $n_h = 2$, the control parameters obtained are: $\omega_r = 8.21 \text{ rad/s}$, $Y_r = 0.01$, $\omega_{-1} = 2.3 \text{ rad/s}$, $a_{-1} = 3.7$, $b_{-1} = 3.8$, $\omega_0 = 2.57 \text{ rad/s}$, $a_0 = -1.33$, $b_0 = -1.75$, $\omega_1 = 6 \text{ rad/s}$, $a_1 = 2.18$, $b_1 = 0.55$, and $\omega_2 = 12 \text{ rad/s}$. The resulting open-loop crossover frequency is $\omega_u = 8.3 \text{ rad/s}$ for the nominal plant. Then the PID control parameters are computed as follows: $\omega_i = 0.28 \text{ rad/s}$, $\omega_b = 1.43 \text{ rad/s}$, $\omega_h = 48 \text{ rad/s}$, and $C_0 = 0.246$. Figure 5.29 shows the Bode plot of the transfer function of the two controllers and Figure 5.30 presents the Bode response of the open-loop transfer functions with the two designed controllers.

Figures 5.18 and 5.19 show the Nichols chart of the open-loop transfer function for the three uncertain plants for both controllers. It can be seen that the open-loop transfer function for the nominal plant for both controllers is tangent to the 3dB contour.

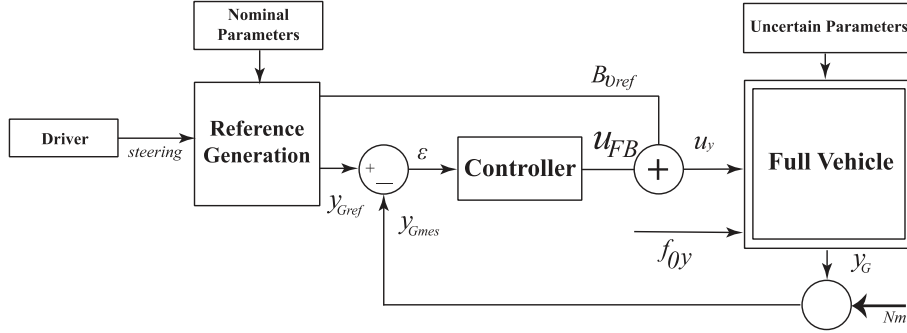


Figure 5.28. Functional diagram of lateral position control by active steering

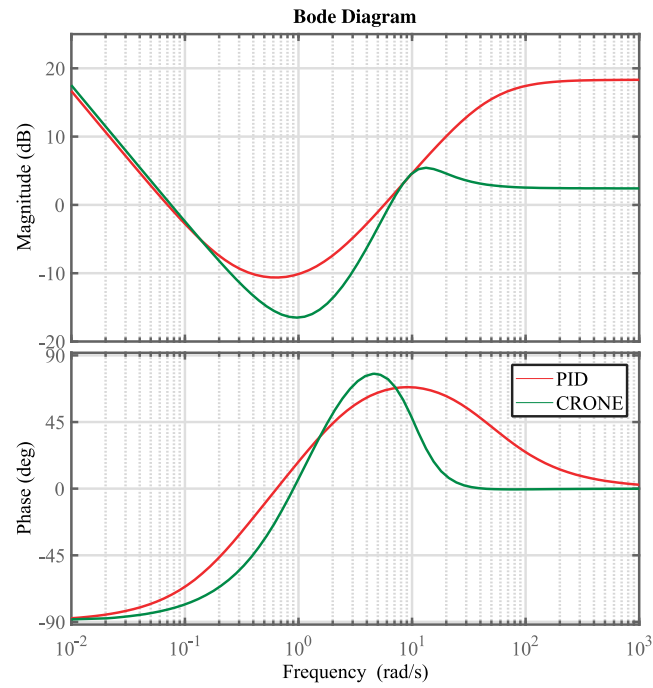


Figure 5.29. Bode response of the transfer functions of the controllers.

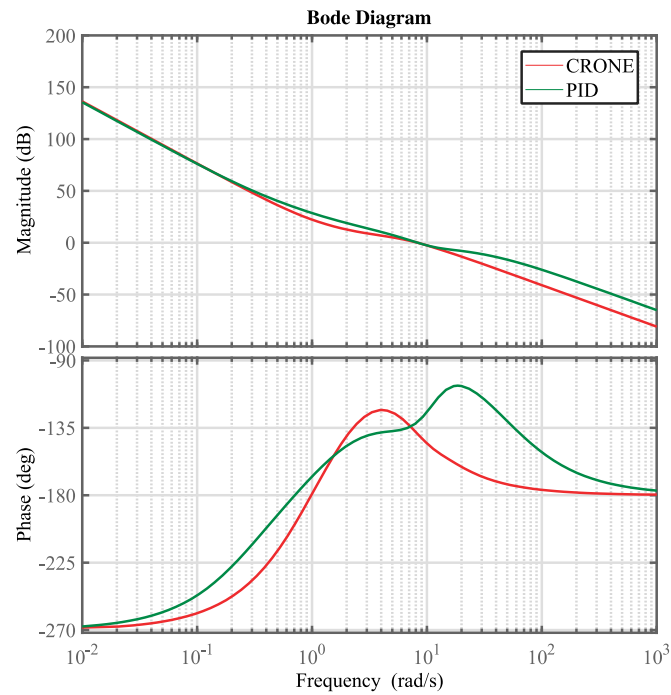


Figure 5.30. Bode plot of the open-loop transfer functions with both controllers.

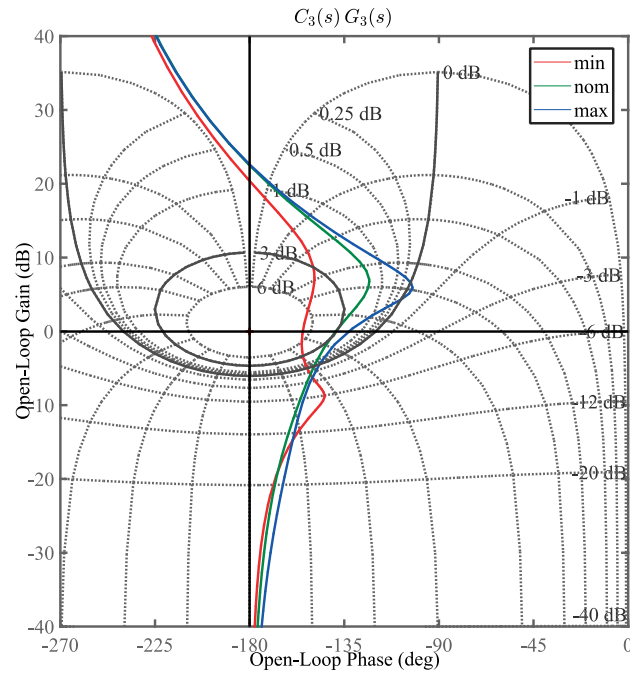


Figure 5.31. Nichols chart for open-loop transfer functions with CRONE controller $C_3(s)$.

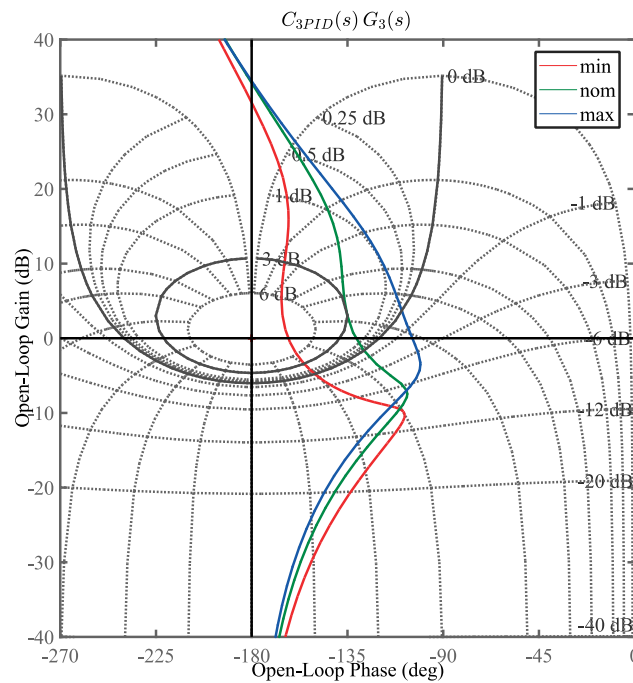


Figure 5.32. Nichols chart for open-loop transfer functions with $C_{3PID}(s)$.

5.5.5 Test simulations

In order to assess the performance of the lateral position control, a vehicle driven with an initial speed of 55km/h is simulated with a steering profile similar to that used in scenarios (A). At $t=1$ s, a lateral wind gust force of 400N hit the vehicle and last for 1.5s. In this simulation, the road is assumed perfectly dry and even.

Figure 5.33 plots the yaw rate performance of the controlled system and the passive system compared to the generated reference yaw rate. In this study, the objective is not to track the yaw rate, so it is anticipated that the controlled systems are not tracking the yaw rate reference. However, it can be seen that they have less deviation compared to the uncontrolled system. Figure 5.34 shows the active steering control angle of both controllers. Figure 5.35 shows the lateral acceleration of the controlled system compared to the passive one, and Figure 5.36 plots the vehicle trajectories. It can be deduced that the control systems are perfectly tracking the reference trajectory but at the expense of higher lateral acceleration.

In some situations, higher values of the lateral acceleration mean degradation in vehicle's stability. For this reason, a compromise must be done between the tracking trajectory and vehicle stability based on the sensing data from the environment and the situation in which the vehicle is operating.

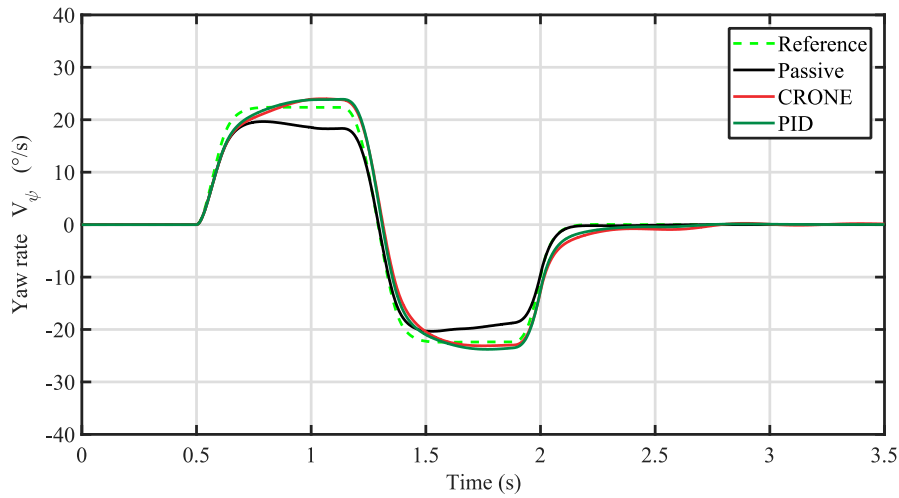


Figure 5.33. Yaw motion with lateral position control.

5.5 Lateral position Control

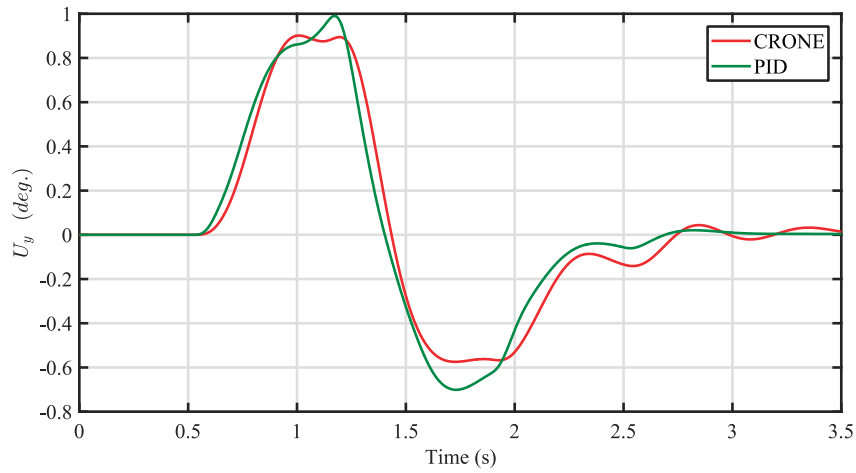


Figure 5.34. Active steering control angles.

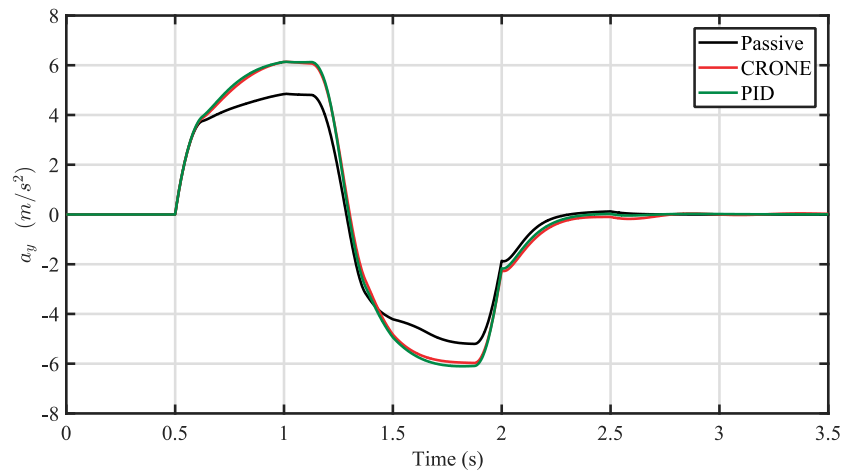


Figure 5.35. Lateral acceleration with lateral position control.

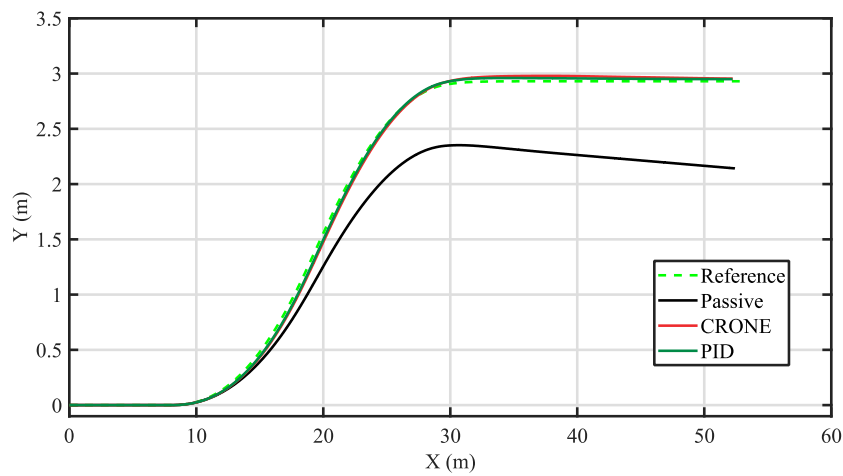


Figure 5.36. Vehicle trajectories with lateral position control.

5.6 Effect of the Vertical dynamics on the lateral stability control

The objective of the following section is to analyze the effect of the vertical dynamics of the vehicle on the designed lateral stability control systems. For this purpose, a simulation was done on a complete 14DoF vehicle model that includes a passive suspension configuration and compared to the results obtained with a model neglecting the vertical dynamics.

Scenario (A) is replicated here and only the CRONE controllers are considered. Then, a comparison is done between a system with the vertical dynamics, denoted by (with VD) and another one neglecting the vertical dynamics (without VD). It should be noted that the performance of the passive system that appears in the following figures includes the effect of the vertical dynamics.

In the first simulation, the controlled system is regulating the yaw rate dynamics by braking torques, that is $C_1(s)$ is used. Figure 5.37 shows the yaw rate response that compares the controlled systems with and without vertical dynamics with the passive system. It is shown that the two controlled systems differ at the end of the maneuvering, approximately around $2 < t < 3s$. It can be noticed that the yaw motions are higher for systems with vertical dynamics. Figure 5.38 shows the control effort of the controllers in both cases, in which it is clear that with vertical dynamics, higher control effort torques are needed to track the generated reference.

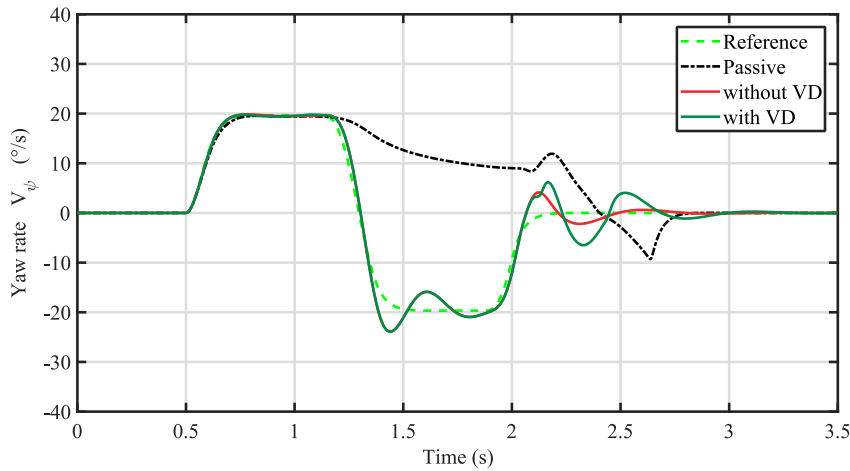


Figure 5.37. Yaw rate motions with CRONE controller.

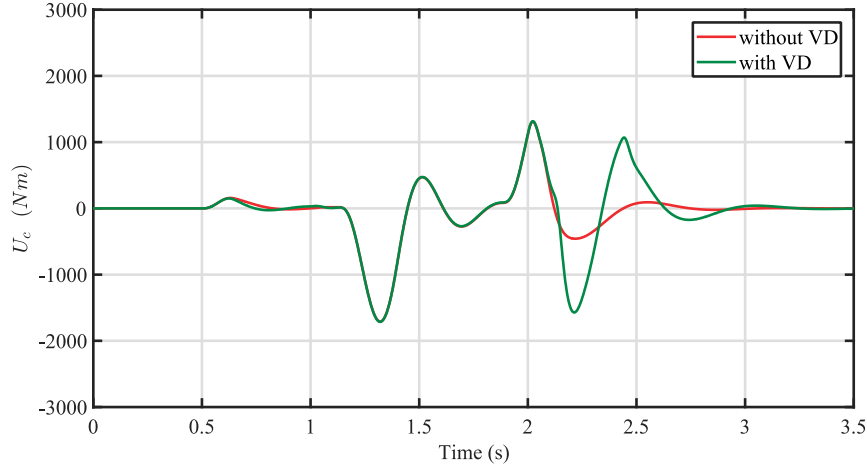


Figure 5.38. Yaw moment control efforts.

The reason for increasing the needed control effort for tracking the yaw rate reference is well illustrated in Figures 5.39 and 5.40. In fact, the significant variation of normal wheel forces (F_z) leads to the difference between the lateral forces at each tire between the two compared system. Figure 5.39 shows the lateral forces generated on each tire for the CRONE controlled system, comparing the systems with and without vertical dynamics.

The big difference occurred at instances where the lateral acceleration is higher than $0.4g$, namely the emergency operating region, as shown in Figure 5.40. In this region, the high value of lateral acceleration increases the transverse load transfer and this leads to a higher variation of F_z . Consequently, the system will go far from the nominal behavior of the reference model (bicycle model), which requires a higher control effort to be able to track the generated reference.

These results translated in Figure 5.41: the uncontrolled system went out of the trajectory, where the vehicle lost its maneuverability. On the other hand, the controlled systems attain stability with a small difference in the obtained trajectories between the systems with and without the vertical dynamics.

5.6 Effect of the Vertical dynamics on the lateral stability control

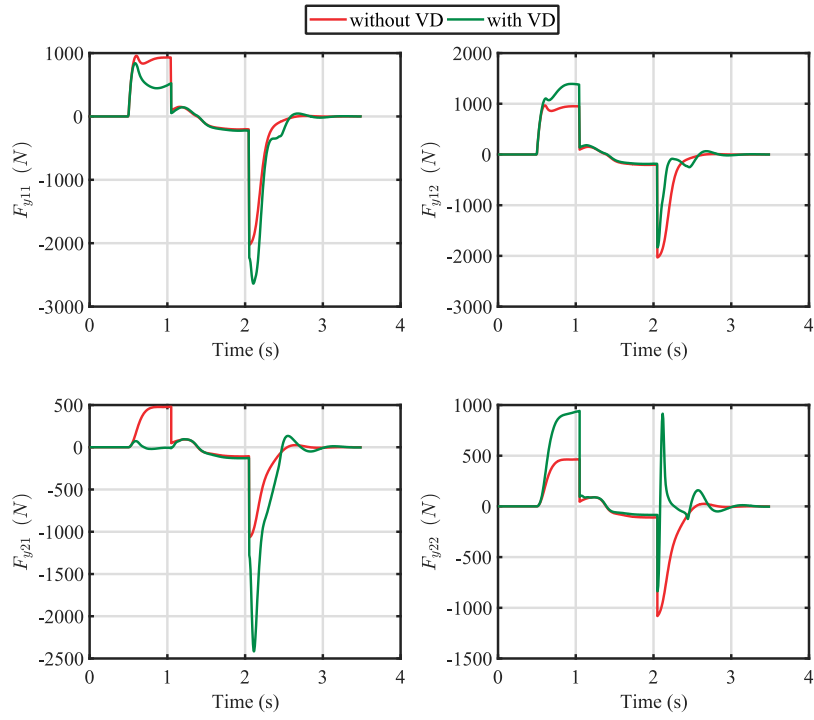


Figure 5.39. Lateral forces of four tires.

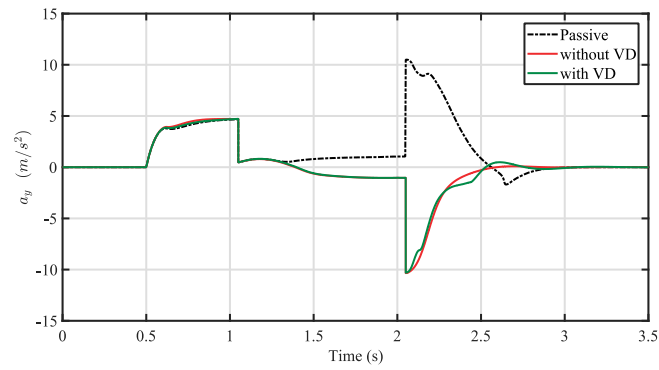


Figure 5.40. Lateral accelerations comparison.

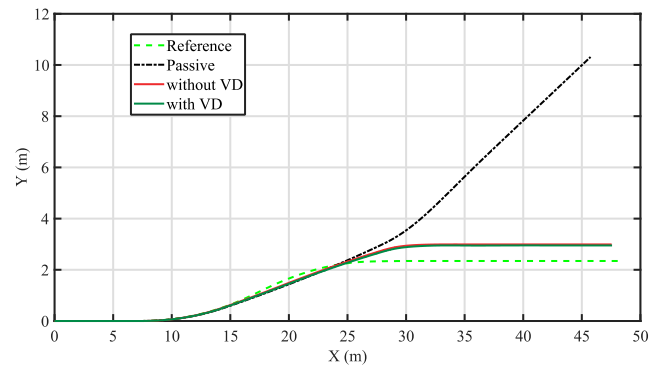


Figure 5.41. Vehicle's trajectory.

The second simulation will examine the limitations of the designed controller in stabilizing the vehicle. In this scenario, a vehicle with an initial speed of 90km/h will undergo a double lane maneuver (DLM) whose steering profile plotted in Figure 5.42. The road surface is considered perfectly dry, which is $\mu = 1$. In fact, this kind of scenario is considered as critical and emergent maneuvering in which the driver is trying to avoid an obstacle.

Figure 5.43, 5.44, and 5.45 show the yaw rate response, active steering control angle, and the lateral accelerations in the double lane maneuver scenario, respectively. The controlled systems show a good tracking of yaw rate references whether with vertical dynamic or not, with a little advantage to the system without vertical dynamics. However, as shown in Figure 5.44, the control effort of the system without vertical dynamics was saturated for around 0.25s, in addition to the higher mean value of the active steering angle demanded to regulate the yaw rate dynamics. Figure 5.45 shows the high lateral accelerations, that admits the nonlinear behavior of the vehicle (outside the linear zone).

Figure 5.46 shows the difference in the lateral forces between the two systems, where it is obvious that the transverse load transfer is highly influencing the forces distribution. Finally, Figure 5.47 plots the vehicle trajectories in which the uncontrolled system deviates from the reference path and the controlled systems have stabilized the vehicle around the generated reference.

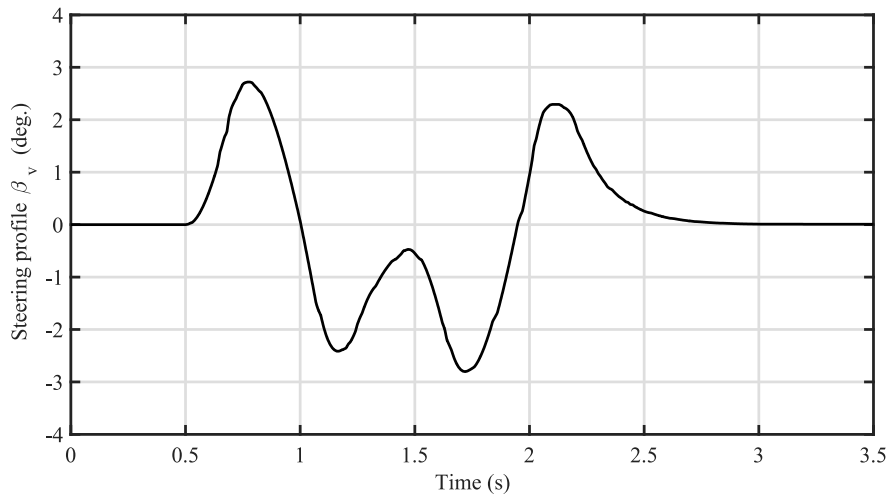


Figure 5.42. Steering profile of double lane maneuver.

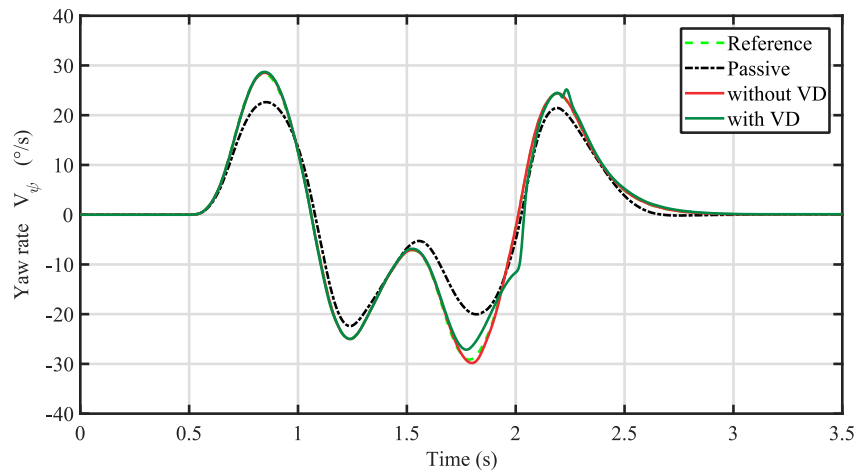


Figure 5.43. Yaw rate response in a double lane maneuver scenario.

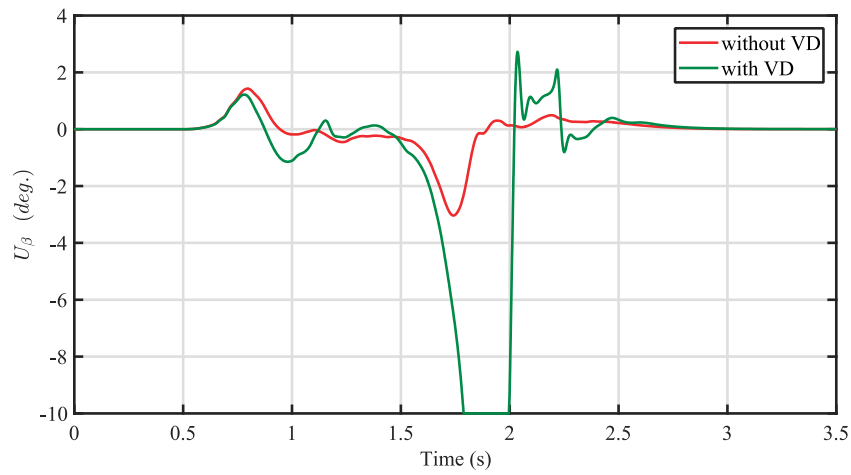


Figure 5.44. Active steering control angle in a double lane maneuver scenario.

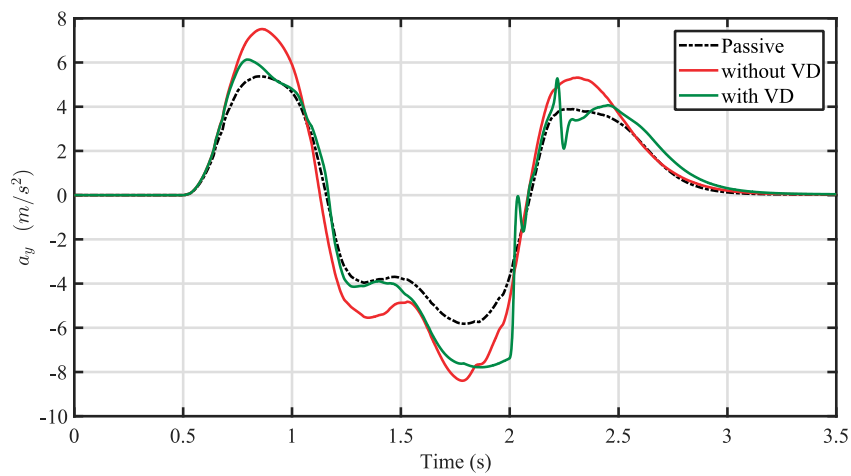


Figure 5.45. Lateral accelerations in a double lane maneuver scenario.

5.6 Effect of the Vertical dynamics on the lateral stability control

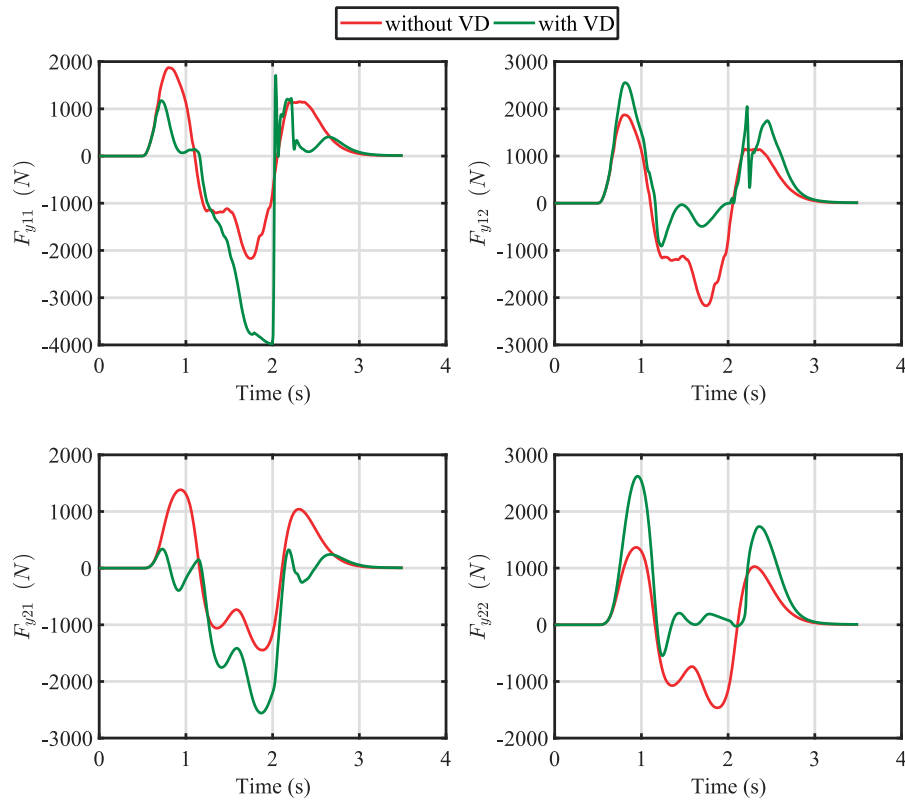


Figure 5.46. Lateral forces at four tires in a double lane maneuver scenario.

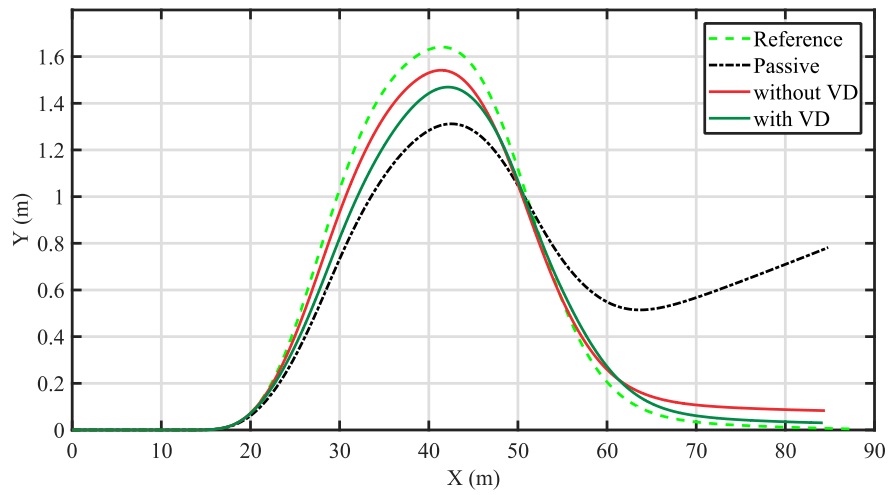


Figure 5.47. Vehicle trajectories in a double lane maneuver scenario.

5.7 Conclusion

Vehicle lateral instability may be caused by many factors such as a sudden side wind or sudden braking and maneuvering on different road conditions. It is necessary to generate a corrective yaw moment to compensate for the lateral instability under such situations. There are two main methods to achieve a corrective yaw moment: first, by active steering and, second, by active braking. In addition, the control of the lateral position of the vehicle is of high interest nowadays, particularly incongruent with the new trend of autonomous vehicles.

Three control strategies were designed and tested in this chapter in order to enhance the vehicle's stability and lateral position of the vehicle. Each controller was tested individually against external disturbances and parametric variations. The designed controllers proved their ability to attain good performance in stabilizing the vehicle in different testing conditions. The study adopted the assumption of a vehicle with a constant speed and low steering profiles. For this reason, these studies can be extended to consider higher speeds and higher steering profiles as well, where different controllers are expected to be implemented.

Moreover, the effect of vertical dynamics on the lateral stability control was studied in this chapter. It was shown that the influence of the load transfer leads to a significant effect on the stability control in scenarios where the vehicle is no longer operating in the comfort zone, in which the lateral acceleration is higher than $0.4g$. In fact, these active control systems were designed independently for improving specific vehicle performance, and so their functions are limited because, mainly, of the non-linearity of tires forces and the essential dynamic coupling between these systems.

Finally, the coordination between these systems is needed to optimize further the overall performance of vehicle dynamics. Nowadays, the integration of these active control systems has become an interesting topic in vehicle dynamics and control fields. For this reason, this study is assigned as future work where a coordinating strategy should be done for yaw rate regulation, that takes into account the actuator dynamics (braking and active steering),

5.7 *Conclusion*

combined with the lateral position control, in the sense of improving the overall performance of the electric vehicle's safety and stability.

General Conclusion and Perspectives

General Conclusion

This thesis has been devoted to the problem of improving the vehicle dynamics in terms of comfort, road holding, and safety. Being aware of the new rising trend of autonomous vehicles, and the fact that the world is shifting towards mobile electrification, the study adopted the light electric vehicle as a study platform. Moreover, as all-in-wheels considered one of the promising technologies in this new trend, the Active Wheel structure was introduced.

The thesis has been addressed various studies aiming at enhancing the vertical, longitudinal, and lateral dynamics of the vehicle using the different active systems. For this purpose, several control problems have been solved through the use of the CRONE methodology CSD. Emphasis was placed on using the CRONE controller in order to take advantage of its robustness against plant uncertainties (or perturbations) that are taken into account with no distinction of their nature in control design, whether they are structured (parametric) or unstructured. More importantly, the CRONE studies paved the way for further studies related to fractional-order controllers, which have become of high interest to the author as future concerns.

In summary, the works of the thesis are presented in 3 main parts and 5 chapters as follows:

- In the first chapter, a general introduction to the automotive suspension systems have been presented. Then, some well-known vehicle models, used for design and simulation and focusing on the vertical dynamics, are given. A general introduction of the suspension role and the three generations of CRONE controllers are presented. In addition,

it introduced the strategies adopted, the used approach, and the assigned objectives.

- The second Chapter recalls some background regarding the vertical dynamics of the vehicle, where it focuses on the vertical dynamics of the quarter vehicle model. Then, it addressed in detail the frequency-domain studies of this model. The first investigation has been made in designing a low bandwidth control that adjusts the height of the vehicle, and the chassis dynamics as well, that is the roll and pitch angle. Then, for the purpose of ride comfort and road holding enhancement, two oriented fractional-order damping controllers were designed using the 2nd generation CRONE control approach.
- In the third chapter, a hierarchical control strategy, based on two-level controllers (global and local), is proposed for the active suspension system embedded in the Active Wheel, for driver disturbance rejection. The study aims to control the three main chassis dynamics to compensate for the heave, pitch, and roll motion simultaneously by a global controller. Moreover, the study adopted the 2DOF quarter vehicle model that had been controlled by a local controller, in order to investigate the level of disturbance rejection of road unevenness and vibration isolation. The hierarchical approach is then stated as a validated approach for certain road structures and classes.
- In the fourth chapter, investigations have been done on improving the braking performance of ABS control on even and rough terrains. At first, a 3rd generation CRONE controller is designed to maximize the efficiency of the braking system of Active Wheel. The study takes into consideration the road adhesion variations, vehicle mass variation, and vehicle velocity variations. The final objective of this system is to reduce the braking distances while taking into consideration system limitations and noise measurement criterion. Then, the half-vehicle model is used to study the effect of the load transfer disturbance on the performance of the ABS

controller. In the end, the road disturbances were taken into account, and some testing scenarios made to find out its effect on the ABS performance. In order to minimize the performance deterioration, the fractional-order damping controllers introduced in Chapter 2, are also implemented to test for its influence on the overall system, in its different orientation, i.e. comfort-oriented and road holding oriented controllers.

- In the last chapter, the study is shifted towards lateral dynamics control. The study was focused on yaw motion control, and the objective is to enhance the performance of the lateral dynamics of the vehicle. Three 3rd generation CRONE controllers were designed: two for yaw rate regulation using either braking torques or by additive active steering angle, and the third one addresses the lateral position control of the vehicle. Finally, the effect of the vertical dynamics of the chassis was analyzed on the performance of the designed lateral controllers.

Perspectives

During the thesis, several developments were made and some results have been obtained. Besides, regarding the presented works, various studies seem to be of great interest to be continued and developed in the future.

In terms of control methodologies, more rigorous investigations on comparing the designed controllers with other robust controllers are of high value. Mainly in the short term, the priority is given for fractional-order controllers. In this sense, different optimization algorithms are found in the literature, related to control parameters selection, could be used.

For suspension control design and analysis, more strategies have to be designed to fulfill the objectives related to high road classes and singular road disturbances. The study can consider various road characteristics to place a more convenient controller for each case. In fact, due to the continuous improvement on the sensing technologies, the road structure and characteristics can be now extracted and then managed by the vehicle's

supervisor. Thus, it facilitates control switching to achieve an optimized suspension performance.

Due to the fact that most controllers consider that the vehicle is operating in the comfort zone, other control strategies should be implemented so that it deals with critical driving scenarios, either in the level of suspension control or lateral stability controls.

Moreover, as mentioned in Chapter 4, the study can be extended to consider the performance of the ABS function in cornering critical scenarios. In fact, the system should also be able to ensure that handling stability and steerability are maintained. The combination of ABS control and suspension control is an area of improvement, where more suspension control strategies might be designed to enhance the overall performance of maneuvering.

Up to now, the suspension systems, steering systems, and braking systems have been studied, mostly, in a separate manner. The well understanding of the overall vehicle dynamics, motivate us for focusing on deep global chassis control studies in the near future. In fact, well-coordinated strategies between the different active systems should inevitably optimize the overall performance of the vehicle in terms of comfort, handling, and safety.

Finally, it is critically important that the study will be extended later on to consider the dynamics of the actuators of different used active systems, and hopefully, a test of the proposed methods on the real platform will be performed someday in the near future...

References

- AAA Foundation for Traffic Safety, 2019. 2018 Forum on the Impact of Vehicle Technologies and Automation on Vulnerable Road Users and Driver Behavior and Performance : A Summary Report.
- Abe, M., 1994. Study on effects of roll moment distribution control in active suspension on improvement of limit performance of vehicle handling. *Int. J. Veh. Des.* 15, 326–336.
<https://doi.org/10.1504/IJVD.1994.061865>
- Adcox, J., Ayalew, B., Rhyne, T., Cron, S., Knauff, M., 2012. Interaction of anti-lock braking systems with tire torsional dynamics. *Tire Sci. Technol.*
- Agostinacchio, M., Ciampa, D., Olita, S., 2014. The vibrations induced by surface irregularities in road pavements - a Matlab® approach. *Eur. Transp. Res. Rev.* 6, 267–275. <https://doi.org/10.1007/s12544-013-0127-8>
- Ahmad, A., Khan, Z.A., Saad Alam, M., Khateeb, S., 2018. A Review of the Electric Vehicle Charging Techniques, Standards, Progression and Evolution of EV Technologies in Germany. *Smart Sci.* 6, 36–53.
<https://doi.org/10.1080/23080477.2017.1420132>
- Ahmadian, M., Blanchard, E., 2007. Ride Performance Analysis of Semiactive Suspension Systems Based on a Full-Car Model.
<https://doi.org/10.1115/DETC2007-35658>
- Ahn, J.K., Jung, K.H., Kim, D.H., Jin, H.B., Kim, H.S., Hwang, S.H., 2009. Analysis of a regenerative braking system for Hybrid Electric Vehicles using an Electro-Mechanical Brake. *Int. J. Automot. Technol.* 10, 229–234. <https://doi.org/10.1007/s12239-009-0027-z>
- Akbari, A., Lohmann, B., 2010. Output feedback H_∞ /GH2 preview control of active vehicle suspensions: A comparison study of LQG preview. *Veh. Syst. Dyn.* 48, 1475–1494.
<https://doi.org/10.1080/00423110903509327>

- Allen, K.W., 1985. Air Suspension Systems.
<https://doi.org/10.1201/b15560-26>
- Altet, O., Nouillant, C., Buisson, J., Moreau, X., Oustaloup, A., 2003.
 Stability of Hydractive CRONE Suspension. IFAC Proc. Vol. 36, 153–157. [https://doi.org/10.1016/S1474-6670\(17\)36423-6](https://doi.org/10.1016/S1474-6670(17)36423-6)
- Aly, A.A., Zeidan, E.-S., Hamed, A., Salem, F., 2011. An Antilock-Braking Systems (ABS) Control: A Technical Review. *Intell. Control Autom.*
<https://doi.org/10.4236/ica.2011.23023>
- Anderson, J., Kalra, N., Stanley, K., Sorensen, P., Samaras, C., Oluwatola, O., 2016. Autonomous Vehicle Technology: A Guide for Policymakers, Autonomous Vehicle Technology: A Guide for Policymakers. Santa Monica, Calif. <https://doi.org/10.7249/rr443-2>
- Andr  n, P., 2006. Power spectral density approximations of longitudinal road profiles. *Int. J. Veh. Des.* 40, 2–14.
<https://doi.org/10.1504/IJVD.2006.008450>
- Aubouet, S., 2010. Semi-active SOBEN suspensions modeling and control. Institut National Polytechnique de Grenoble - INPG.
- Benine-Neto, A., Moreau, X., Lanusse, P., 2017. Robust control for an electro-mechanical anti-lock braking system: the CRONE approach. *IFAC-PapersOnLine* 50, 12575–12581.
<https://doi.org/10.1016/j.ifacol.2017.08.2198>
- Benine-Neto, A., Scalzi, S., Netto, M., Mammar, S., Pasillas-Lepine, W., 2010. Vehicle yaw rate control based on piecewise affine regions, in: 2010 IEEE Intelligent Vehicles Symposium. pp. 20–25.
<https://doi.org/10.1109/IVS.2010.5548062>
- Benson, A.J., Tefft, B.C., Svancara, A.M., Horrey, W.J., 2018. Potential Reductions in Crashes , Injuries , and Deaths from Large-Scale Deployment of Advanced Driver Assistance Systems (Research Brief). Washington, D.C.
- Berger, C., 2014. From a Competition for Self-Driving Miniature Cars to a Standardized Experimental Platform: Concept, Models, Architecture, and Evaluation 5, 63–79.
- Berlin, C., Adams, C., 2017. Production Ergonomics: Designing Work Systems to Support Optimal Human Performance, Production

- Ergonomics: Designing Work Systems to Support Optimal Human Performance. <https://doi.org/10.5334/bbe>
- Bischoff, J., Marquez-Fernandez, F.J., Domingues-Olavarria, G., Maciejewski, M., Nagel, K., 2019. Impacts of vehicle fleet electrification in Sweden-a simulation-based assessment of long-distance trips. MT-ITS 2019 - 6th Int. Conf. Model. Technol. Intell. Transp. Syst. <https://doi.org/10.1109/MTITS.2019.8883384>
- Blanco, M., Atwood, J., Russell, S., Trimble, T., McClafferty, J., Perez, M., 2016. Automated vehicle crash rate comparison using naturalistic data. Virginia Tech Transportation Institute, Blacksburg,.
- Bohgard, M., Karlsson, S., Lovén, E., Mikaelsson, L.-Å., Mårtensson, L., Osvalder, A.-L., Rose, L., Ulfvengren, P. (Eds.), 2009. Work and Technology on Human Terms. Prevent.
- Bosch, R., 2007. Automotive handbook / Bosch. Bentley Robert Inc, Cambridge, United States.
- Bouvin, J.-L., 2019. Towards an alternative version of the Hydractive CRONE car suspension. Université de Bordeaux.
- Bouvin, J.L., Hamrouni, E., Moreau, X., Benine-Neto, A., Hetnetette, V., Serrier, P., Oustaloup, A., 2018. Hierarchical approach for Global Chassis Control. 2018 Eur. Control Conf. ECC 2018 2555–2560. <https://doi.org/10.23919/ECC.2018.8550398>
- Breuer, B.J., Bill, K.H., 2008. Brake Technology Handbook. SAE. Warrendale. Pennsylvania. USA 117–119.
- Brugger, F., Burckhardt, M., Faulhaber, A., 1989. Anti-lock brake system. US Pat. 4,861,118.
- Casciati, F., Rodellar, J., Yildirim, U., 2012. Active and semi-active control of structures-theory and applications: A review of recent advances. J. Intell. Mater. Syst. Struct. <https://doi.org/10.1177/1045389X12445029>
- Chamseddine, A., Raharijaona, T., Noura, H., 2006. Sliding Mode Control Applied to Active Suspension Using Nonlinear Full Vehicle and Actuator Dynamics. Proc. 45th IEEE Conf. Decis. Control 3597–3602. <https://doi.org/10.1109/CDC.2006.376829>
- Chen, F., Taylor, N., Kringos, N., 2015. Electrification of roads :

- Opportunities and challenges. *Appl. Energy* 150, 109–119.
<https://doi.org/10.1016/j.apenergy.2015.03.067>
- Cicchino, J.B., 2018. Effects of blind spot monitoring systems on police-reported lane-change crashes. *Traffic Inj. Prev.* 19, 615–622.
<https://doi.org/10.1080/15389588.2018.1476973>
- Connair, K.M., Bodie, M.O., Chaumette, P., Catalan, A., 1999. Development of a common vehicle model for chassis control design, in: SAE Technical Papers. <https://doi.org/10.4271/1999-01-0732>
- COP21, 2015. Sustainable Innovation Forum [WWW Document]. URL <http://www.cop21paris.org/>
- Daou, R.A.Z., Moreau, X., Francis, C., 2012. Effect of hydropneumatic components nonlinearities on the CRONE suspension. *IEEE Trans. Veh. Technol.* <https://doi.org/10.1109/TVT.2011.2174168>
- Deur, J., Assadian, F., Hancock, M., 2010. Parameter optimization of PID class of yaw rate controllers. “Control 2010, UKACC Int. Conf. on.” <https://doi.org/10.1049/ic.2010.0293>
- Dix, P., Ashrafi, B., Drakunov, S., Özgüner, U., 1995. ABS Control Using Optimum Search via Sliding Modes. *IEEE Trans. Control Syst. Technol.* <https://doi.org/10.1109/87.370698>
- Dugdale, M., 2018. European countries banning fossil fuel cars and switching to electric [WWW Document]. URL www.roadtraffic-technology.com
- Dunn, N., Dingus, T., Soccolich, S., 2019. Understanding the Impact of Technology : Do Advanced Driver Assistance and Semi- Automated Vehicle Systems Lead to Improper Driving Behavior ? Washington, D.C.
- Eckermann, E., 2001. World History of the Automobile, World History of the Automobile. <https://doi.org/10.4271/r-272>
- EEA, 2015. EEA signals 2013 – Improving air quality in Europe. Copenhagen.
- EEA, 2012. Greenhouse gas emission trends and projections in Europe 2012, Europe. Copenhagen. <https://doi.org/10.2800/56770>
- Ekchian, J., Graves, W., Anderson, Z., Giovanardi, M., Godwin, O.,

- Kaplan, J., Ventura, J., Lackner, J.R., Dizio, P., 2016. A High-Bandwidth Active Suspension for Motion Sickness Mitigation in Autonomous Vehicles. SAE Tech. Pap. 2016-April.
<https://doi.org/10.4271/2016-01-1555>
- ERTRAC, EPoSS, ETIP SNET, 2017. European Roadmap Electrification of Road Transport Status: final for publication.
- European Commission, 2017. Electrification of the Transport System: Studies and Reports.
- Ferguson, S.A., 2007. The effectiveness of electronic stability control in reducing real-world crashes: a literature review. *Traffic Inj. Prev.* 8, 329–338.
- Fialho, I., Balas, G.J., 2002. Road adaptive active suspension design using linear parameter-varying gain-scheduling. *IEEE Trans. Control Syst. Technol.* <https://doi.org/10.1109/87.974337>
- Gáspár, P., Szabó, Z., Bokor, J., Poussot-Vassal, C., Sename, O., Dugard, L., 2007. Towards Global Chassis Control By Integrating the Brake and Suspension Systems. *IFAC Proc.* Vol. 40, 563–570.
<https://doi.org/10.3182/20070820-3-US-2918.00076>
- Gharavi, H., Prasad, K.V., Ioannou, P., 2007. Scanning advanced automobile technology. *Proc. IEEE* 95, 328–333.
<https://doi.org/10.1109/JPROC.2006.888380>
- Giangiulio, E., 2006. 14 dof VERTEC vehicle model VDSIM--Vehicle Dynamic SIMulator Implementation and validation, in: 3rd International Colloquium on Vehicle-Tyre-Road Interaction, Stuttgart, Germany.
- Gillespie, T.D., 1992. Fundamentals of Vehicle Dynamics, Fundamentals of Vehicle Dynamics. <https://doi.org/10.4271/r-114>
- Gohrle, C., Schindler, A., Wagner, A., Sawodny, O., 2014. Design and vehicle implementation of preview active suspension controllers. *IEEE Trans. Control Syst. Technol.*
<https://doi.org/10.1109/TCST.2013.2272342>
- Gombert, B., 2008. eCorner: Propulsion by Hub Motors. *Adv. Eng. Mater.*
<https://doi.org/10.1002/adem.200700310>
- Google, 2019. Waymo: The Google Self-Driving Car [WWW Document].

- URL <https://waymo.com/>
- Gordon, T., Howell, M., Brandao, F., 2003. Integrated control methodologies for road vehicles. *Veh. Syst. Dyn.* <https://doi.org/10.1076/vesd.40.1.157.15877>
- Gotsch, S., 2018. *Crash Course: Putting the AI in the Automotive Industry*. Chicago.
- Haddar, Maroua, Chaari, R., Baslamisli, S.C., Chaari, F., Haddar, Mohamed, 2019. Intelligent PD controller design for active suspension system based on robust model-free control strategy. *Proc. Inst. Mech. Eng. Part C J. Mech. Eng. Sci.* 233, 4863–4880. <https://doi.org/10.1177/0954406219836443>
- Hamersma, H.A., Schalk Els, P., 2014. Improving the braking performance of a vehicle with ABS and a semi-active suspension system on a rough road. *J. Terramechanics* 56, 94–101. <https://doi.org/10.1016/j.jterra.2014.09.004>
- Hamrouni, E., Bouvin, J.-L., Moreau, X., Benine-Neto, A., Hernette, V., Serrier, P., Oustaloup, A., 2018. Hierarchical approach for Global Chassis Control. *ISTE OpenScience ,Control* 2. <https://doi.org/10.21494/ISTE.OP.2018.0281>
- Hamrouni, E., Moreau, X., Benine-Neto, A., Hernette, V., 2019. Skyhook and CRONE active suspensions: A comparative study. *IFAC-PapersOnLine* 52, 243–248. <https://doi.org/10.1016/j.ifacol.2019.09.039>
- Hashemi, E., Zarringhalam, R., Khajepour, A., Melek, W., Kasaiezadeh, A., Chen, S.K., 2017. Real-time estimation of the road bank and grade angles with unknown input observers. *Veh. Syst. Dyn.* 55, 648–667. <https://doi.org/10.1080/00423114.2016.1275706>
- Held, T., Gerrits, L., 2019. On the road to electrification – A qualitative comparative analysis of urban e-mobility policies in 15 European cities. *Transp. Policy* 81, 12–23. <https://doi.org/10.1016/j.tranpol.2019.05.014>
- Highway Loss Data Institute, 2018. *Compendium of HLDI collision avoidance research*.
- Holtz, M., 2016. *Décryptage-nouveau plan " push to pass" de psa peugeot-*

- citroen: l'ambition raisonnable de carlos tavares, son patron.
Retrieved April 15th 2016.
- Hrovat, D., 1997. Survey of Advanced Suspension Developments and Related Optimal Control Applications. *Automatica* 33, 1781–1817.
[https://doi.org/10.1016/S0005-1098\(97\)00101-5](https://doi.org/10.1016/S0005-1098(97)00101-5)
- Huang, C.J., Lin, J.S., Chen, C.C., 2010. Road-adaptive algorithm design of half-car active suspension system. *Expert Syst. Appl.*
<https://doi.org/10.1016/j.eswa.2009.11.089>
- Huang, K., Yu, F., Zhang, Y., 2011. Active controller design for an electromagnetic energy-regenerative suspension. *Int. J. Automot. Technol.* <https://doi.org/10.1007/s12239-011-0100-2>
- Hummel, T., Kühn, M., Bende, J., Lang, A., 2011. Advanced Driver Assistance Systems: An investigation of their potential safety benefits based on an analysis of insurance claims in Germany, Research Report FS 03.
- Iannaccone, I., 2004. NOËL GOLVERS, Ferdinand Verbiest, S.J. (1623-1688) and the Chinese Heaven, University Press, 2003, 676 pp., 46 ill., 4 mappe. ISBN 90-5867-293-X. *Nuncius* 19, 762–763.
<https://doi.org/10.1163/221058704x00533>
- ISO-8608, 2011. International Standard 8608: Mechanical Vibration – Road Surface Profiles – Reporting of Measured Data 2016, 29.
[https://doi.org/ISO 8608:1995 \(E\)](https://doi.org/ISO%208608:1995%20(E))
- Jazar, R.N., 2014. Suspension Mechanisms, in: *Vehicle Dynamics: Theory and Application*. Springer New York, New York, NY, pp. 497–565.
https://doi.org/10.1007/978-1-4614-8544-5_8
- Jing, H., Wang, R., Li, C., Bao, J., 2019. Robust finite-frequency H_∞ control of full-car active suspension. *J. Sound Vib.* 441, 221–239.
<https://doi.org/10.1016/j.jsv.2018.06.047>
- Jost, K., Challen, J., 2019. EVs and AVs for 2020 and beyond. *Auton. Veh. Technol.*
- Kala, R., 2016. On-Road Intelligent Vehicles Motion Planning for Intelligent Transportation Systems British Library Cataloguing-in-Publication Data. Elsevier, Butterworth-Heinemann.
- Kaldas, M.M.S., Henze, R., Küçükay, F., 2011. Improvement of Heavy

- Vehicles Ride and Braking Performance via Combined Suspension and Braking Systems Control. *SAE Int. J. Mater. Manuf.*
<https://doi.org/10.4271/2011-01-0437>
- Karnopp, D., 1983. Active Damping in Road Vehicle Suspension Systems. *Veh. Syst. Dyn.* 12, 291–311.
<https://doi.org/10.1080/00423118308968758>
- Kiencke, U., Nielsen, L., 2005. Automotive control systems: For engine, driveline, and vehicle: Second edition, *Automotive Control Systems: For Engine, Driveline, and Vehicle: Second Edition*.
<https://doi.org/10.1007/b137654>
- Koch, G., Kloiber, T., 2014. Driving state adaptive control of an active vehicle suspension system. *IEEE Trans. Control Syst. Technol.* 22, 44–57. <https://doi.org/10.1109/TCST.2013.2240455>
- Kühn, M., Bende, J., 2014. Accident statistics and the potential of driver assistance systems. Berlin.
- Lanusse, P., Gruel, D.N., Lamara, A., 2016. Toward a CRONE toolbox for the design of full MIMO controllers. 7th International Conference on Fractional Differentiation and its Applications, Novi Sad, Serbia.
- Lanusse, P., Malti, R., Melchior, P., 2013. CRONE control system design toolbox for the control engineering community: Tutorial and case study. *Philos. Trans. R. Soc. A Math. Phys. Eng. Sci.* 371.
<https://doi.org/10.1098/rsta.2012.0149>
- Laurent, D., Sebe, M., Walser, D., 2000. Assembly comprising a wheel and a suspension integrated into the wheel.
- Létévé, A., 2014. Study of the influence of passenger vehicle suspension on vibrational comfort, driving behaviour and operating limits : CRONE approach to formalization, analysis and synthesis. Université de Bordeaux.
- Li, H., Liu, H., Gao, H., Shi, P., 2012. Reliable fuzzy control for active suspension systems with actuator delay and fault. *IEEE Trans. Fuzzy Syst.* <https://doi.org/10.1109/TFUZZ.2011.2174244>
- Li, H., Member, Student, Yu, J., Hilton, C., Liu, H., Member, Senior, 2013. Adaptive Sliding-Mode Control for Nonlinear Active Suspension Vehicle Systems Using T – S Fuzzy Approach 60, 3328–3338.

- Li, P., Lam, J., Cheung, K.C., 2018. Motion-based active disturbance rejection control for a non-linear full-car suspension system. *Proc. Inst. Mech. Eng. Part D J. Automob. Eng.* 232, 616–631.
<https://doi.org/10.1177/0954407017704781>
- Li, X., Liu, W., Zhang, B., Meng, D., 2019. New entrants versus establishers in China and US electric vehicle marketplace: a comparative analysis. *Asia Pacific Bus. Rev.* 25, 19–39.
<https://doi.org/10.1080/13602381.2018.1512258>
- LIAN, Y.F., WANG, X.Y., ZHAO, Y., TIAN, Y.T., 2015. Direct Yaw-moment Robust Control for Electric Vehicles Based on Simplified Lateral Tire Dynamic Models and Vehicle Model. *IFAC-PapersOnLine*. <https://doi.org/10.1016/j.ifacol.2015.12.096>
- Lin, J.S., Huang, C.J., 2004. Nonlinear backstepping active suspension design applied to a half-car model. *Veh. Syst. Dyn.* 42, 373–393.
<https://doi.org/10.1080/0042311042000266784>
- Lin, J.S., Kanellakopoulos, I., 1997. Nonlinear Design of Active Suspensions, in: *Proceedings of the IEEE Conference on Decision and Control*. pp. 45–59. <https://doi.org/10.1109/37.588129>
- Lin, J.S., Ting, W.E., 2007. Nonlinear control design of anti-lock braking systems with assistance of active suspension. *IET Control Theory Appl.* 1, 343–348. <https://doi.org/10.1049/iet-cta:20050218>
- Linder, A., Dukic, T., Hjort, M., Matstoms, Y., Mardh, S., Sundstrom, J., Vadeby, A., Wiklund, M., Ostlund, J., 2007. Methods for the evaluation of traffic safety effects of Antilock Braking System (ABS) and Electronic Stability Control (ESC): A literature review. *Statens väg-och transportforskningsinstitut*.
- Litman, T., 2019. *Autonomous Vehicle Implementation Predictions Implications for Transport Planning*.
- Lucendo, J., 2019. *Cars of Legend: First Cars of History*. Jorge Lucendo.
- Malik, S., Sahu, P.K., 2019. A comparative study on routing protocols for VANETs. *Heliyon* 5, e02340.
<https://doi.org/10.1016/j.heliyon.2019.e02340>
- Malti, R., Melchior, P., Lanusse, P., Oustaloup, A., 2012. Object-oriented CRONE toolbox for fractional differential signal processing. *Signal,*

- Image Video Process. <https://doi.org/10.1007/s11760-012-0323-3>
- Malti, R., Melchior, P., Lanusse, P., Oustaloup, A., 2011. Towards an object oriented CRONE Toolbox for fractional differential systems, in: IFAC Proceedings Volumes (IFAC-PapersOnline). <https://doi.org/10.3182/20110828-6-IT-1002.02443>
- Malti, R., Victor, S., 2015. CRONE Toolbox for system identification using fractional differentiation models. IFAC-PapersOnLine. <https://doi.org/10.1016/j.ifacol.2015.12.223>
- Margolis, D., Shim, T., 2001. Bond graph model incorporating sensors, actuators, and vehicle dynamics for developing controllers for vehicle safety. J. Franklin Inst. [https://doi.org/10.1016/S0016-0032\(00\)00068-5](https://doi.org/10.1016/S0016-0032(00)00068-5)
- Marzbanrad, J., Ahmadi, G., Zohoor, H., Hojjat, Y., 2004. Stochastic optimal preview control of a vehicle suspension. J. Sound Vib. 275, 973–990. [https://doi.org/10.1016/S0022-460X\(03\)00812-5](https://doi.org/10.1016/S0022-460X(03)00812-5)
- McDonald, A., Carney, C., McGehee, D.V., 2018. Vehicle Owners' Experiences with and Reactions to Advanced Driver Assistance Systems.
- McShane, C., 2019. The Automobile: A Chronology of Its Antecedents, Development, and Impact, Routledge Library Editions: The Automobile Industry. Routledge.
- Mechanical Simulation Corporation, 2020. CarSim [WWW Document]. URL <https://www.carsim.com/>
- Millikin, M., 2019. Audi's predictive active suspension in the A8 [WWW Document]. URL <https://www.greencarcongress.com/2019/07/20190719-a8.html>
- Mitschke, M., Wallentowitz, H., 2014. Beurteilungsmaßstäbe und ihre Berechnung (Assessment standards and their calculation), in: Dynamik Der Kraftfahrzeuge (Vehicle Dynamics). Springer FachmedienWiesbaden, pp. 349–367. <https://doi.org/10.1007/978-3-662-06802-1>
- Monot, N., Moreau, X., Benine-Neto, A., Rizzo, A., Aioun, F., 2017. Dynamic Stability Control system: the CRONE approach. IFAC-PapersOnLine 50, 13822–13827.

<https://doi.org/10.1016/j.ifacol.2017.08.2188>

- Morand, A., Moreau, X., Melchior, P., Moze, M., 2013. Robust cruise control using CRONE approach, IFAC Proceedings Volumes (IFAC-PapersOnline). IFAC. <https://doi.org/10.3182/20130204-3-FR-4032.00191>
- Moreau, X., Altet, O., Oustaloup, A., 2004. The CRONE suspension: Management of the dilemma comfort-road holding, in: Nonlinear Dynamics. <https://doi.org/10.1007/s11071-004-3772-6>
- Moreau, X., Nouillant, C., Oustaloup, A., 2001. Effect of the Crone Suspension Control System on Braking. IFAC Proc. Vol. 34, 53–58. [https://doi.org/10.1016/S1474-6670\(17\)34377-X](https://doi.org/10.1016/S1474-6670(17)34377-X)
- Moreau, X., Oustaloup, A., Nouillant, M., 1996. The CRONE Suspension. IFAC Proc. Vol. [https://doi.org/10.1016/s1474-6670\(17\)44677-5](https://doi.org/10.1016/s1474-6670(17)44677-5)
- Moreau, X., Rizzo, A., Oustaloup, A., Libération, D., 2009. Application of the CRONE control-design method to a low-frequency active suspension system. Int. J. Veh. Auton. Syst. 7, 172–200. <https://doi.org/10.1504/IJVAS.2009.033260>
- Mourad, M., Mahmoud, K., 2019. Electrification Strategy of Hybrid Electric Vehicle as a Solution to Decrease CO2 Emission in Cities. Int. J. Electr. Electron. Commun. Sci. 13, 558–564. <https://doi.org/10.5281/ZENODO.3455561>
- Nguyen, D.N., Deng, Z., Cao, Y., 2011. Direct current linear actuator using in the active suspension system of automobile. 2011 Int. Conf. Electr. Inf. Control Eng. ICEICE 2011 - Proc. 5855–5860. <https://doi.org/10.1109/ICEICE.2011.5777281>
- Niemz, T., Winner, H., 2006. Improving Braking Performance By Control of Semi-Active Suspension, in: FISITA 2006 World Automotive Congress.
- Nowakowski, C., Shladover, S.E., Chan, C.Y., 2016. Determining the readiness of automated driving systems for public operation: Development of behavioral competency requirements. Transp. Res. Rec. 2559, 65–72. <https://doi.org/10.3141/2559-08>
- Nyandoro, O.T., Pedro, J.O., Dahunsi, O.A., Dwolatzky, B., 2011. Linear slip control formulation for vehicular anti-lock braking system with

- suspension effects, in: IFAC Proceedings Volumes (IFAC-PapersOnline). <https://doi.org/10.3182/20110828-6-IT-1002.02971>
- OKTALS YDAC, 2018. SCANeR™ studio [WWW Document]. URL www.avsimulation.com/scanerstudio
- Oustaloup, A., 1995. La dérivation non entière. Théorie, synthèse et applications, coll. Traité des nouvelles technologies Série automatique.
- Oustaloup, A., 1991a. La commande CRONE: commande robuste d'ordre non entier, Hermès, Paris. Hermès, Paris.
- Oustaloup, A., 1991b. La dérivation non entière, Hermès, Paris. Hermes.
- Oustaloup, A., 1981. Linear feedback control systems of fractional order between 1 and 2. Proc. - IEEE Int. Symp. Circuits Syst.
- Oustaloup, A., Levron, F., Mathieu, B., Nanot, F.M., 2000. Frequency-band complex noninteger differentiator: Characterization and synthesis. IEEE Trans. Circuits Syst. I Fundam. Theory Appl. 47, 25–39. <https://doi.org/10.1109/81.817385>
- Oustaloup, A., Melchior, P., Lanusse, P., Cois, O., Dancla, F., 2002. The CRONE toolbox for Matlab, in: CACSD. Conference Proceedings. IEEE International Symposium on Computer-Aided Control System Design (Cat. No.00TH8537). pp. 190–195. <https://doi.org/10.1109/cacsd.2000.900210>
- Oustaloup, A., Moreau, X., Nouillant, M., 1996. The crone suspension. Control Eng. Pract. [https://doi.org/10.1016/0967-0661\(96\)00109-8](https://doi.org/10.1016/0967-0661(96)00109-8)
- Pacejka, H.B., 2012. Basic Tire Modeling Considerations, in: Tire and Vehicle Dynamics. pp. 59–85. <https://doi.org/10.1016/b978-0-08-097016-5.00002-4>
- Pan, H., Sun, W., 2019. Nonlinear Output Feedback Finite-Time Control for Vehicle Active Suspension Systems. IEEE Trans. Ind. Informatics 15, 2073–2082. <https://doi.org/10.1109/TII.2018.2866518>
- Pan, H., Sun, W., Jing, X., Gao, H., Yao, J., 2017. Adaptive tracking control for active suspension systems with non-ideal actuators. J. Sound Vib. 399, 2–20. <https://doi.org/10.1016/j.jsv.2017.03.011>
- Parker, L.K., 2002. Henry Ford and the Automobile Industry, American Tycoons. Rosen Publishing Group.

- Peeie, M.H. Bin, Ogino, H., Oshinoya, Y., 2016. Skid control of a small electric vehicle with two in-wheel motors: simulation model of ABS and regenerative brake control. *Int. J. Crashworthiness*.
<https://doi.org/10.1080/13588265.2016.1147731>
- Pendleton, S.D., Andersen, H., Du, X., Shen, X., Meghjani, M., Eng, Y.H., Rus, D., Ang, M.H., 2017. Perception, planning, control, and coordination for autonomous vehicles. *Machines* 5, 1–54.
<https://doi.org/10.3390/machines5010006>
- Penmetsa, P., Adanu, E.K., Wood, D., Wang, T., Jones, S.L., 2019. Perceptions and expectations of autonomous vehicles – A snapshot of vulnerable road user opinion. *Technol. Forecast. Soc. Change* 143, 9–13. <https://doi.org/10.1016/j.techfore.2019.02.010>
- Penny, W.C.W., Els, P.S., 2016. The test and simulation of ABS on rough, non-deformable terrains. *J. Terramechanics* 67, 1–10.
<https://doi.org/10.1016/j.jterra.2016.05.001>
- Pereirinha, P.G., González, M., Carrilero, I., Anseán, D., Alonso, J., Viera, J.C., 2018. Main Trends and Challenges in Road Transportation Electrification, in: *Transportation Research Procedia*. Elsevier B.V., pp. 235–242. <https://doi.org/10.1016/j.trpro.2018.10.096>
- PSA Group, 2017. AVA Autnomous Vehicle for ALL on the road, On board the safe and intuitive autonomous car.
- PSA Group, 2016. Push to Pass Strategy [WWW Document]. URL pushtopass.groupe-psa.com
- Rahiman, W., Zainal, Z., 2013. An overview of development GPS navigation for autonomous car. *Proc. 2013 IEEE 8th Conf. Ind. Electron. Appl. ICIEA 2013* 1112–1118.
<https://doi.org/10.1109/ICIEA.2013.6566533>
- Rajamani, R., 2012a. Active Automotive Suspensions, in: *Vehicle Dynamics and Control*. Springer US, Boston, MA, pp. 301–328.
https://doi.org/10.1007/978-1-4614-1433-9_11
- Rajamani, R., 2012b. Electronic Stability Control, in: *Vehicle Dynamics and Control*. Springer US, Boston, MA, pp. 201–240.
https://doi.org/10.1007/978-1-4614-1433-9_8
- Rajamani, R., 2012c. Adaptive Cruise Control, in: *Vehicle Dynamics and*

- Control. Springer US, Boston, MA, pp. 141–170.
https://doi.org/10.1007/978-1-4614-1433-9_6
- Rajamani, R., 2006. Vehicle Dynamics and Control, Mechanical Engineering Series. Springer US, New York, NY,.
- Rakshith, M., L, Y.K., Vikas, S.G., 2014. Bose Automotive Suspension. Int. J. Recent Technol. Eng. 3, 13–18.
- Rasmussen, G., 1982. HUMAN BODY VIBRATION EXPOSURE AND ITS MEASUREMENT. Tech. Rev. - Bruel Kjaer English ed.
<https://doi.org/10.1121/1.389513>
- Regolin, E., Alatorre, A., Zambelli, M., Victorino, A., Charara, A., Ferrara, A., 2019. A Sliding-Mode Virtual Sensor for Wheel Forces Estimation with Accuracy Enhancement via EKF. IEEE Trans. Veh. Technol. 68, 3457–3471. <https://doi.org/10.1109/TVT.2019.2903598>
- Reif, K., 2014. Antilock braking system (ABS), in: Brakes, Brake Control and Driver Assistance Systems: Function, Regulation and Components. Springer, Friedrichshafen, Germany, pp. 74–93.
<https://doi.org/10.1007/978-3-658-03978-3>
- Reul, M., Winner, H., 2009. Enhanced braking performance by integrated ABS and semi-active damping control, in: Proceedings of the 21st (Esv) International Technical Conference on the Enhanced Safety of Vehicles.
- Rizzo, A., 2012. L'approche CRONE dans le domaine des architectures complexes des suspensions de véhicules automobiles : la suspension CRONE Hydractive. Université de Bordeaux.
- Ruhnau, O., Bannik, S., Otten, S., Praktiknjo, A., Robinius, M., 2019. Direct or indirect electrification? A review of heat generation and road transport decarbonisation scenarios for Germany 2050. Energy 166, 989–999. <https://doi.org/10.1016/j.energy.2018.10.114>
- S, E.C., 1932. Nikolaus August Otto, 1832–1891. Nature 129, 892.
<https://doi.org/10.1038/129892a0>
- Sabatier, J., Lanusse, P., Melchior, P., Oustaloup, A., 2015a. Fractional Order PID and First Generation CRONE Control System Design, in: Fractional Order Differentiation and Robust Control Design. Springer, Dordrecht, Bordeaux, pp. 63–105. <https://doi.org/10.1007/978-94-017->

- Sabatier, J., Lanusse, P., Melchior, P., Oustaloup, A., 2015b. Fractional Order Differentiation and Robust Control Design, *Intelligent Systems, Control and Automation: Science and Engineering*.
<https://doi.org/10.1007/978-94-017-9807-5>
- SAE International, 2018. Taxonomy and definitions for terms related to driving automation [WWW Document]. SAE Int.
https://doi.org/10.4271/J3016_201609
- Sammier, D., Sename, O., Dugard, L., 2003. Skyhook and H8 Control of Semi-active Suspensions: Some Practical Aspects. *Veh. Syst. Dyn.* 39, 279–308. <https://doi.org/10.1076/vesd.39.4.279.14149>
- Sanchez-Torres, J.D., De Loza, A.F., Galicia, M.I., Loukianov, A.G., 2013. ABS design and active suspension control based on HOSM, in: *Proceedings of the American Control Conference*.
<https://doi.org/10.1109/acc.2013.6580862>
- Savaresi, S., Poussot-Vassal, C., Spelta, C., Sename, O., Dugard, L., 2010. Semi-Active Suspension Control Design for Vehicles, *Semi-Active Suspension Control Design for Vehicles*.
<https://doi.org/10.1016/C2009-0-63839-3>
- Schinkel, M., Hunt, K., 2002. Anti-lock braking control using a sliding mode like approach, in: *Proceedings of the American Control Conference*. <https://doi.org/10.1109/acc.2002.1023999>
- Schoettle, B., Sivak, M., 2015. A preliminary analysis of real-world crashes involving self-driving vehicles. *Univ. Michigan Transp. Res. Inst.*
- Shao, X., Naghdy, F., Du, H., Li, H., 2019. Output feedback H_∞ control for active suspension of in-wheel motor driven electric vehicle with control faults and input delay. *ISA Trans.* 92, 94–108.
<https://doi.org/10.1016/j.isatra.2019.02.016>
- Sheikh, M.S., Liang, J., 2019. A comprehensive survey on VANET security services in traffic management system. *Wirel. Commun. Mob. Comput.* 2019. <https://doi.org/10.1155/2019/2423915>
- Shladover, S.E., 2018. Connected and automated vehicle systems: Introduction and overview. *J. Intell. Transp. Syst. Technol. Planning, Oper.* 2450, 190–200. <https://doi.org/10.1080/15472450.2017.1336053>

- Slowik, P., 2019. EXPANDING ZERO-EMISSION MOBILITY EQUITY AND ACCESS.
- SMMT, 2019. CONNECTED AND AUTONOMOUS VEHICLES.
- Soliman, A.M.A., Kaldas, M.M.S., 2012. An investigation of anti-lock braking system for automobiles, in: SAE Technical Papers. <https://doi.org/10.4271/2012-01-0209>
- Standard, 1997. ISO 2631-1 - Mechanical vibration and shock- Evaluation of human exposure to whole-body vibration, ISO - International Organization for Standardization.
- Sternlund, S., Strandroth, J., Rizzi, M., Lie, A., Tingvall, C., 2017. The effectiveness of lane departure warning systems—A reduction in real-world passenger car injury crashes. *Traffic Inj. Prev.* 18, 225–229. <https://doi.org/10.1080/15389588.2016.1230672>
- Sun, W., Gao, H., Kaynak, O., 2015. Vibration isolation for active suspensions with performance constraints and actuator saturation. *IEEE/ASME Trans. Mechatronics* 20, 675–683. <https://doi.org/10.1109/TMECH.2014.2319355>
- Sun, W., Gao, H., Kaynak, O., 2013. Adaptive backstepping control for active suspension systems with hard constraints. *IEEE/ASME Trans. Mechatronics* 18, 1072–1079. <https://doi.org/10.1109/TMECH.2012.2204765>
- Sun, W., Pan, H., Gao, H., 2016. Filter-Based Adaptive Vibration Control for Active Vehicle Suspensions with Electrohydraulic Actuators. *IEEE Trans. Veh. Technol.* 65, 4619–4626. <https://doi.org/10.1109/TVT.2015.2437455>
- Sustainable Innovation Forum, 2019. Accelerating Solutions for Climate Action at COP25, 10-11 December, Madrid, Spain. [WWW Document]. URL cop-25.org
- Tang, Y., Zhang, X., Zhang, D., Zhao, G., Guan, X., 2013. Fractional order sliding mode controller design for antilock braking systems. *Neurocomputing*. <https://doi.org/10.1016/j.neucom.2012.12.019>
- Tchamna, R., Youn, I., 2013. Yaw rate and side-slip control considering vehicle longitudinal dynamics. *Int. J. Automot. Technol.* <https://doi.org/10.1007/s12239-013-0007-1>

- Termous, H., Moreau, X., Francis, C., Shraim, H., 2018a. From the standard PID to the CRONE first generation controller: Application to an anti-roll system for Electric Vehicles. *IFAC-PapersOnLine* 51, 733–738. <https://doi.org/10.1016/j.ifacol.2018.06.209>
- Termous, H., Shraim, H., Talj, R., Francis, C., Charara, A., 2018b. Coordinated control strategies for active steering, differential braking and active suspension for vehicle stability, handling and safety improvement. *Veh. Syst. Dyn.* 3114, 1–36. <https://doi.org/10.1080/00423114.2018.1521001>
- TESIS, 2020. *veDYNA: Real-Time Simulation of Vehicle Dynamics*.
- Till Bunsen, Cazzola, P., D’Amore, L., Gerner, M., Scheffer, S., Schuitmaker, R., Signollet, H., Tattini, J., Paoli, J.T.L., 2019. Global EV Outlook 2019 to electric mobility. OECD iea.org.
- Tran, A., 2017. ProteanDRIVE® in-wheel motors on show at auto Shanghai 2017. *Automot. Ind. AI*.
- Tseng, H.E., Hrovat, D., 2015. State of the art survey: Active and semi-active suspension control. *Veh. Syst. Dyn.* 53, 1034–1062. <https://doi.org/10.1080/00423114.2015.1037313>
- Tyan, F., Hong, Y.-F., Tu, S.-H., Jeng, W.S., 2009. Generation of random road profiles. *J. Adv. Eng.* 4, 151–156. <https://doi.org/10.1016/j.adveng.2009.10.001>
- US DOT, 2016. Bureau of Transportation Statistics [WWW Document]. U.S. Transportation. URL http://www.rita.dot.gov/bts/data_and_statistics/by_mode/airline_and_airports/airline_passengers.html
- van der Merwe, N.A., Els, P.S., Žuraulis, V., 2018. ABS braking on rough terrain. *J. Terramechanics* 80, 49–57. <https://doi.org/10.1016/j.jterra.2018.10.003>
- Vellinga, N.E., 2017. From the testing to the deployment of self-driving cars: Legal challenges to policymakers on the road ahead. *Comput. Law Secur. Rev.* 33, 847–863. <https://doi.org/10.1016/j.clsr.2017.05.006>
- Viehweiger, M., Vaseur, C., Aalst, S. Van, Acosta, M., Regolin, E., Alatorre, A., Desmet, W., Naets, F., Ivanov, V., Ferrara, A., Victorino, A., Regolin, E., Alatorre, A., Desmet, W., Naets, F.,

- Ivanov, V., Ferrara, A., 2020. Vehicle state and tyre force estimation : demonstrations and guidelines. *Veh. Syst. Dyn.* 0, 1–28.
<https://doi.org/10.1080/00423114.2020.1714672>
- Vivas-López, C.A., Hernandez-Alcantara, D., Tudón-Martínez, J.C., Morales-Menendez, R., 2013. Review on global chassis control, in: *IFAC Proceedings Volumes (IFAC-PapersOnline)*. pp. 875–880.
<https://doi.org/10.3182/20130204-3-FR-2033.00040>
- Wadud, Z., MacKenzie, D., Leiby, P., 2016. Help or hindrance? The travel, energy and carbon impacts of highly automated vehicles. *Transp. Res. Part A Policy Pract.* 86, 1–18.
<https://doi.org/10.1016/j.tra.2015.12.001>
- Wakeman, K., Moore, M., Zubby, D., Hellinga, L., 2018. Effect of Subaru EyeSight on pedestrian-related bodily injury liability claim frequencies. *Highw. Loss Data Institute, Bulletin* 34, 1–7.
- Wang, H.P., Mustafa, G.I.Y., Tian, Y., 2018. Model-free fractional-order sliding mode control for an active vehicle suspension system. *Adv. Eng. Softw.* 115, 452–461.
<https://doi.org/10.1016/j.advengsoft.2017.11.001>
- Wang, J., Wang, Q., Jin, L., Song, C., 2011. Independent wheel torque control of 4WD electric vehicle for differential drive assisted steering. *Mechatronics* 21, 63–76.
<https://doi.org/https://doi.org/10.1016/j.mechatronics.2010.08.005>
- Wang, R., Tran, V.T., Gu, F., Ball, A.D., 2013. An investigation on energy recovery analysis of active suspension system. *ICAC 2013 - Proc. 19th Int. Conf. Autom. Comput. Futur. Energy Autom.* 1, 287–292.
- Winner, H., Hakuli, S., Lotz, F., Singer, C., 2015. Handbook of driver assistance systems: Basic information, components and systems for active safety and comfort. *Handb. Driv. Assist. Syst. Basic Information, Components Syst. Act. Saf. Comf.* 1–1602.
<https://doi.org/10.1007/978-3-319-12352-3>
- Wong, P.K., Huang, W., Wong, K.I., Vong, C.M., 2019. Adaptive Control of Vehicle Yaw Rate with Active Steering System and Extreme Learning Machine - A Pilot Study, in: Cao, J., Vong, C.M., Miche, Y., Lendasse, A. (Eds.), *Proceedings of ELM-2017*. Springer

- International Publishing, Cham, pp. 1–11.
- Wu, J.L., 2017. A Simultaneous Mixed LQR/ H_∞ Control Approach to the Design of Reliable Active Suspension Controllers. *Asian J. Control* 19, 415–427. <https://doi.org/10.1002/asjc.1058>
- Xu, S., Peng, H., Lu, P., Zhu, M., Tang, Y., 2020. Design and Experiments of Safeguard Protected Preview Lane Keeping Control for Autonomous Vehicles. *IEEE Access* 8, 29944–29953. <https://doi.org/10.1109/ACCESS.2020.2972329>
- Yu, M., Arana, C., Evangelou, S.A., Dini, D., Cleaver, G.D., 2018. Parallel Active Link Suspension: A Quarter-Car Experimental Study. *IEEE/ASME Trans. Mechatronics* 23, 2066–2077. <https://doi.org/10.1109/TMECH.2018.2864785>
- Zhao, J., Hua, X., Cao, Y., Fan, L., Mei, X., Xie, Z., 2019. Design of an integrated controller for active suspension systems based on wheelbase preview and wavelet noise filter. *J. Intell. Fuzzy Syst.* 36, 3911–3921. <https://doi.org/10.3233/JIFS-181117>
- Zhou, H., Liu, Z., 2010. Vehicle yaw stability-control system design based on sliding mode and backstepping control approach. *IEEE Trans. Veh. Technol.* <https://doi.org/10.1109/TVT.2010.2050790>
- Zhuo, G., Xue, R., Zhang, S., Wu, C., Xiong, K., 2017. The Design and Evaluation of EMB Actuator Scheme The Establishment of Parametric 3D Model. *SAE Tech. Pap.* <https://doi.org/10.4271/2017-01-2509>. Copyright
- Zuo, L., Nayfeh, S.A., 2003. Low order continuous-time filters for approximation of the ISO 2631-1 human vibration sensitivity weightings. *J. Sound Vib.* 265, 459–465. [https://doi.org/10.1016/S0022-460X\(02\)01567-5](https://doi.org/10.1016/S0022-460X(02)01567-5)

Production scientifique de l'auteur

A1 - Revues Internationales avec Comité de Lecture

2020

- [A1.20.1] - H. TERMOUS, X. MOREAU, C. FRANCIS and H. SHRAIM – Hierarchical Approach for Driver Disturbance Rejection in an Electric Vehicle: The CRONE Approach – Regular paper, IEEE Transactions on Vehicular Technology, ISSN: 0018-9545, DOI: ?????, Vol. ??, N°??, pp. ??-??, Date of publication: ?????. Manuscript ID: VT-2020-00524, 1ère soumission le 12 Février 2020. IF: 5.339 en 2018.

C1 – Colloques Internationaux avec Actes et Comité de Lecture

2018

- [C1.18.1] - H. TERMOUS, X. MOREAU, C. FRANCIS and H. SHRAIM – From the standard PID to the CRONE first generation controller : application to an anti-roll system for Electric Vehicles – 3rd IFAC Conference on Advances in Proportional-Integral-Derivative Control PID 2018, IFAC, Vol.51, Issue 4, pp.733-738, Ghent, Belgium, 9-11 May 2018. <https://doi.org/10.1016/j.ifacol.2018.06.209>

2019

- [C1.19.1] - H. TERMOUS, X. MOREAU, C. FRANCIS and H. SHRAIM – Effect of fractional order damping control on braking performance for electric vehicles – 9th **IFAC** International Symposium on Advances in Automotive Control (AAC'19), Orléans, France, 24-27 June 2019. <https://doi.org/10.1016/j.ifacol.2019.09.037>
- [C1.19.2] - H. TERMOUS, X. MOREAU, C. FRANCIS and H. SHRAIM – Effect of Vertical Dynamics on the Lateral Stability Control System – 30th **IEEE** Intelligent Vehicles Symposium, IV19, DOI: [10.1109/IVS.2019.8814199](https://doi.org/10.1109/IVS.2019.8814199) - Paris, France, 9-12 June 2019.

C2 – Colloques Nationaux avec Actes et Comité de Lecture

2019

- [C2.19.1] - H. TERMOUS, X. MOREAU, C. FRANCIS and H. SHRAIM – Effect of vertical dynamics on vehicle's lateral stability control system – 8ème Journées Doctorales et Journées Nationales du GDR MACS, JDMACS 2019, Bordeaux, France, 5 - 7 Juin 2019.

